THE MANESS SHALE: A COMPARISON OF THE GEOMECHANICAL AND MINERALOGICAL PROPERTIES WITHIN THE LOWER EAGLE FORD FORMATION, SOUTH TEXAS

BY

SAMANTHA A. PATTERSON

Bachelor of Science, 2013
Texas Christian University
Fort Worth, Texas

Submitted to the Graduate Faculty of
The College of Science and Engineering
Texas Christian University
In partial fulfillment of the requirements for the degree of

MASTER OF SCIENCE

December, 2018

ACKNOWLEDGMENTS

I would like to thank the TCU Department of Geological Sciences for the support I received throughout both my undergraduate and graduate careers. The relationships I developed during my time at TCU are irreplaceable.

This project would not have been the same without the support, patience, and knowledge of my thesis advisor, Dr. Richard Denne. His willingness to take me on as his first graduate student and share his passion of mudrocks truly inspired me to take my work one step further. I would also like to express my gratitude to Dr. Helge Alsleben, who has been a mentor to me since my time at TCU began nearly ten years ago. His leadership and insight have always proven extremely helpful. I have been incredibly fortunate to have Ms. Jana Payne as my mentor, friend, and manager. Her passion for her work is motivating and inspiring. I would like to thank Alec Burns, as he assisted me in the geomechanical data collection.

Without Lonestar Resources, especially Mr. Frank Bracken, this journey may have never begun. Without hiring me years ago, I may never have become a geologist. Without the willingness to support this project with data and cores, this project would not have started. Thank you Lonestar. Also supporting this project with data was Drilling Info. Their generosity is very much appreciated.

I would like to thank my parents, for their constant support throughout my life. They have continuously expressed their support and praise and have always pushed me to higher standards. Without their encouragement, I would not be where I am today.

Finally, I would like to thank my graduate student tribe that turned into family, and my boyfriend Joe Kuntz, for being my source of support, in more ways than one.

Table of Contents

List of Figures

List of Tables

Introduction

Unconventional shale plays have been a significant source of natural gas, gas condensates, and crude oil throughout North America since the mid-2000's. The Eagle Ford Shale in South Texas is among the top shale producers, producing over 1,400 MMBO/Day (EIA, 2018). This play extends from College Station to the USA-Mexico border following the trend of the coast line, covering several million acres (million hectares).

The Lower Cenomanian Maness Shale is a clay-rich mudrock originally identified in the East Texas field lying between the Woodbine and Buda Limestone that has been correlated to the basal Lower Eagle Ford in the vicinity of the San Marcos Arch (Denne et al., 2016). Where present, the Maness has been known to pose instability problems for horizontal wells that have encountered it. However, presence of the Maness may prove beneficial if it acts as a fracture barrier between hydraulically fractured Eagle Ford wellbores and underlying aquifers. The present study is an attempt to determine if the Maness has different geomechanical and mineralogic properties than the overlying Eagle Ford, and if so, are they sufficient to enable the Maness to act as a fracture barrier, preventing water production from underlying aquifers? This study tested the following hypotheses within the study area marked by a royal blue polygon (Figure 1):

1. Maness Shale is geomechanically weaker than the Eagle Ford Shale.
2. Maness Shale has a higher clay and lower calcite content than the Eagle Ford Shale.
3. The Maness acts as a fracture barrier between the Eagle Ford and the underlying water wet formation.

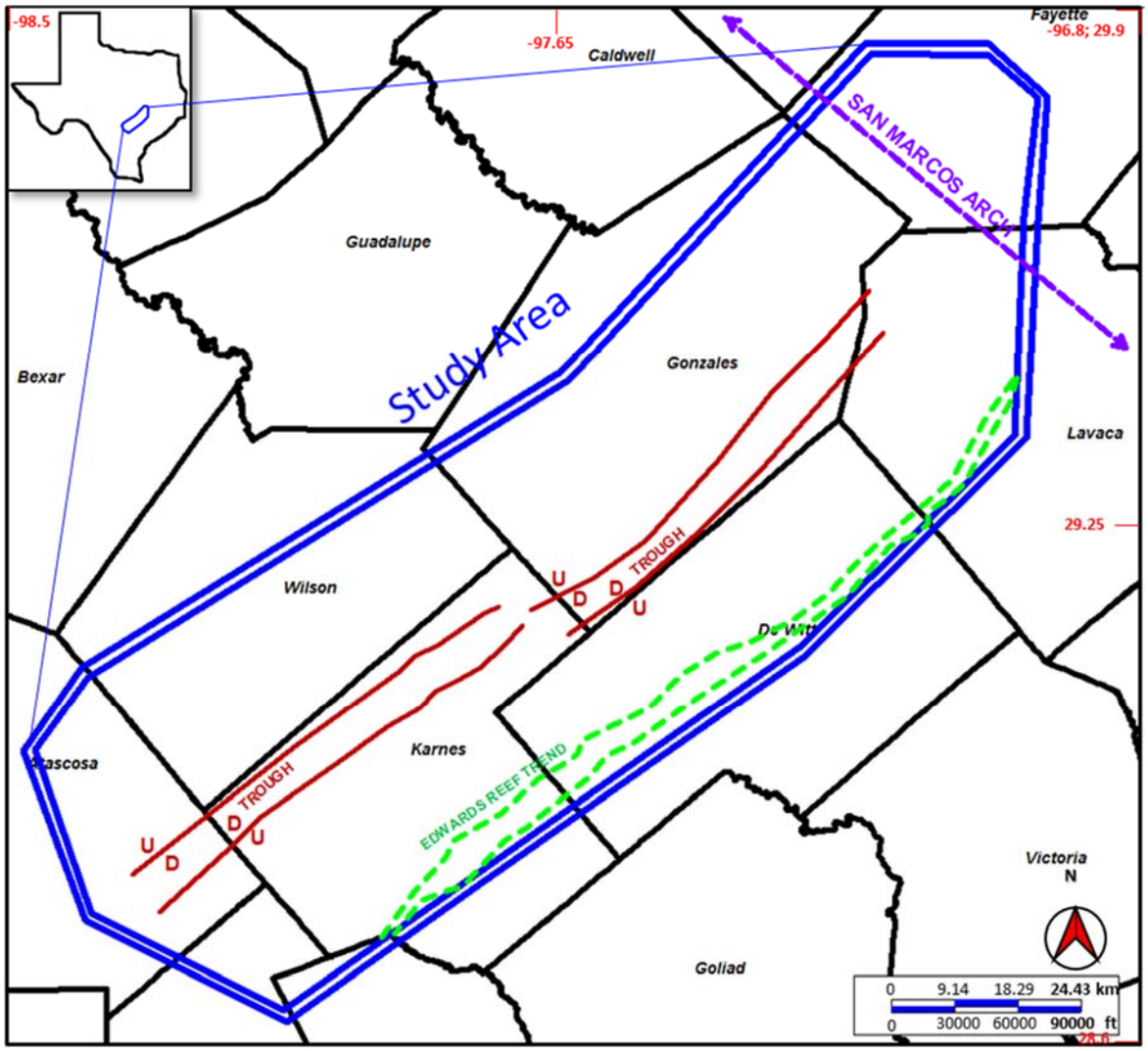

FIGURE 1. SOUTH TEXAS COUNTIES MAP SHOWING THE STUDY AREA POLYGON IN ROYAL BLUE AND DISPLAYING MAJOR FEATURES WITHIN THE STUDY AREA.

Regional Geology

In South Texas near the San Marcos Arch, the Lower Cenomanian Maness Shale is the basal member of the hydrocarbon-rich mudrock, the Eagle Ford Group, which was deposited within the Gulf Basin. The Gulf Basin was formed as a result of rifting of the Pangean supercontinent during the Late Triassic to the Early Jurassic, which was followed by spreading of transitional oceanic and continental crust during the opening of the Gulf of Mexico (Phelps et al., 2014; 2015). Deposition of the Middle to Lower Jurassic Louann Salt within isolated sub-basins, including the Maverick and East Texas basins, produced differential subsidence and sedimentation throughout the Cretaceous (Phelps et al., 2014). The structural features that influenced sedimentation patterns and paleoceanography in the Texas portion of the Gulf Basin include the Sligo and Stuart City reef margins to the south and east, the Ouachita Uplift on the northern margin, the Sabine Uplift to the northeast, and the Mexia-Talco fault zone to the west (Figure 2). The Llano Uplift and the associated San Marcos Arch formed the southern boundary of the greater East Texas Basin as they were structural highs at the time of deposition (Denne and Breyer, 2016).

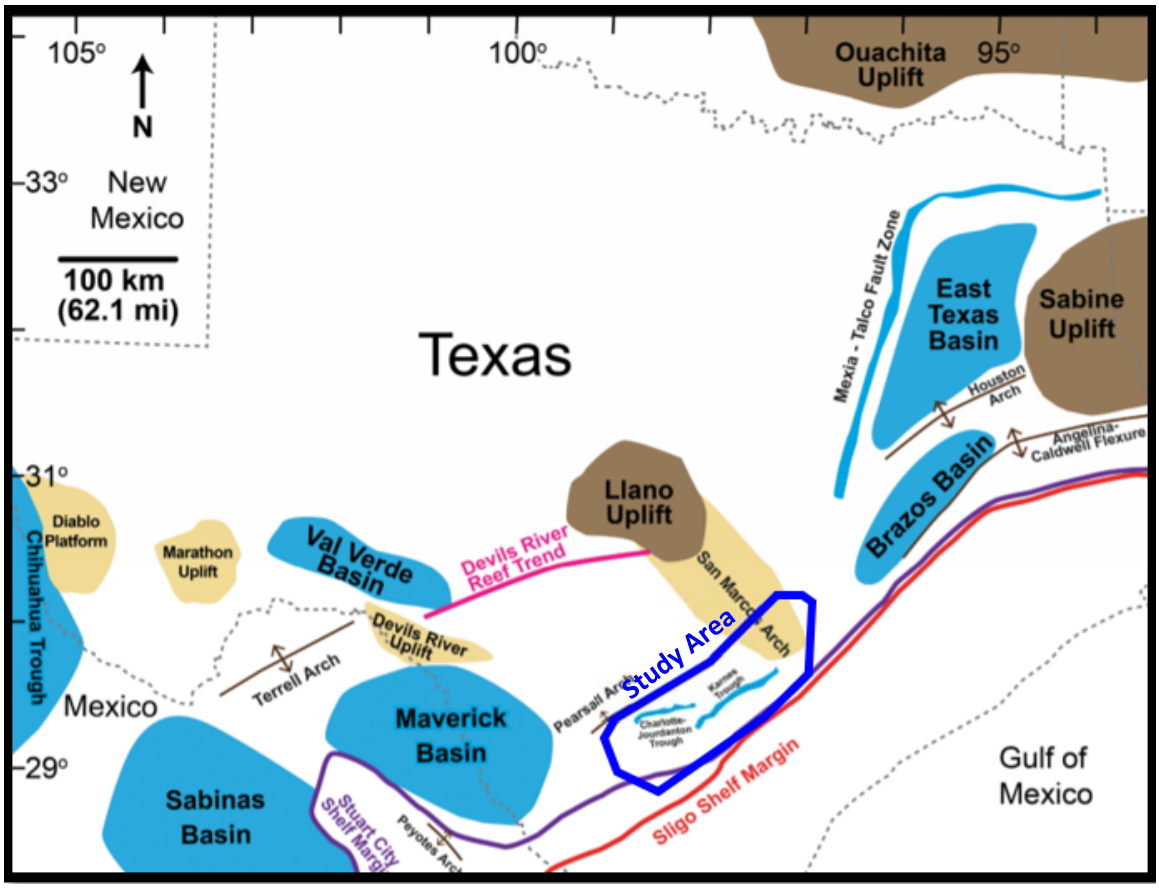

FIGURE 2. MAP OF STRUCTURAL FEATURES IN TEXAS THAT AFFECTED EAGLE FORD DEPOSITION. NOTE IN BROWN AND TAN THE UPLIFTS THAT RESTRICTED THE GULF BASIN AND PROVIDED SEDIMENT SOURCES DURING EAGLE FORD TIME. STUDY AREA OUTLINED IN ROYAL BLUE. (DENNE AND BREYER, 2016).

The Sligo and Stuart City reefs developed during the Hauterivian-Barremian and Albian, respectively, along the southeastern rim of the Texas shelf, forming a prominent shelf-slope break (Phelps et al., 2015). The shelf to basin slope likely had thousands of feet (hundreds of meters) of relief, sporadically isolating the Texas shelf from the deeper Gulf Basin (Phelps et al., 2015). A series of drowning and recovery events of the reefs during the Cretaceous produced platform deposition of anoxic to dysoxic shales adjacent to nonmarine siliciclastic deposits sourced from the deltas to the northwest (Sohl et al., 1991; Phelps et al., 2015). The organic-rich shales are associated with oceanic anoxic events, sequence stratigraphic maximum flooding surfaces, and termination of carbonate sedimentation (Phelps et al., 2015).

Throughout most of the Early Cretaceous, deposition on the Texas shelf was predominantly a widespread, continuous blanket of mostly marine sediments. During the Late Cretaceous, however, the Texas shelf was more diverse in its depositional patterns and sediment types (Sohl et al., 1991). Terrigenous deposits in the northeastern part of the Gulf of Mexico were predominantly sourced from the southern Appalachians (Figure 3) (Blum et al., 2016). Topographic highs such as the Sabine and Ouachita uplifts sustained significant erosion during the major regression of the Early to Middle Cenomanian, producing the influx of terrigenous fluvial and deltaic sediments associated with the Woodbine Group into the East Texas Basin (Sohl et al., 1991).

The Eagle Ford Group, which includes the Maness Shale in South Texas, was deposited from the Early Cenomanian through the Early Turonian, during the flooding of the North American continent that established a connection between the Texas shelf and the Western Interior Seaway (Figure 4). This flooding is documented as the highest transgression in the rock record, coincident with Ocean Anoxic Event 2 (OAE2) (Arthur and Sageman, 2004). The OAE2, also referred to as the Bonarelli Event, which marks the transition between the end of the

Cenomanian and the beginning of the Turonian (93.2 Ma), lasted for approximately 580 k.y. and is associated with global deposition of black, organic-rich shales (Saltzman and Thomas, 2012; Denne and Breyer, 2016). On the Texas shelf, the transgression prior to the onset of OAE2 is interpreted to have produced an influx of organic matter preserved by an anoxic-euxinic stratified water column in a silled basin, creating the hydrocarbon-rich mudrocks of the Lower Eagle Ford (Sageman and Arthur, 1994; Denne and Breyer, 2016).

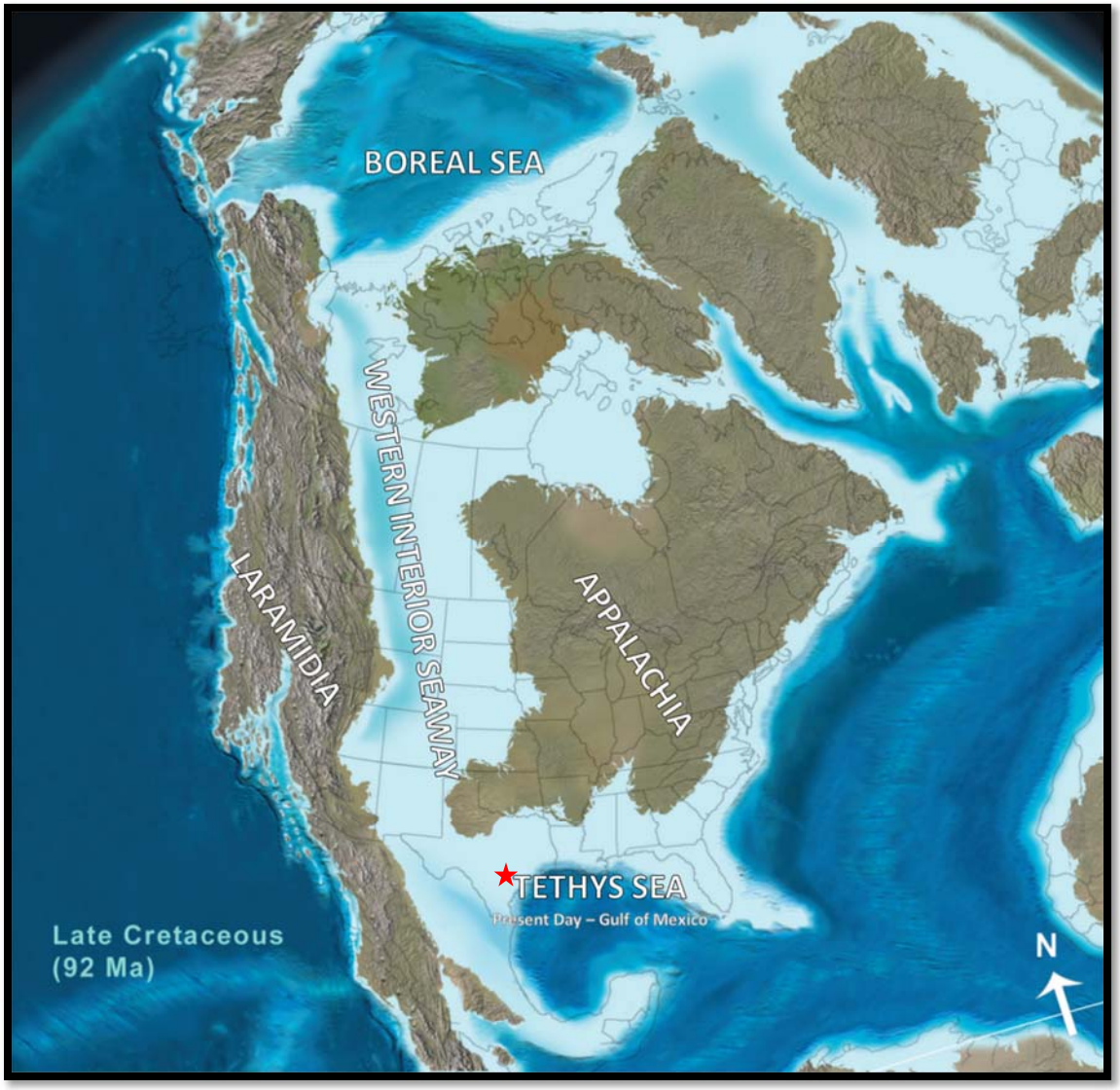

FIGURE 3. PALEOGEOGRAPHIC RECONSTRUCTION OF THE LATE CRETACEOUS – 92 M.A. - DISPLAYING THE TETHYS SEA FLOODING THE COMANCHE PLATFORM. RED STAR INDICATES APPROXIMATE LOCATION OF STUDY AREA (REVISED FROM BLAKEY, 2014).

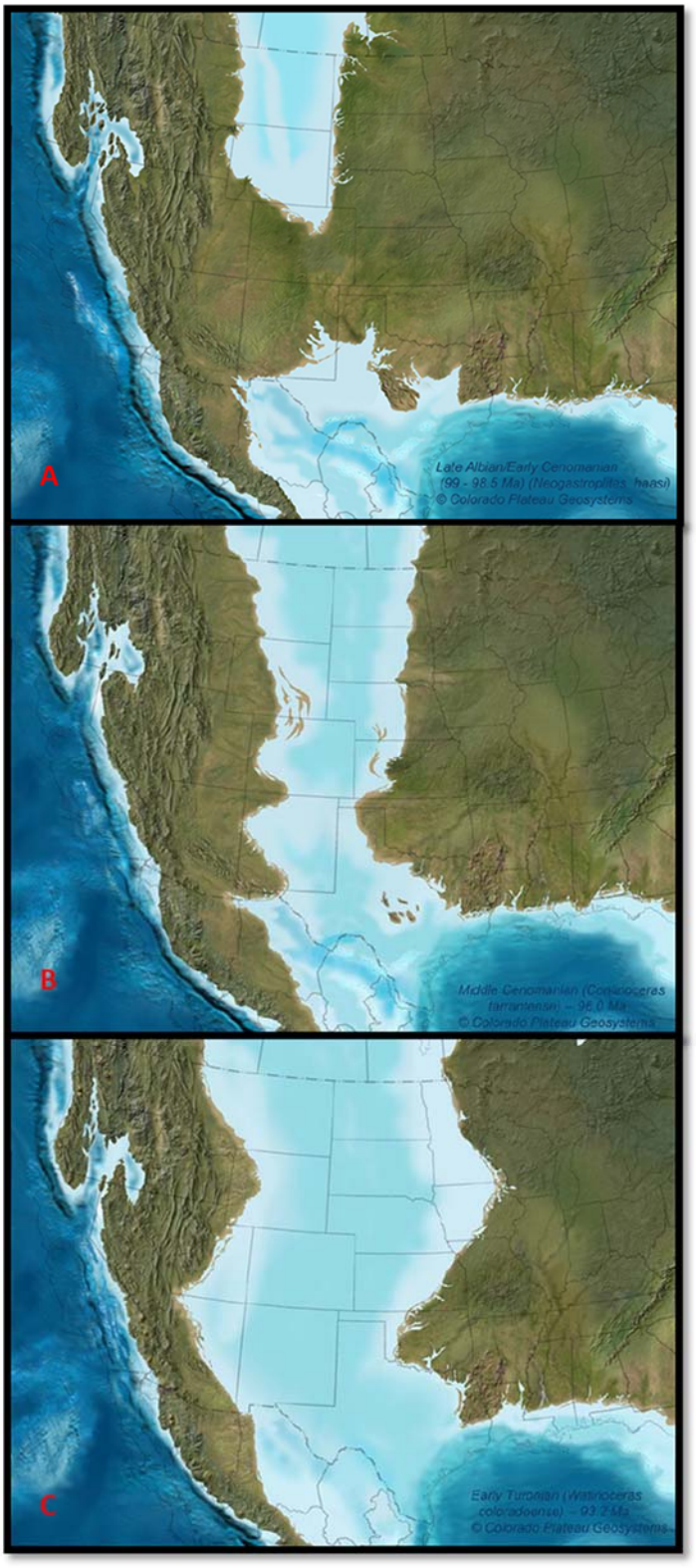

FIGURE 4. THE EVOLUTION OF THE GULF COAST SHELF DURING THE DEVELOPMENT OF THE WESTERN INTERIOR SEAWAY. A) LATE ALBIAN/EARLY CENOMANIAN PALEOGEOGRAPHY (99 M.A.). B) MIDDLE CENOMANIAN PALEOGEOGRAPHY (96 M.A). C) EARLY TURONIAN (93.2 M.A.) PALEOGEOGRAPHY (BLAKEY, 2014).

Stratigraphy

The Buda Limestone overlies the clay-rich Del Rio Formation throughout most of South Texas with the exception of where it pinches out or is truncated across the south side of the Stuart City Reef. In East Texas, the Buda overlies the Grayson Formation that is age-equivalent to the Del Rio in South Texas, and has been subdivided into a mainly white, finely crystalline limestone that transitions to a more marly limestone near the Buda / Maness contact (Figure 5) (Sohl et al., 1991; Phelps et al., 2014). In the northern portion of the South Texas producing region, the Maness Shale overlies the Buda Limestone, where the Buda is typically a white, moderately hard, non-porous to porous, limestone containing abundant calcispheres (Lozo, 1945; Denne et al., 2016).

The unconformable contact between the Eagle Ford and the Buda has been interpreted to represent a regional subaerial exposure surface due to a relative sea level drop that affected the entire Gulf Basin (Hentz et al., 2014; Denne and Breyer, 2016). As noted in Denne et al. 2016, in two cores located in Atascosa and Karnes counties, Texas (Figure 6), the contact between the Eagle Ford to Buda has different characteristics depending on the presence of the Maness. Where present in Karnes County, the Buda is relatively untouched by any erosional or chemical weathering (Figure 7, Karnes County). Where the Maness is absent in Atascosa County, the limestone appears to have been karsted (Figure 7, Atascosa County).

The Maness Shale was initially described from Shell Oil Company's Maness Well No. 1, taken in Cherokee County in East Texas (Figure 8). The Maness No 1. was cored continuously beginning at the basal Austin Chalk through the Woodbine, Maness, and the top portion of the Buda, and was considered a nearly perfect core recovery. The cored interval between the base of the Woodbine and the top of the Buda was named the Maness Shale Formation, and was

described as a bronze or copper-colored to dark gray, partially calcareous, clay shale and claystone with a change in fauna at the top of the Maness that is not seen in the Woodbine as an unconformity lies between the two formations. (Bailey et al., 1945).

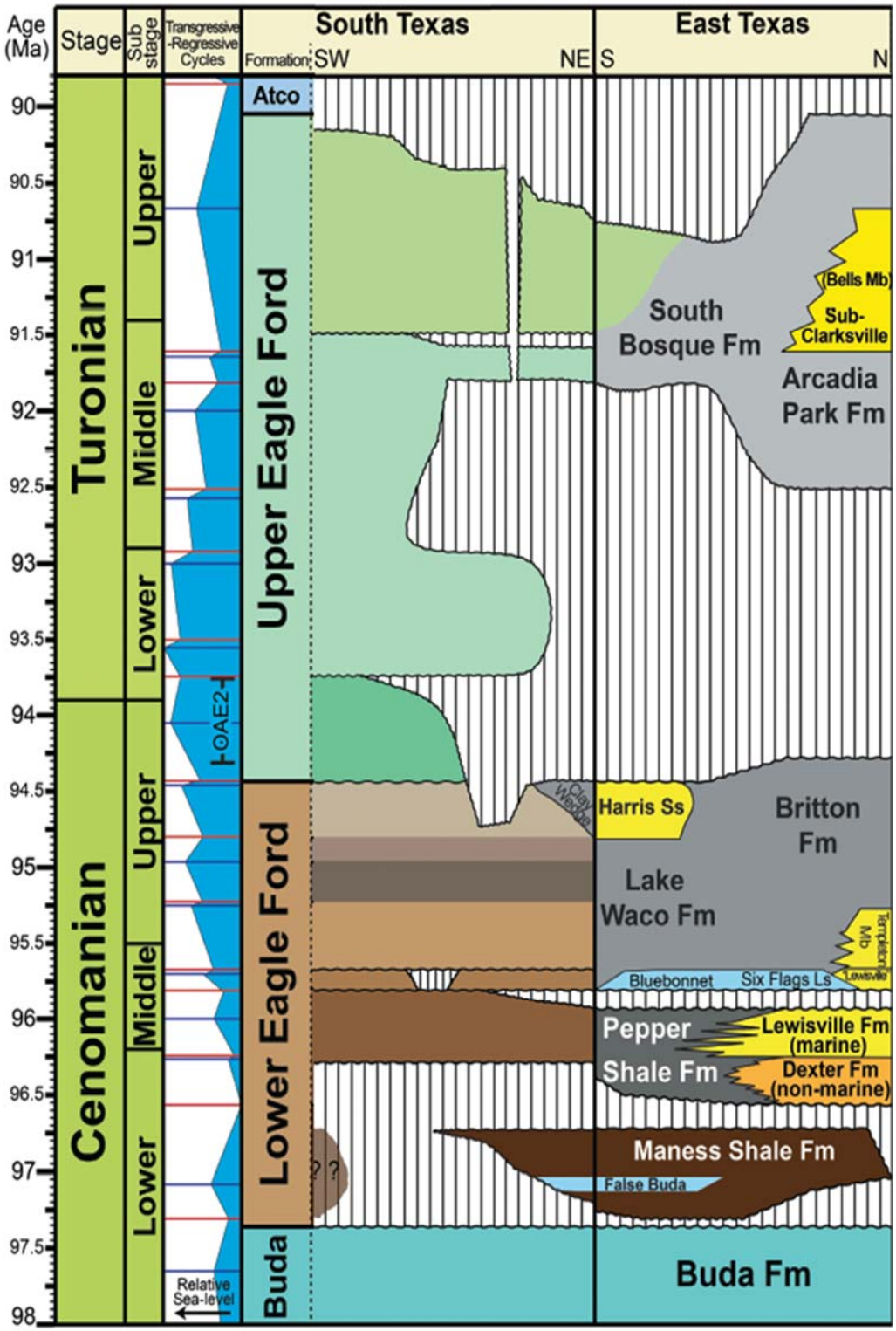

FIGURE 5. STRATIGRAPHIC COLUMN FOR THIS SEMI-REGIONAL STUDY WITH WHEELER DIAGRAMS FOR SOUTH AND EAST TEXAS USING AGE MODELS DEVELOPED BY DENNE ET AL. (2016). THE TRANSGRESSIVE-REGRESSIVE CYCLES ARE BASED ON HARDENBOL ET AL. (1998), ARTHUR AND SAGEMAN (2004), AND DENNE AND BREYER (2016). (REVISED FROM DENNE AND BREYER, 2016).

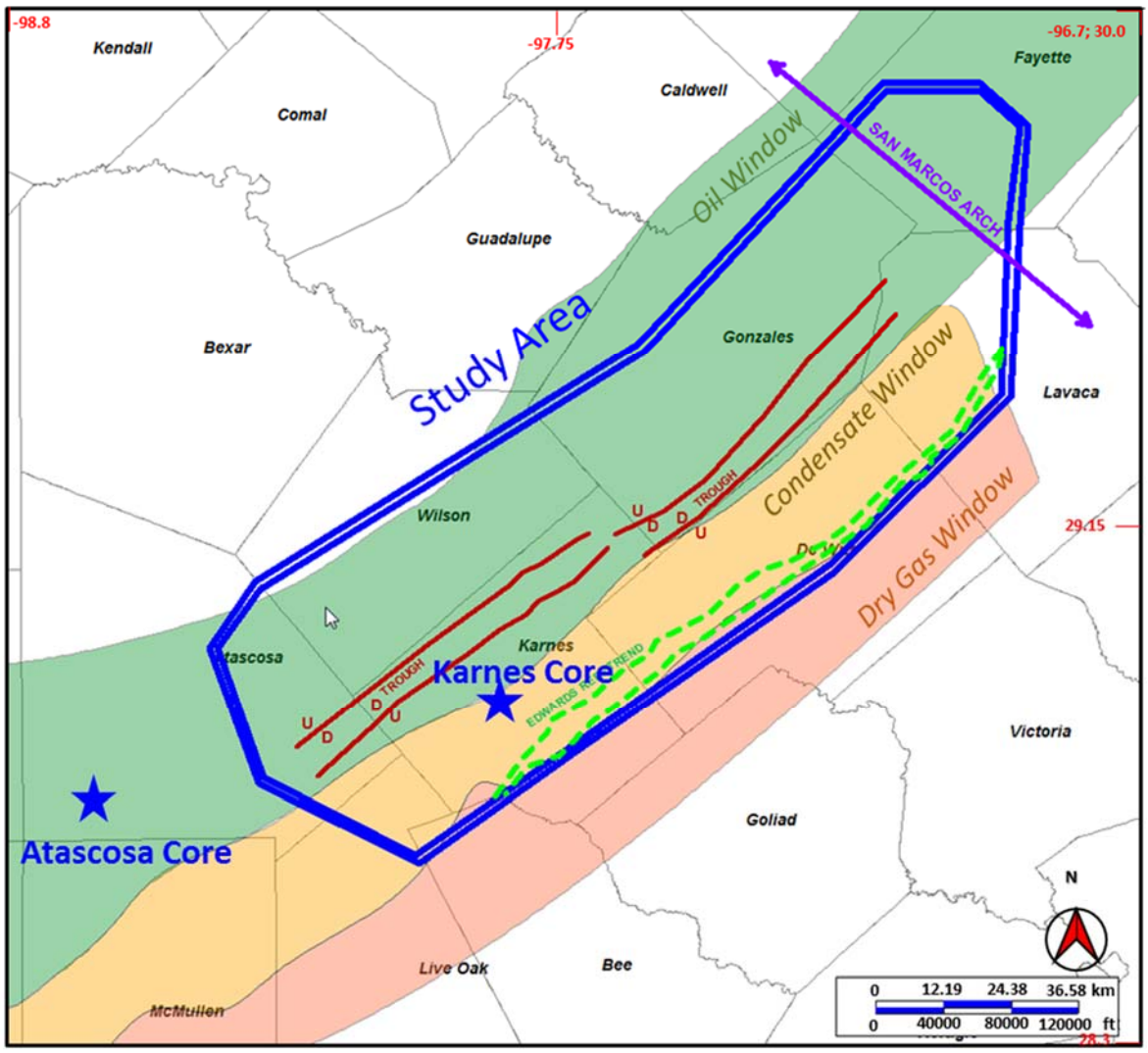

FIGURE 6. MAP OF THE SOUTH TEXAS EAGLE FORD PRODUCING REGION, SHOWING THE EAGLE FORD THERMAL MATURITY (GREEN = OIL; ORANGE = CONDENSATE; RED = DRY GAS) AND LOCATIONS OF THE CORES SHOWN IN FIGURE 7.

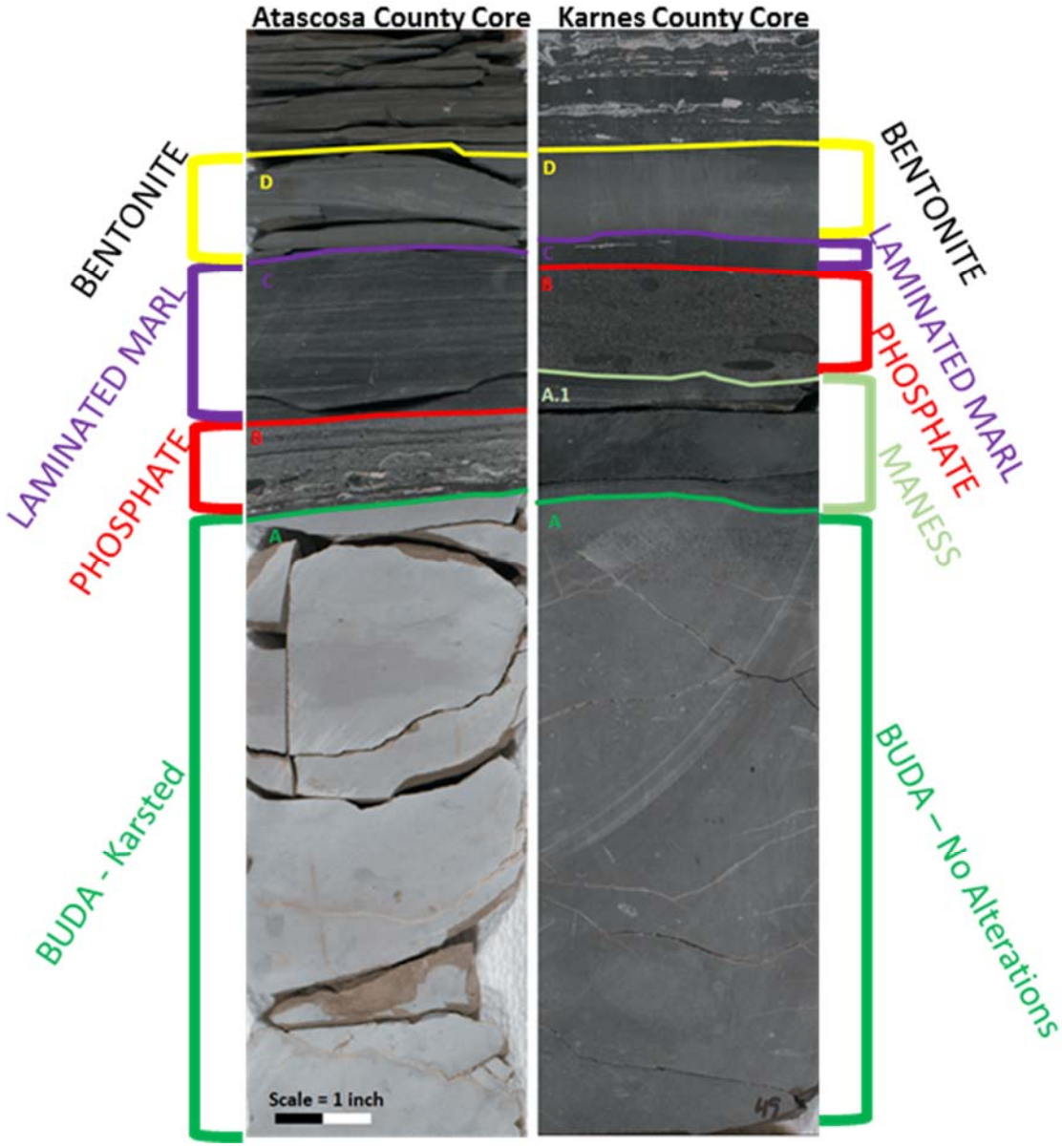

FIGURE 7. PHOTOGRAPHS OF CORES DISPLAYING THE DIFFERENCES BETWEEN THE EAGLE FORD –BUDA CONTACTS WITH AND WITHOUT THE MANESS PRESENT. THE ATASCOSA CORE DOES NOT INCLUDE THE MANESS SHALE WHEREAS THE KARNES COUNTY CORE HAS A THIN INTERVAL OF MANESS SHALE.

IN THE ATASCOSA CORE, THE BUDA (A) SHOWS SIGNS OF ALTERATION AND LIES UNCONFORMABLY BELOW A PHOSPHATIC LAG DEPOSIT (B), OVERLAIN BY A LAMINATED MARL (C) AND A BENTONITE LAYER (D).

IN THE KARNES CORE, THE BUDA (A) SHOWS NO SIGNS OF KARSTING AND IS CONFORMABLY OVERLAIN BY A TRACE OF MANESS SHALE (A.1) OVERLAIN BY A LAMINATED MARL (C) AND A BENTONITE LAYER (D) (DENNE ET AL., 2016).

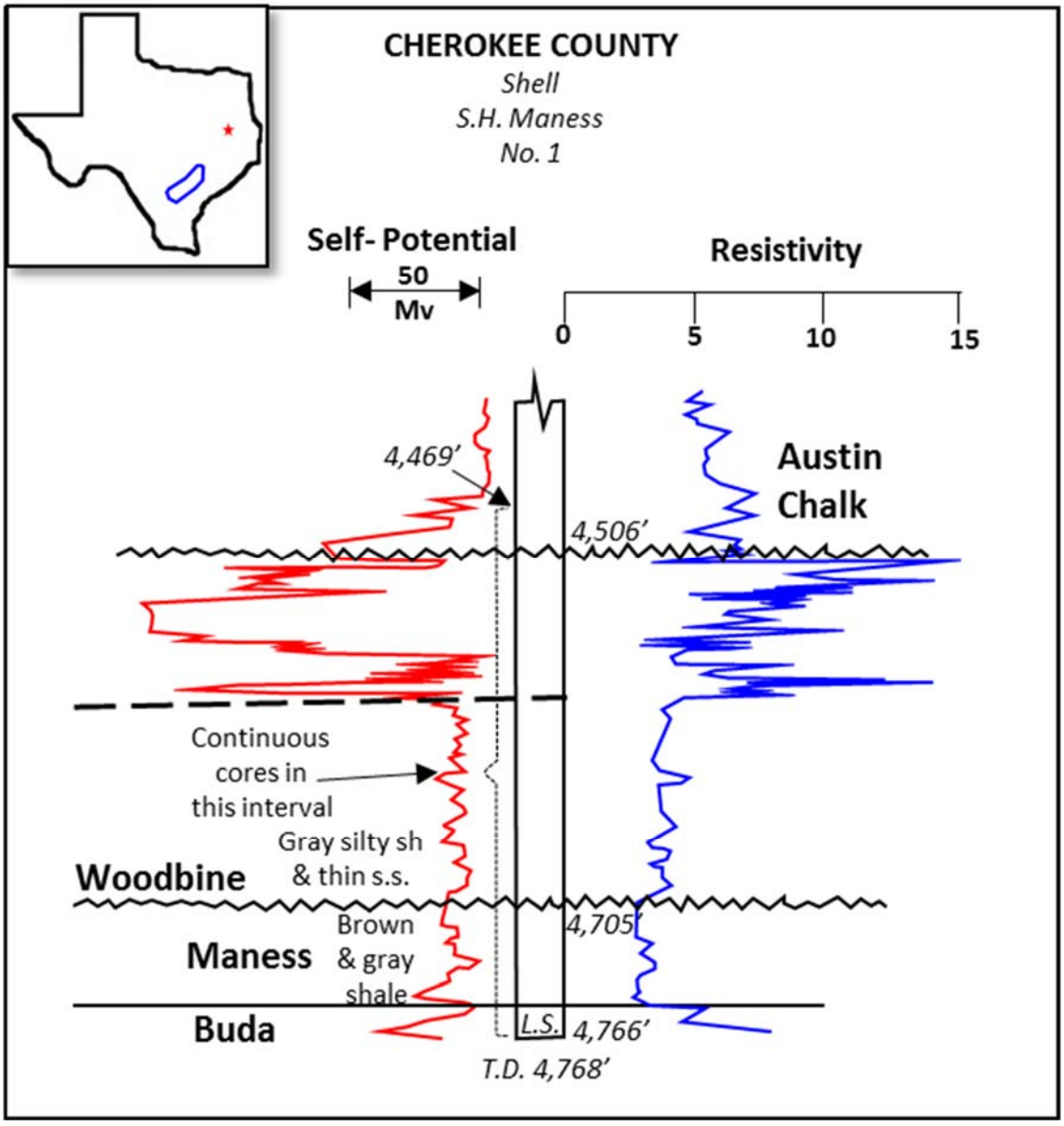

FIGURE 8. WELL LOG WITH SPONTANEOUS-POTENTIAL AND RESISTIVITY FROM THE EAST TEXAS FIELD THAT WAS USED TO INITIALLY DESCRIBE THE MANESS SHALE. STUDY AREA OUTLINED IN ROYAL BLUE AND S.H. MANESS WELL NOTED WITH RED STAR. (L.S. – LIMESTONE; T.D. – TOTAL DEPTH (REVISED FROM BAILEY ET AL., 1945).

In East Texas, the Maness is more clay rich and lacks the calcareous silty sandstones that are present in the overlying silty shales of the Woodbine (Bailey et al., 1945). The Maness Shale was originally considered as a part of the upper Washita sub-group and is the only one of the eight Washita stratigraphic units that does not outcrop (Bailey, et al., 1945; Lozo, 1951), leading to many misinterpretations and miscorrelations. For example, it was noted by Hudson (2014) that the Maness Shale is a producing source rock in the Brazos Basin. This correlation is thought to be inaccurate as it also includes the so-called Lower Woodbine Organic Shale interval of Adams et al. (2014) that sits stratigraphically on top of the Maness Shale in the Brazos Basin. The current study area does not include the Lower Woodbine Organic Shale, as this facies does not extend as far south as the San Marcos Arch.

In the studies of East Texas by Ambrose et al. (2009) and Hentz et al. (2014), the Maness is represented as an argillaceous, marine shale that is divided into lower and upper intervals. The lower unit is a fining-upward section, whereas the upper unit is a coarsening upwards section found throughout the East Texas Basin. These intervals were divided by a high gamma ray spike marking the transition from a transgressive to a highstand systems track. This high gamma ray spike is likely the phosphate lag identified at the top of the Maness (Denne et al., 2016), suggesting that the section described by Ambrose et al. (2009) and Hentz et al. (2014) as highstand Maness is actually the base of the Woodbine. According to Denne et al., 2016 shows biostratigraphically the section on top of the phosphate in East Texas is Woodbine Group (Figure 9). Hentz et al. (2014) represent the top of the Maness to be the initial highstand and the earliest Woodbine deposits, whereas the maximum flooding surface occurs between the lower and upper Maness intervals.

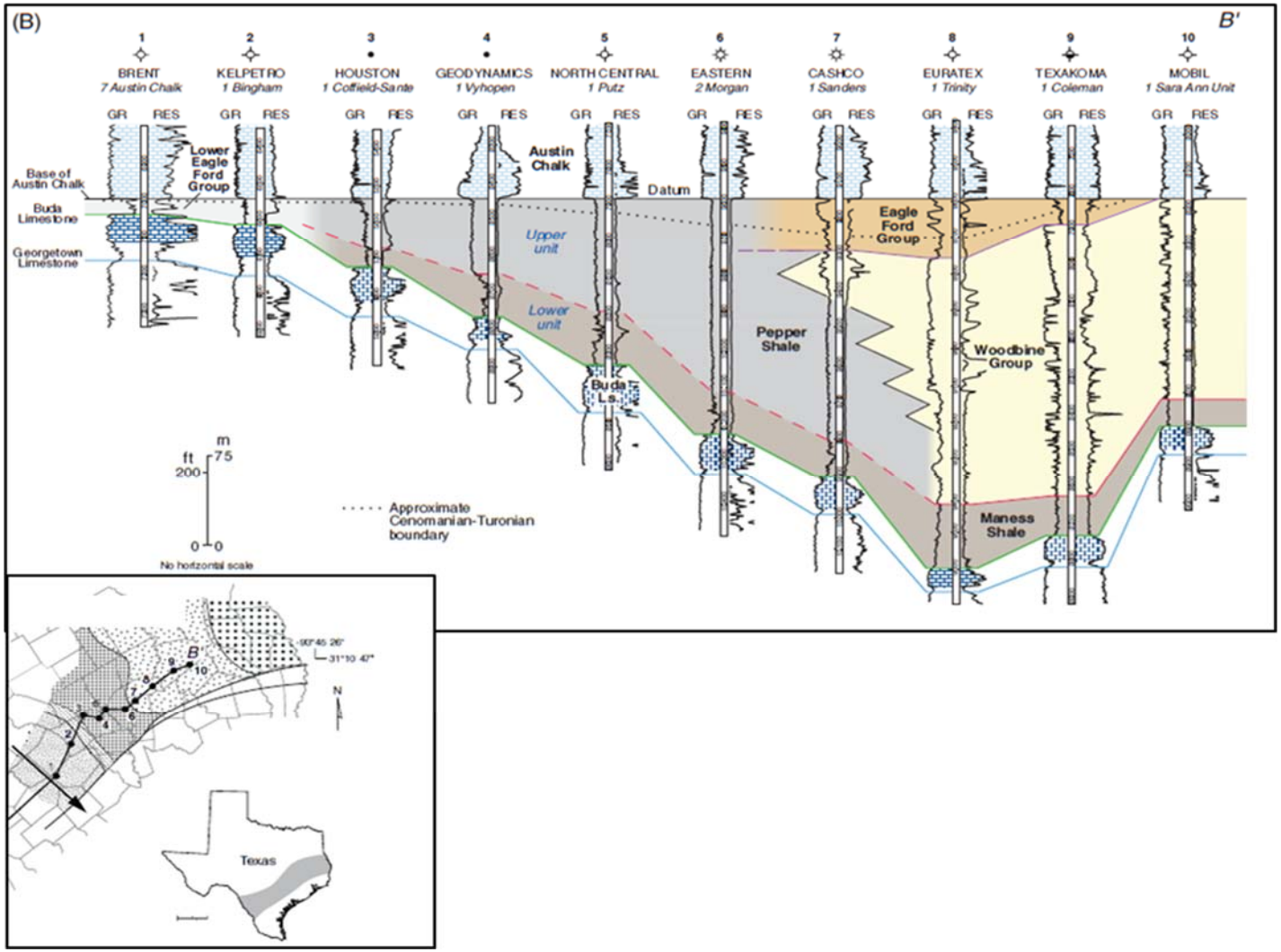

FIGURE 9. CROSS SECTION FROM THE SAN MARCOS ARCH TO THE EAST TEXAS BASIN SHOWING THE LITHOSTRATIGRAPHIC FRAMEWORK OF FORMATIONS ACROSS TEXAS. DATUM IS ON THE BASE OF THE AUSTIN CHALK. (HENTZ ET AL., 2014)

Using petrophysical logs, the Maness Shale in South Texas is distinguished by a high gamma ray spike overlying an interval with lower gamma ray and resistivity values than the overlying Eagle Ford Shale. The Maness is described as an argillaceous mudrock containing an average of 50% clay as determined by x-ray diffraction (XRD) analyses of core plugs, and is also devoid of any sandstone (Jennings and Antia, 2013; Denne et al., 2016; Denne and Breyer, 2016). The regional isopach map of Denne and Breyer (2016) (Figure 10) displays a thick Maness in the Brazos Basin which thins to the southwest near Atascosa County (Denne and Breyer, 2016).

Biostratigraphic studies of subsurface material from the Brazos Basin and the San Marcos Arch region indicate an Early Cenomanian age for the Maness Shale. Ammonite impressions found in the Maness Shale from cores taken in Gonzalez County were identified as *Euhystrichoceras adkinsi* (Figure 11), a biostratigraphic marker for the *Acompsoceras inconstans* Zone from the Early Cenomanian. The planktonic foraminiferal marker *Favusella washitensis* and benthic foraminifera species *Epistomina lacunosa* and *Textularia washitensis* are found in the Buda and overlying Maness Shale, but are not found in the Eagle Ford Shale, also indicative of an Early Cenomanian age. The planktonic foraminiferal assemblage from the Maness is dominated by the genus *Hedbergella,* which predominantly inhabited surface waters. This includes the species *Hedbergella planispira,* which was tolerant of low salinity waters. The calcareous nannofossil assemblage contains high abundance of species associated with eutrophic (high nutrient, low oxygen) surface waters (Denne et al., 2016).

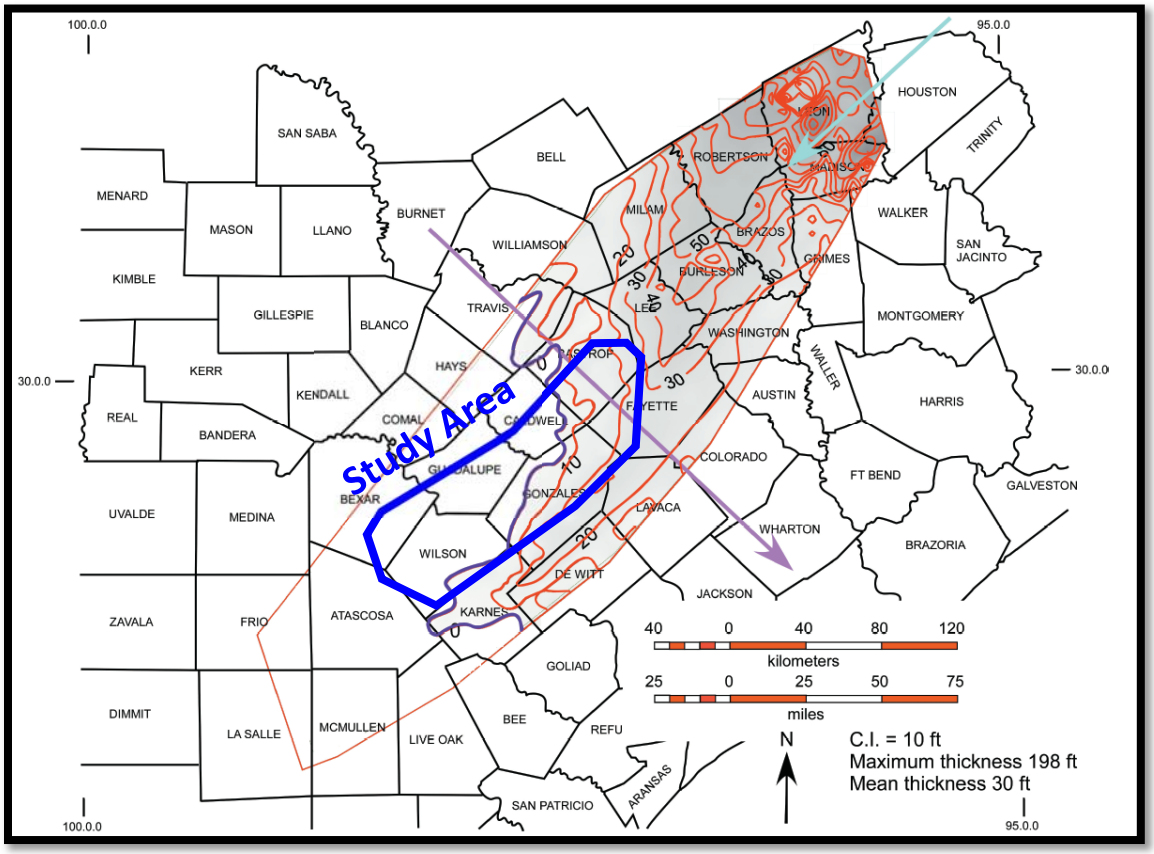

FIGURE 10. MANESS SHALE ISOPACH MAP WITH THE BLUE ARROW INDICATING THE SEDIMENT SOURCE AND THE PURPLE ARROW APPROXIMATING THE LOCATION OF THE SAN MARCOS ARCH. RED OUTLINE IS STUDY AREA OF DENNE AND BREYER, BLUE OUTLINE IS FOR THIS STUDY (FROM DENNE AND BREYER, 2016).

FIGURE 11. PHOTOGRAPHS OF IMPRESSIONS OF THE AMMONITE *EUHYSTRICHOCERAS ADKINSI* FROM THE MANESS SHALE IN GONZALES COUNTY. NOTE GUIDELINES = 0.04 INCH (1MM) INTERVALS (FROM DENNE ET AL., 2016).

From the East Texas Basin to the Brazos Basin to the southwest there is a facies change within the Woodbine Group from the sand-rich Lewisville and Dexter formations to the prodeltaic shales of the Pepper Shale. The type section of the Pepper in Bell County, south of Waco, is described as a purplish-black clay with a phosphate-rich zone at the base. The Maness is absent in this area, as the Pepper Shale sits unconformably on top of the Del Rio (Sohl et al., 1991). In Brazos and Burleson counties the Maness is present and lies below the portion of the Pepper Shale that contains the so-called lower Woodbine Organic Rich Shale (Adams et al., 2014).

In South Texas, the Maness Shale is overlain by the Eagle Ford Group. Deposition of the Eagle Ford in South Texas was initiated during the Early Cenomanian (97.4 Ma), when the flooding of the North American continent established a connection between the Texas shelf and the Western Interior Seaway. The Lower Eagle Ford Formation is a dark gray mudrock with thin, interbedded limestones and organic-rich marls (calcareous mudrocks) with an average clay content of less than 35%. The rocks of the Lower Eagle Ford typically have higher gamma ray and resistivity values than the overlying Upper Eagle Ford Formation due to their higher content of total organic carbon (TOC) and hydrocarbons. The Upper Eagle Ford consists of interbedded limestones and marls that are almost entirely made up of pelagic carbonates (Denne and Breyer, 2016). The entire Eagle Ford is thickest in the Maverick Basin; thickness trends parallel to the Karnes-Gonzales troughs and the Sligo-Stuart City reef trends in a southwest to northeast direction toward the East Texas Basin, thinning over the San Marcos Arch.

Unconventional Hydrocarbon Production

Unconventional oil and gas reservoirs are traditionally referred to as low permeability reservoirs that cannot be produced at economic volumes and rates without stimulation of the rock using methods like hydraulic fracturing (Orangi et al., 2011). The Eagle Ford has been an unconventional hydrocarbon producer since the first well was drilled in 2008 (RRC, 2018). Multiple variables contribute to well production including the abundance of limestones and marls within the Eagle Ford (Breyer et al., 2015).

In order to understand the total water production from wells, Ikonnikova et al. (2017) derived an algorithm using pressure data, oil gravity, water saturation, and hydrocarbon pore volume from petrophysical analyses to estimate water production declines (Figure 12). The study used 9,873 wells with a minimum of 16 months of production and found that the highest water production volumes were mainly dependent on well location, depth, and quantity of hydraulic fracturing fluid injected into wells during the completion stage of the well. Within the study area outlined in yellow, the first year expected formation water production based on modeled historical water production data range from <50 Mbbl/well to >250 Mbbl/well. What this study did not consider in their calculations is the possibility of water production from an adjacent aquifer or overlying fractured Austin Chalk.

The disposal of flowback and reservoir-produced waters continues to be a financial burden carried by all Eagle Ford operators. During the first six months of production an unconventional oil or gas well produces 20% to 50% of the total water production over its lifetime. Of that production, only 4-8% of the flowback and produced waters are from the hydraulic fracturing, whereas 92-96% of waters produced are from surrounding formation (Kondash et al., 2016). Therefore, when a decline in water production does not occur after the

first six months of production, there is reason to believe that as the well is producing water from an adjacent aquifer.

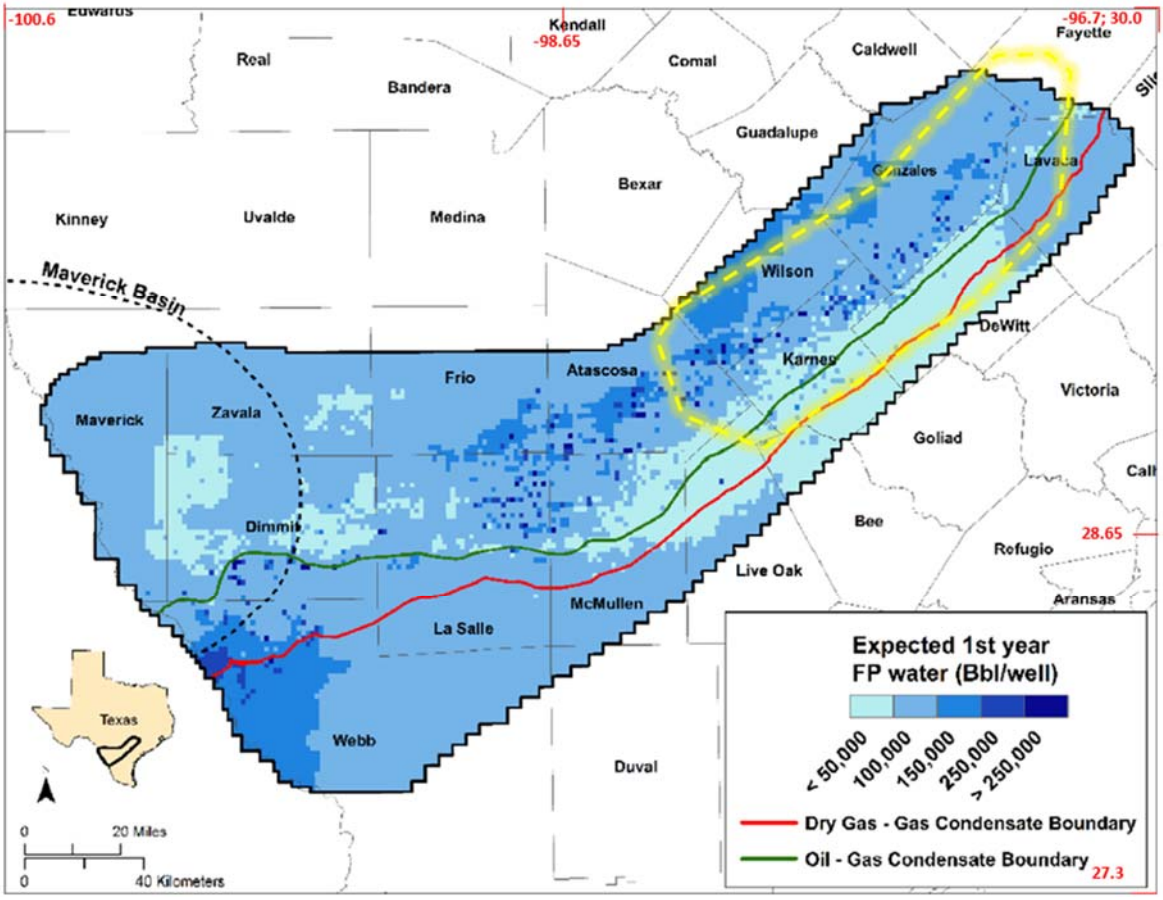

FIGURE 12. PROJECTIONS FOR THE PROJECTED FIRST YEAR'S PRODUCED FORMATION WATER PRODUCTION IN BBL/WELL FOR WELLS TO BE PUT ONLINE IN 2017 BASED ON MULTIPLE INPUTS WITHIN ONE SQUARE MILE.

YELLOW DASHED POLYGON OUTLINES THE STUDY AREA FOR THIS PROJECT. (MODIFIED FROM IKONNIKOVA ET AL, 2017)

Methods and Materials

The purpose of this study is to document the presence and thickness of the Maness Shale across the study area and to determine if the Maness acts as a fracture barrier given sufficient thickness. The area of study is the northern part of the South Texas Eagle Ford producing region, adjacent to the San Marcos Arch (Figure 13). The area includes portions of Fayette, Lavaca, Gonzales, DeWitt, Karnes, Wilson and Atascosa counties.

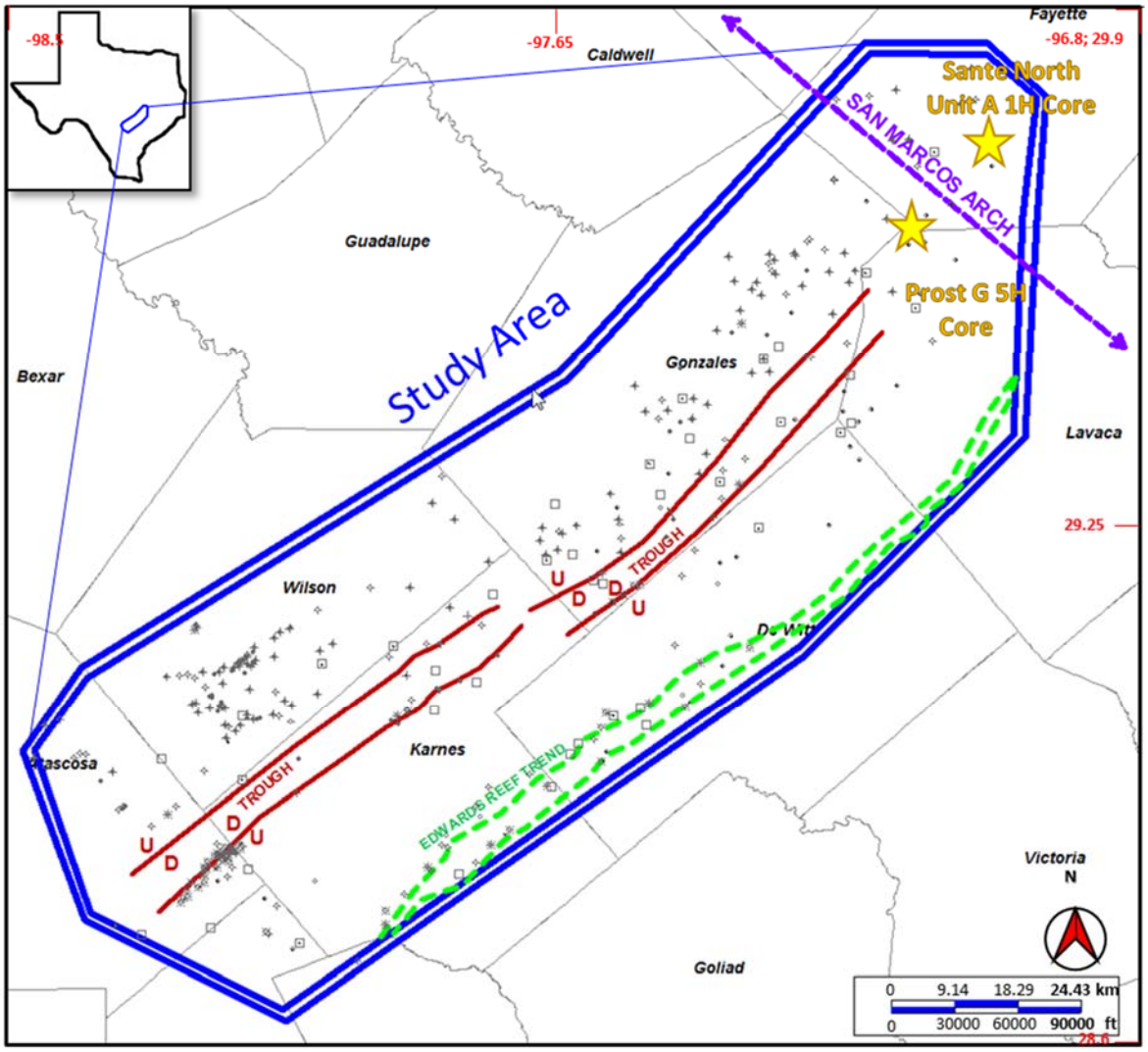

FIGURE 13. MAP OF THE STUDY AREA OUTLINED IN BLUE POLYGON, SHOWING THE WELLS UTILIZED IN THE STUDY, THE LOCATION OF THE TWO CORES REPRESENTED AS YELLOW STARS, AND THE REGIONAL FEATURES INCLUDING FAULT-BOUNDED GRABENS, THE EDWARDS (STUART CITY) REEF, AND THE SAN MARCOS ARCH.

Cores

Conventional cores from two wells provided by Lonestar Resources were utilized for the study (Table 1). These wells were drilled by Sanchez Oil and Gas Corporation in 2013, near the San Marcos Arch in Lavaca and Fayette counties. They are each over 150 ft (45.7 m) in length and contain portions of the Austin Chalk, the entire Eagle Ford and Maness intervals, and the upper portion of the Buda Limestone. Thin section and X-ray Diffraction (XRD) analyses were performed on 23 samples from the two cores. When comparing depths from the core gamma ray to the log gamma ray, the Prost Unit G 5H has a depth shift of -8 ft (-2.5 m) from the core to the log whereas, the Sante North Unit A 1H has a -20 ft (-6.1 m) from the core to the log.

TABLE 1: DEPTH AND FORMATION THICKNESSES FOR THE TWO CORES UTILIZED IN THE STUDY.

Well Name and Number	County, State	Depth (ft / *m*)	Total Cored Footage (ft / *m*)	Total Feet of Eagle Ford (Including Maness) (ft / *m*)	Feet of Maness (ft / *m*)
Prost Unit G 5H	Lavaca,TX	**10,906 -11,089**/ 3,324 - 3,380	**183** / 55.8	**115** / 35.1	**30** / 9.1
Sante North Unit A 1H	Fayette, TX	**11,175 -11,357**/ 3,406 - 3,462	**182** / 55.5	**96** / 29.3	**33** / 10.1

Core and Thin Section Descriptions

Representative thin sections of the Maness and the adjacent formations from the Prost Unit G 5H and Sante North Unit A 1H cores were examined to distinguish microfacies. Locations of thin sections were selected primarily to sample facies transitions. Twelve oversized 3x2 inch (7.62 x 5.08 cm) thin sections from the Prost Unit G 5H and 11 from the Sante North Unit A 1H were made by TPS Enterprises, LLC, in Houston, Texas, to a standard thickness of 20 microns and analyzed using a standard petrographic microscope under transmitted (brightfield and cross-polarized) and reflected light. Microfacies were established by distinguishing composition, stratigraphic features, and appearance changes such as changes in frequency of foraminifera,

pellets, color, or grainsize. The images represented here were photographed by an Epson Perfection V600 Photo flatbed scanner under both transmitted and reflected light to identify specific features such as pyrite, which are black under transmitted light but have a golden shine under reflected light (Appendix A). Lithofacies were described by viewing the core and core photographs, and were subdivided by visible changes of lithology, bedding style, and changes in fossil assemblages, and using the Dunham classification for the carbonate rich zones.

Mineralogy

X-Ray Diffraction (XRD) is a standard method for determining bulk and clay mineral abundances. The samples were prepared by obtaining 1 to 1.7 ounces (30-50 mL) of lithologically representative material that were powdered to a grain size of approximately 10 µm (200 mesh) by a mortar and pestle, and then transferred to a steel vial that contained three steel balls; two with a diameter of 0.275 inch (7 mm) and one with a diameter of 0.118 inch (3 mm). The steel vial was sealed and placed in a SPEX SamplePrep 8000M Mixer/Mill for 10 minutes to be milled to a grain size of <200 mesh. The resulting powder was examined for grain-size consistency and homogeneity before being placed into the X-ray diffractometer (XRD) (Shimadzu Center, 2018).

The sample powders were analyzed using the Shimadzu XRD-7000 (Figure 14) in the Center for Environmental, Forensics, and Material Science at the University of Texas at Arlington. Approximately 1 to 1.7 ounces (30-50 mL) of lithologically representative rock were crushed by mortar and pestle, ultimately powdered to a grain size of <200 mesh, which were then analyzed by the Shimadzu XRD-7000. X-rays are focused toward the sample, bombarding it with electrons. The X-rays are then diffracted off the crystal lattice of the material (Figure 15) at varying intensities that alter the wavelength. Wavelengths are characteristic of a specific

material and can be measured to determine the chemical make-up of different minerals (Poppe et al., 2018). After the scans were collected, they were processed using the MDI Jade9 software package. Sample spectra were compared against the ICDD PDF-4+ 2018 XRD reference spectra database and their modal mineralogy was modelled using the built-in relative intensity ratio (RIR) method of the Jade9 software (Shimadzu Center, 2018).

FIGURE 14. THE MAXIMA X XRD X-RAY DIFFRACTOMETER HAS A CONTAINED TESTING AND ASSOCIATED COMPUTER APPLICATION FOR ANALYSIS (SHIMADZU CENTER, 2014).

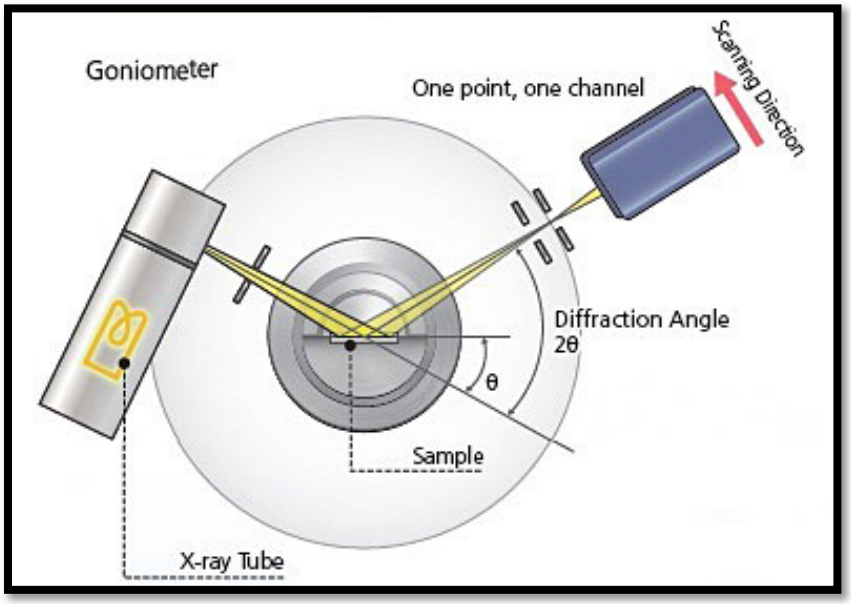

FIGURE 15. SIMPLIFIED VISUAL OF THE DATA COLLECTION OBTAINED FROM SHIMADZU'S XRD DISPLAYING THE X-RAY BEING PROJECTED FROM THE GONIOMETER, REFLECTED OFF A SAMPLE AND RECEIVED AT A CERTAIN DIFFRACTION ANGLE THEN IS ABLE TO HELP IDENTIFY THE MINERALOGY (SHIMADZU, 2018).

Geomechanical Analyses

Geomechanical analysis are frequently used in the petroleum industry to develop an understanding of the mechanical responses of rock formations. Understanding the overburden pressure of overlying rocks, or confining stress, helps differentiate the stiffness and elasticity of the rock. In this particular study, rock strength was studies by two independent methods; a point load penetrometer and a micro-rebound hammer. Alec Burns, a TCU geology undergraduate student, conducted and recorded all geomechanical tests at the TCU Core Facility.

The point load penetrometer, also known as the "Dimpler", tests rock strength by applying a constant force on a carbide tip. Once the butt end of the cores were cleaned of any debris, sample tape for the point-load penetrometer data samples were placed in the center of the core, furthest away from any edges or visible fracture. The sample tape was placed approximately every six inches (15.24 cm) in the Maness and the first few feet above and below. The remainder of the Buda and Eagle Ford were tested at one-foot (30.48 cm) intervals throughout the rest of the core. The tape was 3M tan paper masking tape measuring 0.033 inch (0.085 cm) in thickness. To perform the exercise, the Dimpler's carbide tip was dipped into a red ink pad then placed on the tape. Pressure was applied to the top portion of the Dimpler, compressing the device onto the tape placed on the core, creating a slight depression, or dimple, colored in red. Each Dimpler sample was taken by removing the core section from the core box, and placing it in a box filled with sand to ensure that the pressure applied would have the same supporting matrix for every data point collected. Three data points were gathered at each depth after moving slightly for each test to ensure that the same part of the core was not sampled twice, which might produce an erroneous reading. The section of the core that was sampled was measured for length as these measurements varied and the height and width did

not. Once the three dimples were created, the tape was removed from the core and placed on a transparent paper in preparation for reading the samples (Figure 16 A and B). The dimple diameter sizes were measured using a lighted graduated surface magnifying glass that has a set of evenly spaced "ticks'. The measurements were made by counting the number of tick marks for the diameter of the dimple, with a scale of one tick mark equaling 0.005 inch (0.0127 cm). Enderlin (2014) outlines the correlation between the diameter (Figure 17) created by the Dimpler to UCS (psi) from triaxial testing. The tick mark values were converted to unconfined compressive strength in psi (lbs/in^2) using the following equations:

Tick Average < 5.5: UCS = (154978.9*Tick Average-1.86399)+(-12992.97+(60507.13*Tick Average)+(-27346.5*Tick Average2)+ (4293.111*Tick Average^3)+(- 226*Tick Average^4))

Tick Average > 5.5: UCS = 154978.9 * Tick Average-1.86399

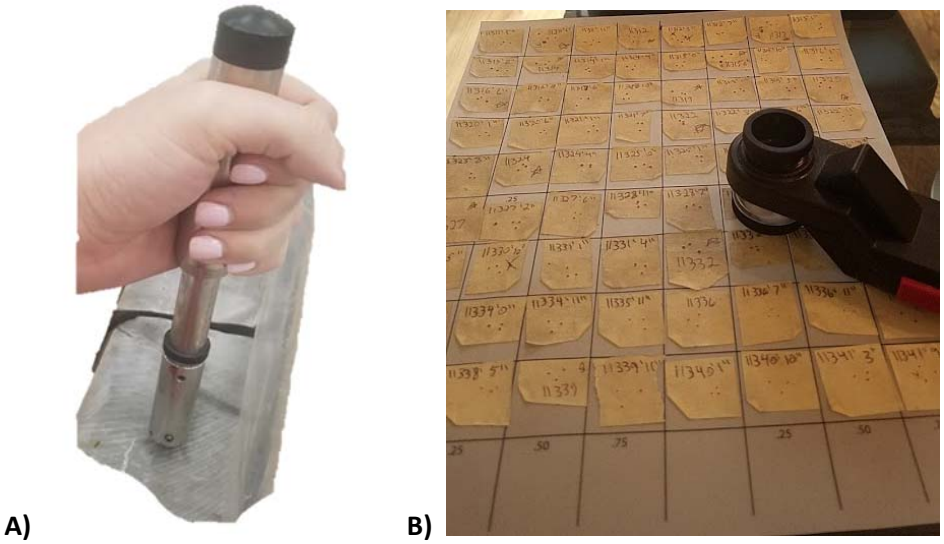

A) B)

FIGURE 16. A) IMAGE OF DIMPLER BEFORE FORCE IS APPLIED TO THE TOP HANDLE OF THE DEVICE. B) ARCHIVED DATA SHEET DISPLAYING RED INDENTATIONS, LABELED CORE DEPTH AND A HAND LENS WITH SCALED TICK MARKS.

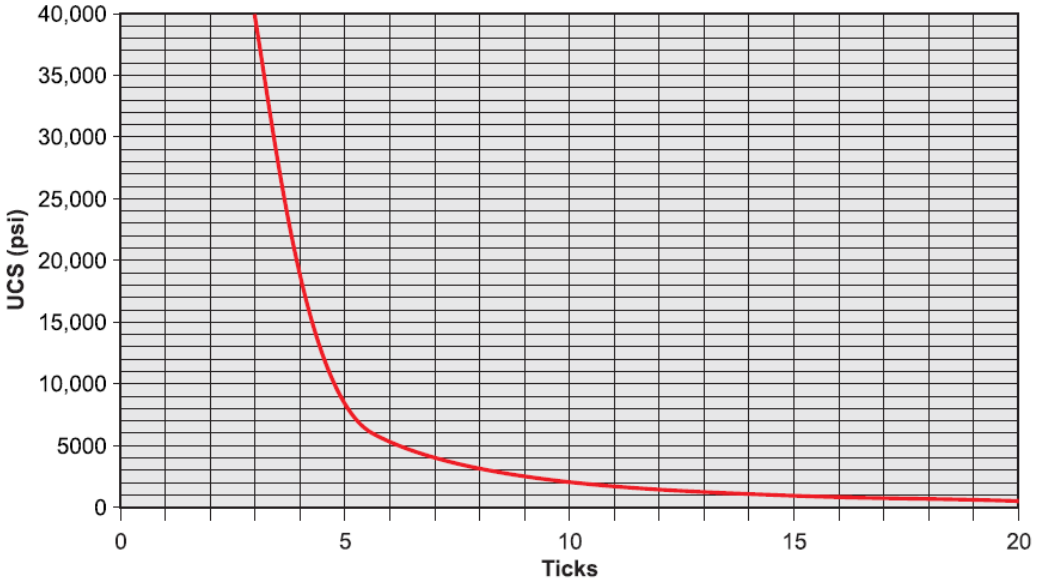

FIGURE 17. THE CORRELATION BETWEEN THE DIAMETER OF THE TICK MARKS READINGS FROM DIMPLER TO UNCONFINED COMPRESSIVE STRENGTH FROM TRIAXIAL TESTING (ENDERLIN, 2014).

The Equotip Bambino is a spring loaded, digital, battery operated, micro-rebound hammer that measures hardness of surfaces by compressing a lever that launches a hard metal ball indenter, which then rebounds off the surface being tested. The Bambino is a non-destructive, easily repeatable test that was originally designed for testing of metals, but has been adopted to the testing of rock strength.

The Bambino tests were conducted at the same depths as the Dimpler readings but away from the indentations made by the Dimpler. Each core sample's length was measured, removed from the core box and placed on a box of sand to ensure the same supporting matrix for each data point collected. The mechanical process of the Bambino is measured based on the movement velocity of the metal ball at two times, before and after the impact. The rebound velocity is converted to Leeb's Hardness values (L') (Figure 18 A and B). Leeb's Hardness is the ratio of the velocity of the metal ball at impact versus the velocity of the metal ball's rebound and is unitless (Daniels et al., 2012). The faster the velocity, the higher the Leeb's Hardness value, and therefore the harder the surface being tested. The Leeb's Hardness values can be used to derive unconfined compressive strength (UCS) after converting the hardness values (HLD or L') using several different empirical algorithms.

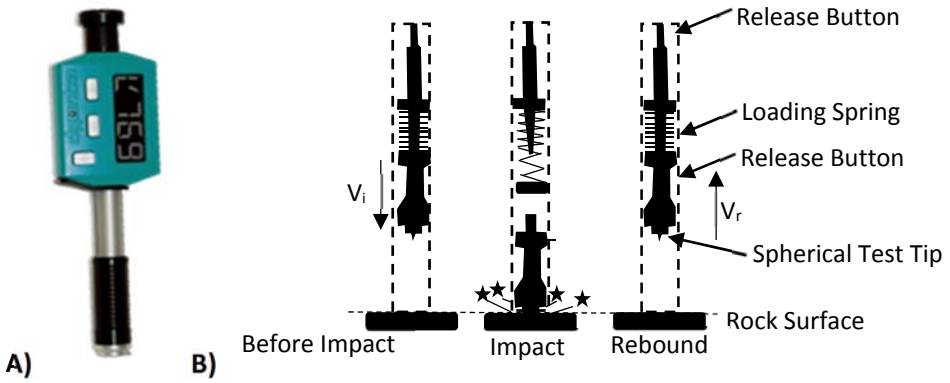

FIGURE 18. A) PROCEQ EQUOTIP BAMBINO 2 (PROCEQ, 2018). B) SCHEMATIC ADAPTED FROM AOKI AND MATSUKURA (2008) ILLUSTRATING THE BAMBINO'S INTERNAL OPERATIONS.

The Leeb's Hardness values are converted to unconfined compressive strength in psi (lbs/in^2) using the following equations:

$$psi = 0.0000000746*(0.99725158^{L'})*(L'^{4.2961784}) \text{ (Enderlin, 2017)}$$

$$psi = (8*10^{-6}*(L'^{2.5}))*145.03773801 \text{ (Aoki and Matsukura, 2008)}$$

$$psi = (0.000000683*L'^{2.9})*145.03773801 \text{ (Zahm et al, 2014)}$$

Five data point measurements were taken from the Bambino and averaged at each sample location. Each of the five data points collected at the same depth were moved slightly to ensure that the same part of the core was not sampled twice, which might produce an erroneous reading. The Maness data points were collected at six-inch (15.24 cm) intervals and then modified to one-foot (30.48 cm) intervals in the Buda, Lower Eagle Ford and the Austin Chalk.

In summary, the rock strength is measured by two independent calculations:

1.) Rock strength is a function of dimple indentation size based on the Dimpler's imprint and converted to UCS using the Enderlin algorithm.
2.) Rock stringing is a function of Leeb's hardness that was measured using a Bambino hammer and converted to UCS using three different algorithms.

Well Logs and Maps

Four horizons, the top of the basal Eagle Ford phosphate lag, top of Maness Shale, top of intra-Maness limestone, and top of the Buda Limestone, were initially identified in the two cores, converted to log depth, and then correlated across the study area (Figure 19). These horizons were picked in 94 wells that contained a robust log suite dataset, including gamma ray, resistivity, neutron porosity, and density porosity logs. The neutron density log was a key log for correlations, as an increase in neutron density in unconventional shales generally indicates an increase in overall clay content. Additional wells with a less robust log data set that included only gamma ray and resistivity logs were correlated, yielding a total 345 wells for the study.

The phosphate lag zone, marked by a strong gamma ray spike, usually over 200 API, is readily identified in core (Figure 20) and is found in the basal Lower Eagle Ford across most of the study area. The phosphate lag interval contains limestone and shaley zones with abundant phosphate clasts and moderate amounts of inoceramid fragments and pyrite nodules. The shales below the pyrite nodule zone are indistinctly laminated mudstones. The lag's gamma ray spike is produced by an increase in potassium and uranium (Figure 21). Occasionally there is an ash bed in addition to the phosphate lag that contributes to the gamma ray spike, which is also apparent in the neutron porosity log.

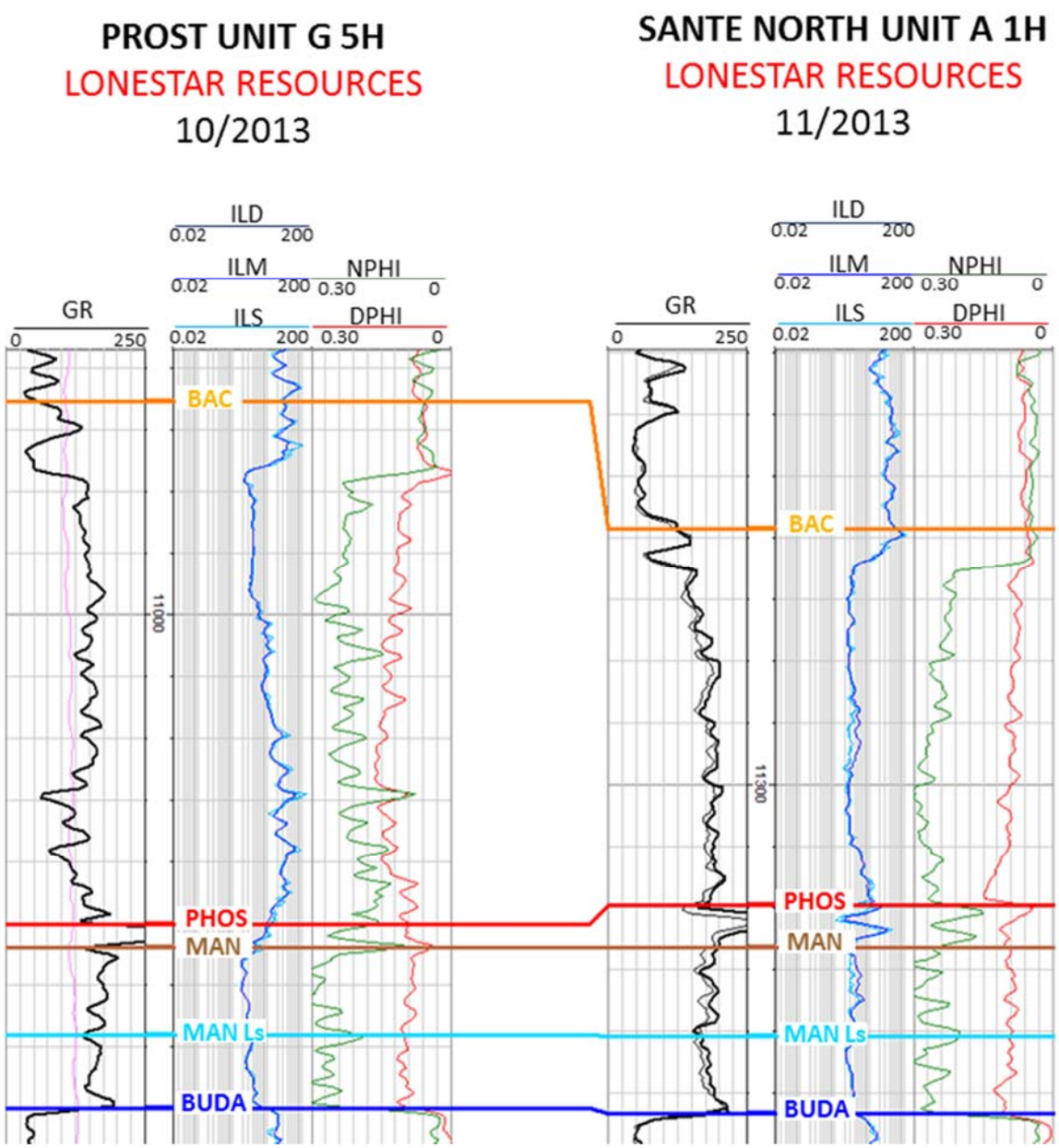

FIGURE 19. FORMATION TOPS FOR THE PROST UNIT G 5H AND SANTE NORTH UNIT A 1H CORES. (GR – GAMMA RAY, IL – INDUCTION RESISTIVITY LOG (D-DEEP, M-MEDIUM, S-SHALLOW), NPHI – NEUTRON POROSITY, DPHI – DENSITY POROSITY; BAC – BASE OF AUSTIN CHALK, PHOS – PHOSPHATE, MAN – MANESS, MAN LS – INTRA-MANESS LIMESTONE, BUDA – BUDA LIMESTONE)

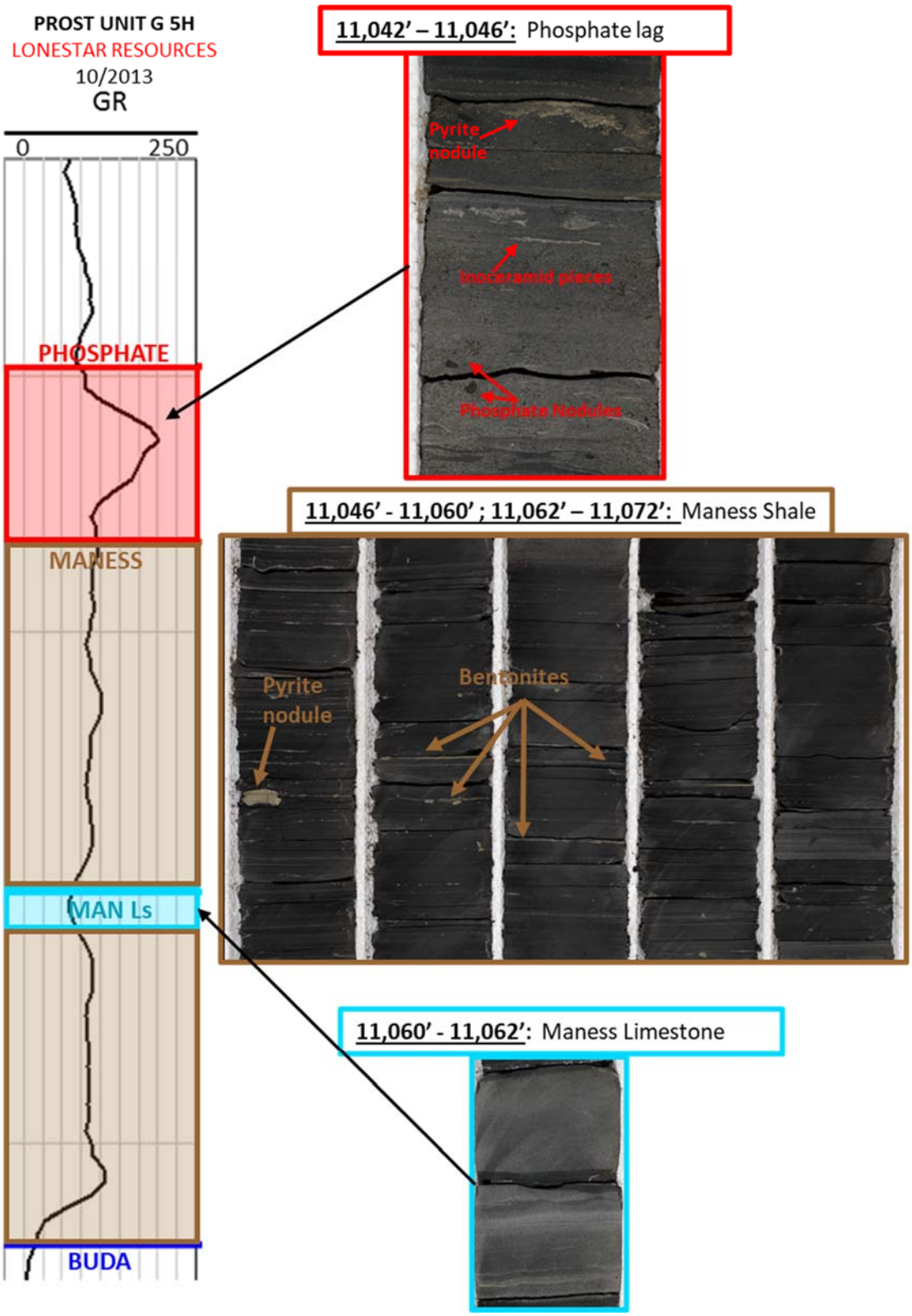

FIGURE 20. THE GAMMA RAY OF THE TYPE LOG AND CORRESPONDING CORE IMAGES NOTING THE FORMATION TOPS CORRELATED THROUGHOUT THE STUDY AREA.

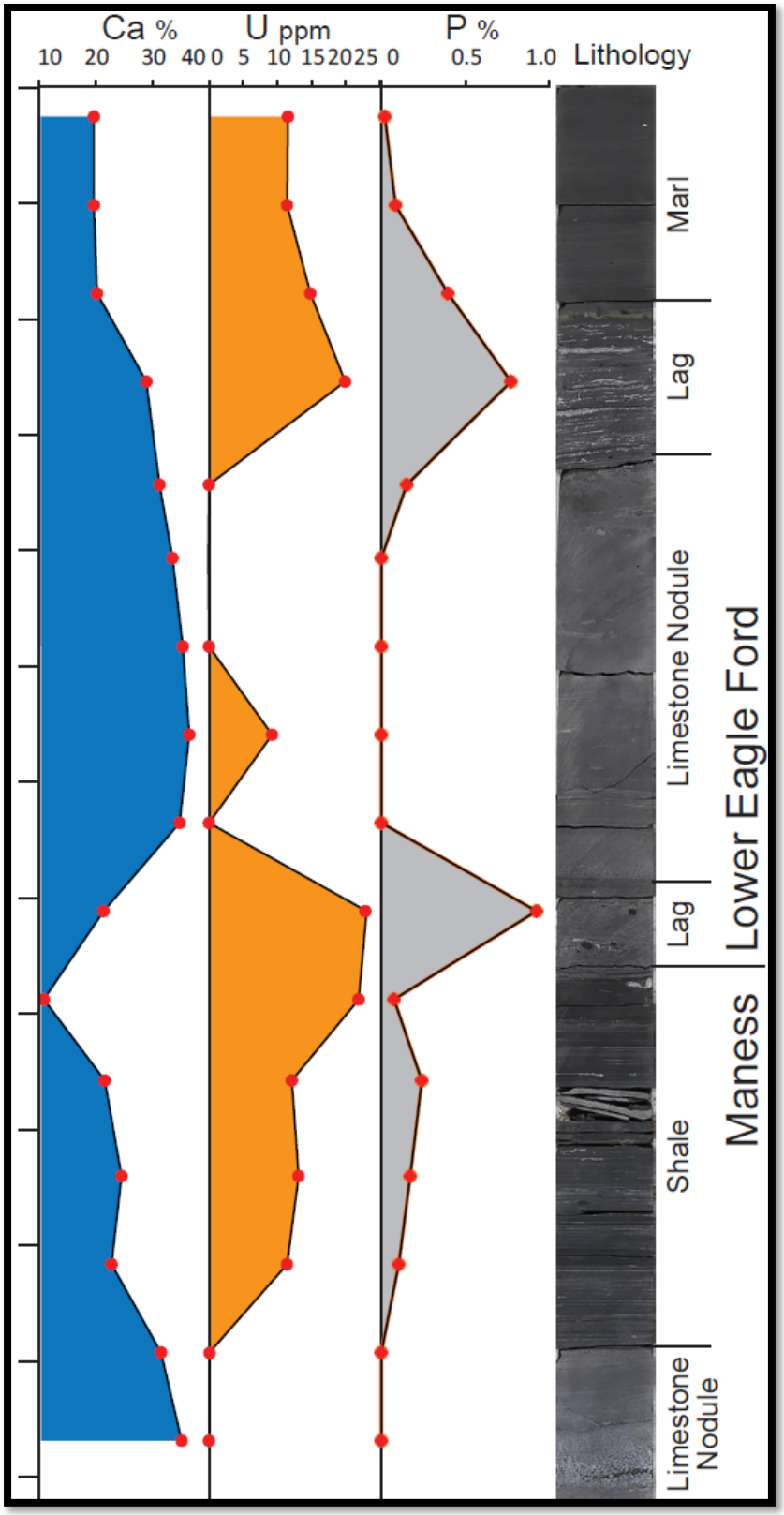

FIGURE 21. XRF-DERIVED CONCENTRATIONS OF CALCIUM, URANIUM, AND PHOSPHORUS OVER THE MANESS / PHOSPHATE LAG CONTACT IN A CORE FROM GONZALES COUNTY (DENNE, IN PRESS 2019).

Underlying the phosphate lag is the Maness Shale, which has an average gamma ray value of about 120 API, 30 API units less than the overlying Eagle Ford. The top of the Maness is also marked by a reduction in resistivity and an increase in neutron porosity, ranging from 20% to 30% NPHI (Figure 22). Although correlating the top of the phosphate and Maness sections is straightforward on the cores in Lavaca and Fayette counties, the top becomes more difficult to identify southwest of the San Marcos Arch. In core, the top of the Maness Shale is predominantly made up of black shales that are composed of thinly interbedded dark gray, massive argillaceous mudstones alternating with light gray, indistinctly laminated mudstones containing higher concentrations of planktonic foraminifera and recrystallized limestone. Pyrite nodules are common to abundant, whereas thin, greenish gray ash beds occur sparsely, usually surrounded by a calcite-rich zone. Additional cores from Karnes and Atascosa counties were described by Denne et al. (2016). The K-1 core from Karnes County has one inch (2.5 cm) of Maness, whereas the A-1 core from Atascosa County contains no Maness. The A-1 core has a gamma ray spike at the contact between the Eagle Ford and the Buda generated by the phosphate lag.

A nodular limestone, termed here the intra-Maness limestone, is identified within the Maness in the cores and can be identified on logs in many of the wells in the study area (Figure 22). Where present, it divides the upper and lower Maness sections. The bed has lower API gamma ray readings, slightly higher resistivity values, and a notable reduction in neutron porosity, indicating lower clay content. In core, this interval is composed of recrystallized limestone beds associated with thin ash beds. Pyrite nodules are abundant throughout this section.

The Buda Limestone top was picked on a sharp decrease in gamma ray, neutron porosity, and density porosity along with an increase in resistivity. It is one of the most diagnostic horizons in the Gulf Basin.

To test the hypothesis that the Maness acts as a fracture barrier from underlying aquifers, monthly production rate data for several leases were acquired from Lonestar Resources across the study area. The oil to water ratio is cross plotted with Maness thickness to determine if there is a correlation. In addition, 2,002 wells with first year cumulative production data for oil and water were downloaded from Drilling Info. The well list was restricted to only those wells from the study area producing from the Eagle Ford that were operated by Devon Energy, EOG Resources, Hunt Oil, Lonestar Resources, Marathon Oil, and Recoil Resources. The geographic location of these operators creates a wide spread distribution of wells, but limits the variance in production reporting and completion methods by restricting the number of operators.

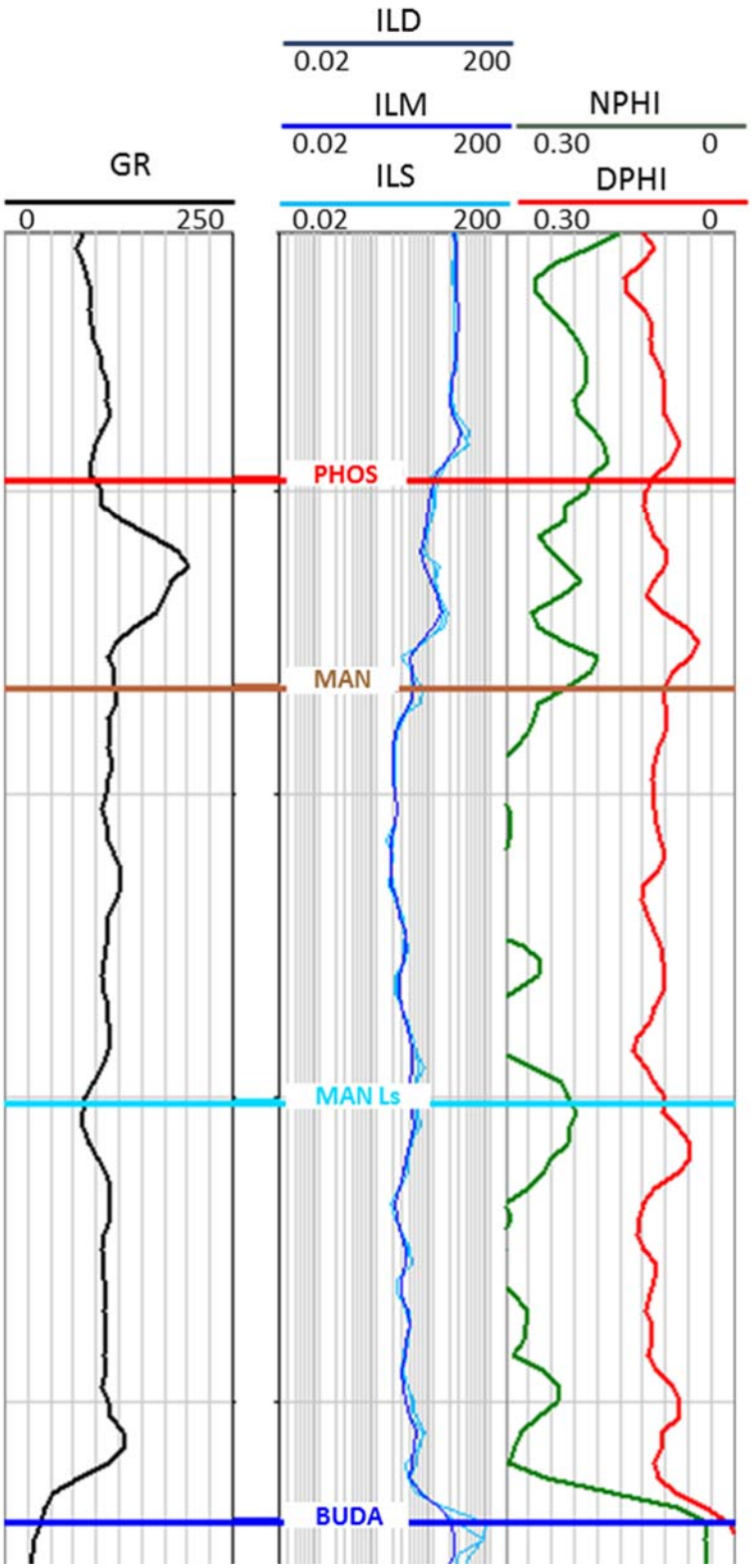

FIGURE 22. PROST G 5H TYPE WELL LOG DISPLAYING THE CHARACTERISTICS OF THE TRIPLE COMBINATION DATA, (GR – GAMMA RAY, IL – INDUCTION RESISTIVITY LOG (D-DEEP, M-MEDIUM, S-SHALLOW), NPHI – NEUTRON POROSITY, DPHI – DENSITY POROSITY), OF THE FOUR HORIZONS CORRELATED THROUGHOUT THE STUDY AREA.

Results

Cores

Thin Sections

Examination of the 23 thin sections from the Prost Unit G 5H and Sante North Unit A 1H cores identified six microfacies from the uppermost Buda limestone through the Maness and into the basal Eagle Ford Shale (Appendix A). The divisions of microfacies are based primarily on grain type, lamination style, and biotic components. Five of the six microfacies are identified within the Maness, whereas microfacies e is found only in the Buda Limestone (Table 2; Figure 23 - 28).

TABLE 2. MICROFACIES OBSERVED IN THIN SECTION.

Microfacies	Name	Description
a	Massive Argillaceous Mudstone	Internally structureless, largely homogeneous mudstone layer, dark brown in color, with frequent pyrite framboids (Ichaso and Dalrymple, 2009)
b	Indistinctly Laminated Mudstone	Displays parallel, discontinuous laminations of planktonic foraminifera, pyrite framboids, fish debris, inoceramid pieces, and dark brown clasts.
c	Partially Recrystallized Limestone	Made up of primarily recrystallized limestone, with calcite-filled foraminifera and pyrite framboids; original bedding mostly preserved
d	Fibrous Calcite	Calcite “beef” crystals (Cobbold et al., 2013) ranging up to 0.72 inch (2 cm) in length usually encasing ash beds
e	Calcisphere Packstone	Found only in the Buda Limestone, the fossils are cemented in sparry calcite and is mottled to massive, bioturbated, with abundant calcispheres, agglutinated and planktonic foraminifera, with rare ostracods and echinoid spines
f	Ash beds	Clay rich beds that have no bedding features

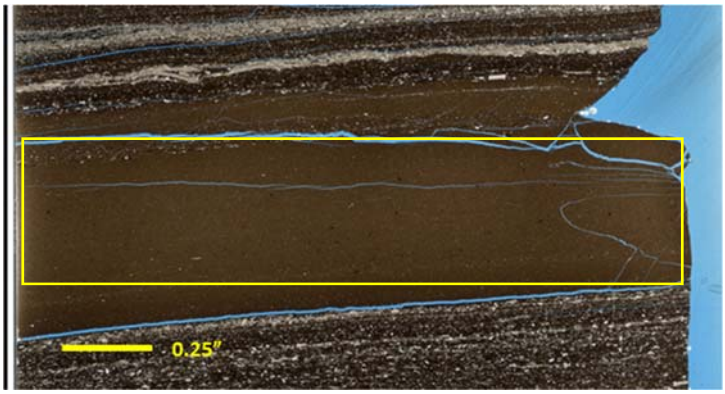

FIGURE 23. MICROFACIES a - SCANNED IMAGE OF THIN SECTION WITH TRANSMITTED LIGHT DISPLAYING MASSIVE ARGILLACEOUS MUDSTONE WITHIN THE YELLOW BOX (0.25 IN = 0.64 CM).

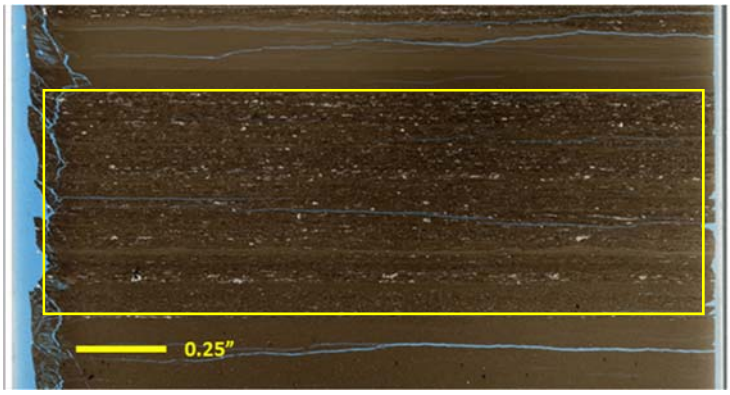

FIGURE 24. MICROFACIES b - SCANNED IMAGE OF THIN SECTION WITH TRANSMITTED LIGHT DISPLAYING INDISTINCTLY LAMINATED MUDSTONE (0.25 IN = 0.64 CM).

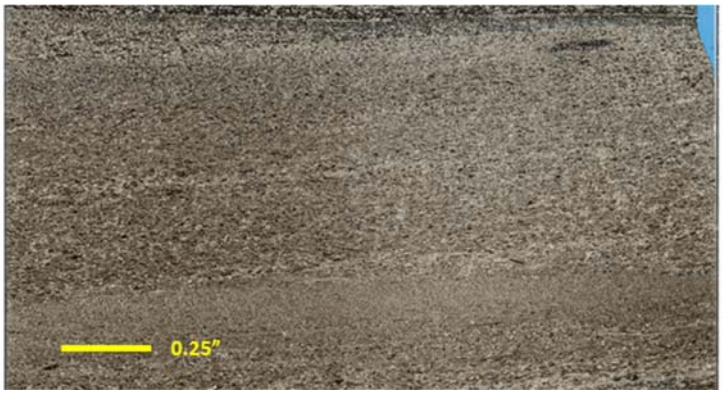

FIGURE 25. MICROFACIES c - SCANNED IMAGE OF THIN SECTION WITH TRANSMITTED LIGHT DISPLAYING PARTIALLY RECRYSTALLIZED LIMESTONE (0.25 IN = 0.64 CM).

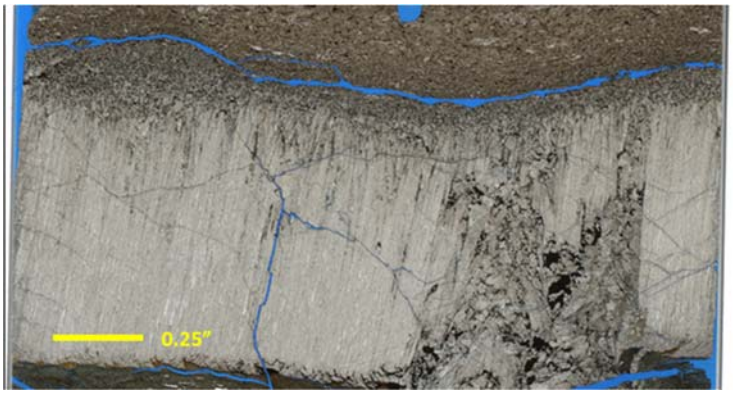

FIGURE 26. MICROFACIES d - SCANNED IMAGE OF THIN SECTION WITH TRANSMITTED LIGHT DISPLAYING FIBROUS CALCITE “BEEF” (0.25 IN = 0.64 CM).

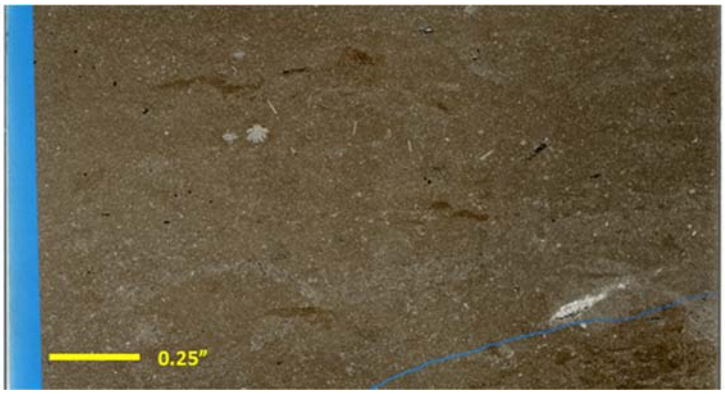

FIGURE 27. MICROFACIES e - SCANNED IMAGE OF THIN SECTION WITH TRANSMITTED LIGHT DISPLAYING CALCISPHERE PACKSTONE (0.25 IN = 0.64 CM).

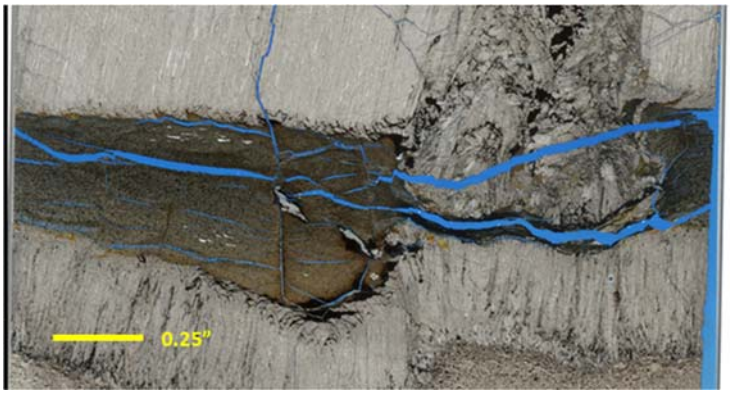

FIGURE 28. MICROFACIES f - SCANNED IMAGE OF THIN SECTION WITH TRANSMITTED LIGHT DISPLAYING AN ASH BED SURROUNDED BY FIBROUS CALCITE (0.25 IN = 0.64 CM).

Lithofacies

Examination of the two cores differentiated eight distinct lithological facies (Table 3; Figure 29) within the Maness Shale and directly adjacent rocks, based on changes in grain type and bedding, abundance of biota, and dominant mineralogy. In addition to these lithofacies, pyrite and phosphate nodules also occur within the section.

One or more of the microfacies make up each lithofacies. These lithofacies create the composition of the lowermost Eagle Ford, Maness, and uppermost Buda, with significant variance within each formation (Appendix B). The Eagle Ford is composed of lithofacies A, B, and D, has a higher lithological frequency, and a higher abundance of lithofacies D than the other rock units. The phosphate lag is also composed of lithofacies A, B, and D, but it is the only unit with lithofacies G. The Maness is composed of lithofacies A, B, C, and D; lithofacies C is present only in the Prost G 5H well and is relatively sparse. The Buda is made up of lithofacies E and F.

TABLE 3. LITHOFACIES OBSERVED IN CORE.

Lithofacies	Name	Description
A	Massive Argillaceous Mudstone	Black to dark gray, massive to indistinctly laminated mudstone. Foraminiferal laminae are sparse to non-existent; if present, they are very thin (0.2 inch or 0.5 cm). The skeletal fragments include inoceramids, fish fragments, and ammonite impressions. The mudstone shows almost no reaction to 10% HCl. Ash beds occur intermittently and range in size up to 1 inch (2.5 cm). Composed of microfacies a, b and f.
B	Indistinctly Laminated Mudstone	Thin interbedded beds made of mudstone, foraminifera laminae, and marls occur in bed thicknesses no thicker than 0.5 inch (1.3 cm). Color ranges from almost black (mudstone) to light gray (marl). Original bedding is preserved and pyrite occurs frequently in the forms of both ellipsoidal nodules and thin bedded layers that are greenish gray to yellow in color. Both the shale and limestones are rich in skeletal fragments of foraminifera, inoceramids, fish fragments, and ammonite impressions. The mudstone shows almost no reaction to 10% HCl. Ash beds occur intermittently and range in size up to 1 inch (2.5 cm). Composed of microfacies b and f.
C	Completely Recrystallized Limestone	Completely recrystallized limestones with fibrous calcite extending 0.72 inch (2 cm) in length and sometimes associated with ash beds. The recrystallized limestones sometimes truncate the bed below. Ash beds occur intermittently and range in size up to 1 inch (2.5 cm). Composed of microfacies d and f.
D	Recrystallized Laminated Limestone	Nodular limestone no thicker than 0.5 foot (15.3 cm); they are light gray in color; usually the original bedding is partially preserved and may pinch out across the width of the core. Composed of microfacies c.
E	Massive Limestone	Completely bioturbated limestone with no visual bedding; horizontal fractures are abundant; light gray in color; composed of microfacies e.

F	Nodular Limestone and Shale	Laminated to indistinctly laminated alternating massive, nodular limestone to laminated shale; medium gray in color; some original bedding is intact; composed of microfacies b and e.
G	Phosphate Lag	Abundant phosphate clasts within a winnowed lag deposit; composed of microfacies b.

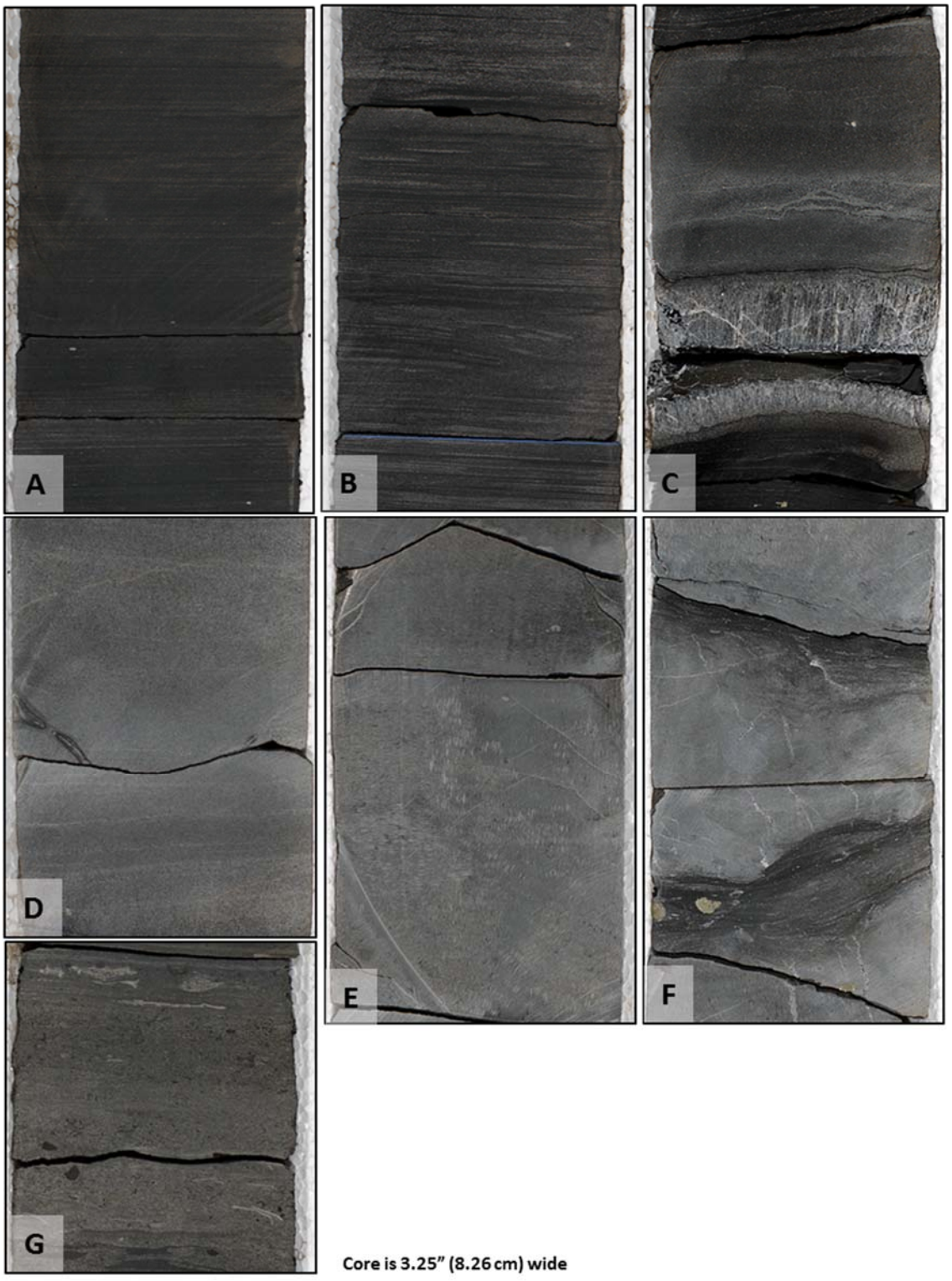

FIGURE 29. PHOTOGRAPHS OF REPRESENTATIVE CORE SECTIONS OF EACH LITHOFACIES. A) MASSIVE ARGILLACEOUS MUDSTONE, B) INDISTINCTLY LAMINATED MUDSTONE, C) COMPLETELY RECRYSTALLIZED LIMESTONE, D) RECRYSTALLIZED LAMINATED LIMESTONE, E) MASSIVE LIMESTONE, F) NODULAR LIMESTONE AND SHALE, AND G) PHOSPHATE LAG

XRD Analyses

Fourteen samples from the Prost G 5H and thirteen samples from the Sante North Unit A 1H were analyzed using XRD (Appendix D). The samples were taken from four different zones, the Eagle Ford, phosphate lag zone, Maness, and the Buda Limestone, most of which are from the same depths as the thin sections.

The average composition of the Eagle Ford marls is 48% calcite, 34% clay, and 12% quartz, with 6% divided among other minerals, including 2-4% pyrite and 0-22% feldspars (Figure 30). The average shale composition within the phosphate zone is 40% clay, 30% calcite, 15% quartz, 4-6% pyrite, and 0-3% feldspars. The average shale composition within the Maness is 50% clay, 18% quartz, 19% calcite, with 13% distributed among minor minerals (Figure 30) including 3-7% pyrite, and 3-12% feldspars. The Eagle Ford and Maness limestones is made up of mostly calcite but they do contain carbonate minerals such as ankerite and magnesium carbonates that are not present in the marls. The Buda averages 90% calcite, 4% quartz, and 4-6% pyrite (Figure 30).

In general, Eagle Ford marls and the phosphate lag have more calcite than the Maness, whereas the Maness has more clay (Figure 31). There are data points within the Eagle Ford and Maness that have greater than 70% calcite; these data points were taken within the nodular limestones that occur within each formation and are outliers to the rest of the data. The Buda is composed of mostly calcite.

The predominant clay type identified in the study was illite+mica, which accounts for ~77% of the clays found in the samples that were tested (Figure 32). The two Eagle Ford samples from the Prost G 5H core averaged 88.5% illite+mica, 7.8% kaolinite, 2.3% chlorite, and 1.4% smectite. The two phosphate lag zone samples averaged 86.4% illite+mica, 10.8% kaolinite,

and 2.8% smectite, whereas the eight Maness samples averaged 70.7% illite+mica, 27.7% kaolinite, and 1.7% smectite. For the Sante North Unit A 1H, the Eagle Ford samples averaged 79.7% illite+mica, 13.9% kaolinite, and 6.4% smectite. The phosphate lag sample had 80.7% illite+mica, 17.8% kaolinite, and 1.5% smectite, whereas the eight Maness samples averaged 76.2% illite+mica, 21.8% kaolinite, and 2.0% smectite. Both cores are located within the Harris Delta clay wedge (Denne and Breyer, 2016), especially the Sante North Unit A 1H, which explains the higher than normal clay percentages found within the Eagle Ford.

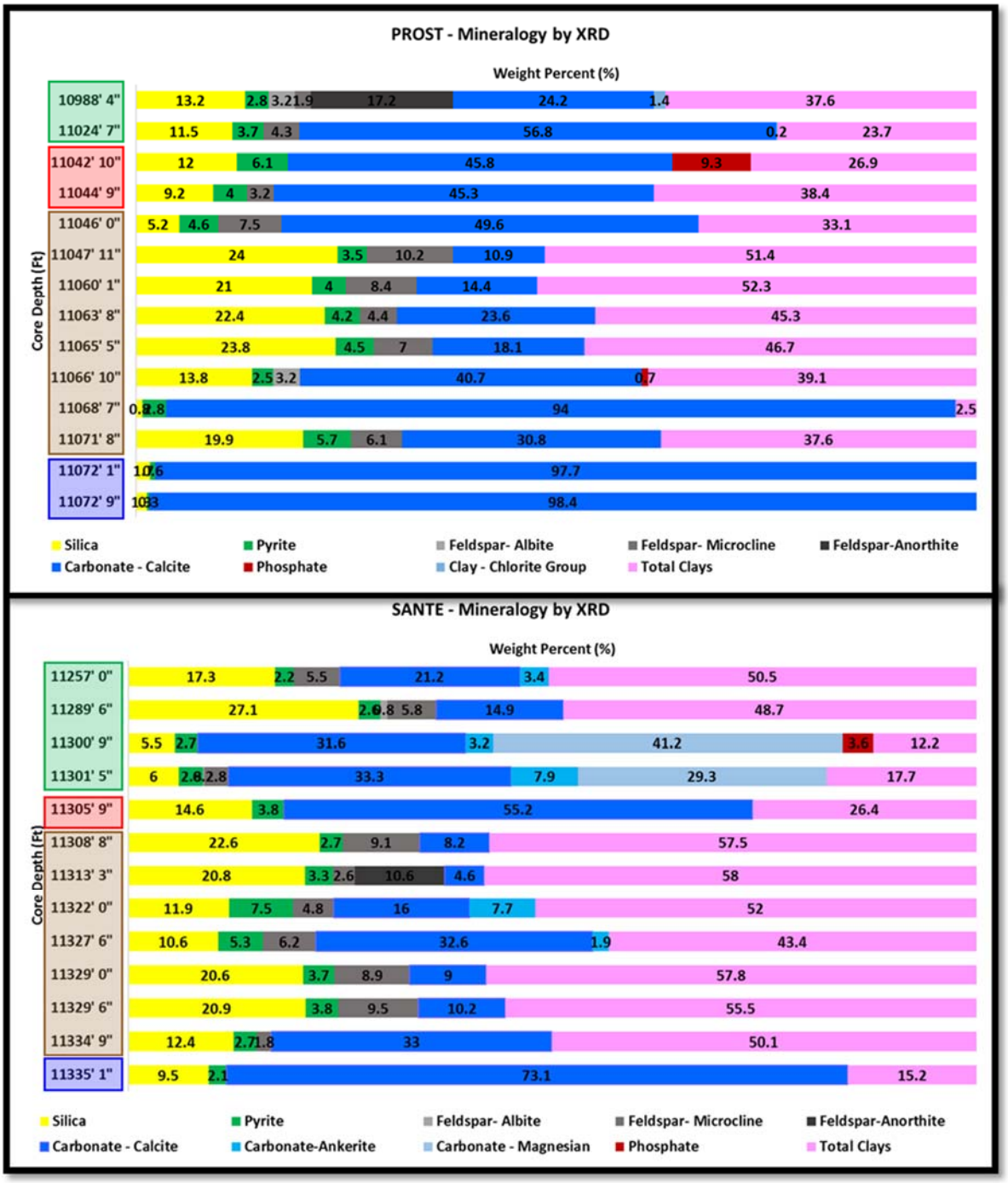

FIGURE 30. MINERAL ABUNDANCES AS DETERMINED BY XRD FOR PROST G 5H (TOP) AND SANTE NORTH UNIT A 1H (BOTTOM). THE CORE DEPTH IS COLOR CODED BY FORMATION (GREEN = EAGLE FORD; RED = PHOSPHATE; BROWN = MANESS; BLUE = BUDA).

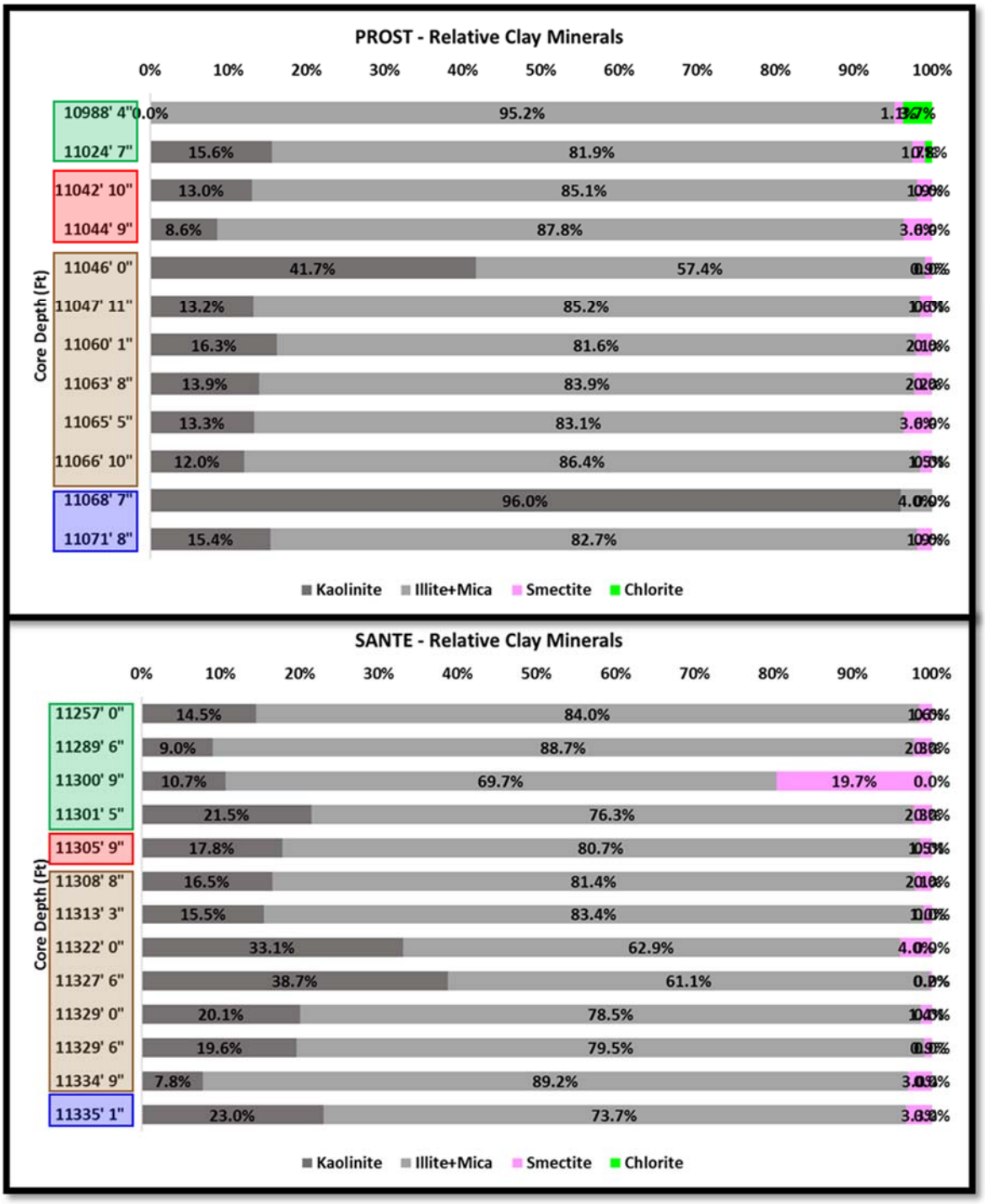

FIGURE 31. CLAY MINERAL ABUNDANCES FOR THE PROST G 5H (TOP) AND SANTE NORTH UNIT A 1H (BOTTOM). THE CORE DEPTH IS COLOR CODED BY FORMATION (GREEN = EAGLE FORD; RED = PHOSPHATE; BROWN = MANESS; BLUE = BUDA).

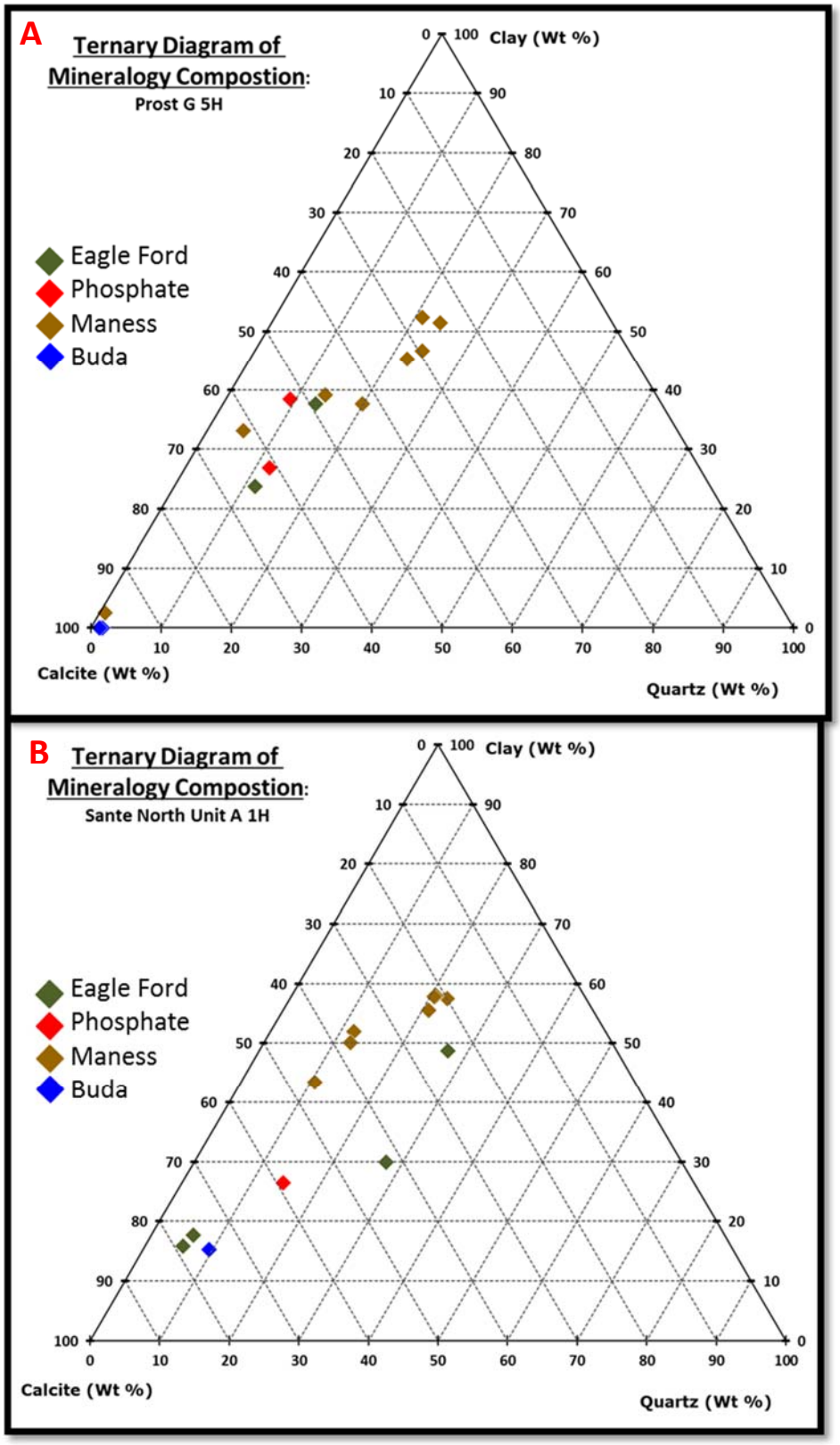

FIGURE 32. TERNARY DIAGRAMS OF THE XRD MINERAL COMPOSITION FOR THE (A) PROST G 5H AND (B) SANTE NORTH UNIT A 1H CORES.

Geomechanical Analyses

Unconfined compressive strength was evaluated using the Equotip Bambino and point load penetrometer ("Dimpler") across both cores. The Prost G 5H has 247 data points, whereas the Sante North Unit A 1H has 236 data points (Appendix E). A positive correlation between the Dimpler and Bambino strength is shown in cross plots of these parameters in Figure 33. A correlation factor of 81.3% was found in the Prost G and 78.1% for the Sante North Unit A 1H. The data points are subdivided between generic lithology descriptions and formations. The generic lithologies are chalk, limestone, shale, and recrystallized limestones. The recrystallized limestones occur within the Eagle Ford and Maness formations, whereas the limestones (as used here) occur only in the Buda. The marls and shales represent the baseline for the curve within the Eagle Ford and the Maness, whereas the interbedded limestones represent the higher values within these formations.

To determine if hardness values are affected by the total volume of the core sections, core section length and hardness values are cross-plotted (Figure 34). These plots show no evidence of correlation between core section length and hardness, as indicated by the very low R^2 values of 0.08 and 0.14 for the Dimpler and 0.07 and 0.16 for the Bambino. As width and depth are consistent throughout the core, section length is used as a proxy for core section volume.

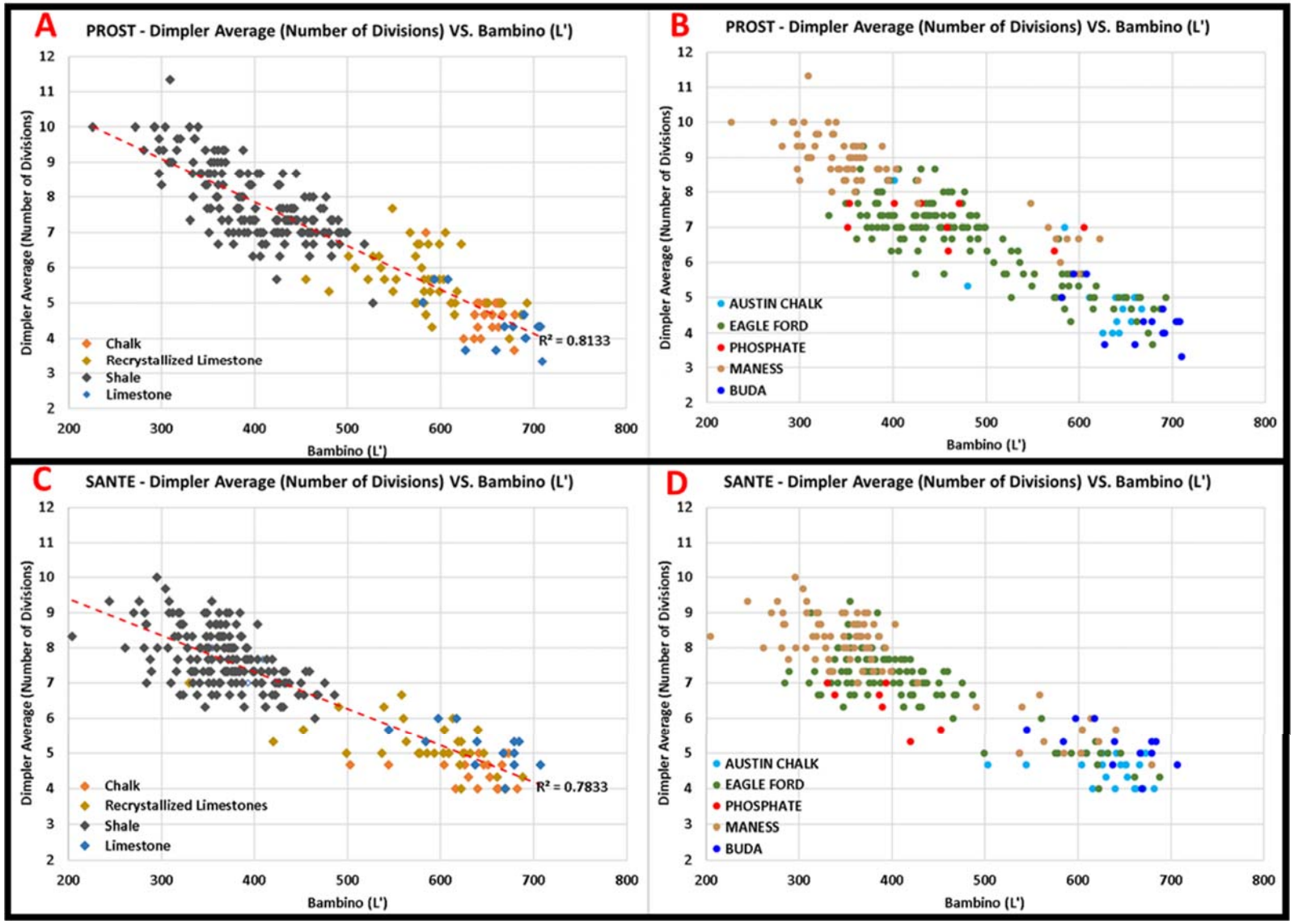

FIGURE 33. CROSS-PLOTS OF RAW DIMPLER DATA VS. RAW BAMBINO DATA. (A) PROST G 5H DATA COLOR-CODED BY FACIES, (B) PROST G 5H DATA COLOR-CODED BY FORMATION, (C) SANTE NORTH UNIT 1H DATA COLOR-CODED BY FACIES, AND (D) SANTE NORTH UNIT 1H DATA COLOR-CODED BY FORMATION

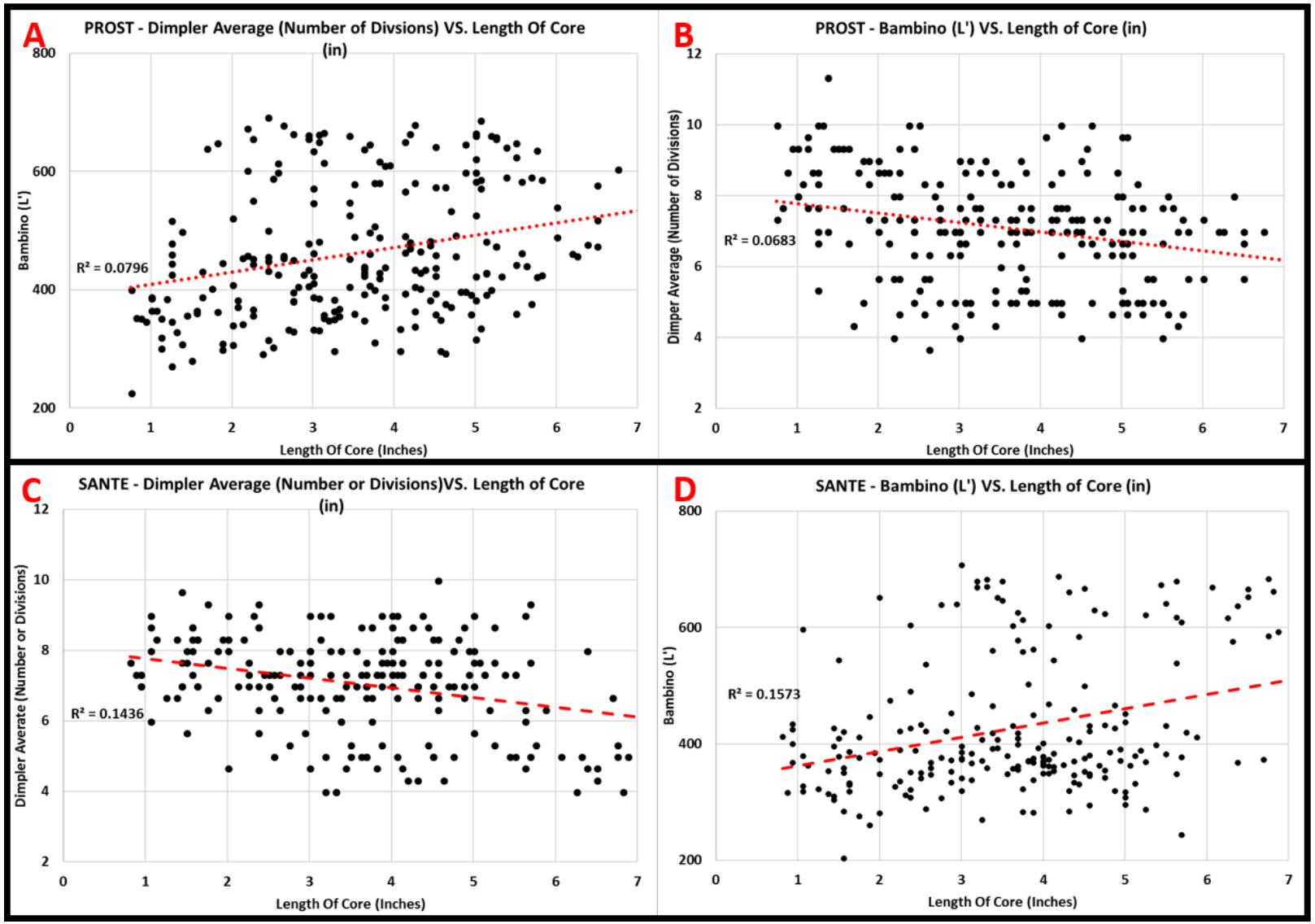

FIGURE 34. RESULTS FROM THE PROST G 5H (A AND B) AND THE SANTE NORTH UNIT 1H (C AND D) SHOWING BAMBINO AND DIMPLER VS. CORE LENGTH - THE LOW R^2 VALUES INDICATE THAT HERE IS NO CORRELATION BETWEEN THE LENGTH OF THE CORE SAMPLE AND HARDNESS VALUE

The point load penetrometer (Dimpler) values of rock strength for each core show significant variation between formations (Table 4; Figure 35). The average UCS is highest in the Austin Chalk and Buda Formations and lowest in the Maness Shale. In the Prost G 5H core UCS values for the Maness Shale range from 1,679 to 6,111 psi (11.6 to 42.1 MPa) with an average of 2,846 psi (19.6 MPa). This is 47.6% less than the average UCS value for the Eagle Ford and 83.0% less than the average for the underlying Buda Limestone. In the Sante North Unit A 1H core, UCS values for the Maness range from 2,120 to 8,958 psi (14.6 to 61.8 MPa) with an average of 3,505 psi (24.2 MPa), 27.0% less than the average for the Eagle Ford and 61.7% less than the Buda average.

Three algorithms were initially utilized to convert the Bambino L' values to unconfined compressive strength (UCS). As the variances were negligible (Figure 36), creating comparisons using all three algorithms is redundant, so only the UCS values using the Enderlin (2017) method will be discussed. Using the Enderlin UCS calculation for psi, the average UCS is highest in the Austin Chalk and Buda Formations and lowest in the Maness Shale (Table 5; Figure 37). UCS values for the Maness Shale in the Prost G 5H core range from 520 to 13,549 psi (3.6 to 93.4 MPa) with an average of 3,506 psi (24.2 MPa), 50.5% less than the Eagle Ford average and 78.3% less than the Buda average. In the Sante North Unit A 1H core UCS values for the Maness Shale range from 356 to 14,575 psi (2.5 to 100.5 MPa) with an average of 3,515 psi (24.3 MPa), 27.7% less than the Eagle Ford average and 76.5% less than the Buda average.

Although the variance between the UCS values derived from the point load penetrometer (Dimpler) and Bambino are marginal (Figure 38), and they show the same overall trends, the Bambino yielded a greater range of values, with higher UCS values in stiffer rocks and lower UCS values in weaker rocks. Even with the slight variance, the data still demonstrates that the Maness is weaker than the surrounding formations.

TABLE 4. POINT LOAD PENETROMETER MEASUREMENT SUMMARY BY WELL AND FORMATION.

	Point Load Penetrometer - Dimpler				
Well	Formation	Number of Samples	Average UCS (psi)	Minimum UCS (psi)	Maximum UCS (psi)
Prost G 5H	Austin Chalk	21	10,738	2,978	20,091
	Eagle Ford	144	5,430	2,411	25,748
	Phosphate	9	4,023	3,478	4,966
	Maness	61	2,846	1,679	6,111
	Buda	14	16,719	6,111	32,380
Sante North Unit A 1H	Austin Chalk	21	13,814	8,985	20,091
	Eagle Ford	116	4,800	2,411	20,091
	Phosphate	9	5,937	4,121	8,985
	Maness	73	3,505	2,120	8,958
	Buda	13	9,141	5,493	20,091

TABLE 5. EQUOTIP BAMBINO MEASUREMENT SUMMARY BY WELL AND FORMATION.

	Equotip Bambino				
Well	Formation	Number of Samples	Enderlin Average UCS (psi)	Enderlin Minimum UCS (psi)	Enderlin Maximum UCS (psi)
Prost G 5H	Austin Chalk	21	13,526	3,776	16,160
	Eagle Ford	144	7,078	2,008	17,730
	Phosphate	9	6,067	2,455	12,604
	Maness	61	3,506	520	13,549
	Buda	14	16,135	11,316	18,776
Sante North Unit A 1H	Austin Chalk	21	14,333	7,550	17,061
	Eagle Ford	116	4,862	1,184	17,425
	Phosphate	9	5,101	1,987	12,495
	Maness	73	3,515	356	14,575
	Buda	13	14,933	9,444	18,591

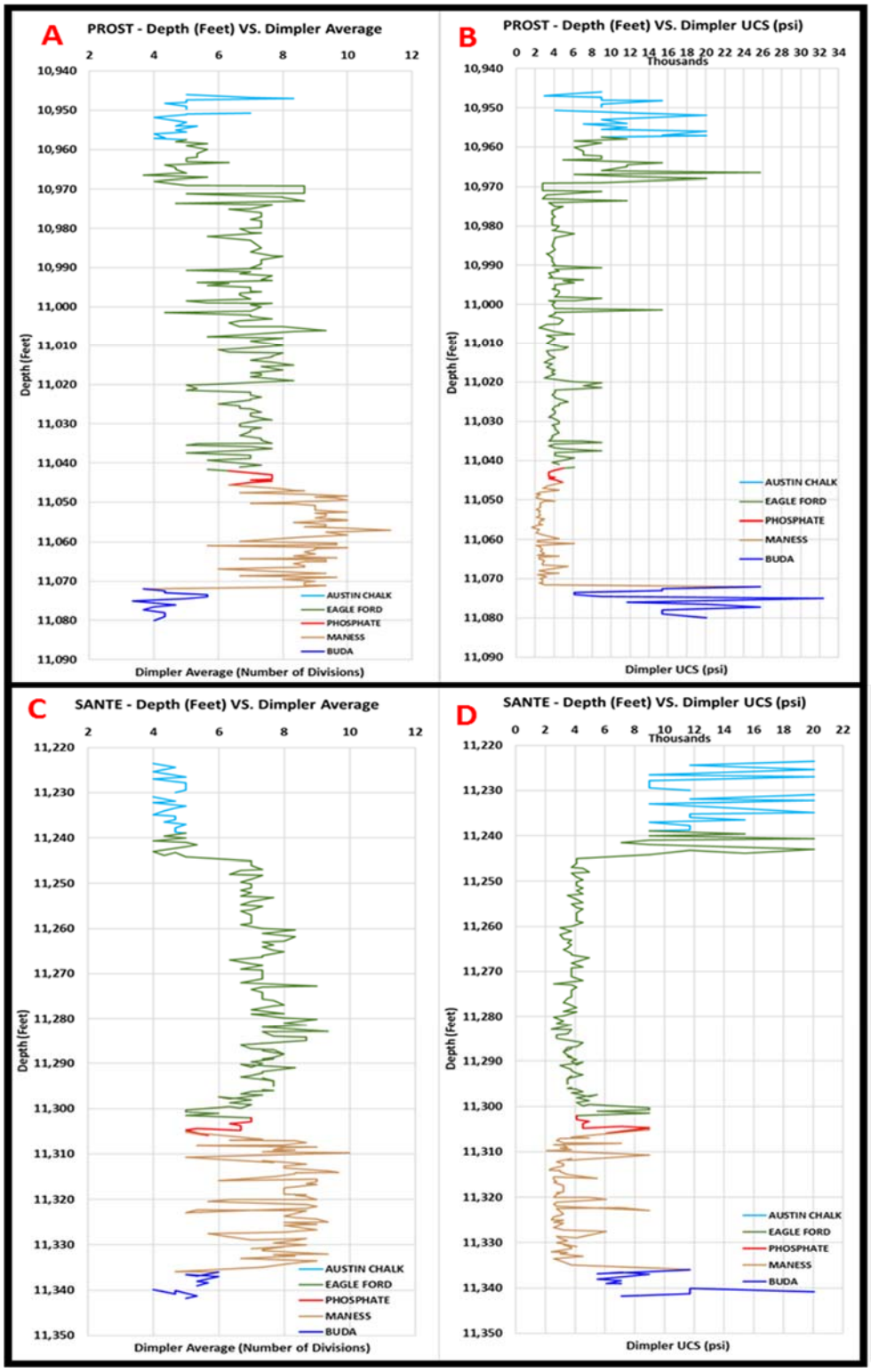

FIGURE 35. GRAPHS OF THE DIMPLER RESULTS FROM THE PROST G 5H AND THE SANTE NORTH UNIT 1H CORES PLOTTED AGAINST DEPTH. (A) AVERAGED RAW DATA FROM PROST G 5H, (B) DATA CONVERTED TO UCS FROM PROST G 5H, (C) AVERAGED RAW DATA FROM SANTE NORTH UNIT 1H, AND (D) DATA CONVERTED TO UCS FROM SANTE NORTH UNIT 1H. COLORS INDICATE THE FORMATION OR LITHOLOGICAL UNIT.

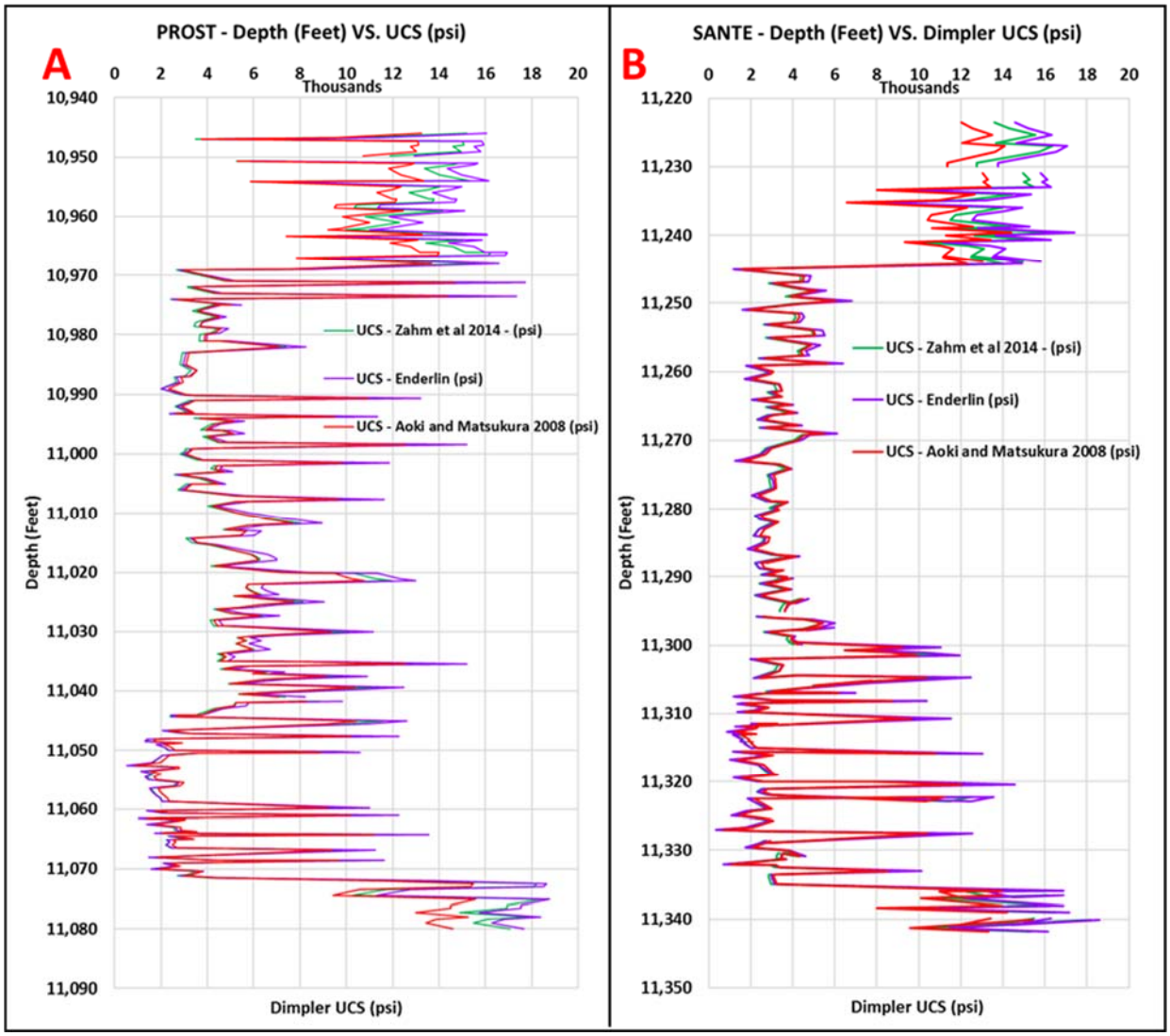

FIGURE 36. DEPTH PLOT OF THE UCS VALUES DERIVED USING THREE DIFFERENT ALGORITHMS FOR CALCULATING UCS (PSI) FROM THE BAMBINO. NOTE THE MINIMAL DIFFERENCES. (A) DATA FROM THE PROST G 5H. (B) DATA FROM THE SANTE NORTH UNIT A 1H.

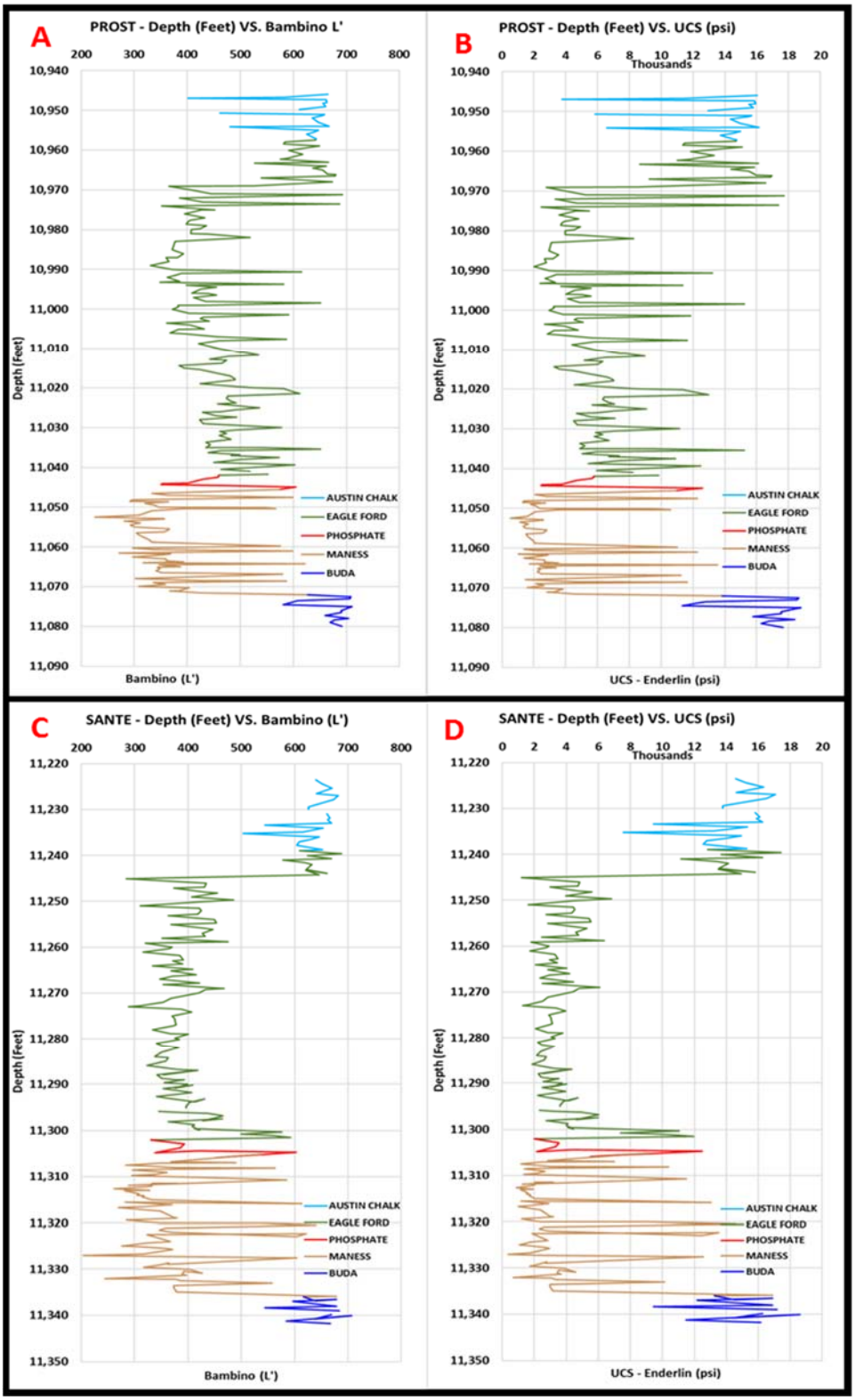

FIGURE 37. GRAPHS OF THE BAMBINO RESULTS FROM THE PROST G 5H (A AND B) AND THE SANTE NORTH UNIT 1H (C AND D) DISPLAYING THE RAW L' (HLD) AVERAGE (A, C), UCS VALUES DERIVED USING THE ENDERLIN (2017) EQUATION (B, D). COLORS INDICATE THE FORMATION OR LITHOLOGICAL UNIT

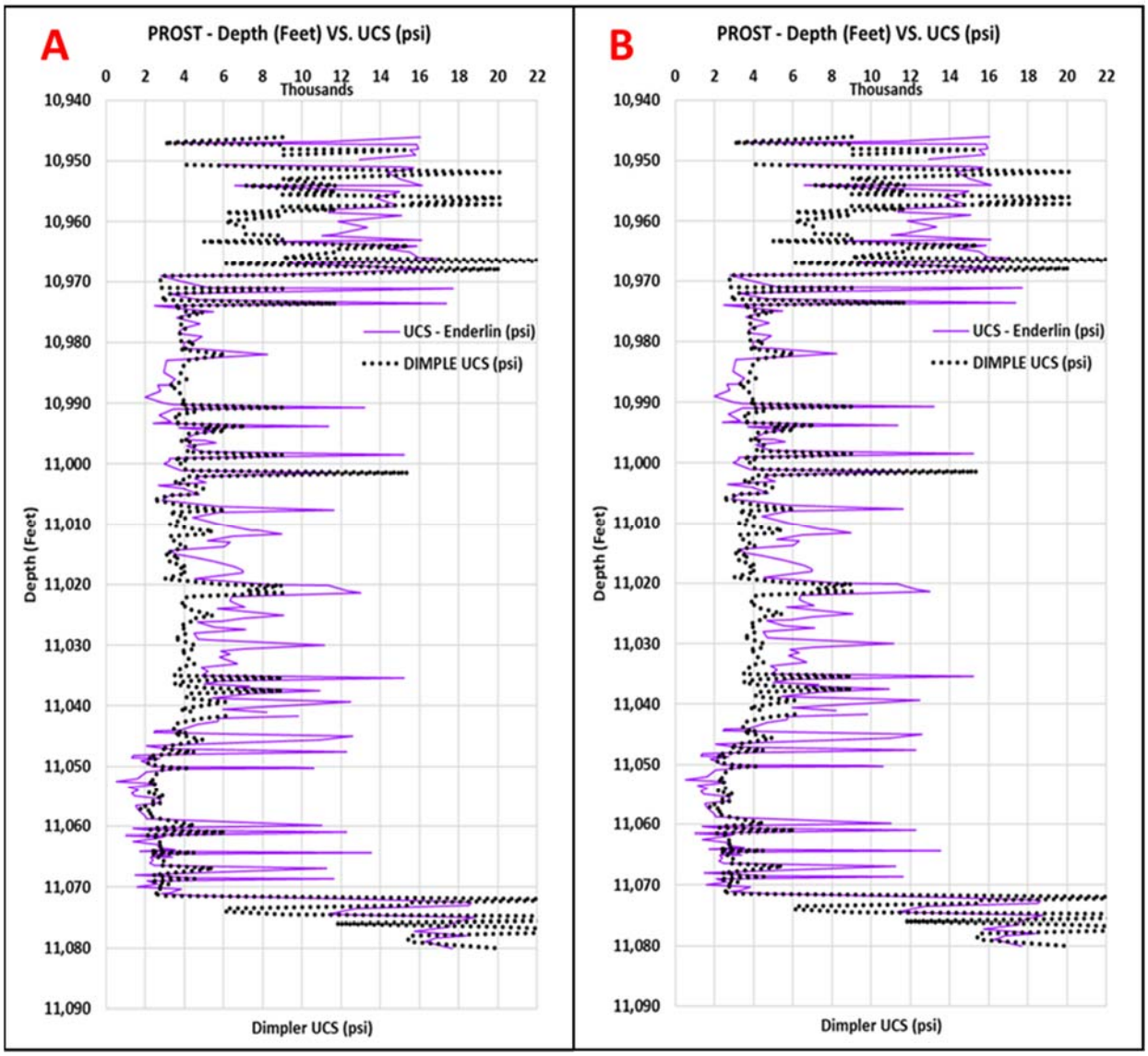

FIGURE 38. A GRAPH OF ALL STRENGTH VALUE CALCULATIONS FOR BOTH THE DIMPER (POINT LOAD PENETROMETER) AND BAMBINO VERSUS DEPTH DISPLAYING THE SAME CHARACTER DESPITE A VARIANCE IN VALUES.

To better understand the geomechanical differences between the marls and shales of the Eagle Ford, phosphate lag, and the Maness, the data from recrystallized limestones are removed from the data set. The number of data points is reduced in the Prost G 5H well by 23% in the Eagle Ford and 13% in the Maness and the Sante North Unit A 1H data points are reduced by 27% in the Eagle Ford and 14% in the Maness. After removing the data for the recrystallized limestones derived from the point load penetrometer, the Maness Shale ranges in strength from 1,900 to 3,800 psi (13.1 to 26.2 MPa) with an average of 2,806 psi (19.4 MPa) (Table 6) for both cores. The Maness is 28.0% weaker than the Eagle Ford. After removing the data from the recrystallized limestones derived from the Equotip Bambino, the Maness Shale ranges in strength 438 to 4,604 psi (3.0 to 31.7 MPa) with an average of 2,275 psi (15.7 MPa) (Table 7) for both cores. The Maness is 45.2% weaker than the Eagle Ford. In summary, the formation averages decrease in UCS (psi) after removing the data for the recrystallized limestones as expected. The Eagle Ford and phosphate lag rocks both have higher UCS (psi) values than the Maness, with or without the data from the recrystallized limestones (Figure 39).

TABLE 6. AVERAGE DIMPLER MEASUREMENT SUMMARY FOR BOTH WELLS AND FORMATION WITH DATA FOR THE LIMESTONES REMOVED.

Point Load Penetrometer - Dimpler				
Formation	Number Of Samples	Enderlin Average UCS (psi)	Enderlin Minimum UCS (psi)	Enderlin Maximum UCS (psi)
Eagle Ford	181	3,899	2,411	7,239
Phosphate	11	4,202	3,800	4,966
Maness	116	2,806	1,900	3,800

TABLE 7. AVERAGE BAMBINO MEASUREMENT SUMMARY FOR BOTH WELLS AND FORMATION WITH DATA FOR THE LIMESTONES REMOVED.

Equotip Bambino				
Formation	Number Of Samples	Enderlin Average UCS (psi)	Enderlin Minimum UCS (psi)	Enderlin Maximum UCS (psi)
Eagle Ford	181	4,153	1,596	7,730
Phosphate	11	3,779	2,300	4,878
Maness	116	2,275	438	4,604

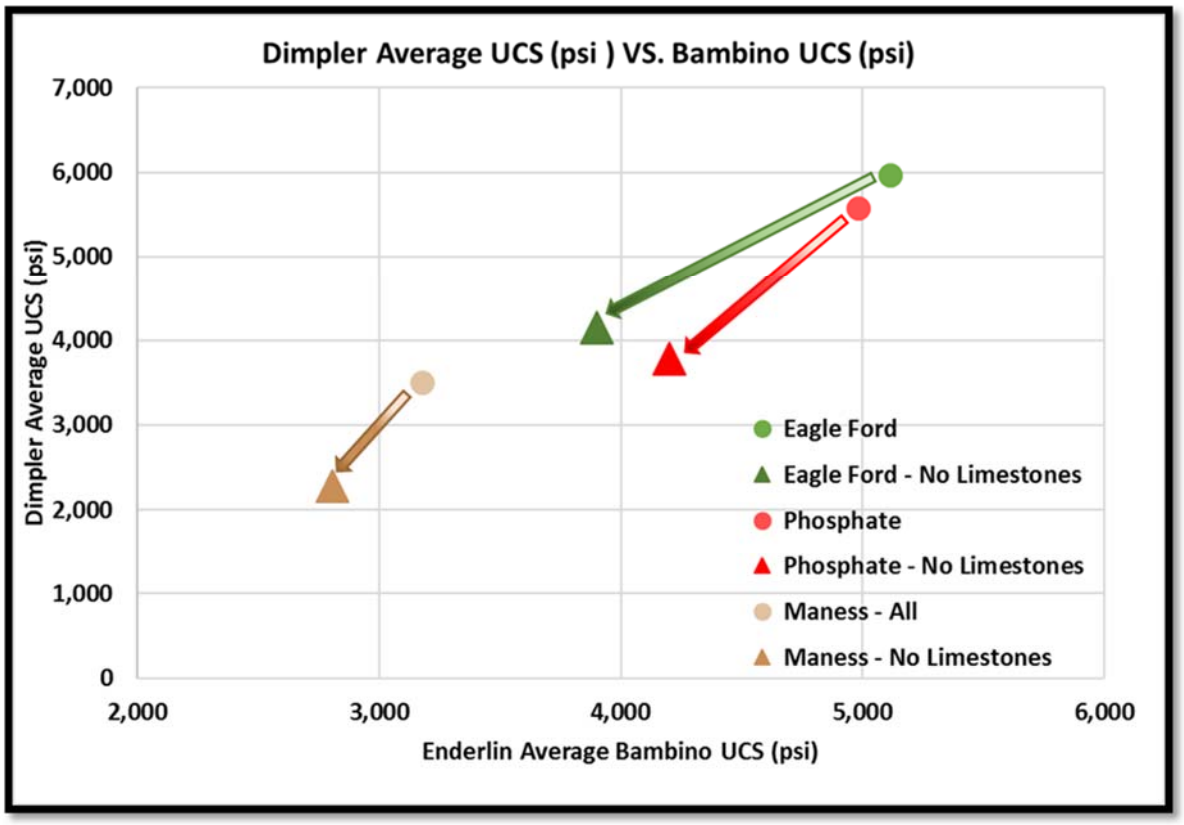

FIGURE 39. GRAPH DISPLAYING AVERAGE UCS FOR DIMPLER AND BAMBINO INDICATING THE DIRECTION OF CHANGE AFTER REMOVING THE DATA FROM RECRYSTALLIZED LIMESTONES.

Mineralogy, Geomechanics and Lithofacies

Cross-plots between UCS values and calcite and total clay volume (Figure 40) show an inverse relationship between calcite and clay content in relation to strength. Clay volume has a negative correlation, implying that the higher the volume of clay the lower the UCS value for both the Dimpler and the Bambino. The opposite relationship holds for calcite, which has a positive correlation, signifying that an increase in UCS is linked to an increase in calcite volume.

The R^2 values for strength versus calcite range from 9.7% to 36.0% and range from 32.6% to 37.6% for strength versus clay (Figure 40), which are considered to be poor to moderate correlations. The Sante Unit A 1H generally has higher correlations than that of the Prost G 5H well. This is likely due to the larger number of outlier data in the Prost well, which are an artifact of UCS measurements taken within recrystallized limestones that were paired with XRD analyses that sampled both the limestone and the adjacent mudstone. The inverse relationship between calcite and clay with respect to strength is not unexpected, as higher abundances of brittle minerals such as calcite should produce higher UCS and higher abundances of ductile clays should produce lower UCS values.

The Eagle Ford Shale and the Buda Limestone are mechanically stronger than the Maness Shale. The weakness associated with the Maness is due to the increase in ductility, except for the intra-Maness Limestone which is composed of lithofacies C. The Maness section of the Prost 5H core is made up of 60.4% lithology A, 22.6% lithology B, 3.8% lithology C, 13.2% lithology D, and 0% for E, F and G lithofacies as those are only found in the phosphate and Buda Limestone (Table 8). The Maness portion of the Sante North Unit A 1H core is made up of 58.7% lithology A, 36.5% lithology B, 0% lithology C, 4.8% lithology D, and 0% for E, F and, G lithofacies. The Maness has an abundance of lithologies A and B that average a UCS of 2,488 psi (17.15

MPa) psi for both strength tools (Table 9). The Eagle Ford is the only formation to have A/B as the laminations of lithology A and B are thin and thus are combined in portions of the core. The average UCS for lithologies A/B, A, and B for both strength tools within the Eagle Ford is 4,802 psi (33.11 MPa), which is 48.2 % higher than the Maness.

When incorporating the calcite and clay mineralogy, strength values, and lithofacies (Figure 40), there are a few things to note. The expected trend is that the high calcite (circles) should have higher UCS, whereas the high clay (triangles) should have low UCS values. In general, the graphs show these expected trends. As noted above, the XRD and the strength data are not taken from the exact same intervals, producing a few outliers.

TABLE 8. TABLE DISPLAYING THE PERCENT OF LITHOLOGY PER FORMATION.

Number of Samples per Lithology									
		Lithology for Every Sample Aquired							
Well	Formation	A/B	A	B	C	D	E	F	G
Prost G 5H	EAGLE FORD	75.2%	2.1%	2.1%	0.0%	20.6%	0.0%	0.0%	0.0%
	PHOSPHATE	0.0%	57.1%	28.6%	0.0%	0.0%	0.0%	0.0%	14.3%
	MANESS	0.0%	60.4%	22.6%	3.8%	13.2%	0.0%	0.0%	0.0%
	BUDA	0.0%	0.0%	0.0%	0.0%	0.0%	92.9%	7.1%	0.0%
Sante North Unit A 1H	EAGLE FORD	86.0%	10.5%	0.9%	0.0%	2.6%	0.0%	0.0%	0.0%
	PHOSPHATE	0.0%	25.0%	50.0%	0.0%	0.0%	0.0%	0.0%	25.0%
	MANESS	0.0%	58.7%	36.5%	0.0%	4.8%	0.0%	0.0%	0.0%
	BUDA	0.0%	0.0%	0.0%	0.0%	0.0%	71.4%	28.6%	0.0%

TABLE 9. THE AVERAGE UCS (PSI) VALUES PER LITHOFACIES WITHIN SPECIFIC FORMATIONS.

Point Load Penetrometer

Average UCS (psi) per Lithofacies

Well	Formation	A	B	C	D	E	F	G	Average
Prost G 5H	EAGLE FORD	4,188	4,252		1,890				**3,443**
	PHOSPHATE	4,011	3,800					3,478	**3,763**
	MANESS	2,555	2,607	2,868	2,494				**2,631**
	BUDA					17,535	6,111		**11,823**
	AVERAGE	**3,585**	**3,553**	**2,868**	**2,192**	**17,535**	**6,111**	**3,478**	**5,617**
Sante North Unit A 1H	EAGLE FORD	3,901	4,966						**4,434**
	PHOSPHATE	4,966	4,514					4,121	**4,534**
	MANESS	3,109	2,892		3,305				**3,102**
	BUDA					9,112	6,929		**8,020**
	AVERAGE	**3,992**	**4,124**		**3,305**	**9,112**	**6,929**	**4,121**	**5,264**

Equotip Bambino

Average UCS (psi) per Lithofacies

Well	Formation	A	B	C	D	E	F	G	Average
Prost G 5H	EAGLE FORD	5,711	7,643		2,972				**5,442**
	PHOSPHATE	3,616	5,965					4,706	**4,762**
	MANESS	2,170	2,620	2,994	2,023				**2,452**
	BUDA					16,394	12,769		**14,582**
	AVERAGE	**3,832**	**5,409**	**2,994**	**2,497**	**16,394**	**12,769**	**4,706**	**6,943**
Sante North Unit A 1H	EAGLE FORD	3,943	4,115						**4,029**
	PHOSPHATE	3,425	2,748					4,706	**3,626**
	MANESS	2,199	2,287		2,716				**2,401**
	BUDA					15,680	13,253		**14,466**
	AVERAGE	**3,189**	**3,050**		**2,716**	**15,680**	**13,253**	**4,706**	**7,099**

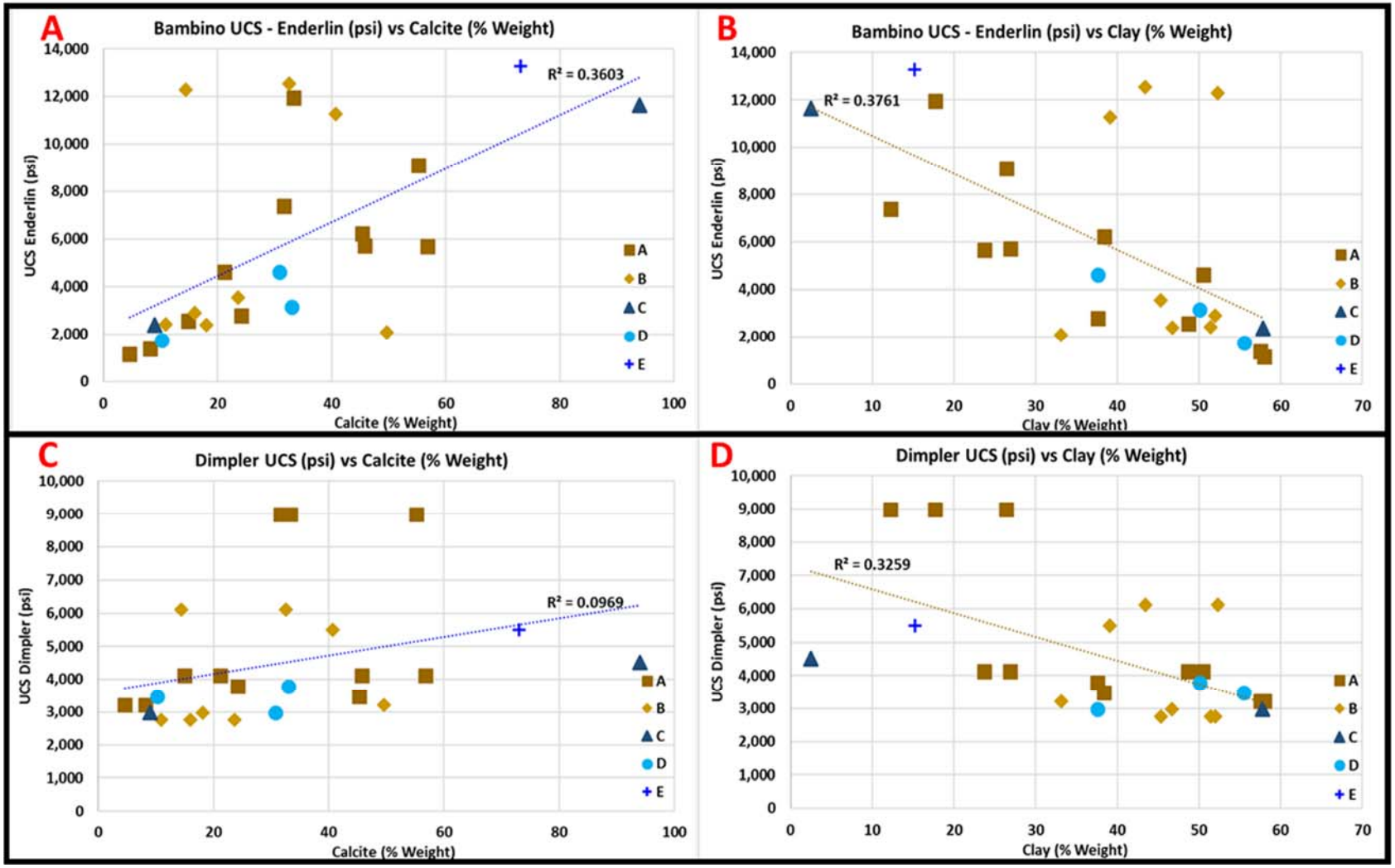

FIGURE 40. CROSS PLOT OF BAMBNIO STRENGTH VERSUS CALCITE AND CLAY (A AND B) AND OF DIMPLER STRENGTH VERSUS CALCITE AND CLAY (C AND D) CODED BY LITHOFACIES.

Well logs and mapping

Four horizons are correlated in 345 wells across the study area: the top of the phosphate lag zone, top of the Maness Shale, top of the intra-Maness limestone, and top of the Buda Limestone (Figure 13). Two cross sections represent the key wells for correlations for wells along strike from Atascosa County to Fayette County (Figure 41), and along dip from Gonzales County, into the Gonzales Trough and South to Dewitt County (Figure 42). These horizons were used to create a structure map for the top of the Buda (Figure 43), and isopach maps for five intervals: top of phosphate to top of Buda, top of Maness to top of Buda, top of phosphate to top of Maness, top of Maness to top of intra-Maness limestone (upper Maness), and top of intra-Maness limestone to top of Buda (lower Maness) (Figures 44 – 48).

Within the study area the top of the Buda ranges in depth from -5,000 to -13,500 ft (-1,524 to -4114.8 m) subsea true vertical depth (SSTVD), with the shallowest depths occurring on the north side and the deepest occurring along the Sligo-Stuart City Reef trend. The two fault grabens, the Karnes and Gonzales troughs, have throws at the Buda level ranging from a few feet to >200 ft (1 to >61 m) (Figure 43).

The phosphate lag zone to top of Buda interval has thicknesses ranging from 5 to 45 ft (1.5–13.7 m) with the thickest section located within the Gonzales Trough (Figure 44). Within the trough the interval ranges from 30 to 45 ft (9.1–13.7 m), whereas thicknesses outside of the trough range from 5 to 25 ft (1.5–7.6 m). The thinnest section is in central Wilson County, where the maximum thickness is 10 ft (3.1 m). In general, the thickest sections are located to the northeast and thin to the southwest.

The Maness has thicknesses ranging from 0 to 25 ft (0–7.6 m), with the thickest interval located within the Gonzales Trough (Figure 45), similar to the phosphate lag to Buda interval.

Maness thicknesses within the Gonzales Trough are found to be relatively constant at 25 ft (7.6 m). The Maness is found to pinch-out south of southern Karnes County. Overall, the Maness trends from thickest in the northeast and thins to the southwest.

The phosphate lag zone ranges from 0 to 15 ft (0 – 4.6 m), with the thickest section (15 ft) (4.6 m) located in the Gonzales County Trough. The thicker intervals align with the orientation of the troughs (Figure 46). The phosphate lag zone is present throughout most of the study area apart from northernmost Gonzales County and near the Lower Cretaceous reef margins. The only obvious trend appears to be related to the troughs.

The upper Maness (Maness top to intra-Maness limestone) ranges from 0 to 15 ft (0 – 4.6 m), with the thickest interval located within the Gonzales Trough and pinching out in central Karnes County (Figure 47). Overall, the thickest intervals are located in the northeastern part of the study area and thin to the southwest, eventually pinching out.

The lower Maness (intra-Maness limestone top to Buda top) ranges from 0 to 15 ft (0 – 4.6 m) (Figure 48). Its overall trend is almost identical to the upper Maness trend, with the thickest sections located within the Gonzales Trough and the interval pinching out in central Karnes County.

The isopach maps all imply a depositional source originating from northeast of the study area, as the Maness has its greatest thicknesses in this region and thins to the southeast. The Gonzales-Karnes troughs appear to have been structural lows at the time of Maness deposition, based on the greater Maness thicknesses found within the troughs in relation to the thinner sections found in wells adjacent to them.

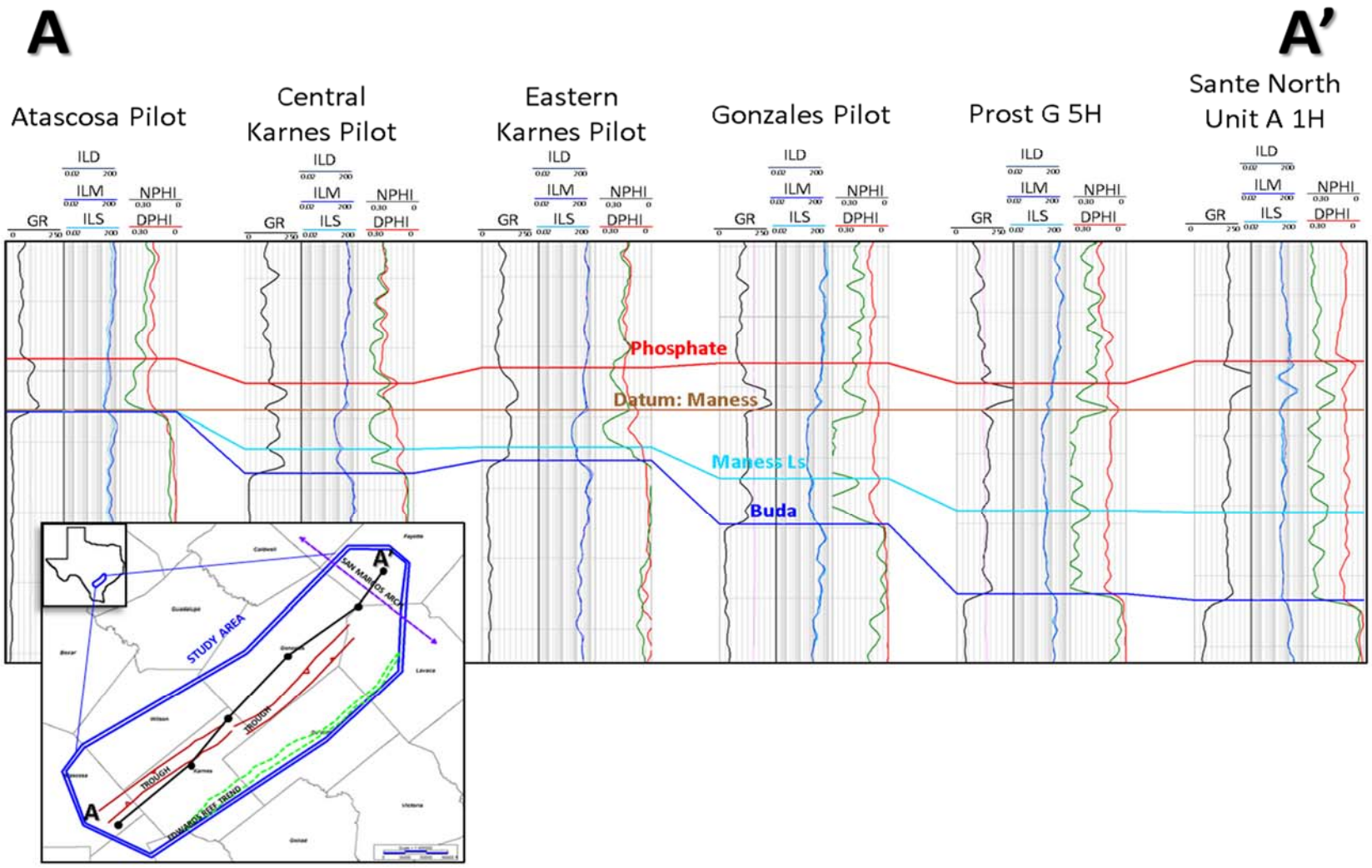

FIGURE 41. STRATIGRAPHIC STRIKE CROSS SECTION (DATUM: MANESS TOP) TRENDING FROM THE SOUTHWEST TO NORTHEAST

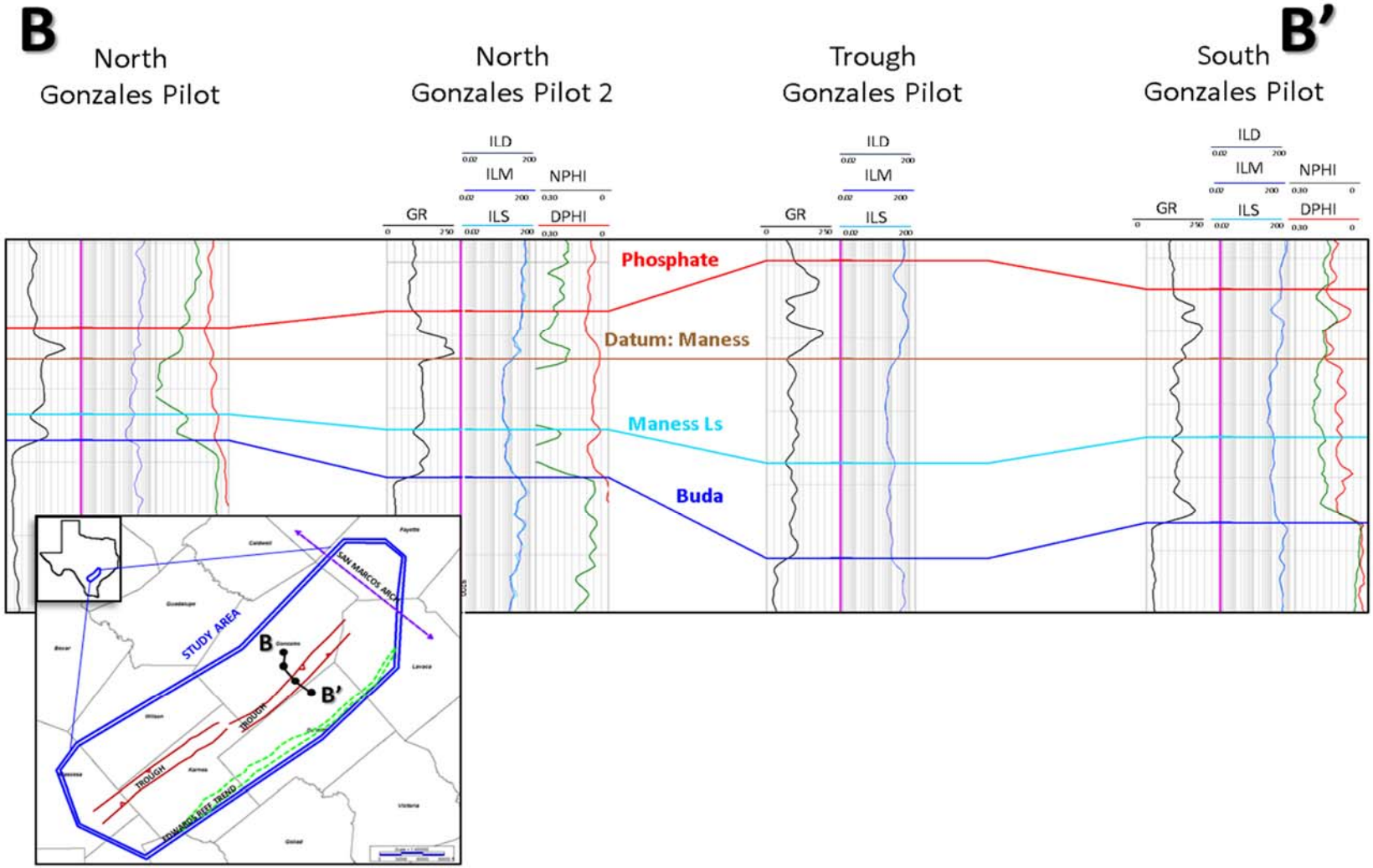

FIGURE 42. STRATIGRAPHIC DIP CROSS SECTION (DATUM: MANESS TOP) TRENDING NORTHWEST TO SOUTHEAST ACROSS THE GONZALES TROUGH

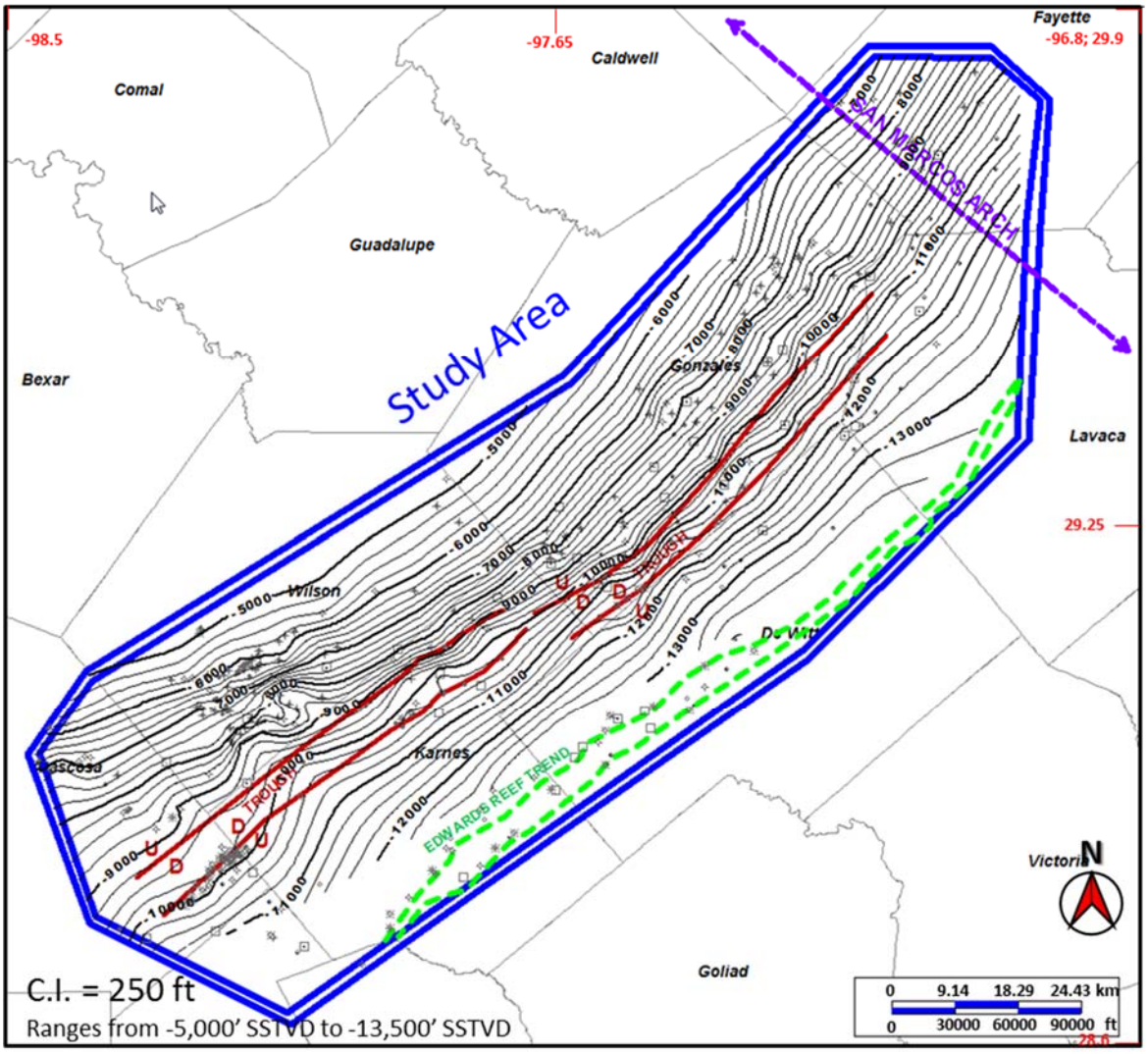

FIGURE 43. TOP OF BUDA STRUCTURE MAP. CONTOUR INTERVAL, 250 FT (76.2 M).

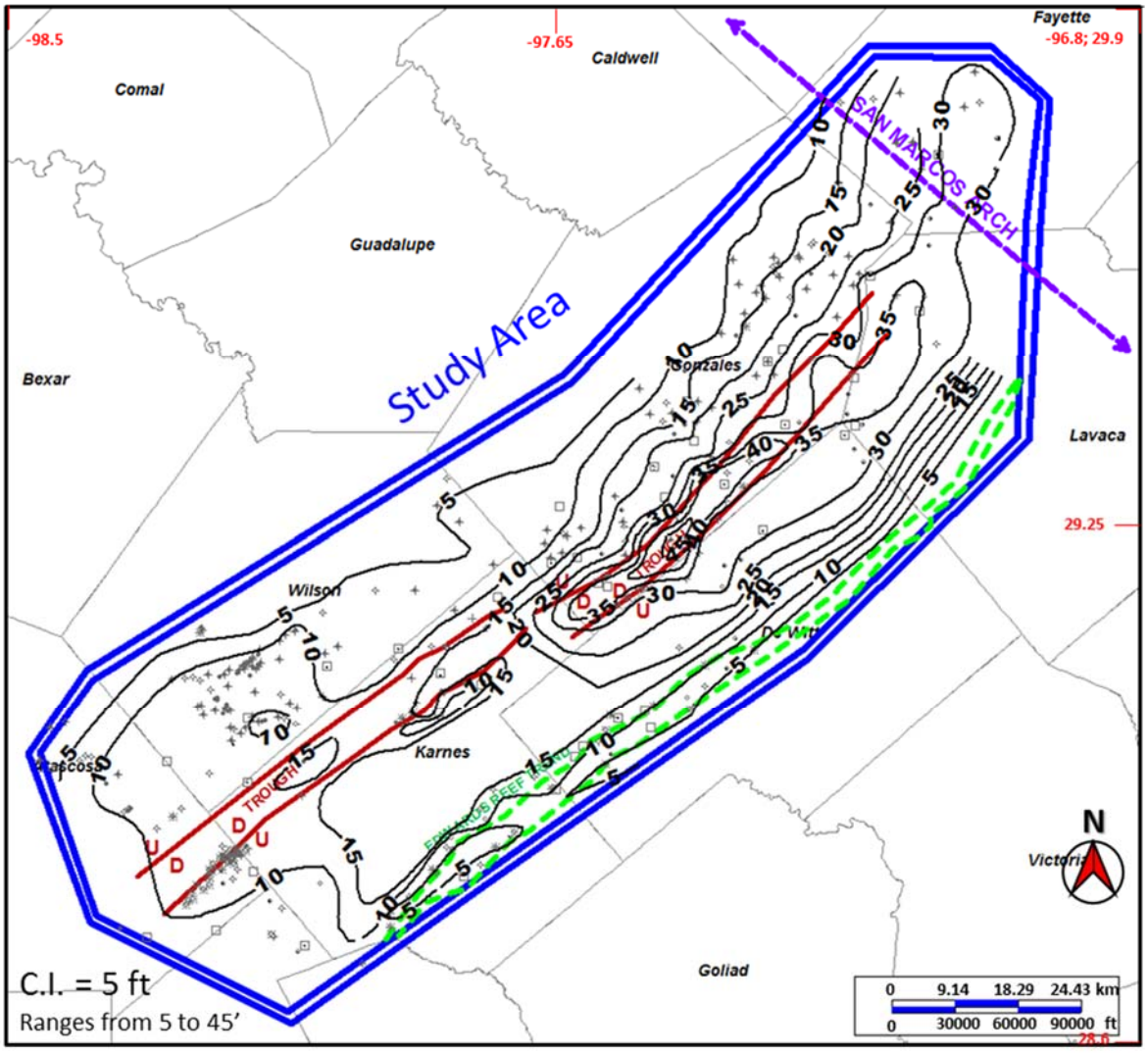

FIGURE 44. ISOPACH MAP OF TOP PHOSPHATE TO TOP BUDA. CONTOUR INTERVAL = 5 FT (1.5 M).

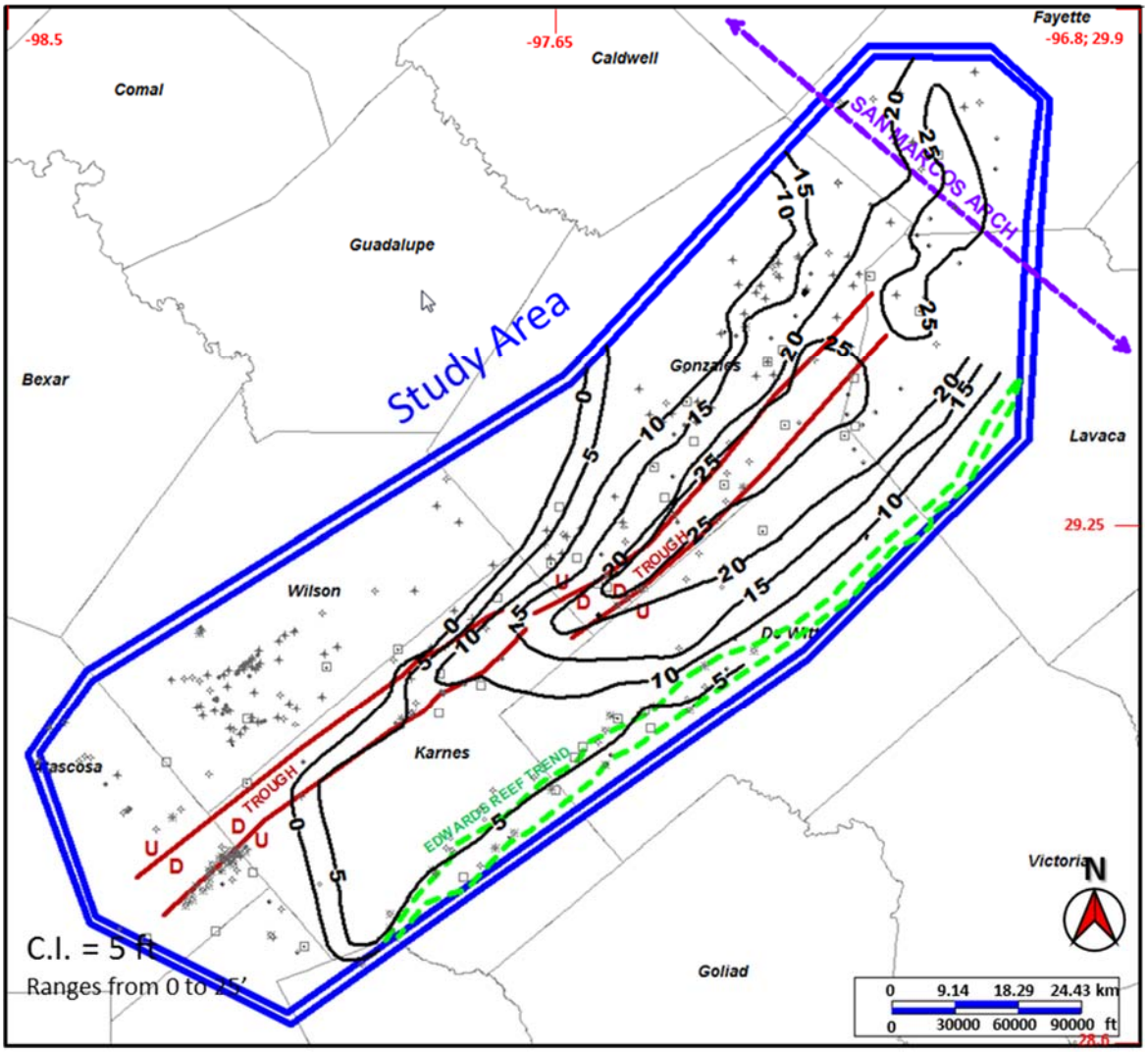

FIGURE 45. ISOPACH MAP OF TOP MANESS TO TOP BUDA. CONTOUR INTERVAL = 5 FT (1.5 M).

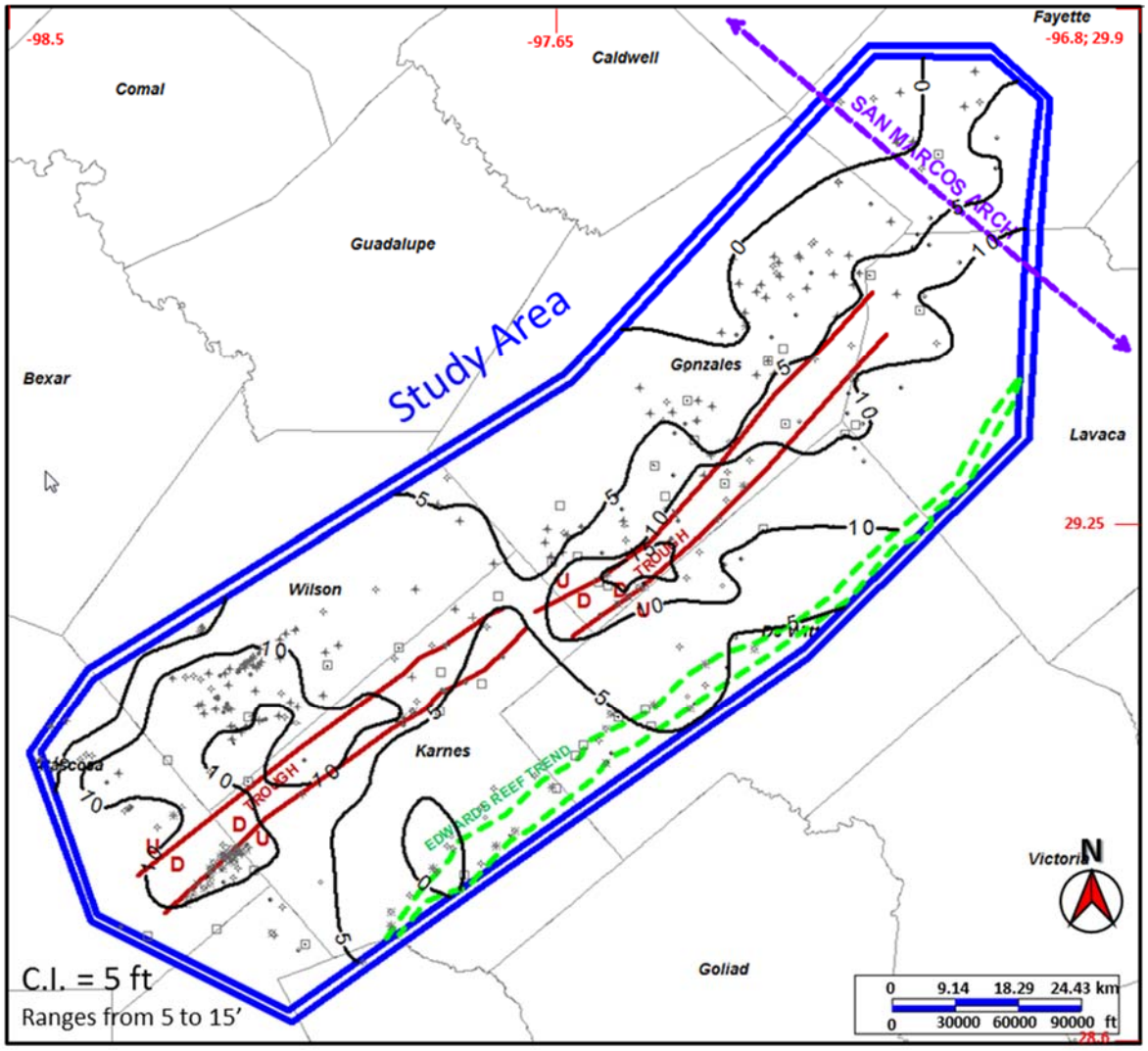

FIGURE 46. ISOPACH MAP OF TOP PHOSPHATE TO TOP MANESS. CONTOUR INTERVAL = 5 FT (1.5 M).

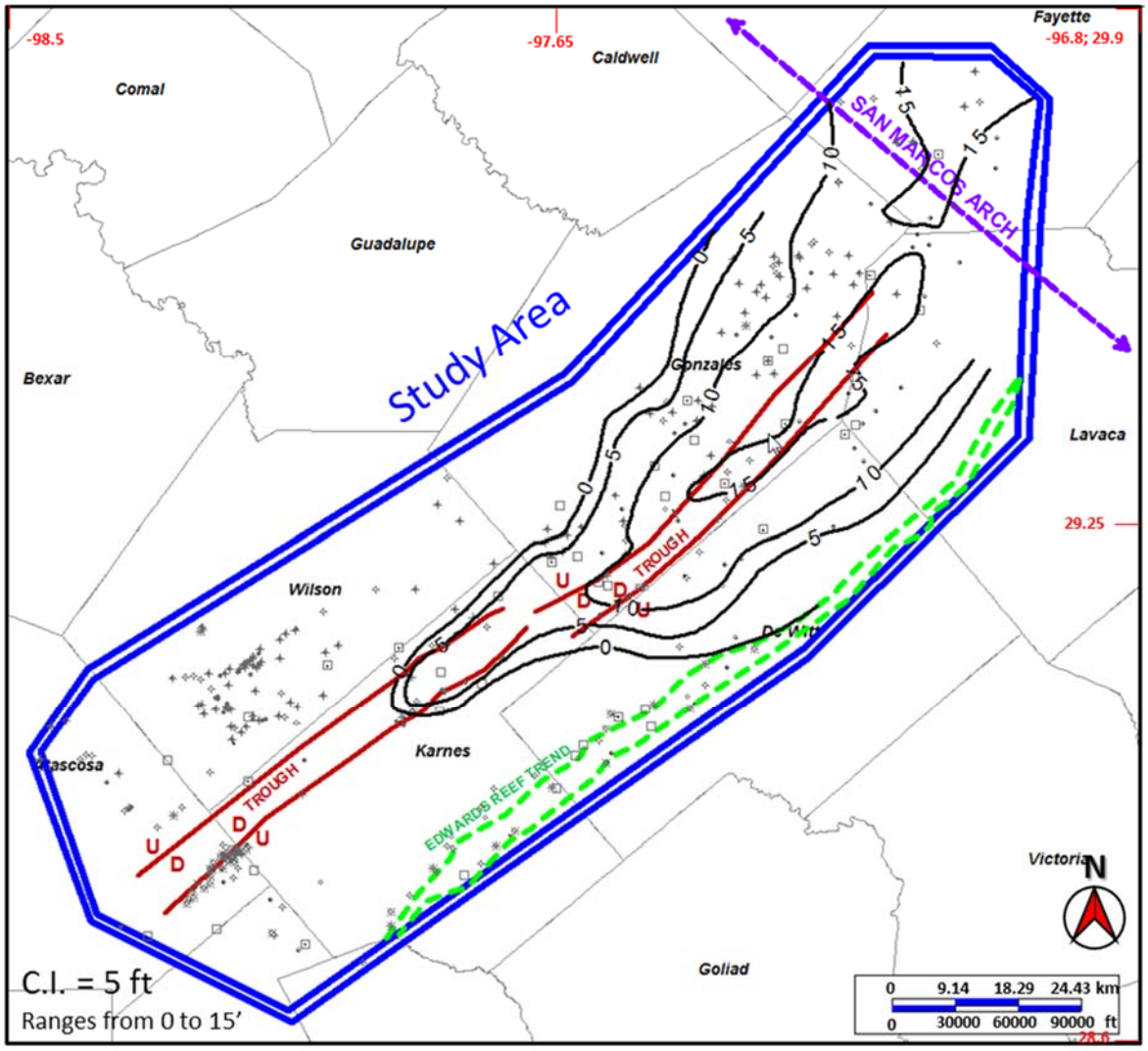

FIGURE 47. ISOPACH MAP OF TOP MANESS TO TOP INTRA-MANESS LS (UPPER MANESS). CONTOUR INTERVAL = 5 FT (1.5 M).

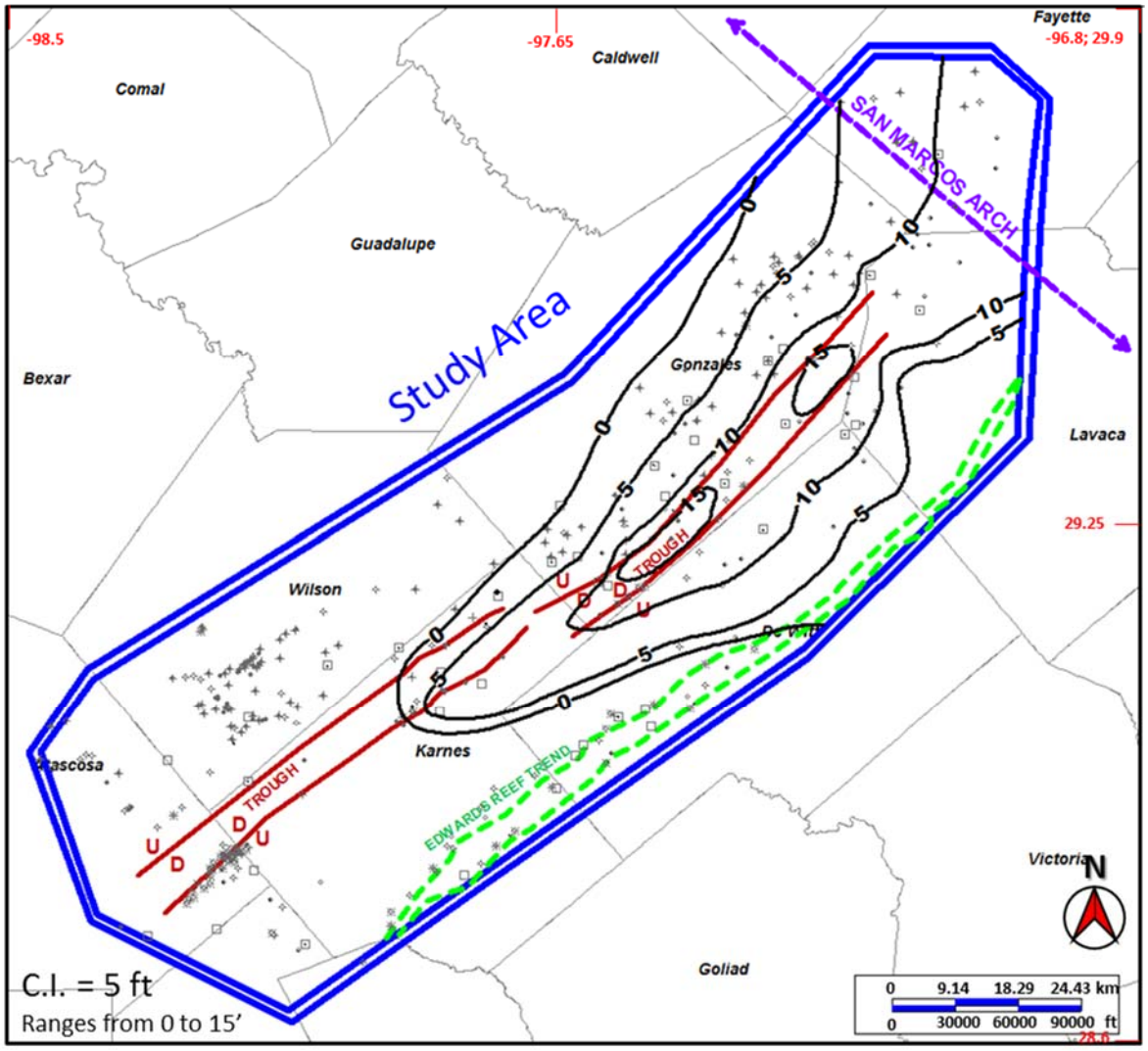

FIGURE 48. ISOPACH MAP OF TOP INTRA-MANESS LS TO TOP BUDA (LOWER MANESS). CONTOUR INTERVAL = 5 FT (1.5 M).

Discussion

The results of the geomechanical study demonstrate that the Maness is weaker than the Eagle Ford and that this is likely due to the higher clay content in the Maness. This difference in clay content is primarily due to the presence of the clay rich microfacies “a” (massive argillaceous mudstone) within the Maness, which does not occur within the Eagle Ford. Microfacies “a” is interpreted to be a fluid mud deposit, as they are internally structureless and thicker than a typical layer, often over 0.2 inch (>0.5cm) thick. These fluid muds are common on coastal shelf margins in association with deltaic environments, where they are defined as a subaqueous body of fine-grained sediment composed of fluvially- sourced organic rich clay and silt particles (Ichaso and Dalrymple, 2009). This definition supports the interpretation that the Maness is sourced from a delta to the northeast of the study area.

Together, the geomechanical and mineralogical data suggest that the Maness can act as a fracture barrier, but does it actually do so? To determine if the Maness acts as a fracture barrier, two different data sources of water and oil production were collected (Figure 49). One source was provided by an operator who drilled, completed, and produced the wells. This dataset has precise production measurements with pilot holes adjacent to the productive wells, enabling a more precise measurement of Maness thicknesses, whereas the other dataset has water and oil production data from a public source and the Maness thicknesses are based on average thicknesses within nearby wells.

Lonestar Resources provided monthly rates of oil and water production for a select set of their wells within the study area. The oil/water is was correlated to the thickness of the phosphate lag to Buda and the Maness to Buda intervals (Figure 50 and 51). The cross-plots below break down the isopach thickness versus months of production. Using the methodology

of Kondash et al. (2016), the isopach thicknesses are compared to the total first year oil to water cumulative ratio, the first six months ratio, and the second six months ratio. All graphs indicate that the thinner isopach values have lower oil/water ratios and, therefore, higher cumulative water production. The isopach thickness versus first six months of production has the lowest correlation and the isopach thickness versus the second six months has the strongest correlation. The linear regression (R^2) value for the second six months for the phosphate lag to Buda interval is 21.5% higher and the Maness to Buda interval is 20.8% higher than the R^2 values for the first six months, due to the production of flowback water (water used in the hydraulic fracturing process) during the first few months of production.

An additional means of analysis was done to see if the geotarget affected water production. Lonestar Resources has several leases throughout the extent of the Eagle Ford play, each of which has a different geologically-derived target zone within the Eagle Ford based on the rock properties within each area. The center of the target zone is known as the geotarget center, which is a specific lithologic bed denoted by its gamma ray signature. The distance between the geotarget center and the top of the phosphate lag or the Maness can be measured (Table 10). While just looking at the Lonestar Resources data, there are two factors affecting the oil to water ratio; the first being the thickness of the Maness and the other being the distance from the geotarget center to the top of the phosphate or Maness (Figure 52). The distance of the geotarget versus the top of the Buda is a critical component when the Maness is thin or non-existent. Generally speaking, the areas that have a thin layer of phosphate lag and or Maness section (areas G and P) have the lowest oil to water ratios, regardless of the distance above the Buda that the well was drilled. For example, area G was targeted 75 ft (22.9 m) above the phosphate zone due to the Maness being absent and the oil to water ratios were still low.

There is a slight increase in oil to water ratio when the distance is more than tripled (area G), but not to the same level as those wells drilled with sizeable phosphate and Maness thicknesses.

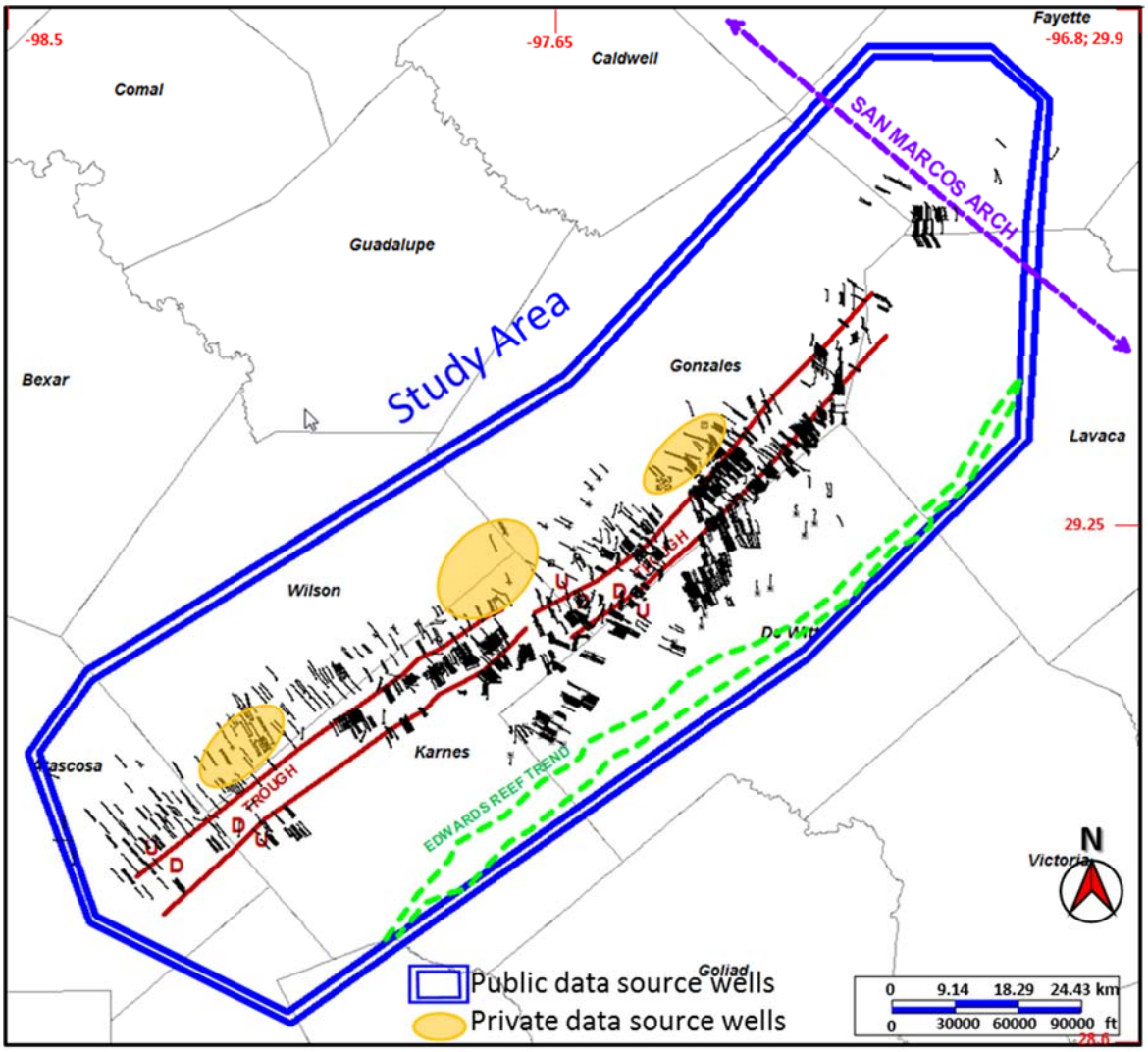

FIGURE 49. MAP DISPLAYING STUDY AREA INCLUDING ALL THE WELLS IN BOTH THE PRIVATE AND PUBLIC DATA SETS WITH THE PRIVATE DATA SETS CIRCLED IN YELLOW.

TABLE 10. TABLE DISPLAYING ISOPACH THICKNESSES AND GEOTARGET CENTER RELATIVE TO THE DISTANCE ABOVE THE FORMATION OF INTEREST.

Geotarget Center - Thickness and Depth to Formation Top					
	Isopach Values (ft / m)		*Distance (ft / m)*		
Area	Phosphate to Buda Thickness	Maness to Buda Thickness	Distance above the Phosphate	Distance above the Maness	Distance Above the Buda
C	**23** / 7.0	**16** / 4.9	**15** / 4.6	**21** / 6.4	**35** / 10.7
G	**6** / 1.8	**0** / 0	**75** / 22.9	N/A	**81** / 24.7
H	**23** / 7.0	**18** / 5.5	**20** / 6.1	**25** / 7.6	**43** / 13.1
K	**15** / 4.6	**10** / 3.0	23 / 7.0	**28** / 8.5	**38** / 11.0
P	**9** / 2.7	**0** / 0	**21** / 6.4	N/A	**30** / 9.1

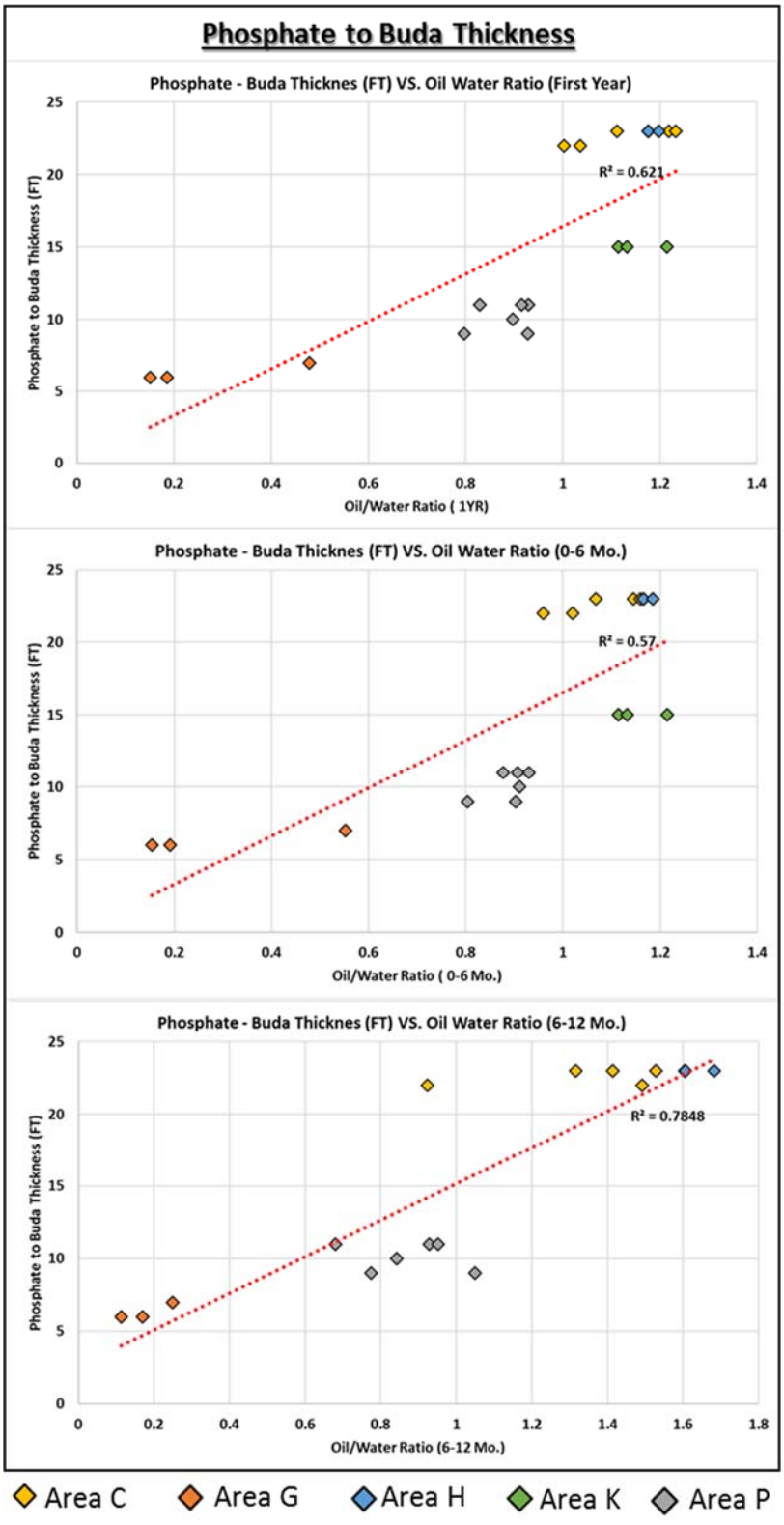

FIGURE 50. PRIVATE DATA SET CROSS-PLOTS COMPARING PHOSPHATE TO BUDA ISOPACH VALUES TO OIL-TO-WATER RATIO FOR THREE DIFFERENT PERIODS OF TIME: 1 YEAR, 0-6 MONTHS, AND 6-12 MONTHS.

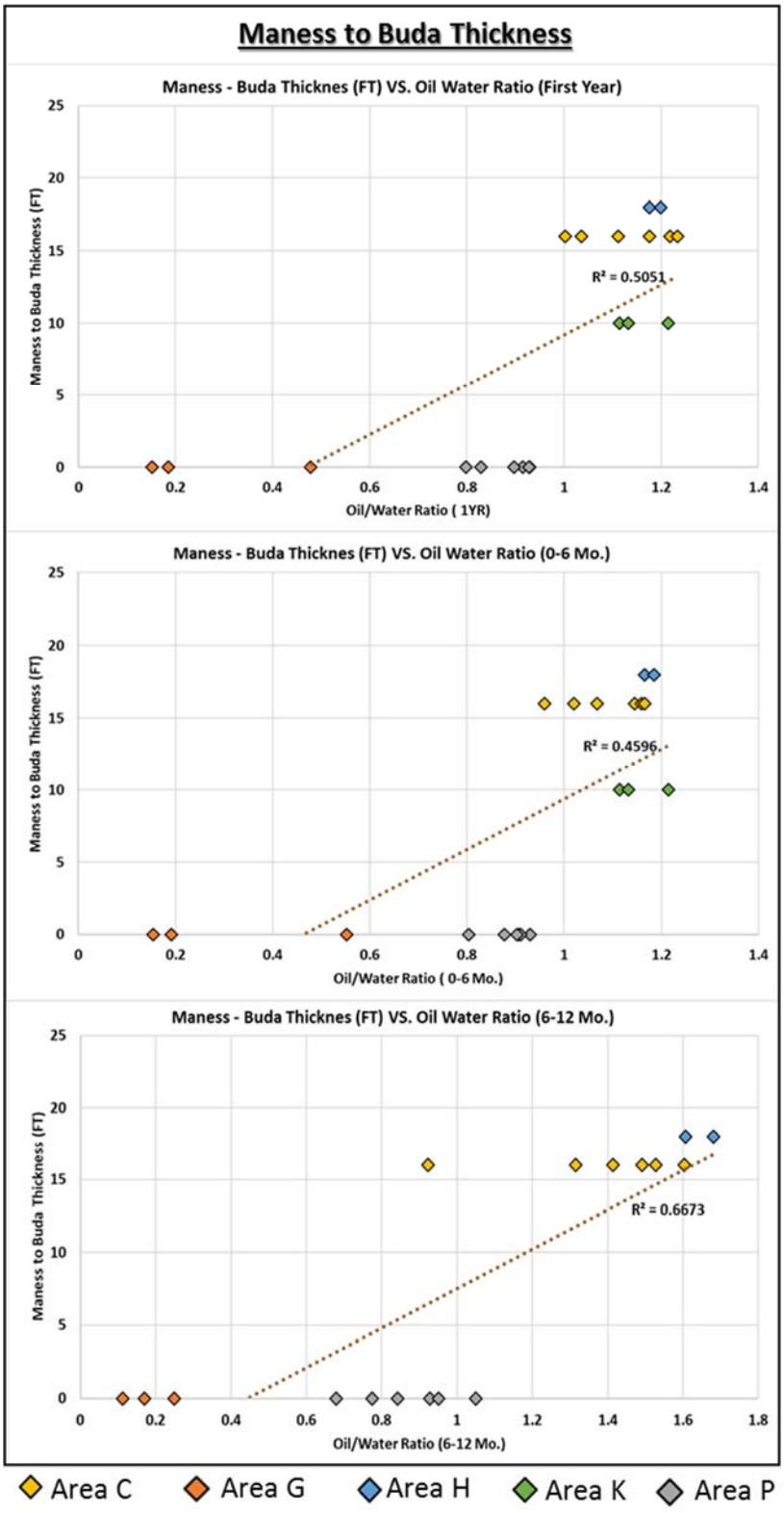

FIGURE 51. PRIVATE DATA SET CROSS-PLOTS COMPARING MANESS TO BUDA ISOPACH VALUES TO OIL-TO-WATER RATIO FOR THREE DIFFERENT PERIODS OF TIME: 1 YEAR, 0-6 MONTHS, AND 6-12 MONTHS.

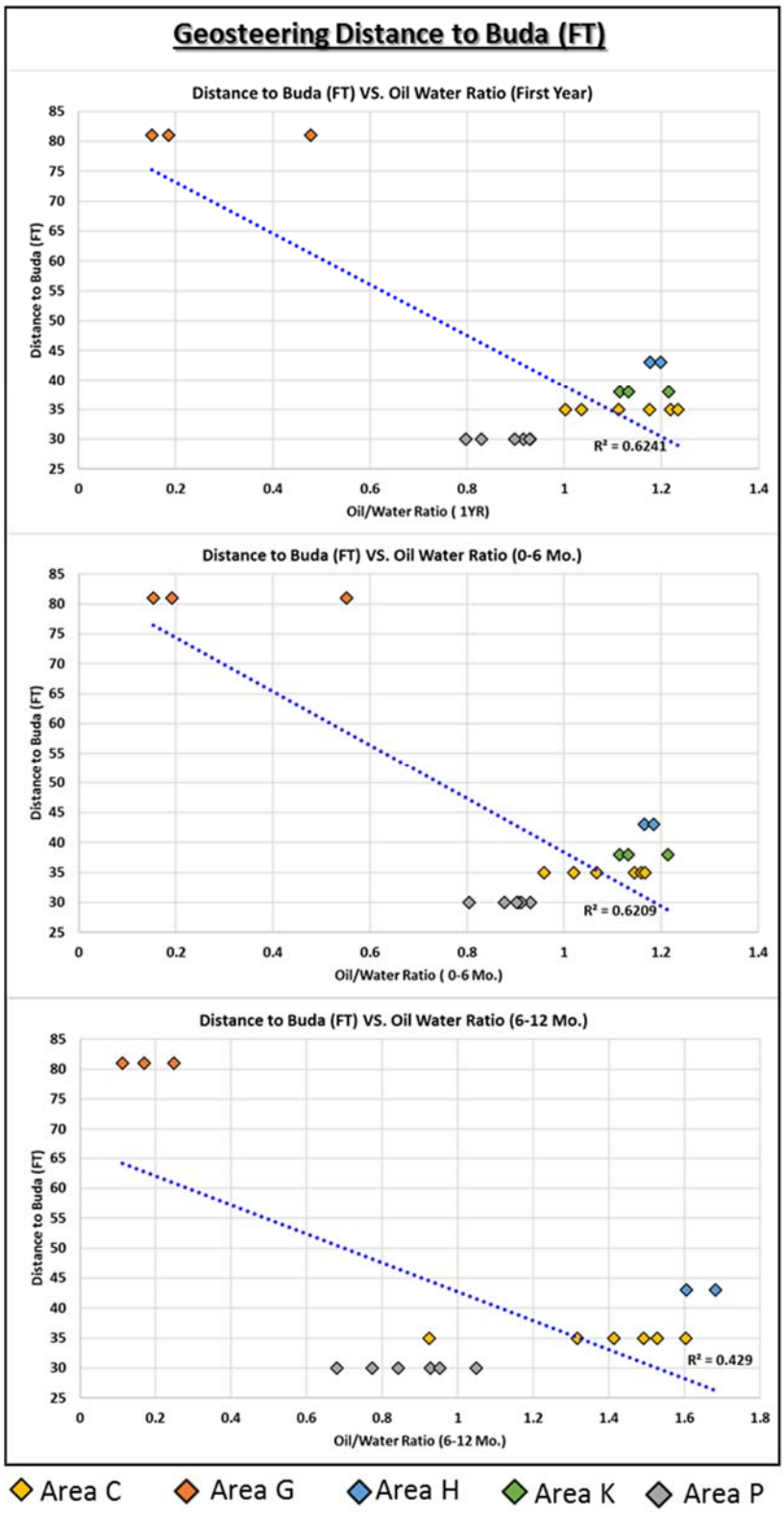

FIGURE 52. PRIVATE DATA SET CROSS-PLOTS COMPARING GEOSTEERING TARGET DISTANCE TO BUDA VALUES TO OIL-TO-WATER RATIO FOR THREE DIFFERENT PERIODS OF TIME: 1 YEAR, 0-6 MONTHS, AND 6-12 MONTHS.

The public data set has cumulative first year water and oil production data included over 2,000 horizontal wells from the study area. For these wells, Maness thicknesses are estimated for each well depending on the well's location within the isopach map. Each well is assigned a thickness based on Maness thickness and within those assigned thickness groups, the oil to water ratio is averaged creating one data point per isopach contour interval. Regression analysis found a 91.7% (Figure 53) correlation between Maness thickness and oil/water ratios, indicating a strong correlation between Maness thickness and water production, and therefore suggesting that the Maness may be acting as a fracture barrier within the region. This analysis also found a 50% increase in oil/water ratios between Maness thicknesses of 5 to 10 ft (1.5 to 3.1 m), suggesting that a minimum of approximately 10 ft (3.1 m) is needed for the Maness to effectively act as a fracture barrier. Both the private and public data sets suggest that the threshold of thickness necessary for the Maness to act as a fracture barrier is minimum of 10 feet (3.1 m) (Figure 53).

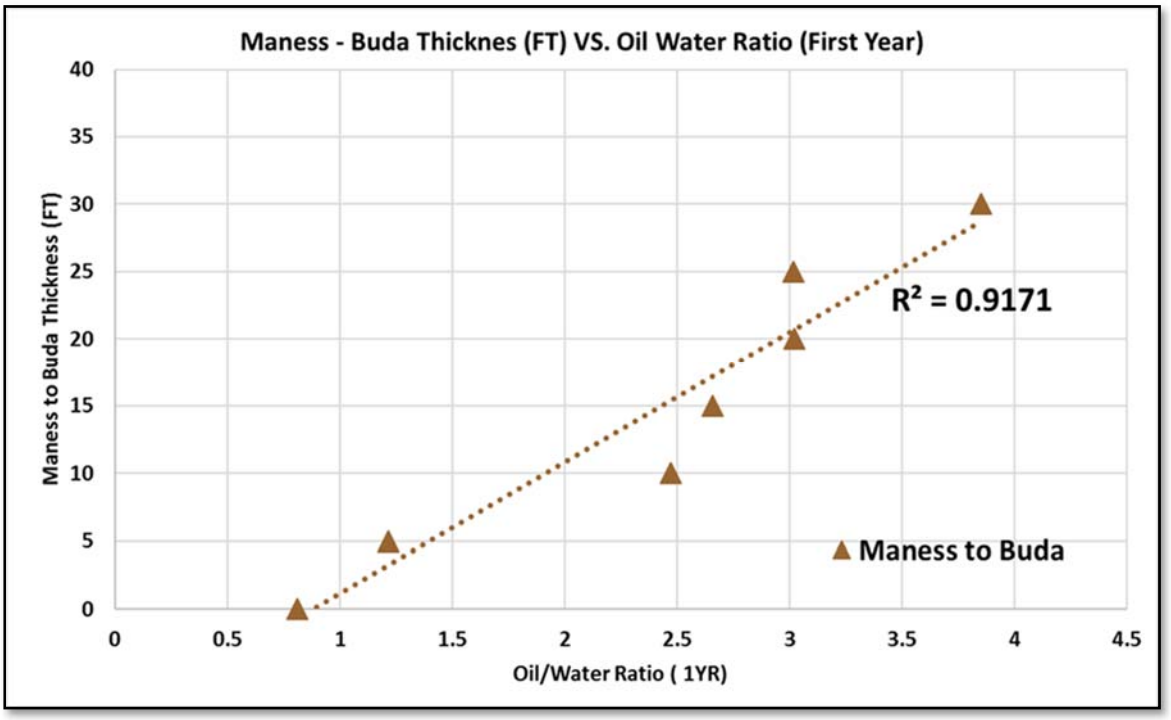

FIGURE 53. PUBLIC DATA SET CROSS-PLOT COMPARING MANESS THICKNESS TO CUMULATIVE (1 YEAR) OIL-TO-WATER RATIOS AVERAGED OVER 5 FT INTERVALS. OIL TO WATER RATIOS INCREASE BY MORE THAN DOUBLE FROM WHERE THE MANESS IS 5FT TO WHERE THE MANESS IS 10FT.

Summary and Conclusions

The present study of the Lower Cenomanian Maness Shale in the vicinity of the San Marcos Arch of South Texas was conducted to better understand the mineralogic and geomechanical properties that contribute to instability issues associated with the Maness while drilling horizontal wells, and to determine if the presence of the Maness acts as a fracture barrier between hydraulically fractured Eagle Ford wellbores and the underlying Buda Formation.

In the vicinity of the San Marcos Arch in South Texas, the Maness forms the basal member of the Eagle Ford Shale. The Maness mineralogic and geomechanical properties are established through petrology, x-ray diffraction (XRD), and geomechanical (point load penetrometer and micro-rebound hammer) analyses. The data was collected from two industry cores taken in the vicinity of the San Marcos Arch that sampled the section from the uppermost Buda, Maness, Eagle Ford, and the lower Austin Chalk.

The hypotheses tested were:

1. Maness Shale is geomechanically weaker than the Eagle Ford Shale.
2. Maness Shale has a higher clay and lower calcite content than the Eagle Ford Shale.
3. The Maness acts as a fracture barrier between the Eagle Ford and the underlying water wet formation.

The geomechanical studies measuring rock strength were performed utilizing the point load penetrometer (Dimpler) and the micro-rebound hammer (Bambino) demonstrate that the Maness is significantly weaker than the other formations, supporting hypothesis 1. After converting the raw geomechanical data to unconfined compressive strength (UCS), average UCS

values derived from the penetrometer for the Maness are 32% lower than those for the Eagle Ford and 75% lower than the Buda. Similarly, average Bambino UCS values for the Maness are 36% lower than the Eagle Ford and 77% lower than the Buda. When the two types of geomechanical data are averaged, the Maness has an average UCS of 2,646 psi (18.2 MPa) compared to the Eagle Ford with an average UCS of 4,337 psi (29.9 MPa), which is 61.0% higher than the Maness.

XRD analyses reveal that an average Maness sample is composed of 45.5 % clay, whereas the average Eagle Ford sample contains 31.7 % clay, 13.8 % less than the Maness, supporting hypothesis 2. The difference in clay content is primarily due to the presence of the clay-rich microfacies “a” (Massive argillaceous mudstone) within the Maness, which does not occur within the Eagle Ford.

The isopach map trends suggest a clay-rich deltaic source to the northeast was active during the time of deposition of the Maness, but was not a significant source of clay during the time of deposition of the Eagle Ford. The thickest Maness intervals occur within the Gonzales and Karnes counties troughs, which suggests that the troughs were relative lows during the time of deposition of Maness.

A comparison of oil to water ratios to Maness thicknesses showed a strong correlation between the two variables; as Maness thicknesses decreased, oil to water ratios also decreased, for both the private and public production data sets suggesting that the Maness is acting as a fracture barrier, supporting hypothesis 3. The threshold of thickness necessary for the Maness to act as a fracture barrier is 10 ft (3.1 m).

In summary, the results of this study suggest that the Maness was deposited by a separate depositional system than the overlying Eagle Ford based on differing depositional

trends and mineralogy. Due to its higher clay content, the Maness is more ductile than the Eagle Ford, enabling the Maness to act as a fracture barrier.

References

Adams, R. L., J. P. Carr, and J. A. Ward, 2014, The Lower Woodbine organic shale of Burleson and Brazos counties, Texas: Anatomy of a new “old” play: Gulf Coast Association of Geological Societies Transactions, v. 64, p. 3–31.

Ambrose, W. A., T. F. Hentz, F. Bonnaffé, R. G. Loucks, L. F. Brown, Jr., F. P. Wang, and E. C. Potter, 2009, Sequence-stratigraphic controls on complex reservoir architecture of highstand fluvial deltaic and lowstand valley-fill deposits in the Upper Cretaceous (Cenomanian) Woodbine Group, East Texas Field: Regional and local perspectives: American Association of Petroleum Geologists Bulletin, v. 93, p. 231–269.

Arthur, M. A., and B. B. Sageman, 2004, Sea-level control on source-rock development: Perspectives from the Holocene Black Sea, the mid-Cretaceous Western Interior Basin of North America, and the Late Devonian Appalachian Basin, in N. B. Harris, The deposition of organic-carbon-rich sediments: Models, mechanisms, and consequences: Society of Economic Paleontologists and Mineralogists Special Publication 82, Tulsa, Oklahoma, p. 35–59.

Bailey, T. L., F. G. Evans, and W. S. Adkins, 1945, Revision of stratigraphy of part of Cretaceous in Tyler Basin, northeast Texas: American Association of Petroleum Geologists Bulletin, v. 29, p. 170–186.

Blakey, R.C., 2014. Paleogeography and paleotectonics of the Western Interior Seaway, Jurassic-Cretaceous of North America. Search and Discovery, Article# 30392, p.72.

Blakey, R., 2017. North American time slice map. Accessed: April 2017. (https://deeptimemaps.com/north-america-key-time-slices/)

Blum, Michael, and Mark Pecha, 2014, Mid-Cretaceous to Paleocene North American drainage reorganization from detrital zircons, Geology v. 42.7, p. 607-610.

Breyer, J. A., et al., 2015, Limestone frequency and well performance, Eagle Ford Shale (Cretaceous), South Texas: AAPG/STGS Geoscience Technology Workshop, Fourth Annual Eagle Ford Shale, San Antonio, Texas.

Brown, GW, and George William Brindley, eds., 1980, Crystal structures of clay minerals and their X-ray identification: London: Mineralogical Society, v. 5.

Cobbold, P.R., Zanella, A., Rodrigues, N. and Løseth, H., 2013, Bedding-parallel fibrous veins (beef and cone-in-cone): Worldwide occurrence and possible significance in terms of fluid overpressure, hydrocarbon generation and mineralization: Marine and Petroleum Geology, v. 43, p. 1-20.

Daniels, Gill, et al., 2012, Non-destructive strength index testing applications for sand failure evaluation: SPE Asia Pacific Oil and Gas Conference and Exhibition, Society of Petroleum Engineers.

Denne, R. A., 2019, Sequence biostratigraphy of organic-rich mudrocks: An example from the Late Cretaceous of Texas, in R. A. Denne and A. Kahn, eds., Geologic Problem Solving with Microfossils IV: SEPM Special Publication 111, in press.

Denne, R. A. and J. A. Breyer, 2016, Regional depositional episodes of the Cenomanian–Turonian Eagle Ford and Woodbine Groups of Texas, in J. A. Breyer, ed., The Eagle Ford Shale: A renaissance in U.S. oil production: AAPG Memoir 110, p. 87–133.

Denne, Richard, et al., 2016, Part 1: Biostratigraphic and geochemical constraints on the stratigraphy and depositional environments of the Eagle Ford and Woodbine Groups of Texas, in J. A. Breyer, ed., The Eagle Ford Shale: A renaissance in U.S. oil production: AAPG Memoir 110, p. 1-86.

Geochemical Instrumentation and Analysis, 2018. Accessed: June 2018. (https://serc.carleton.edu/research_education/geochemsheets/techniques/XRD.html)

Hentz, T. F., W. A. Ambrose, and D. C. Smith, 2014, Eaglebine play of the southwestern East Texas Basin: Stratigraphic and depositional framework of the Upper Cretaceous (Cenomanian–Turonian) Woodbine and Eagle Ford Groups: AAPG Bulletin, v. 98, p. 2551–2580.

Hudson, A. M., 2014, Stratigraphy and depositional controls on source rock formation within the Upper Cretaceous (Lower Cenomanian) Maness Shale, Central Texas: M.S. Thesis, Texas A&M University, College Station.

Ichaso, A.A. and Dalrymple, R.W., 2009, Tide-and wave-generated fluid mud deposits in the Tilje Formation (Jurassic), offshore Norway: Geology, v. 37(6), p. 539-542.

Ikonnikova, S.A., Male, F., Scanlon, B.R., Reedy, R.C. and McDaid, G., 2017, Projecting the water footprint associated with shale resource production: Eagle Ford Shale Case Study. Environmental science & technology, v.51(24), p. 14453-14461.

Jennings, D. S., and J. Antia, 2013, Petrographic characterization of the Eagle Ford Shale, South Texas: Mineralogy, common constituents, and distribution of nanometer scale pore types, in W. Camp, E. Diaz, and B. Wawak, eds., Electron microscopy of shale hydrocarbon reservoirs: AAPG Memoir 102, p. 101–113.

Kondash, A.J., Albright, E. and Vengosh, A., 2017, Quantity of flowback and produced waters from unconventional oil and gas exploration: Science of the Total Environment, v. 574, p.314-321.

Kosanke et al., 2013, Influence of Rock Texture and Composition on Anisotropic Geomechanical Properties in the Eagle Ford Formation, AAPG Search and Discovery Article #90163.

Poppe, L.J., Paskevich V.F., Hathaway J.C., and Blackwood D. S., 2018, A Laboratory Manual for X-Ray Powder Diffraction. USGS. Accessed: June 2018. (http://pubs.usgs.gov/of/2001/of01-041/index.htm)

Lozo, F. E., 1951, Stratigraphic notes on the Maness (Comanche Cretaceous) Shale, in F. E. Lozo, ed., The Woodbine and adjacent strata of the Waco area of central Texas, a symposium for the 1951 field trip sponsored by the East Texas Geological Society: Southern Methodist University Press, Fondren Science Series 2, Dallas, Texas, p. 67–100.

OneSight Wide-Range High-Speed Detector. Shimadzu. Accessed: June 2018. (https://www.ssi.shimadzu.com/products/x-ray/onesight.html)

Orangi, A., Nagarajan, N. R., Honarpour, M. M., & Rosenzweig, J. J., 2015, Unconventional Shale Oil and Gas-Condensate Reservoir Production, Impact of Rock, Fluid, and Hydraulic Fractures, Society of Petroleum Engineers. Unconventional Resources Technology Conference (URTEC) #2170061

Phelps, R.M., Kerans, C., Loucks, R.G., Da Gama, R.O., Jeremiah, J. and Hull, D., 2014, Oceanographic and eustatic control of carbonate platform evolution and sequence stratigraphy on the Cretaceous (Valanginian–Campanian) passive margin, northern Gulf of Mexico: Sedimentology, v. 61(2), p.461-496.

Phelps, R.M., Kerans, C., Da-Gama, R.O., Jeremiah, J., Hull, D. and Loucks, R.G., 2015, Response and recovery of the Comanche carbonate platform surrounding multiple Cretaceous oceanic anoxic events, northern Gulf of Mexico. Cretaceous Research, 54, p.117-144.

Railroad Commission of Texas (RRC), 2014, Wells completed and permitted in the Eagle Ford Shale play, <http://www.rrc.state.tx.us/oil-gas/major-oil-gas-formations/eagle-ford-shale/> Accessed July 19, 2018.

Shimadzu Center for Environmental and Forensics and material Science. MAXima X XRD-7000 X-ray Diffractometer. Accessed: June 2018. (http://www.uta.edu/sirt/cefms/equipment/XRD7000/XRD7000.php)

Saltzman, M. R., and E. Thomas, 2012, Carbon isotope stratigraphy, in F. M. Gradstein, J. G. Ogg, M. Schmitz, and G. Ogg, eds., The Geologic Time Scale 2012: Elsevier, Oxford, U.K., p. 207–232.

Sohl, N.F., Martinez, R.E., Salmeron-Urena, P. and Soto-Jaramillo, F., 1991, Upper Cretaceous. The Gulf of Mexico Basin: Boulder, Colorado, Geological Society of America, The Geology of North America, J, p.205-215.

U.S. Energy Information Administration (EIA), October 2018, Eagle Ford Region Drilling Productivity Report. Accessed: October 2018. (https://www.eia.gov/petroleum/drilling/pdf/eagleford.pdf)

Xu, Jian, et al., 2016, Impact of Ash Beds on Production in Eagle Ford Shale. SPE Hydraulic Fracturing Technology Conference, Society of Petroleum Engineers Hydraulic Fracturing Technology Conference #179110-MS

APPENDIX A – Thin Section Scans

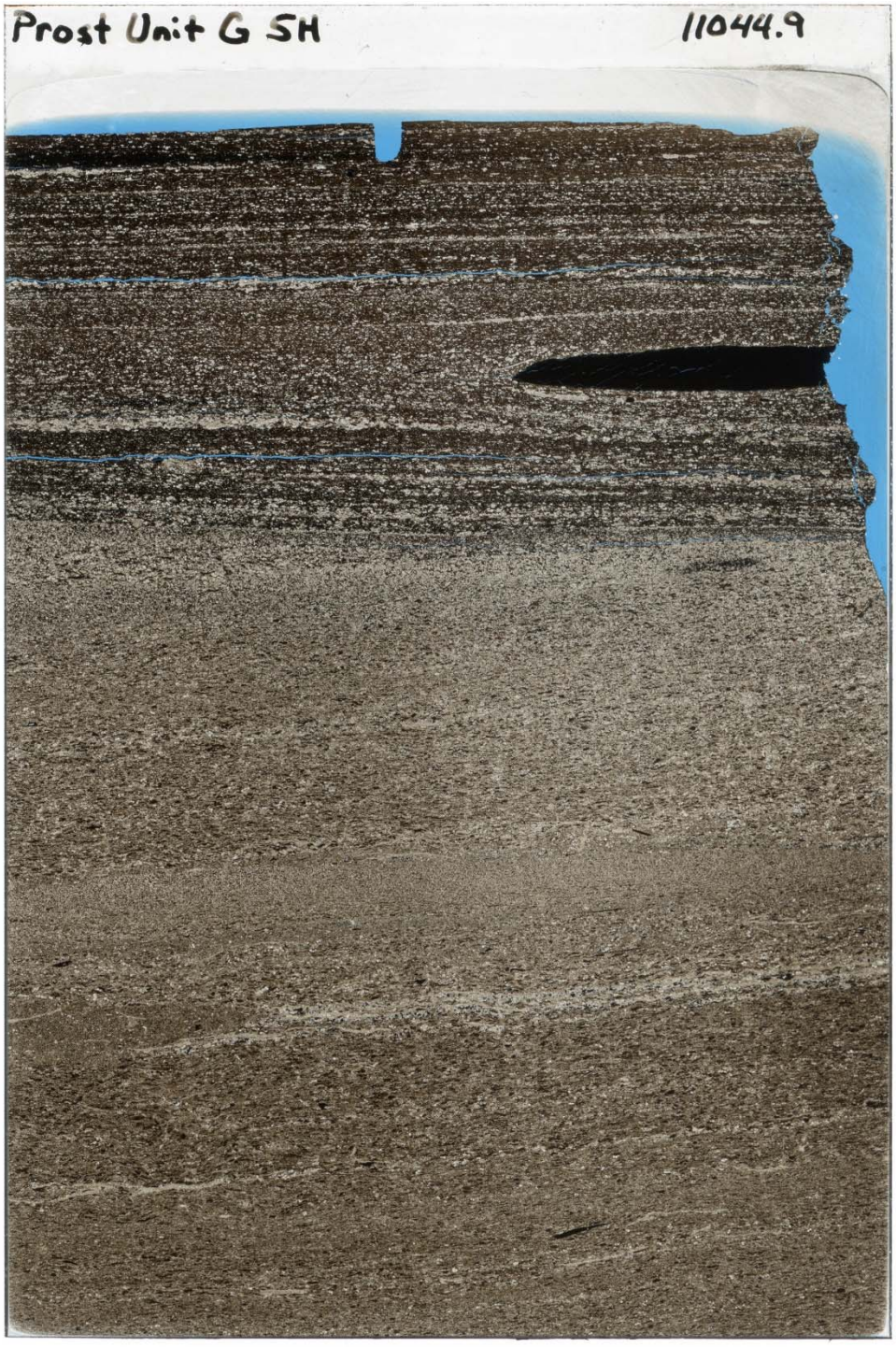

11044’9"- recrystallized laminated limestone; laminated mudstone with high abundances of planktonic foraminifera with a phosphate nodule

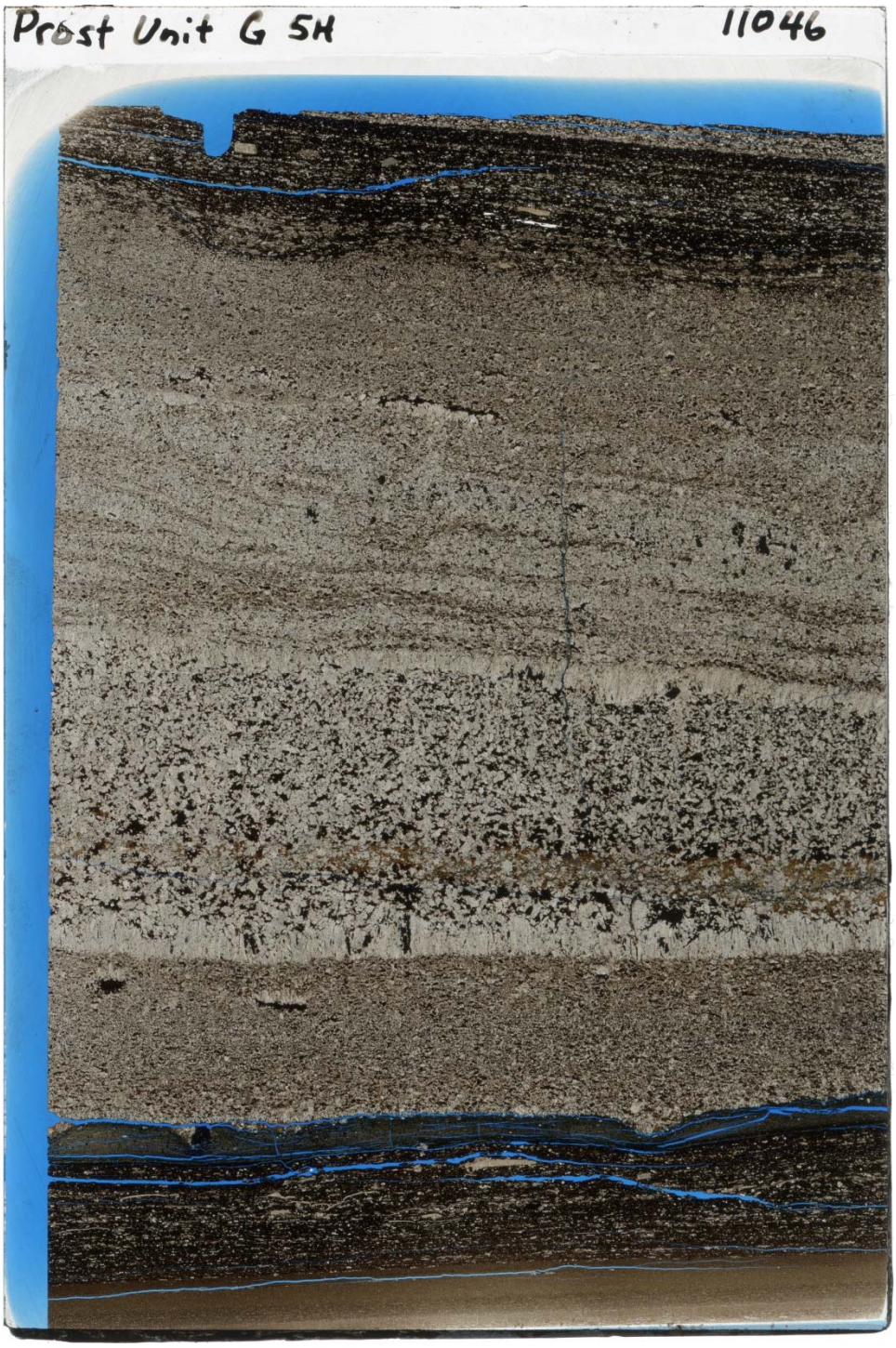

11046'0"- recrystallized laminated limestone with fibrous calcite; pyritized ash bed; laminated mudstone with abundant inoceramid fragments and foraminifera

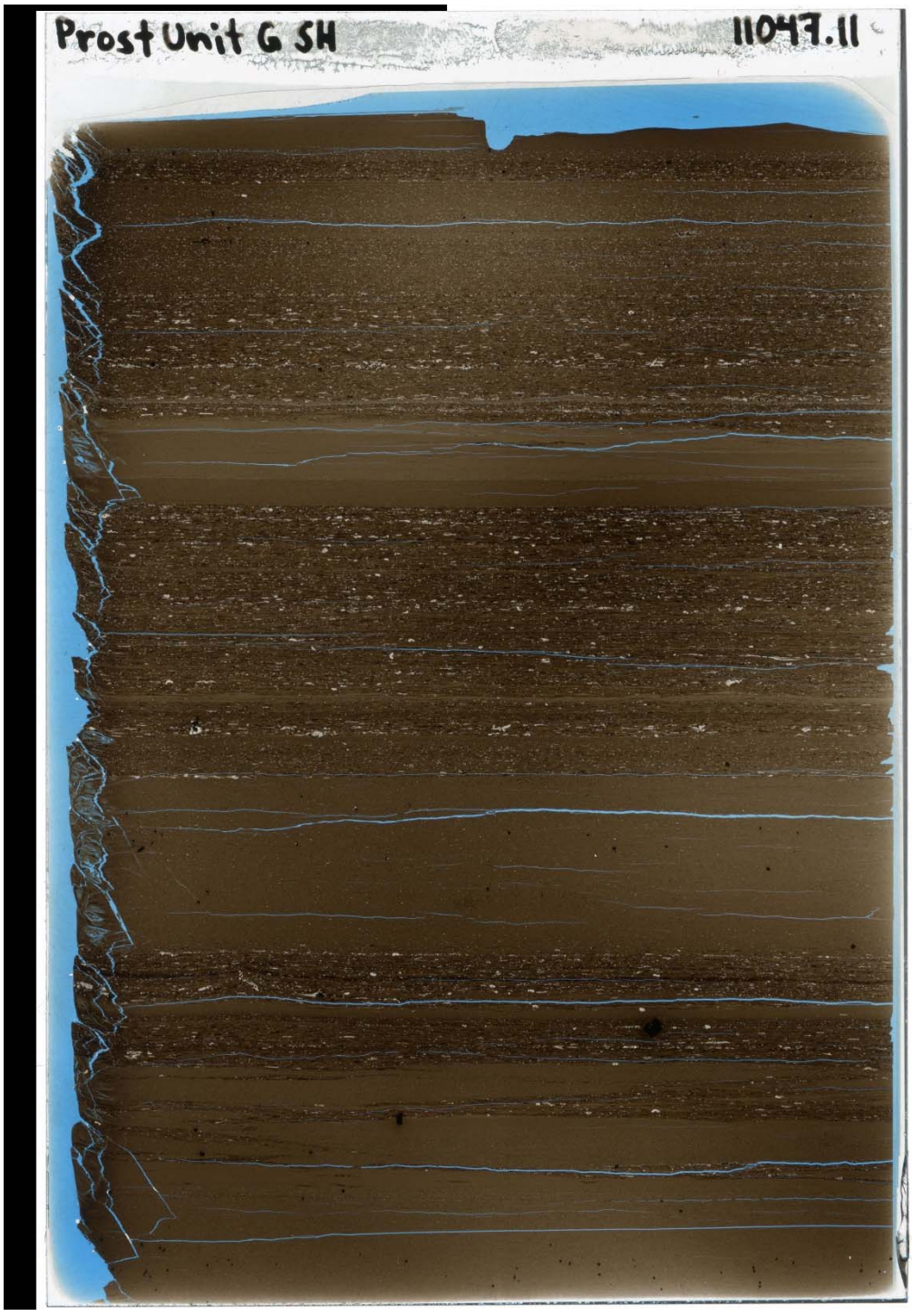

11047'11"- massive argillaceous mudstone (1.5 cm) interbedded with indistinctly laminated mudstone

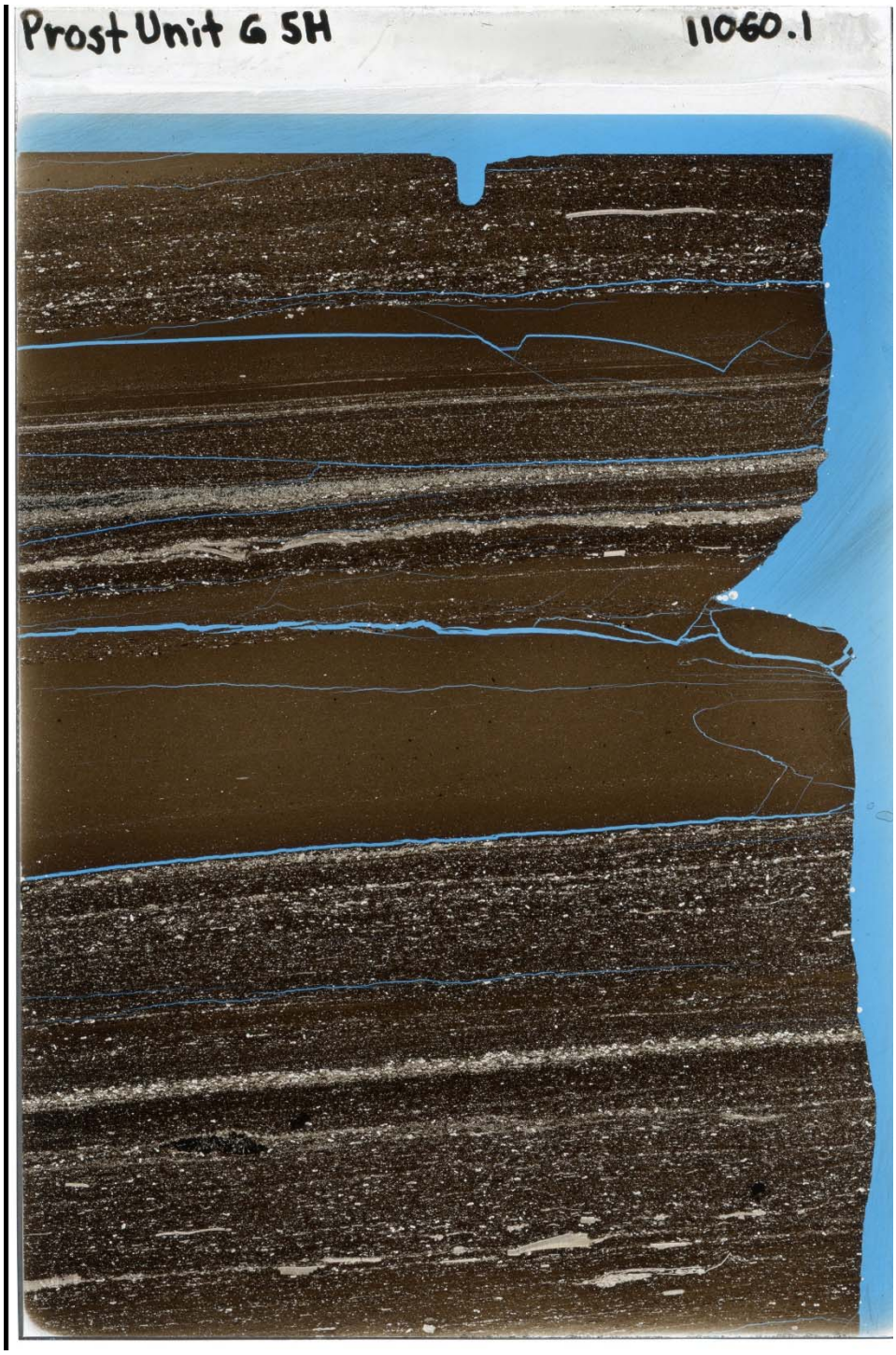

11060'1"- <1mm winnowed lag; multiple (1.5 cm) massive argillaceous mudstone; indistinctly laminated mudstone few inoceramid fragments

11063'8"- very thin winnowed lag; indistinctly laminated mudstone; thin massive argillaceous mudstones

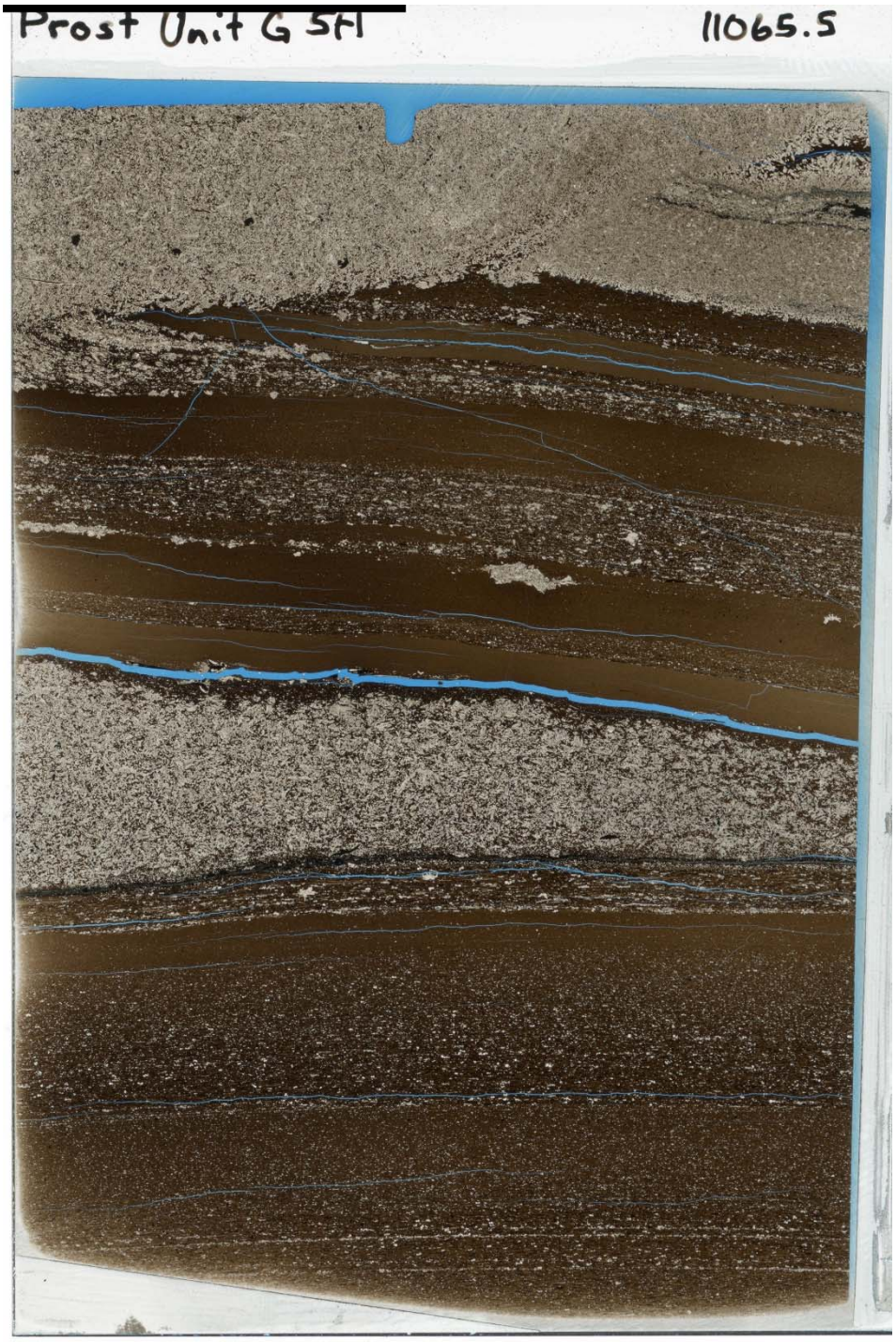

11065’5”- recrystallized limestone truncating indistinctly laminated mudstone and interbedded massive argillaceous mudstones

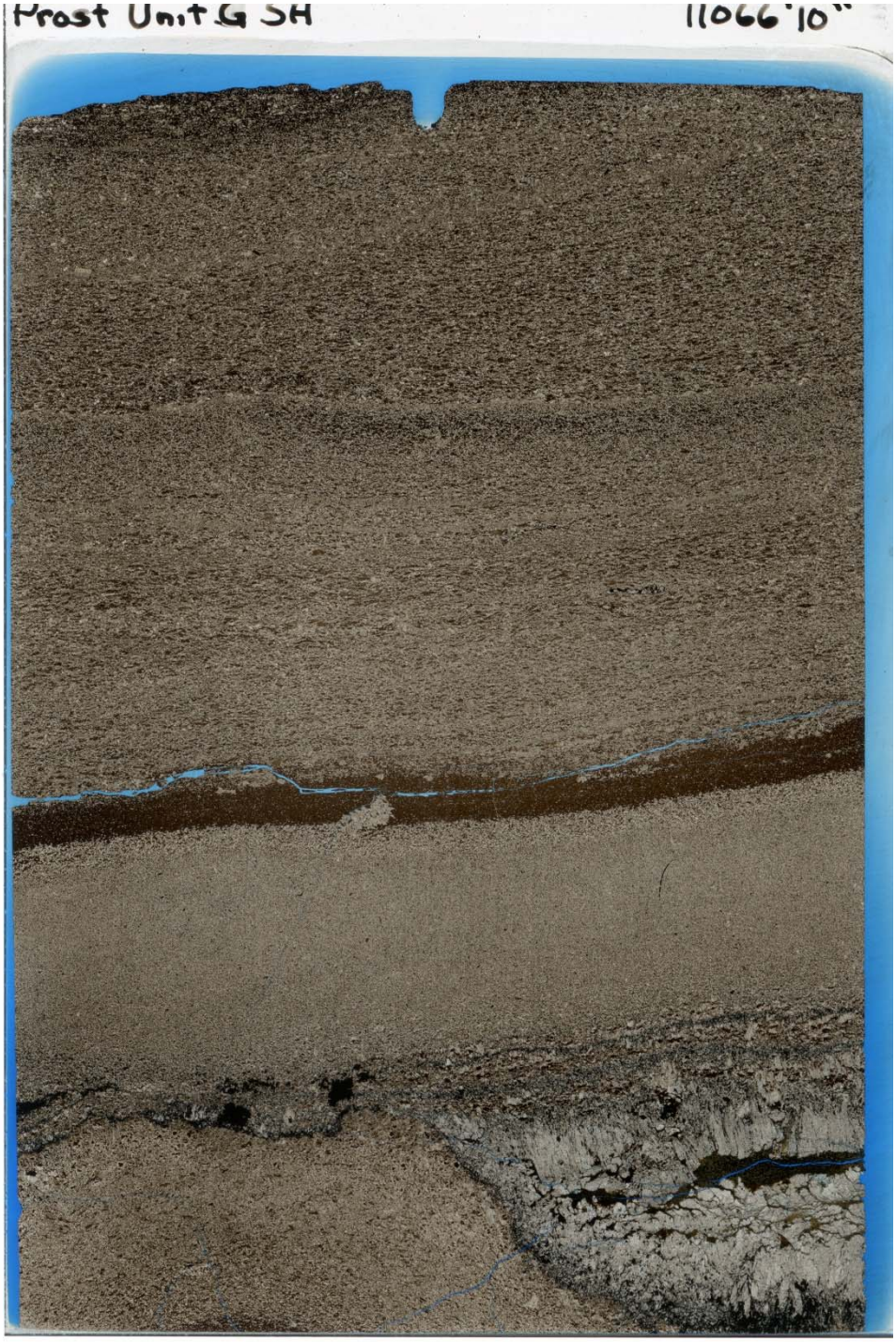

11066'10"- fibrous calcite encasing ash bed; recrystallized laminated limestone

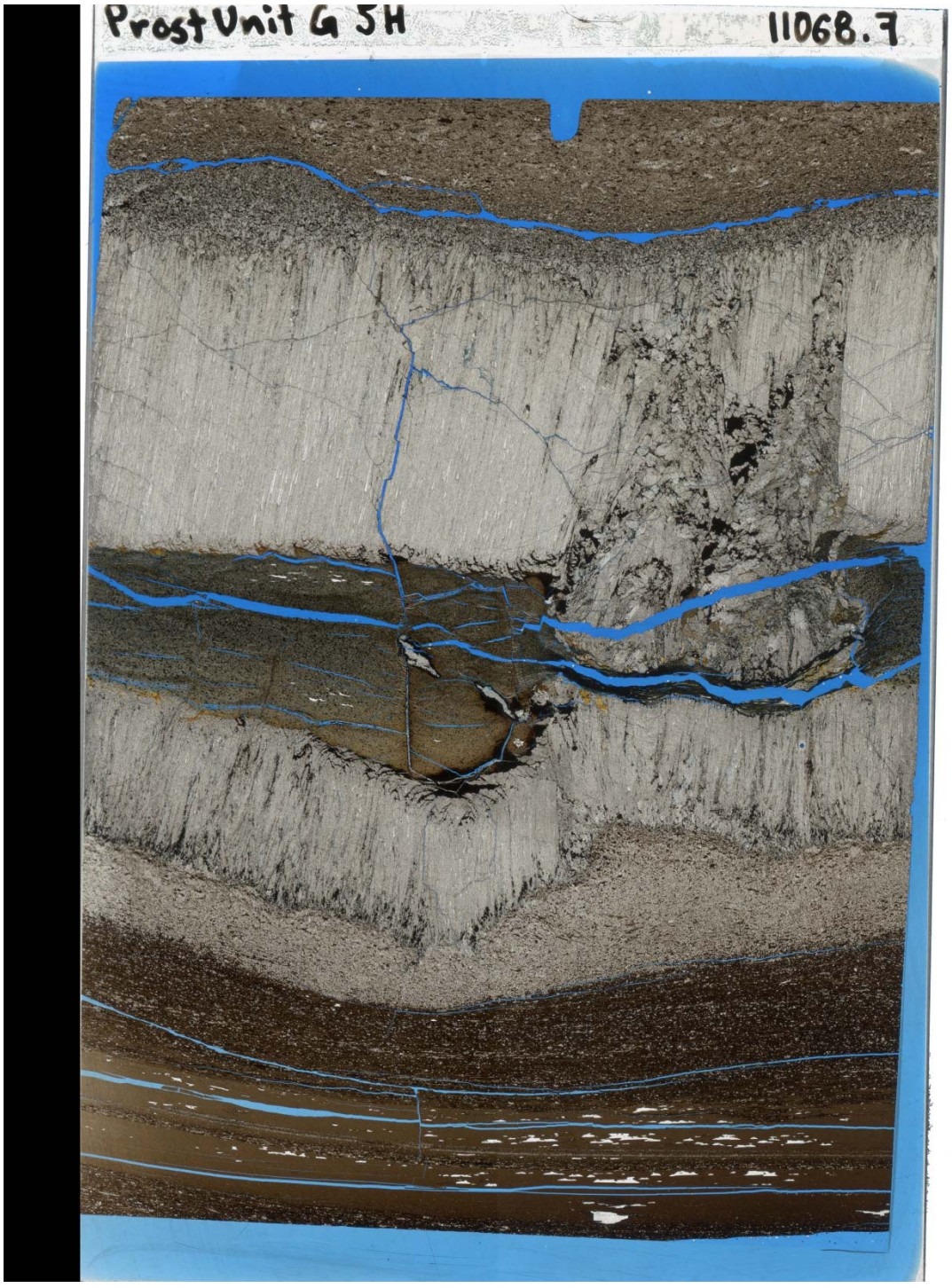

11068'7"- 2 fibrous calcite "beef" – top individual totally recrystallized blades are up to 2 cm in length; recrystallized laminated limestone with inoceramids and planktonic foraminifera and evidence of brown clasts; olive green ash bed with pyrite rhombs; indistinctly laminated mudstone with abundant minute planktonic foraminifera and pyrite

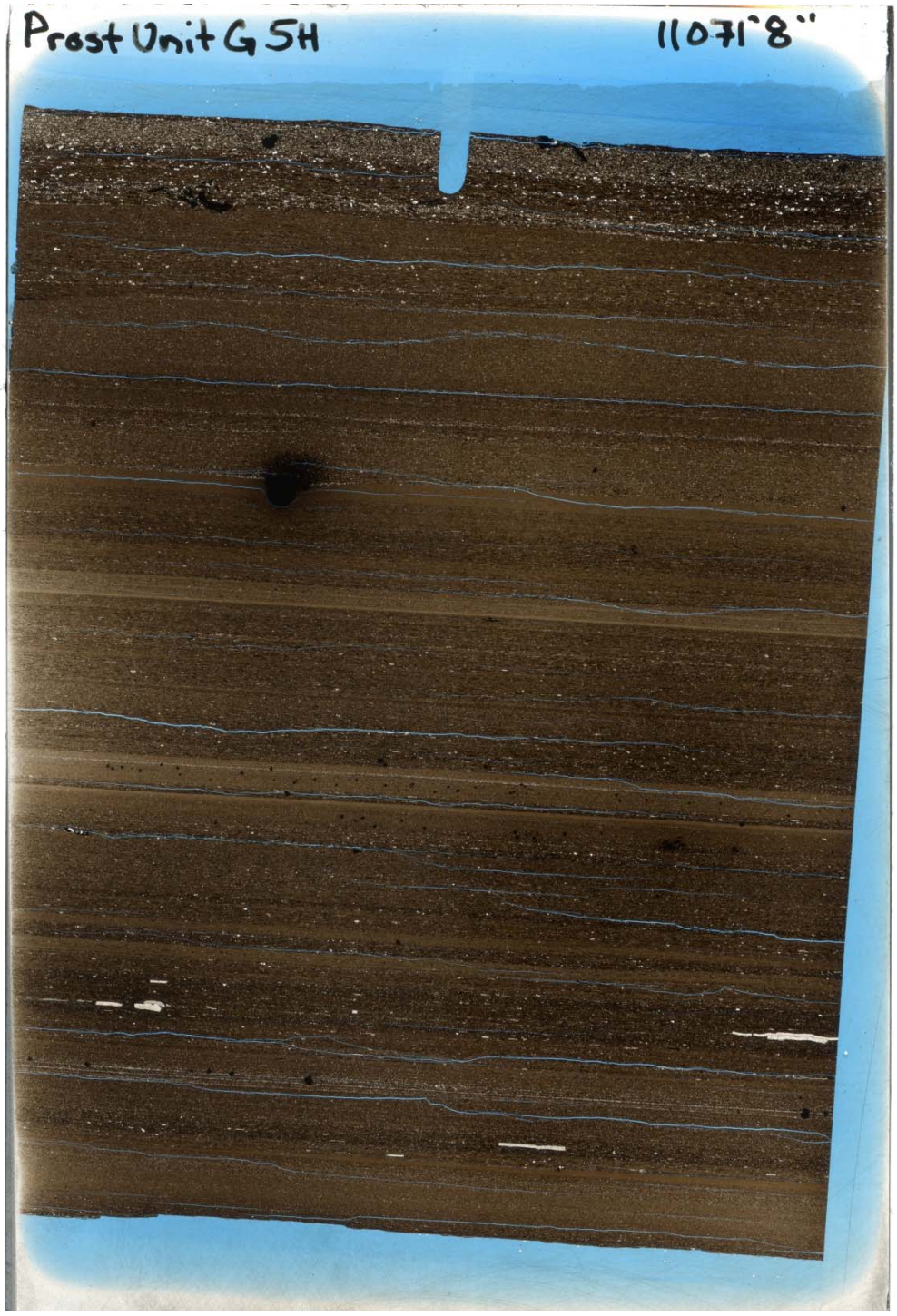

11071'8"- indistinctly laminated mudstone with abundant minute planktonic foraminifera and pyrite

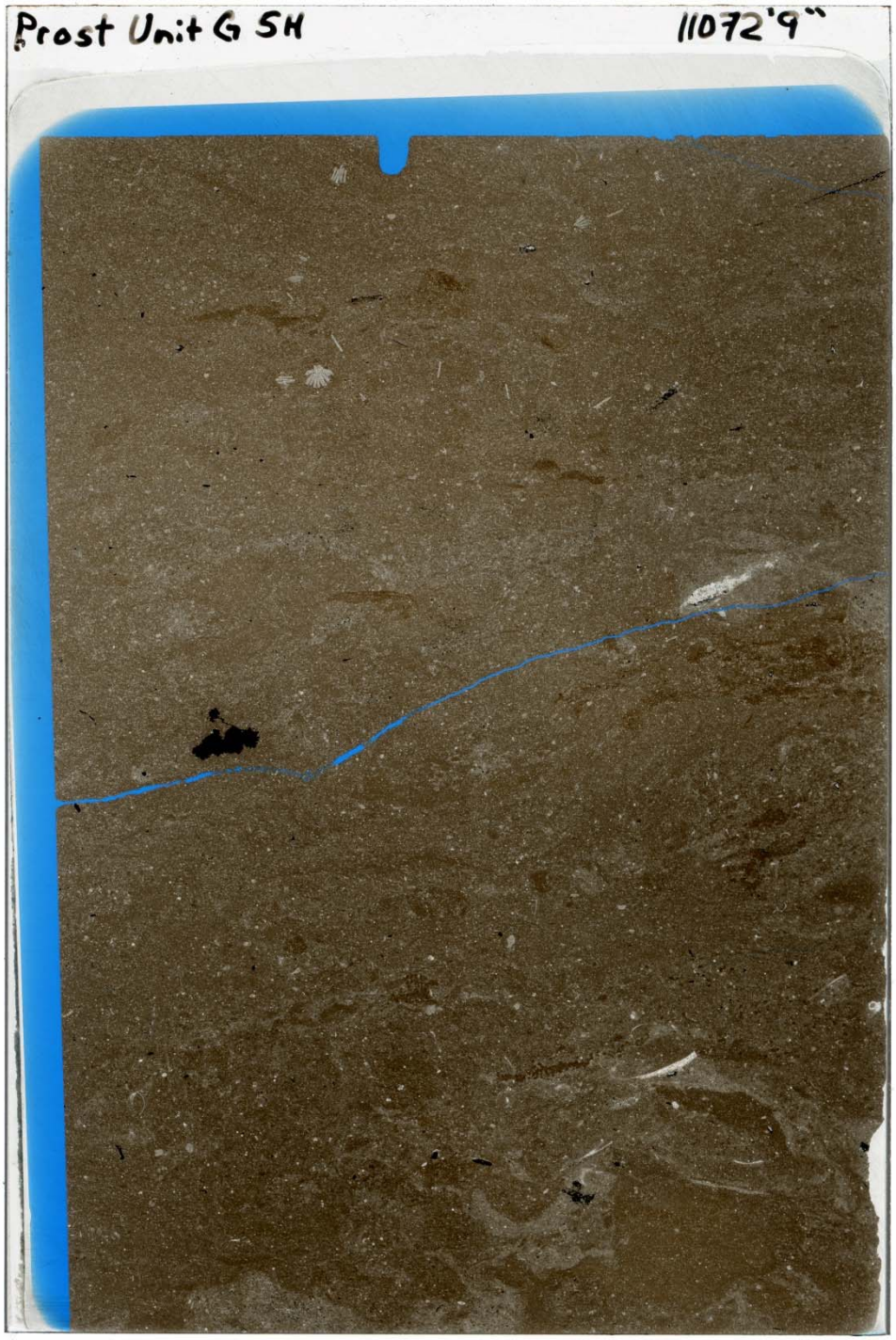

11072'9"- massive limestone, mottled to massively bioturbated with calcispheres, benthic/agglutinated foraminifera, ostracods, and echinoid spine

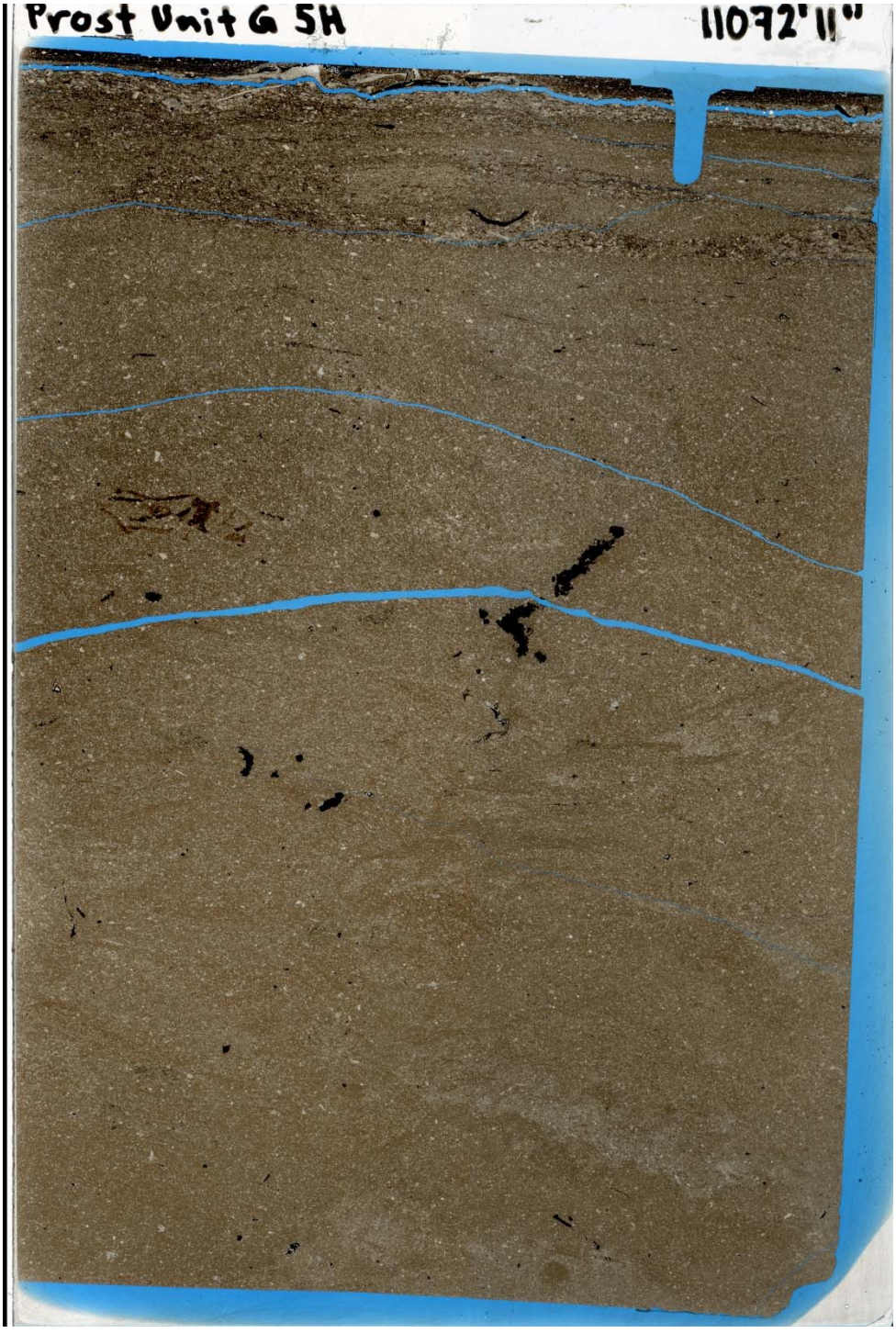

11072’11”- massive limestone, mottled to massively bioturbated with calcispheres, benthic/agglutinated foraminifera, ostracods

SANTE NORTH UNIT A 1H Thin Section Descriptions

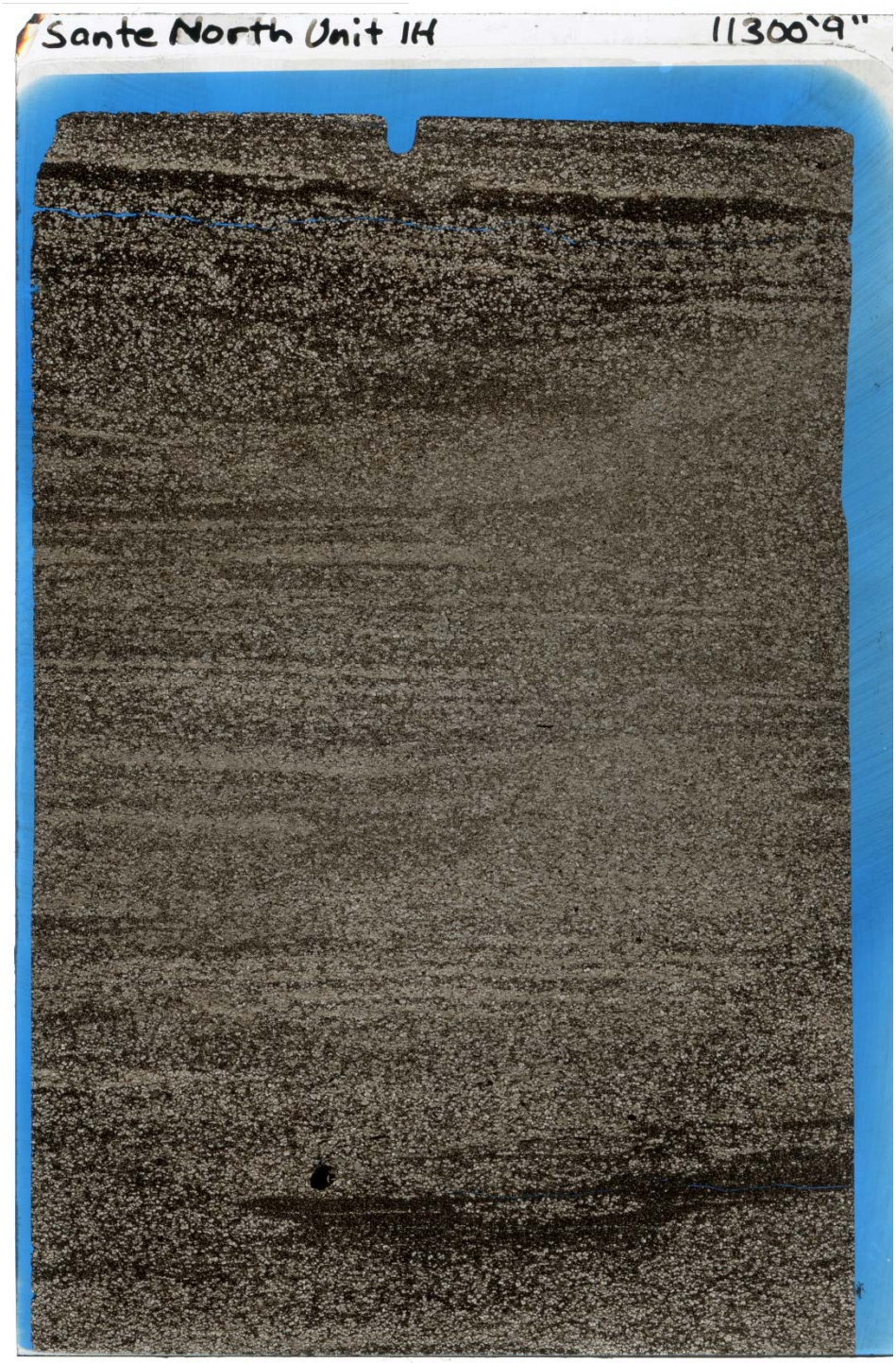

11300'9"- laminated mudstone; recrystallized laminated limestone

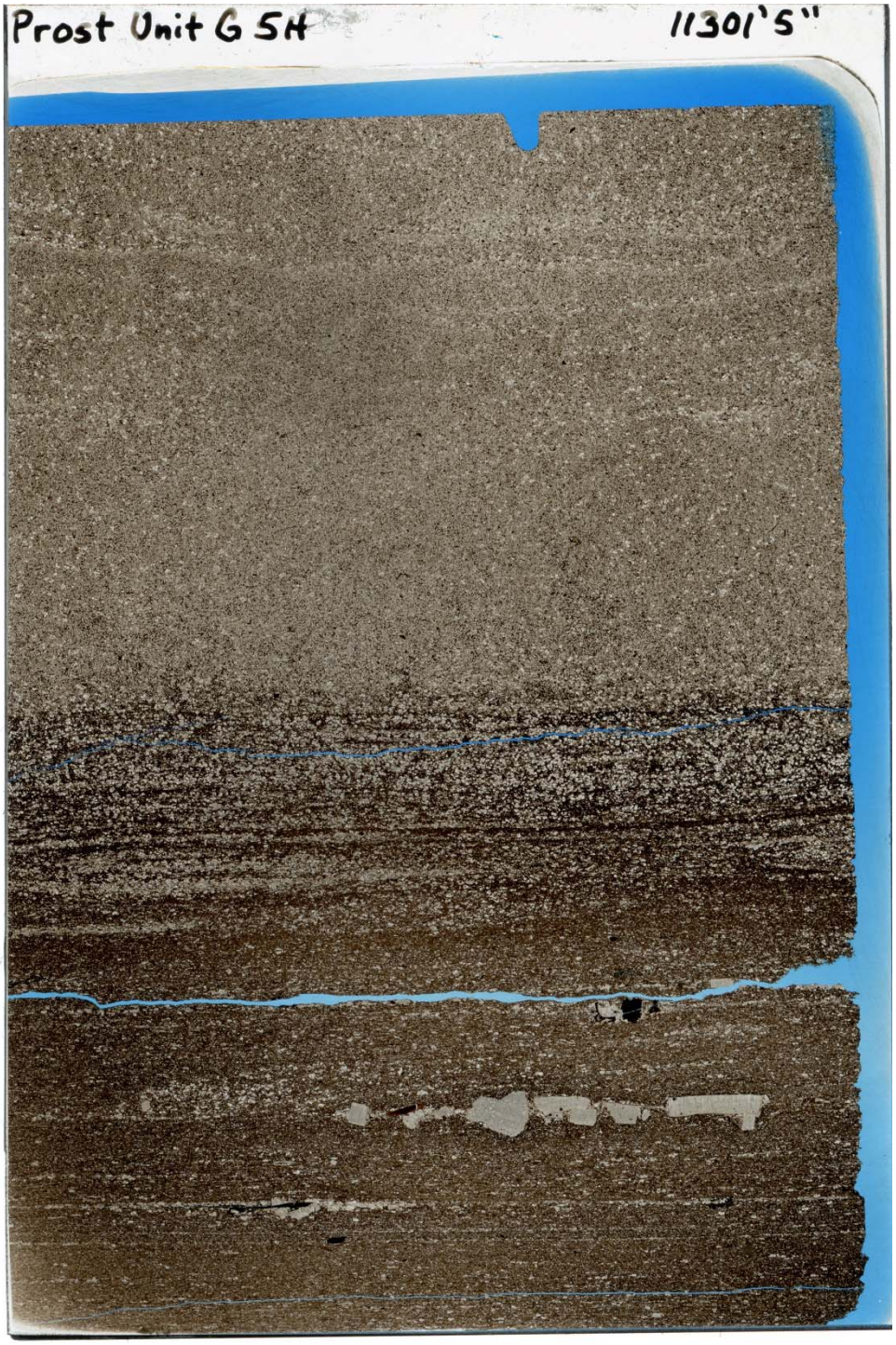

11301’5”- recrystallized laminated limestone; indistinctly laminated mudstone with inoceramid pieces

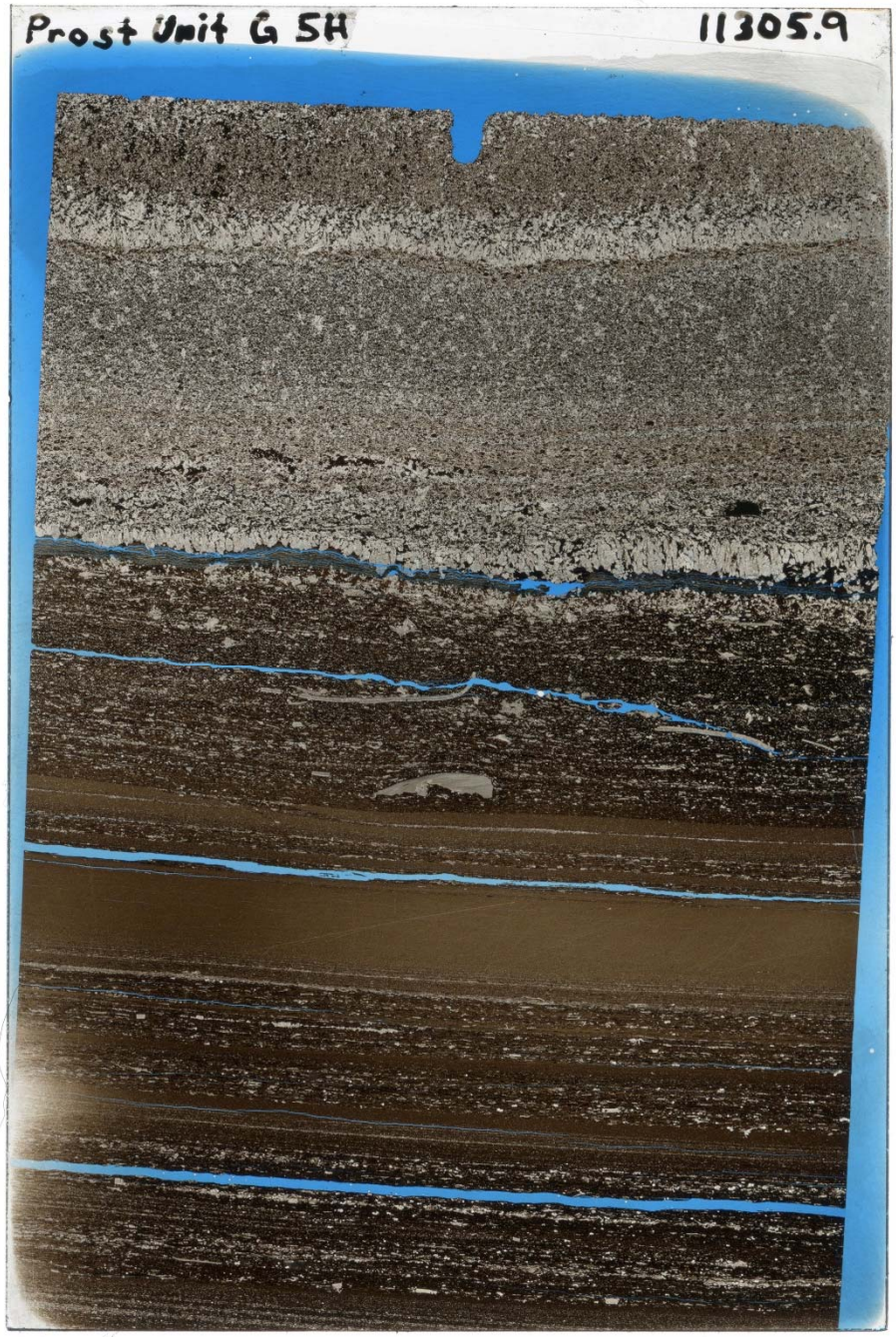

11305’9”- recrystallized laminated limestone with fibrous calcite; indistinctly laminated mudstone with abundant inoceramid and fish pieces; massive argillaceous mudstone

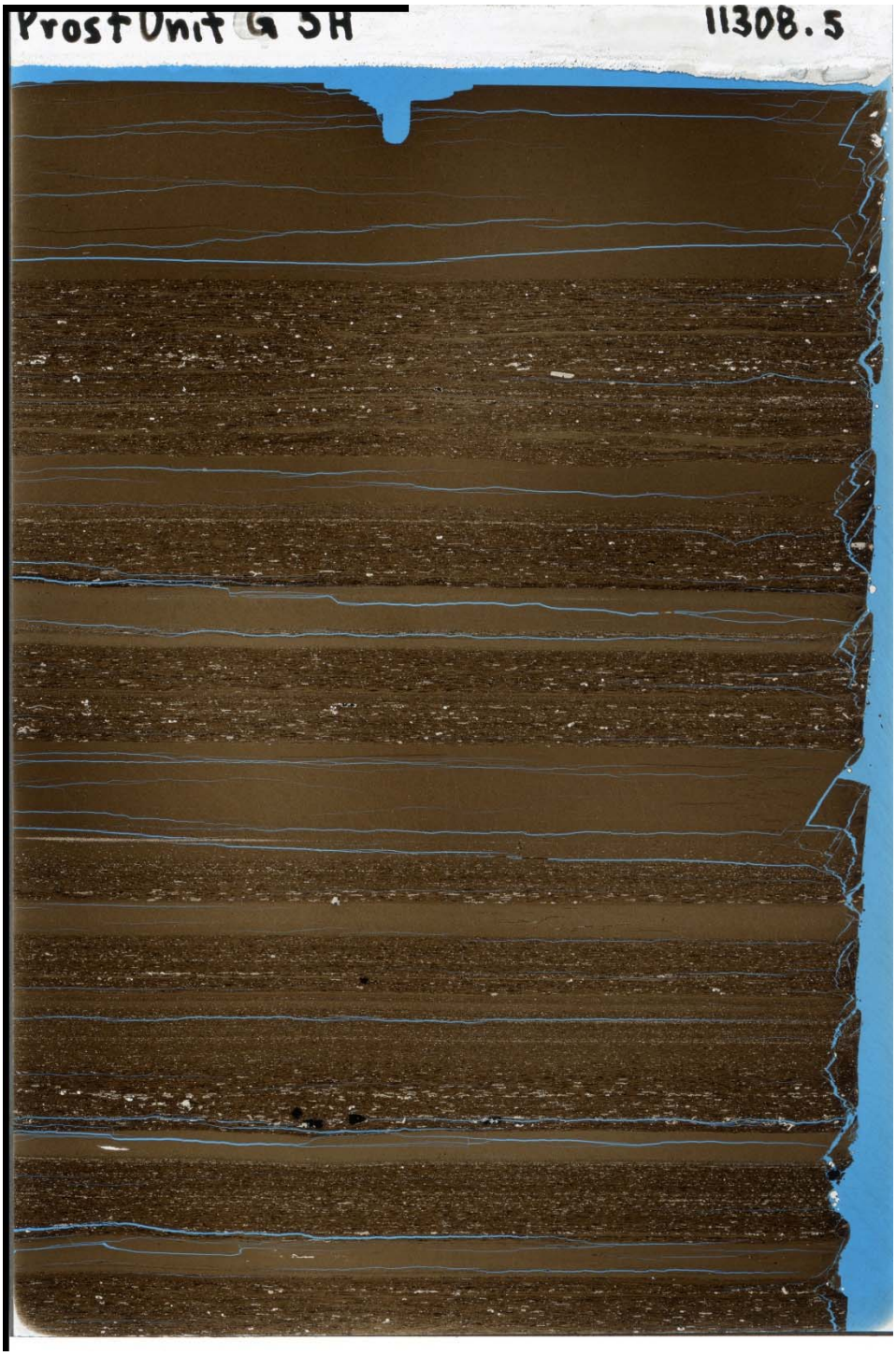

11308’5”- alternating massive argillaceous mudstone (1.5 cm) interbedded with indistinctly laminated mudstone

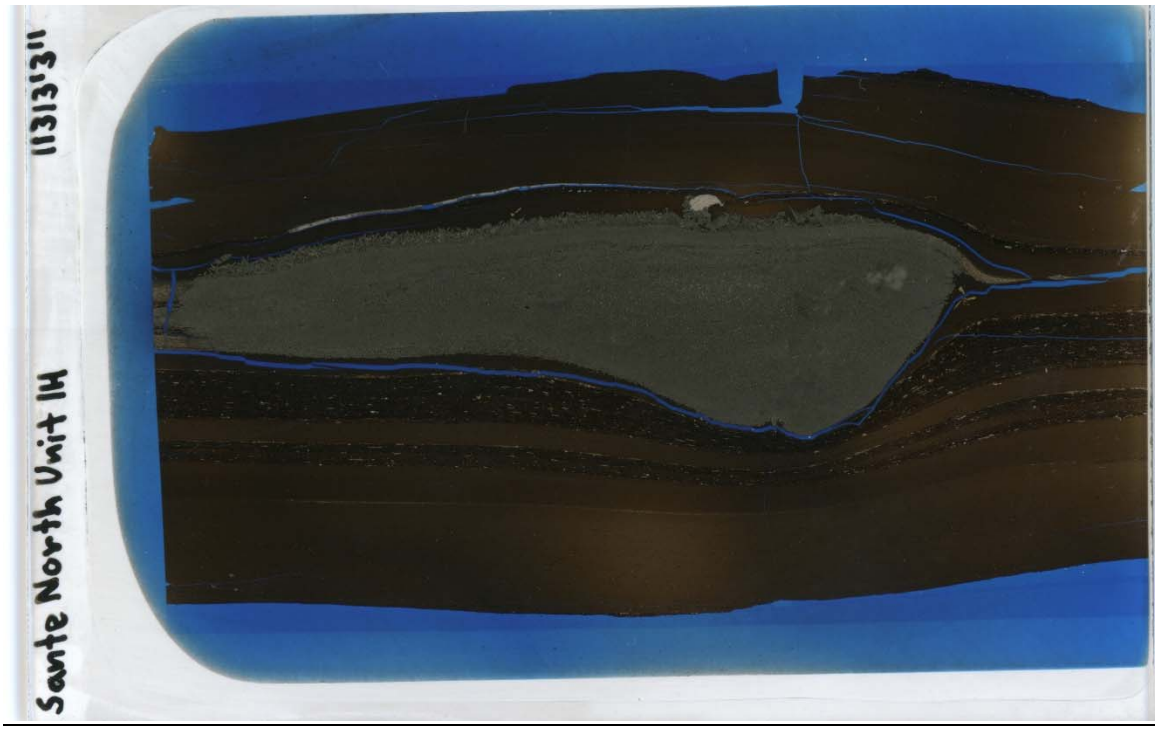

11313'3"- large (1.5 cm) pyrite nodule within massive argillaceous mudstones and thin indistinctly laminated mudstones; taken under reflected light.

11322’0”- recrystallized laminated limestone; large (1cm) fibrous calcite; ash bed

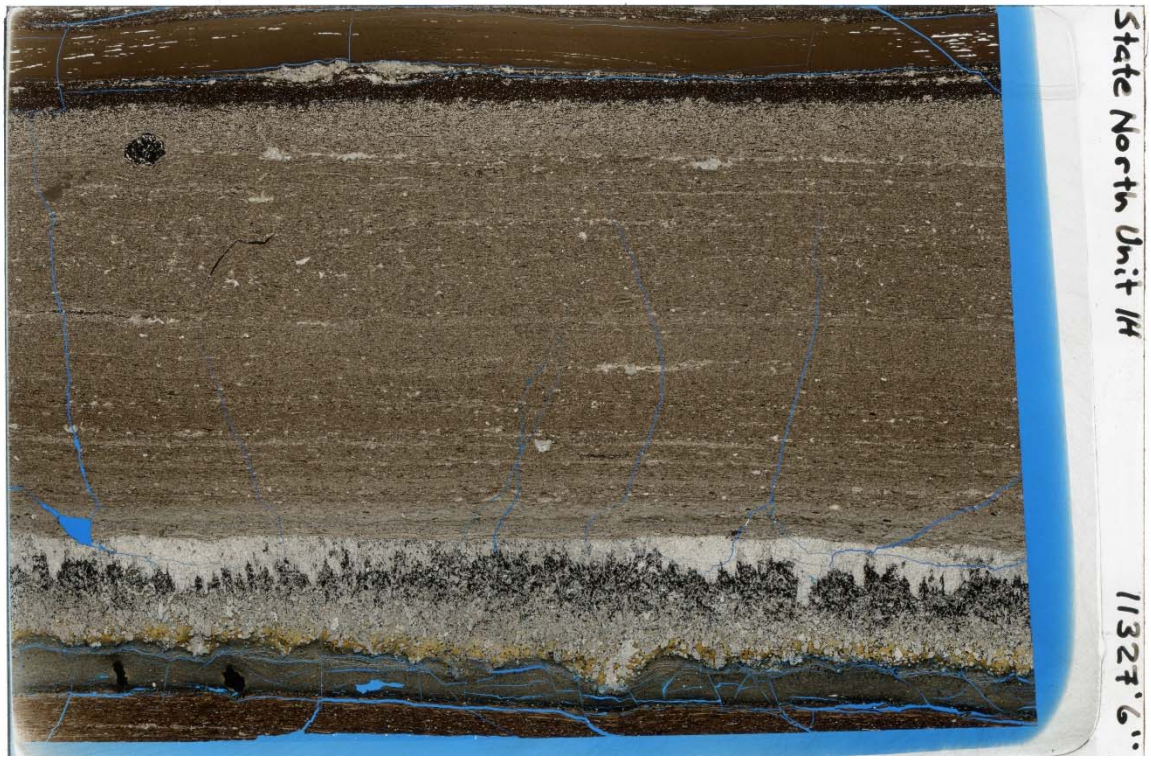

11327'6"- recrystallized laminated limestone with fibrous calcite; indistinctly laminated and massive argillaceous mudstone; ash bed

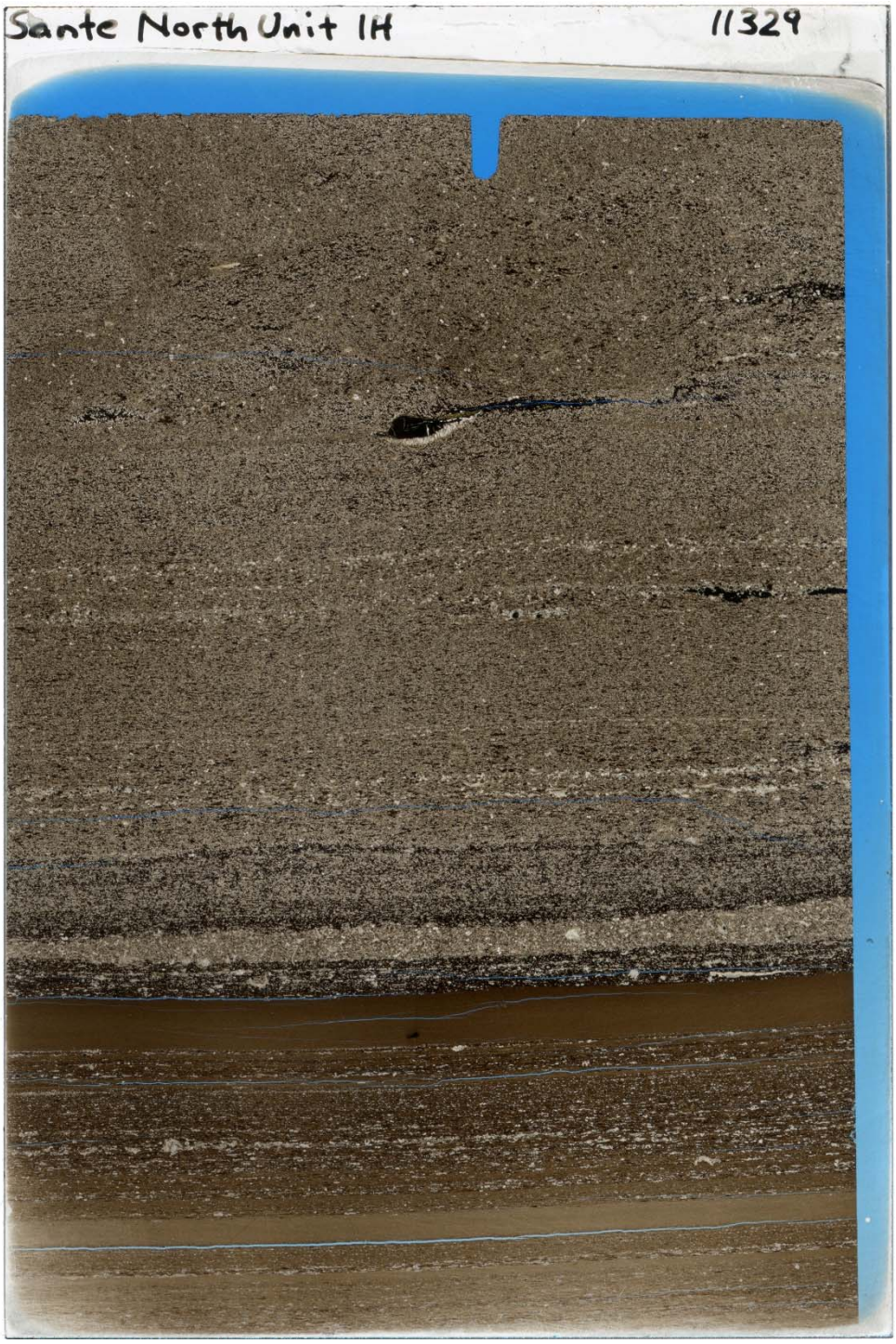

11329’0”- recrystallized laminated limestone with winnowed lags; indistinctly laminated mudstone; few thin massive argillaceous mudstone

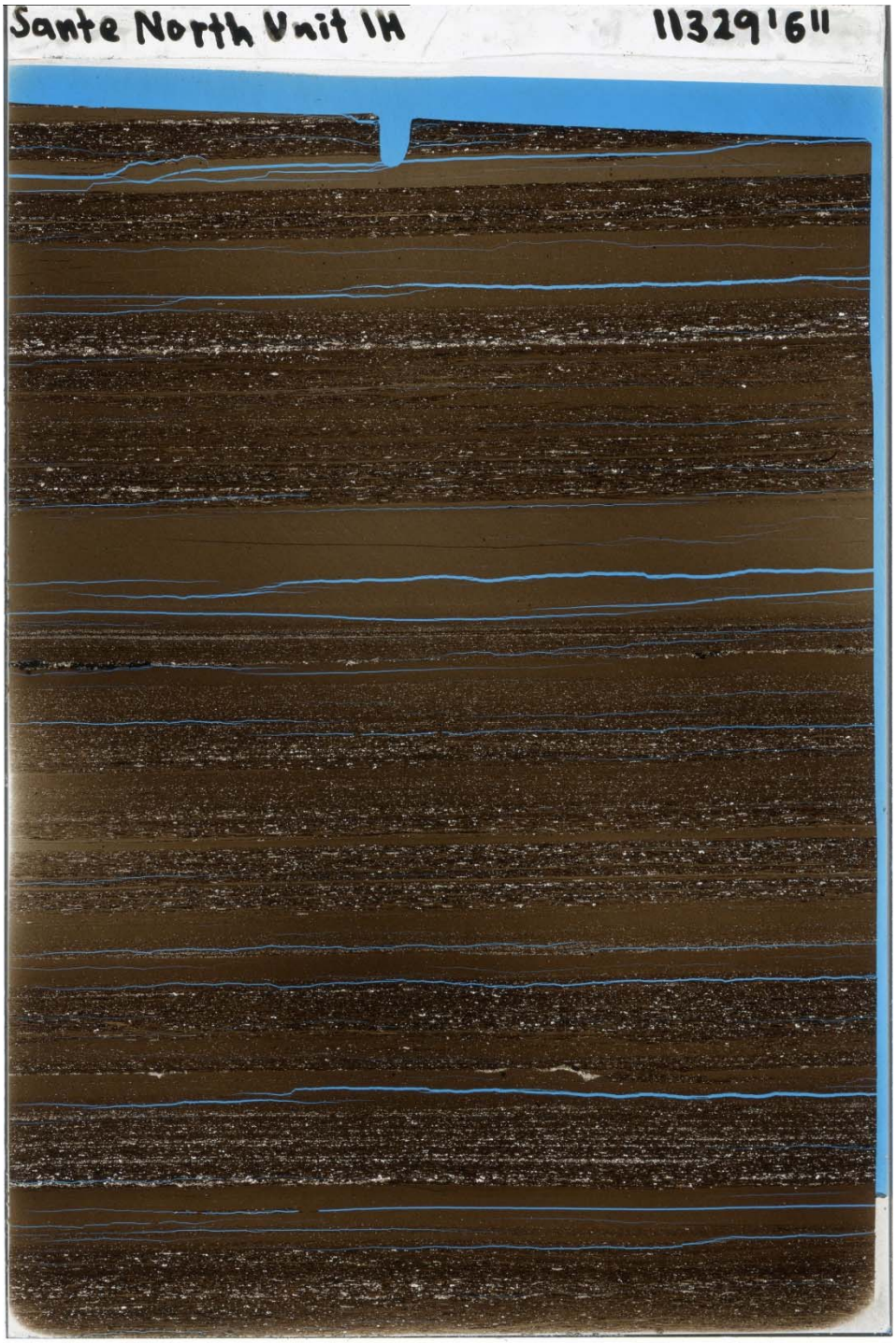

11329’6”- alternating massive argillaceous mudstone interbedded with indistinctly laminated mudstone

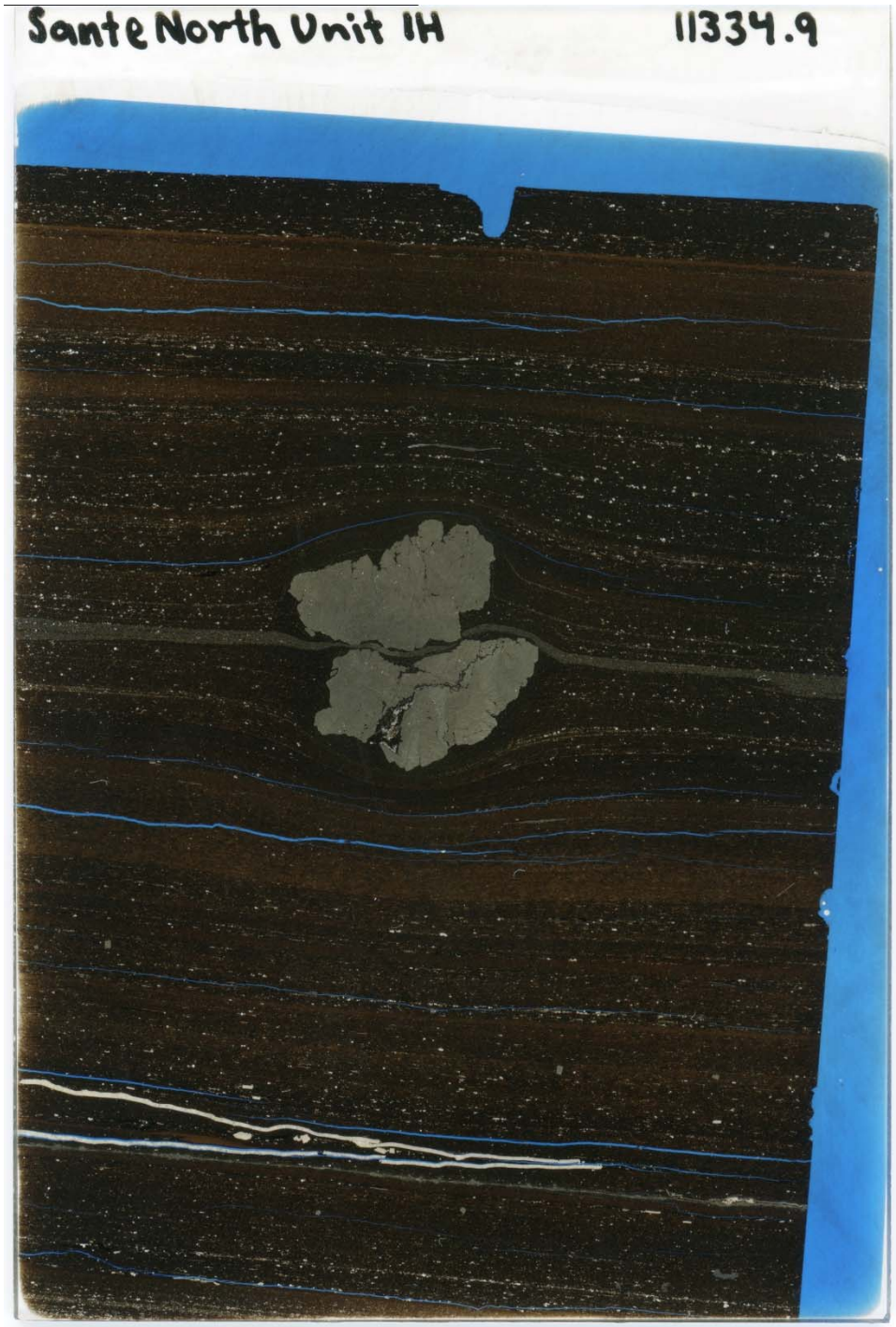

11334’9”- alternating massive argillaceous mudstone interbedded with indistinctly laminated mudstone with sizeable pyrite nodules with a thin ash bed and inoceramids. Taken under reflected light.

11335'1"- massive Limestone, mottled to massively bioturbated with calcispheres, benthic/agglutinated foraminifera, ostracods

APPENDIX B – Core Descriptions

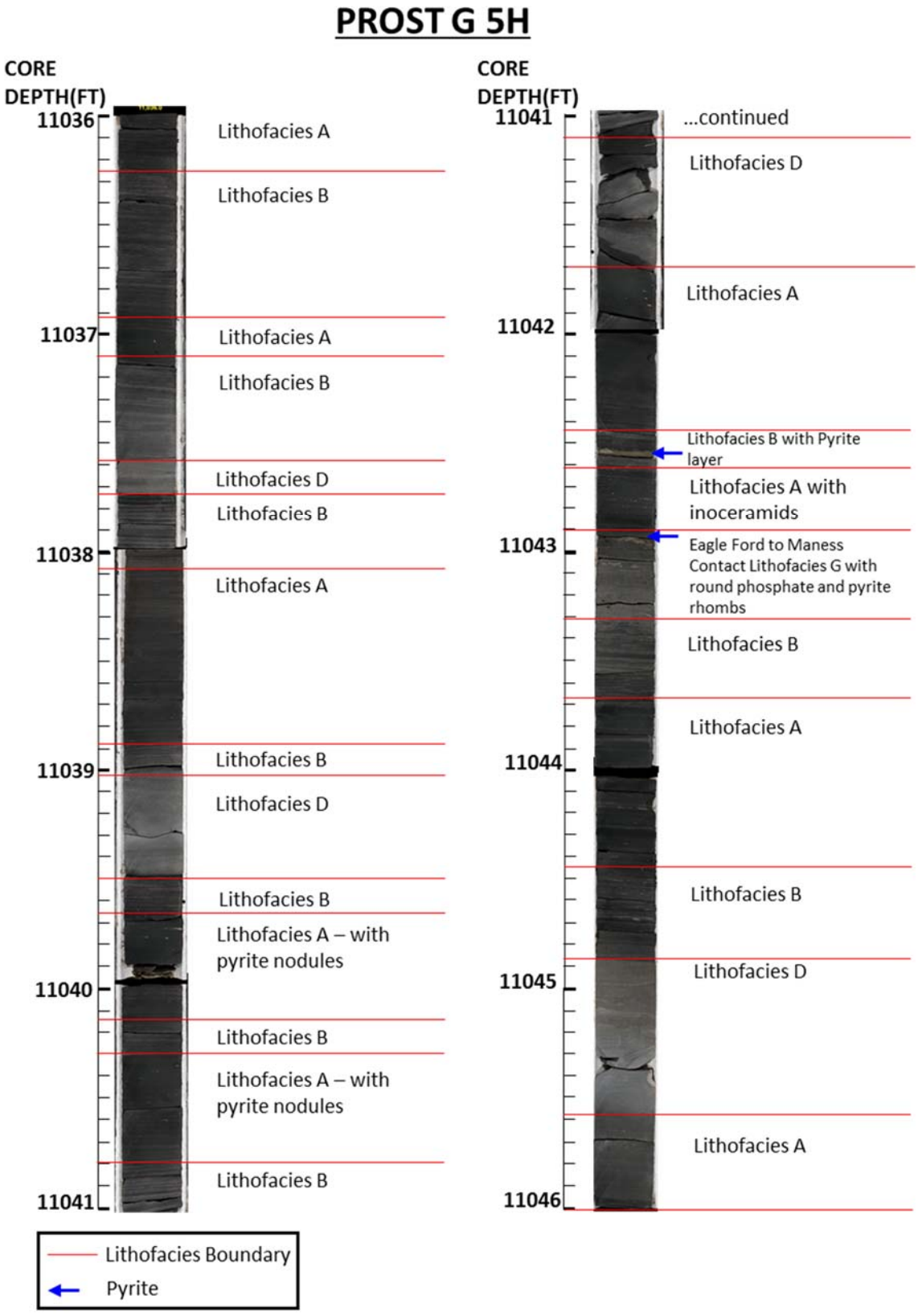

PROST G 5H

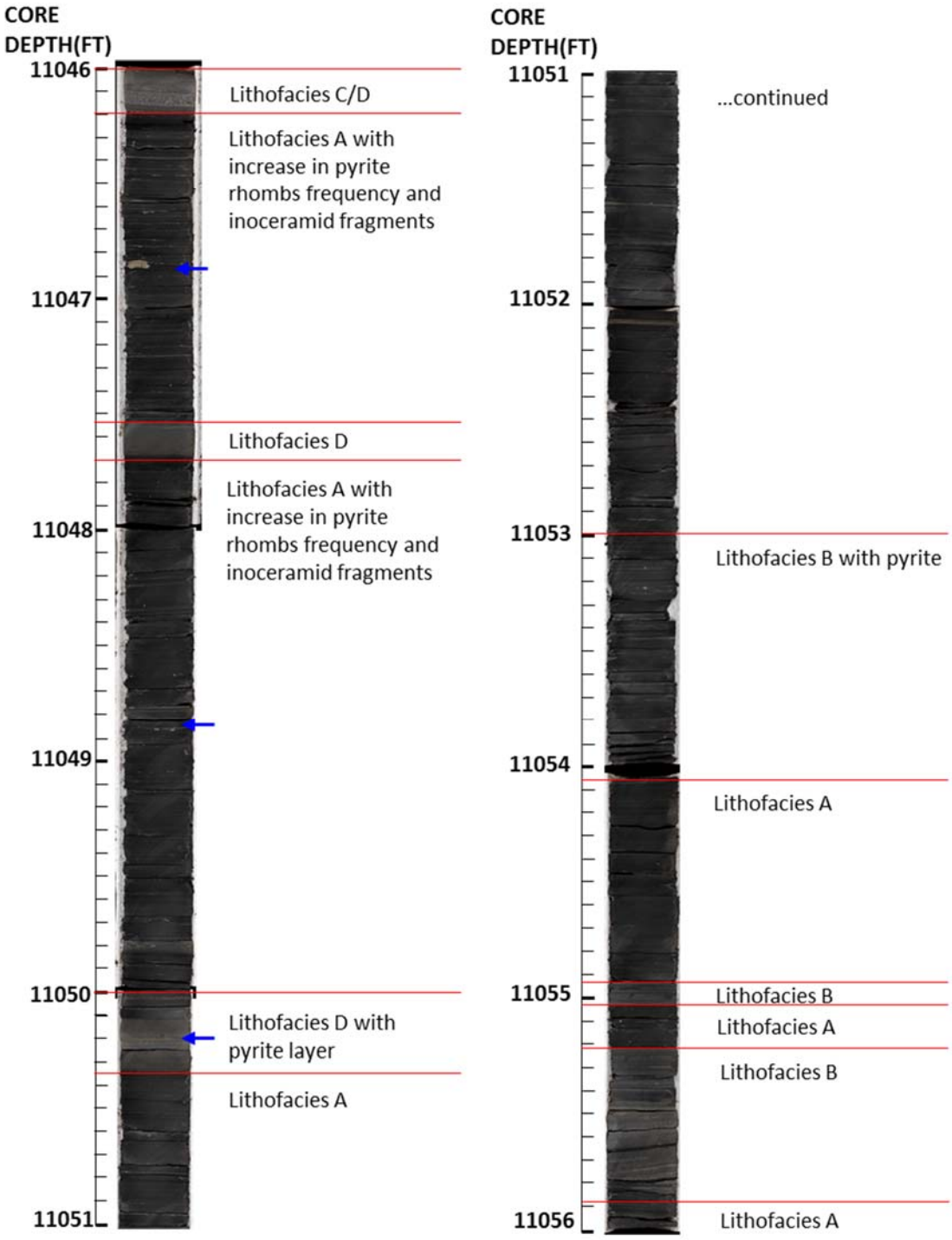
CORE DEPTH(FT)
11046
11047
11048
11049
11050
11051
Lithofacies C/D
Lithofacies A with increase in pyrite rhombs frequency and inoceramid fragments
Lithofacies D
Lithofacies A with increase in pyrite rhombs frequency and inoceramid fragments
Lithofacies D with pyrite layer
Lithofacies A
CORE DEPTH(FT)
11051
11052
11053
11054
11055
11056
...continued
Lithofacies B with pyrite
Lithofacies A
Lithofacies B
Lithofacies A
Lithofacies B
Lithofacies A

PROST G 5H

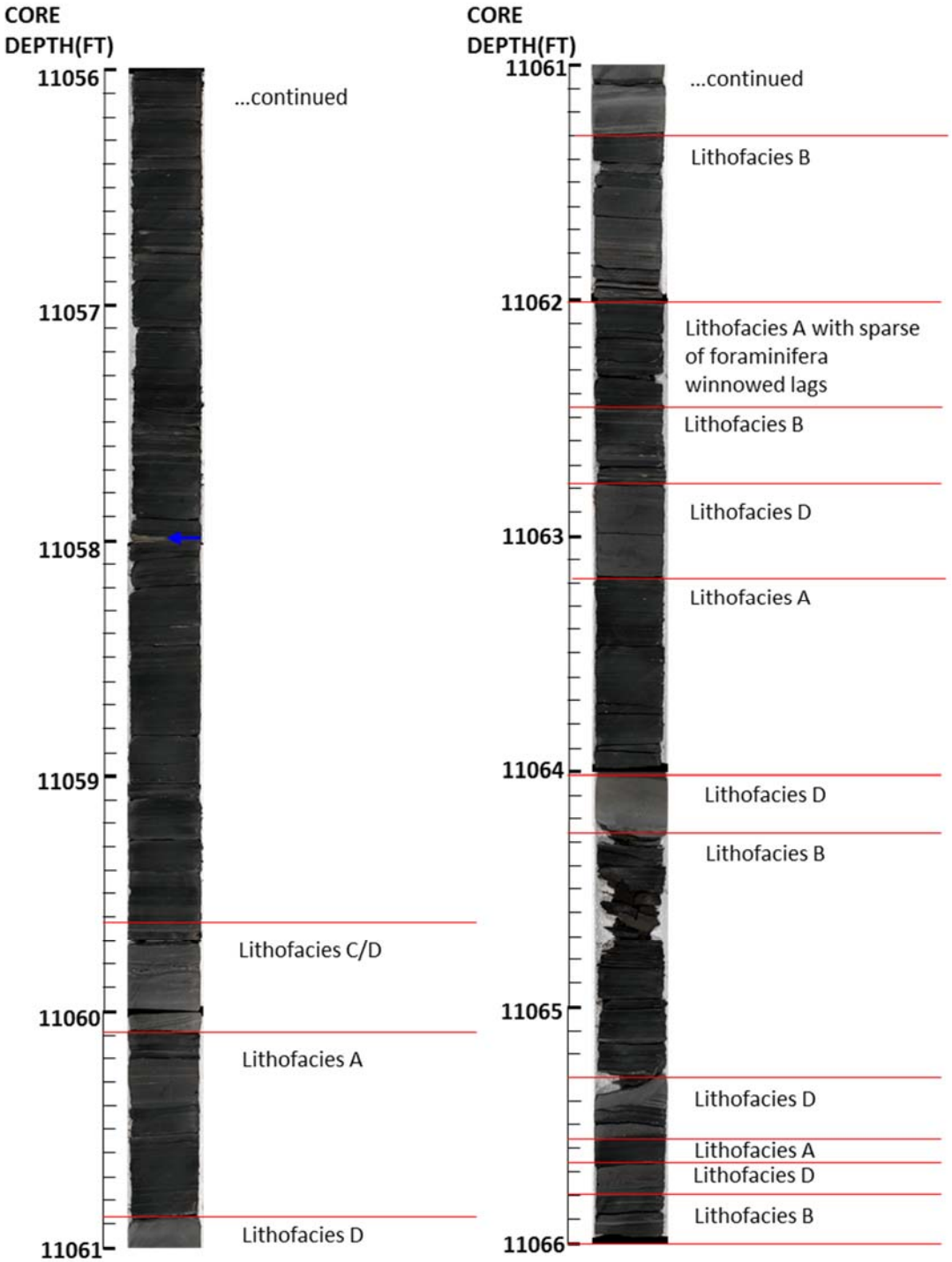
CORE
DEPTH(FT)
11056
...continued
11057
11058
11059
Lithofacies C/D
11060
Lithofacies A
Lithofacies D
11061
CORE
DEPTH(FT)
11061
...continued
Lithofacies B
11062
Lithofacies A with sparse of foraminifera winnowed lags
Lithofacies B
Lithofacies D
11063
Lithofacies A
11064
Lithofacies D
Lithofacies B
11065
Lithofacies D
Lithofacies A
Lithofacies D
Lithofacies B
11066

PROST G 5H

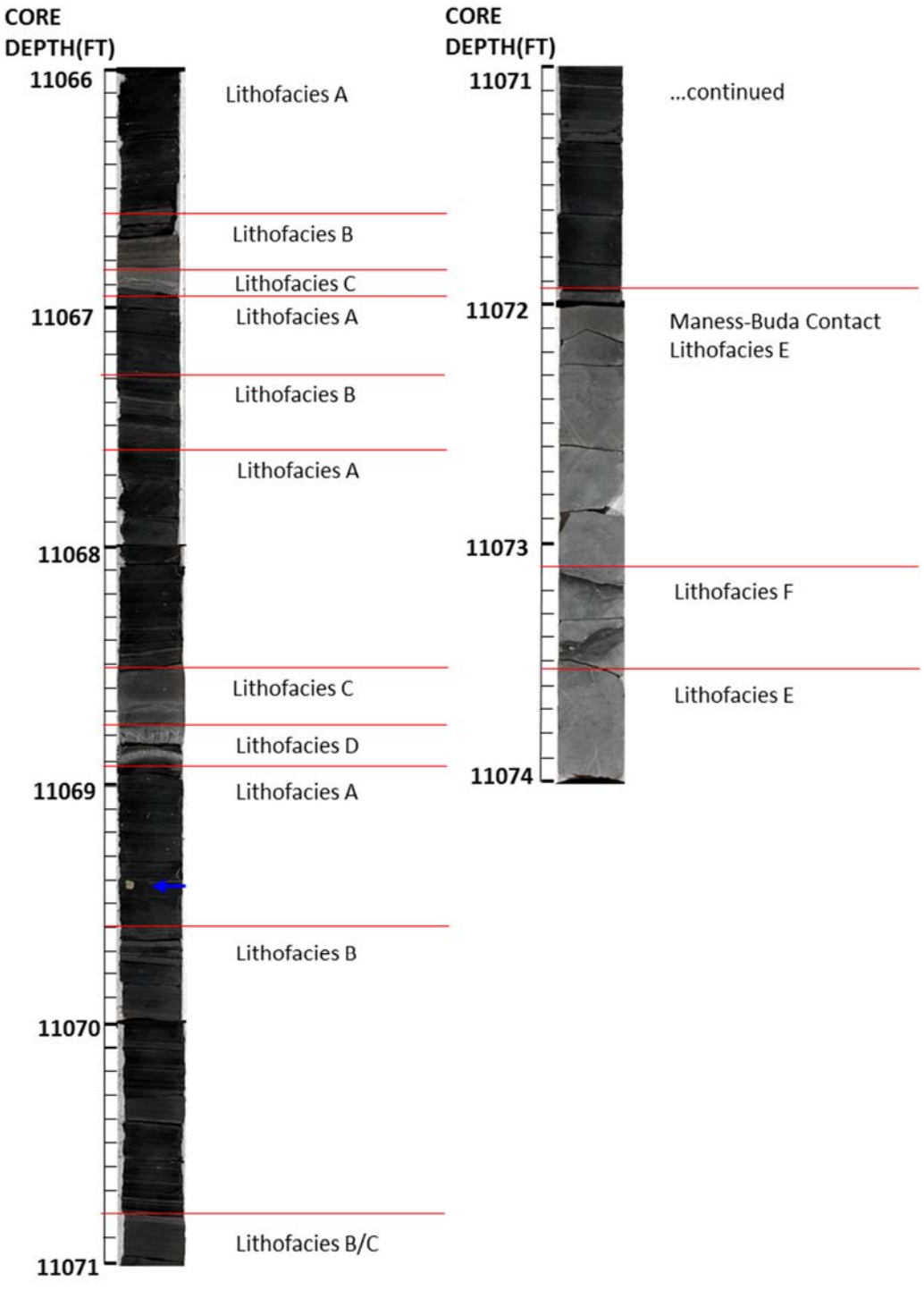
CORE DEPTH(FT)
11066
Lithofacies A
Lithofacies B
Lithofacies C
11067
Lithofacies A
Lithofacies B
Lithofacies A
11068
Lithofacies C
Lithofacies D
11069
Lithofacies A
Lithofacies B
11070
Lithofacies B/C
11071
CORE DEPTH(FT)
11071
...continued
11072
Maness-Buda Contact
Lithofacies E
11073
Lithofacies F
Lithofacies E
11074

SANTE NORTH UNIT A 1H

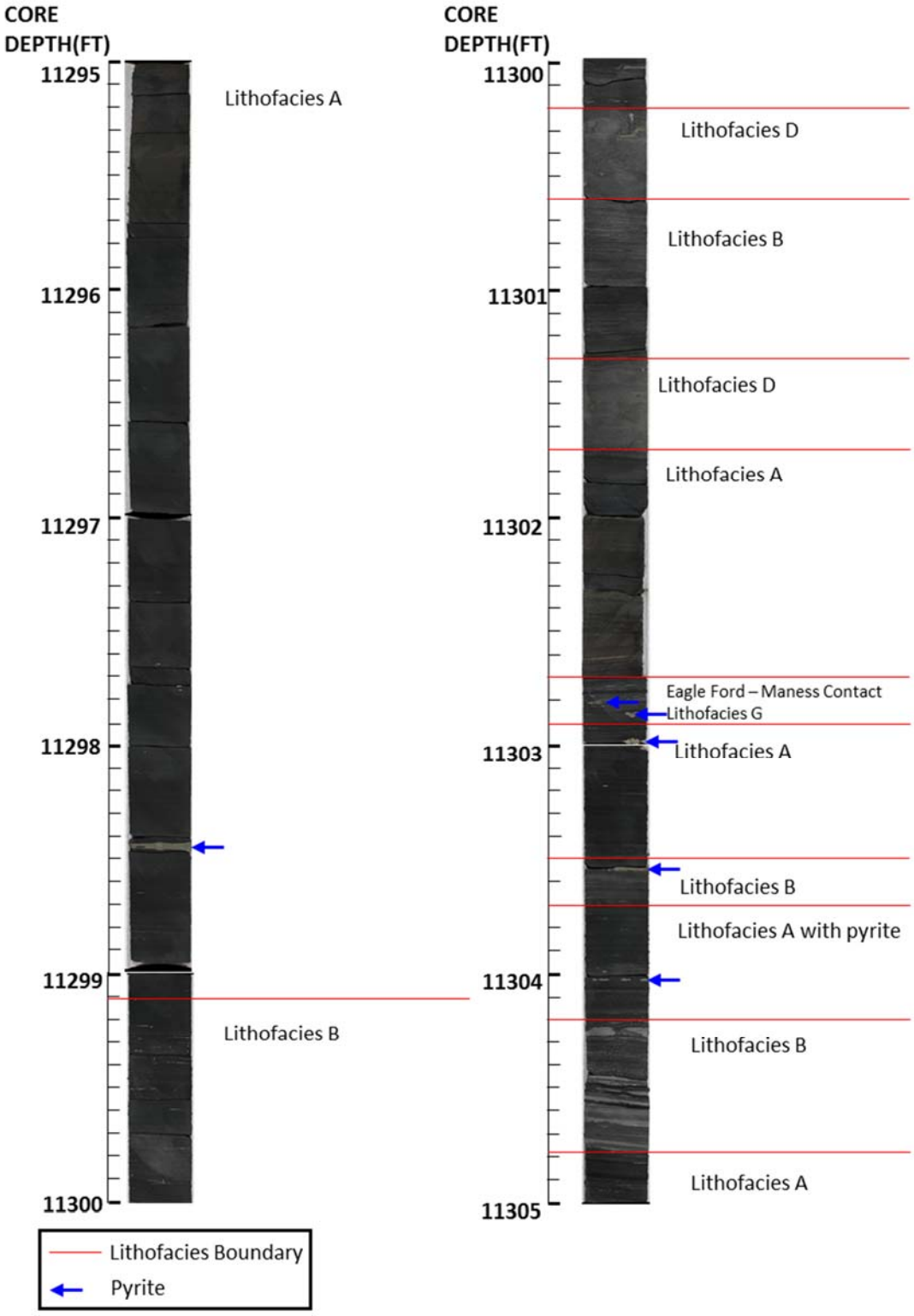

SANTE NORTH UNIT A 1H

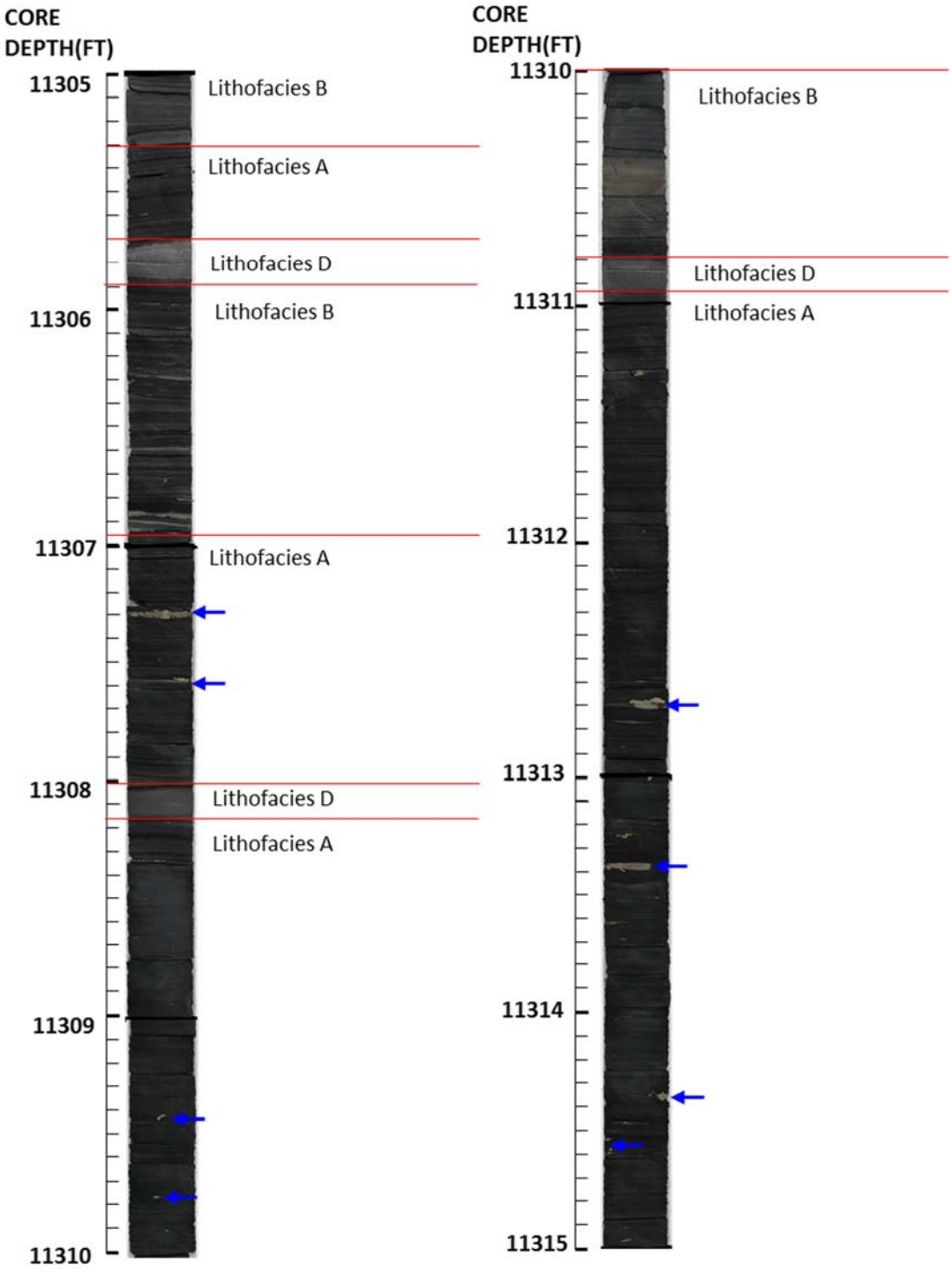

SANTE NORTH UNIT A 1H

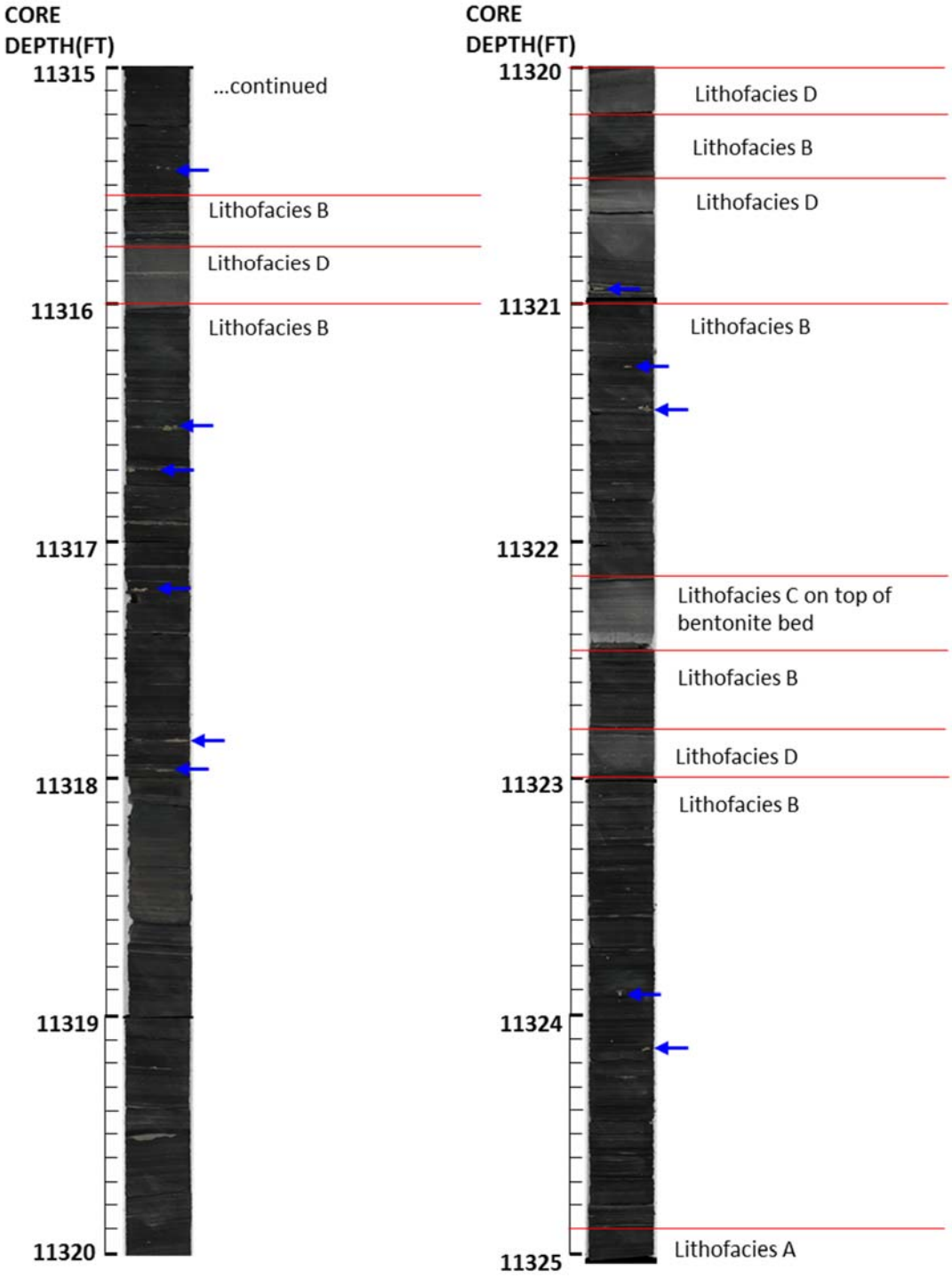

SANTE NORTH UNIT A 1H

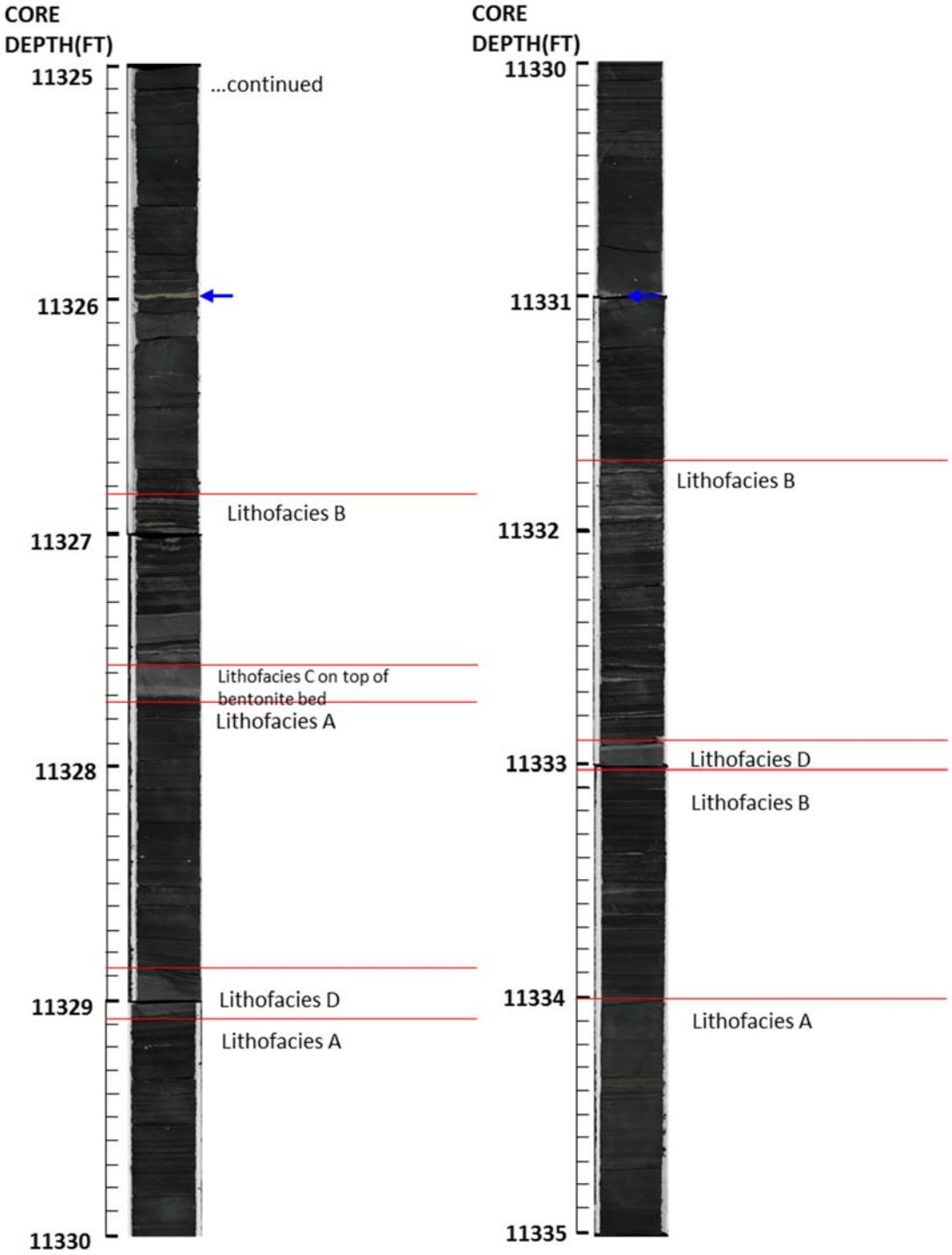

SANTE NORTH UNIT A 1H

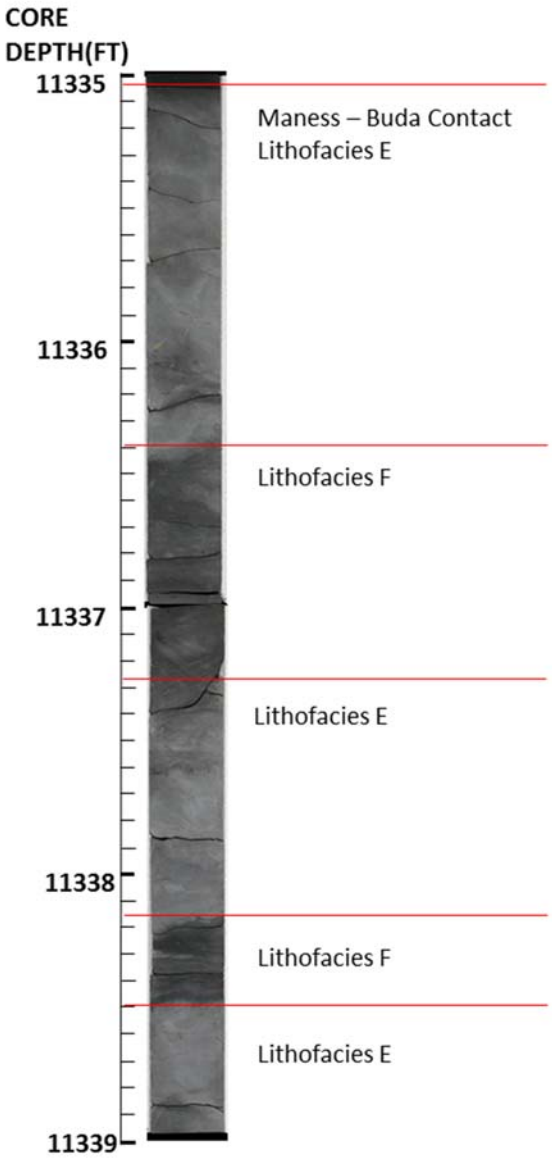

APPENDIX C – Microscope Images

PROST G 5H

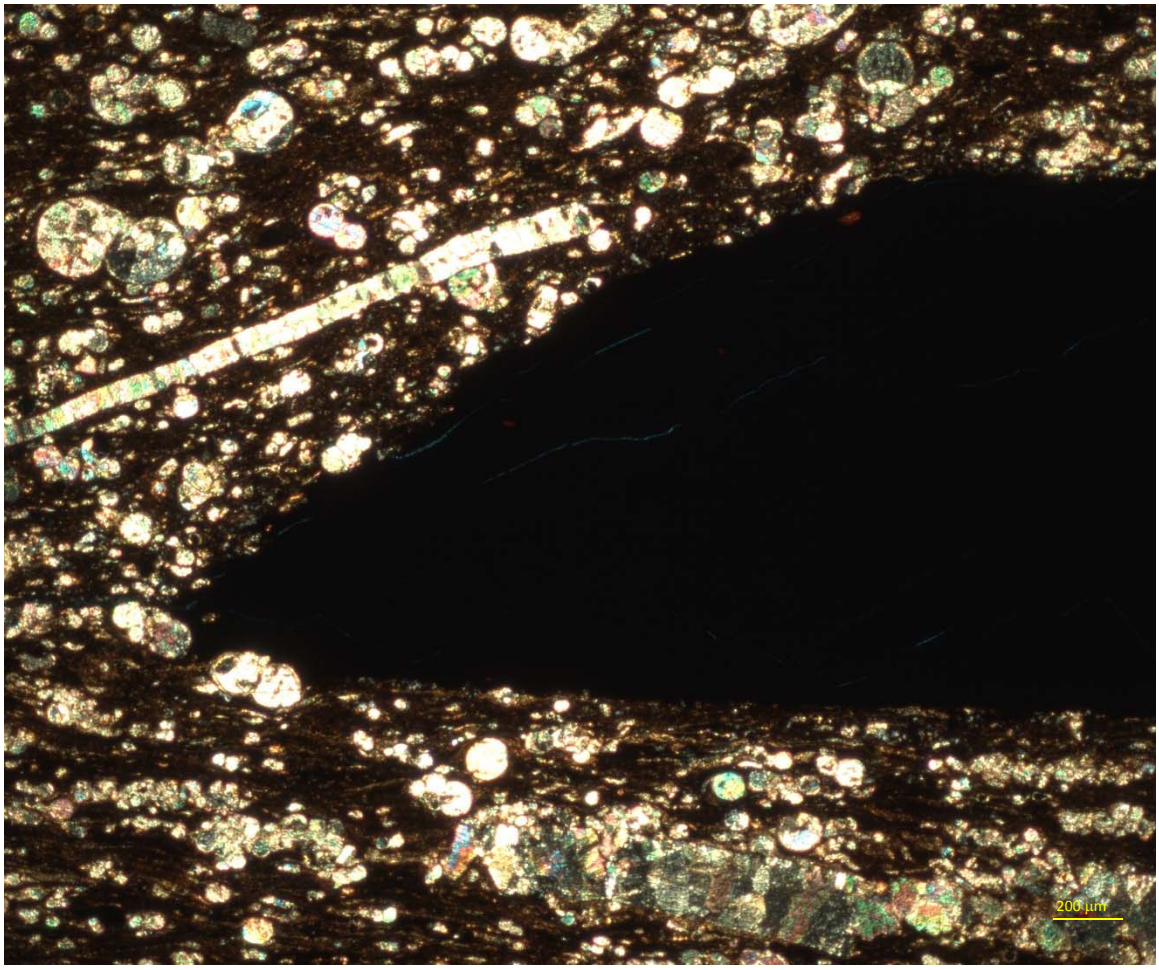

11044’9" - phosphate nodule within indistinctly laminated mudstone with inoceramid fragments and calcite filled foraminifera; taken with cross-polarized light.

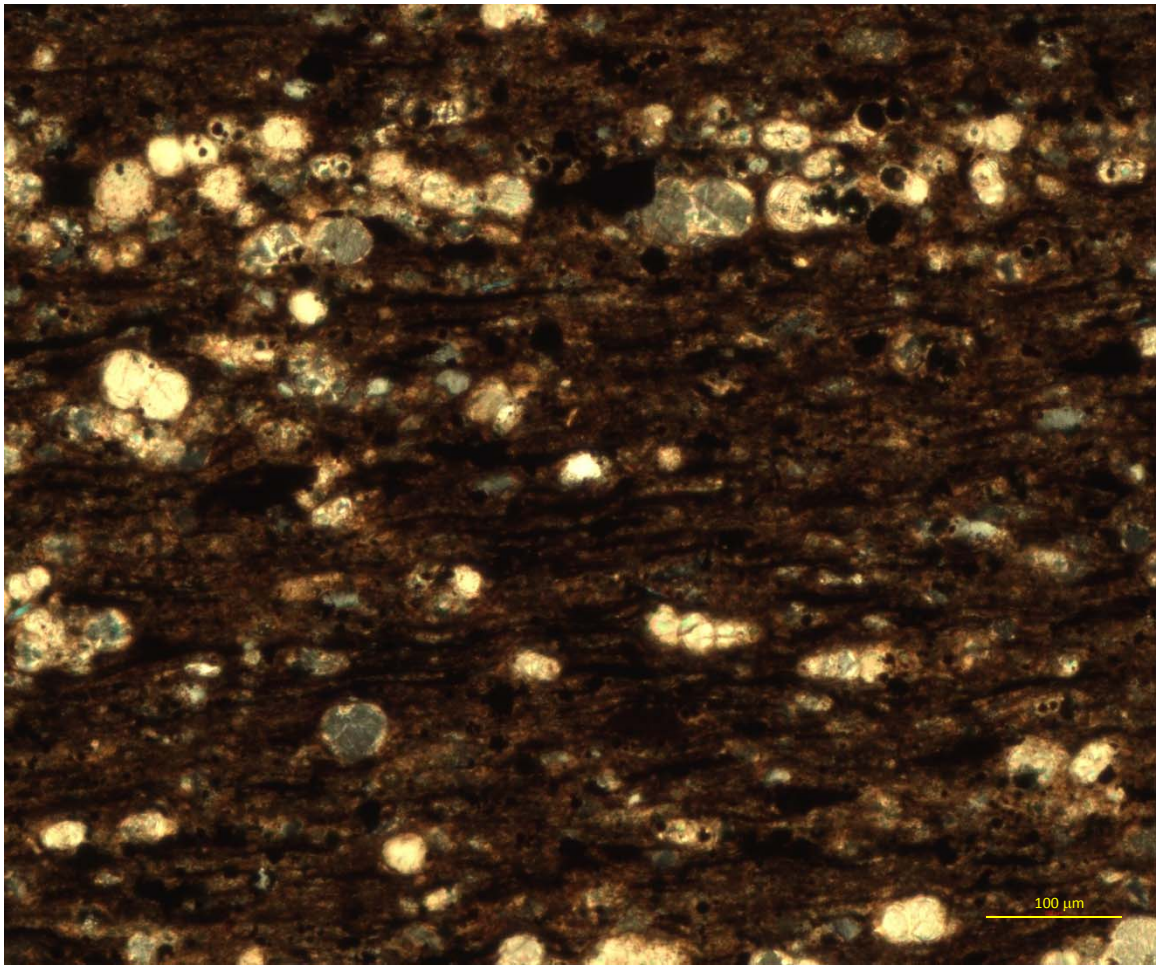

11063’8” - indistinctly laminated mudstone with calcite filled foraminifera; taken with cross-polarized light.

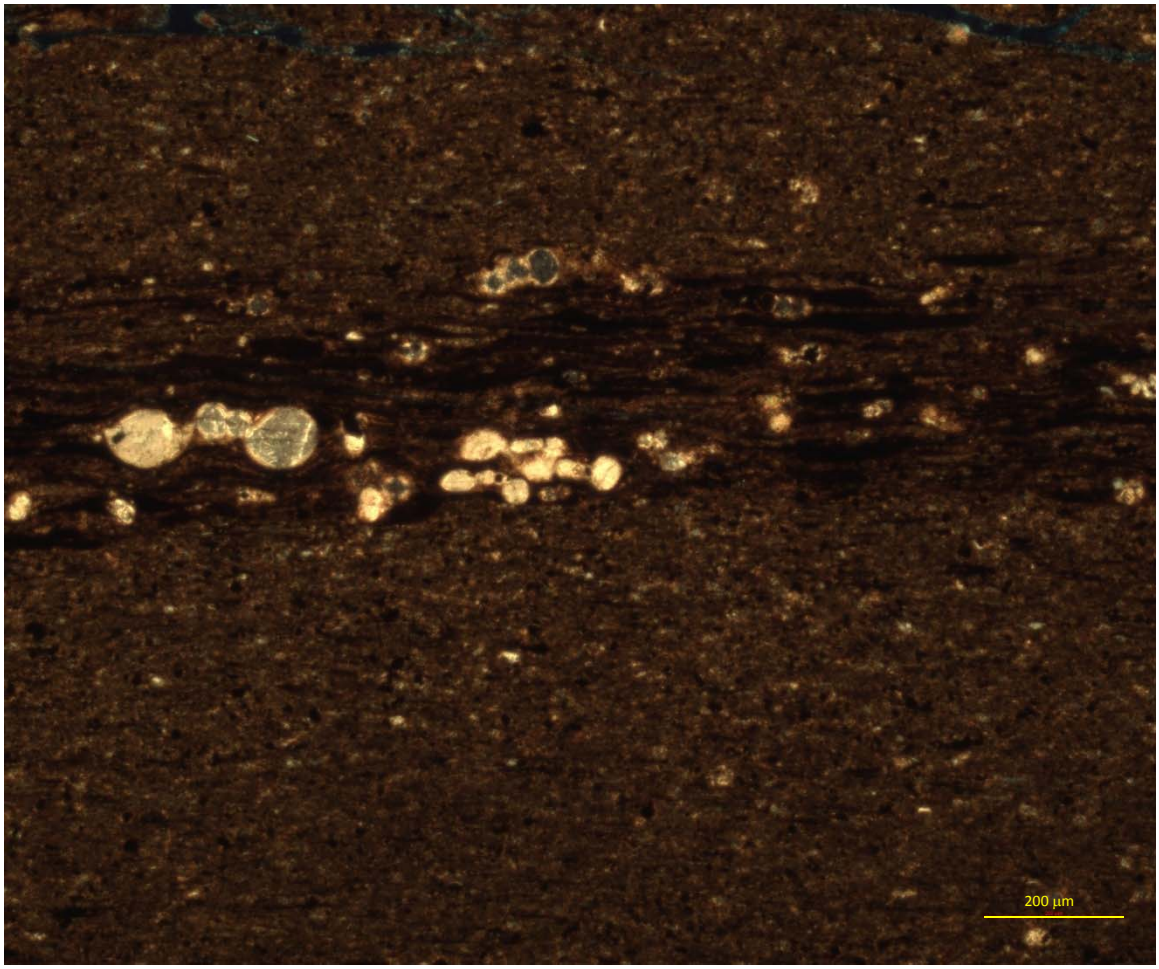

11063’8” - indistinctly laminated mudstone with calcite filled foraminifera; massive argillaceous mudstone; taken with cross-polarized light.

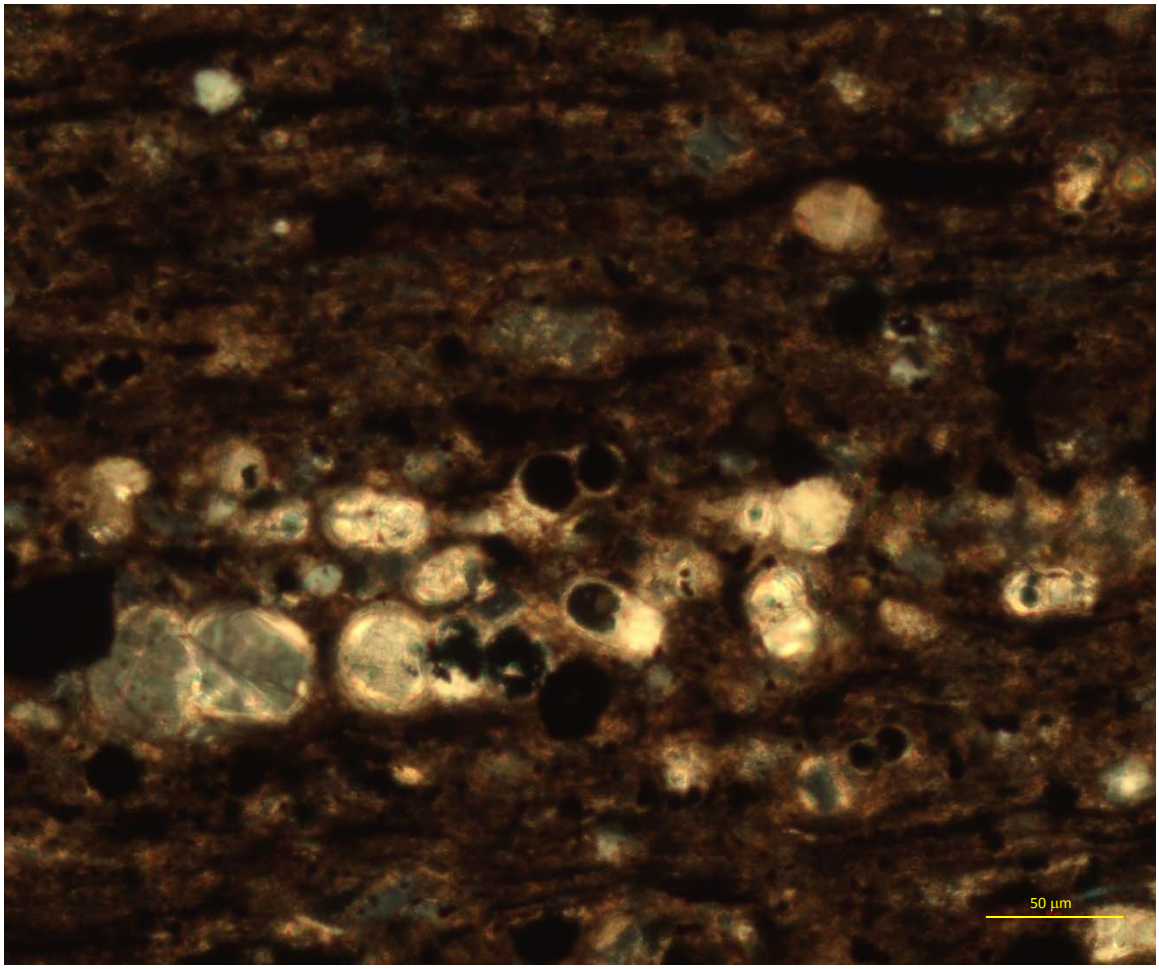

11063’8” - indistinctly laminated mudstone with calcite and pyrite filled foraminifera; taken with cross-polarized light.

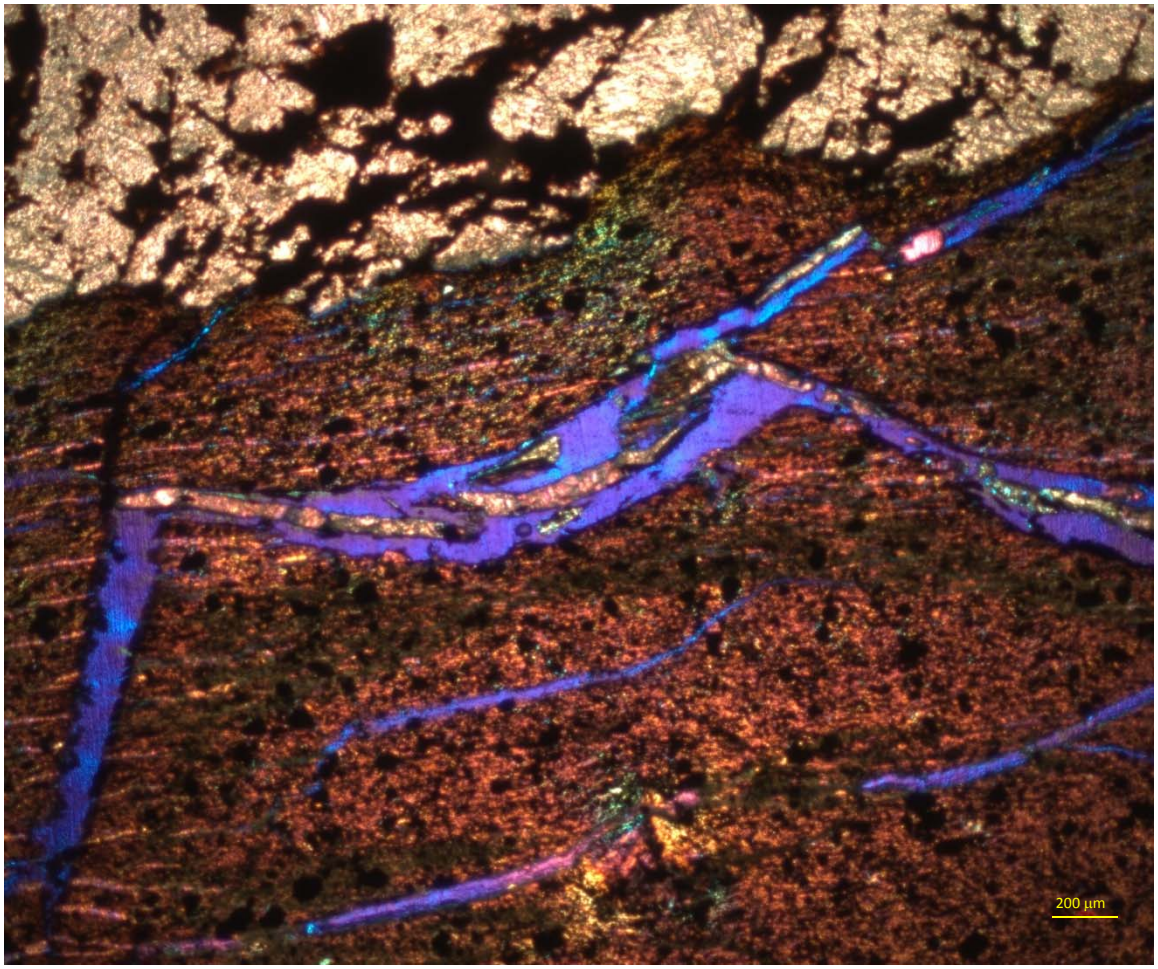

11068’7” - fibrous calcite; ash bed with pyrite; taken with quartz plate under cross-polarized light.

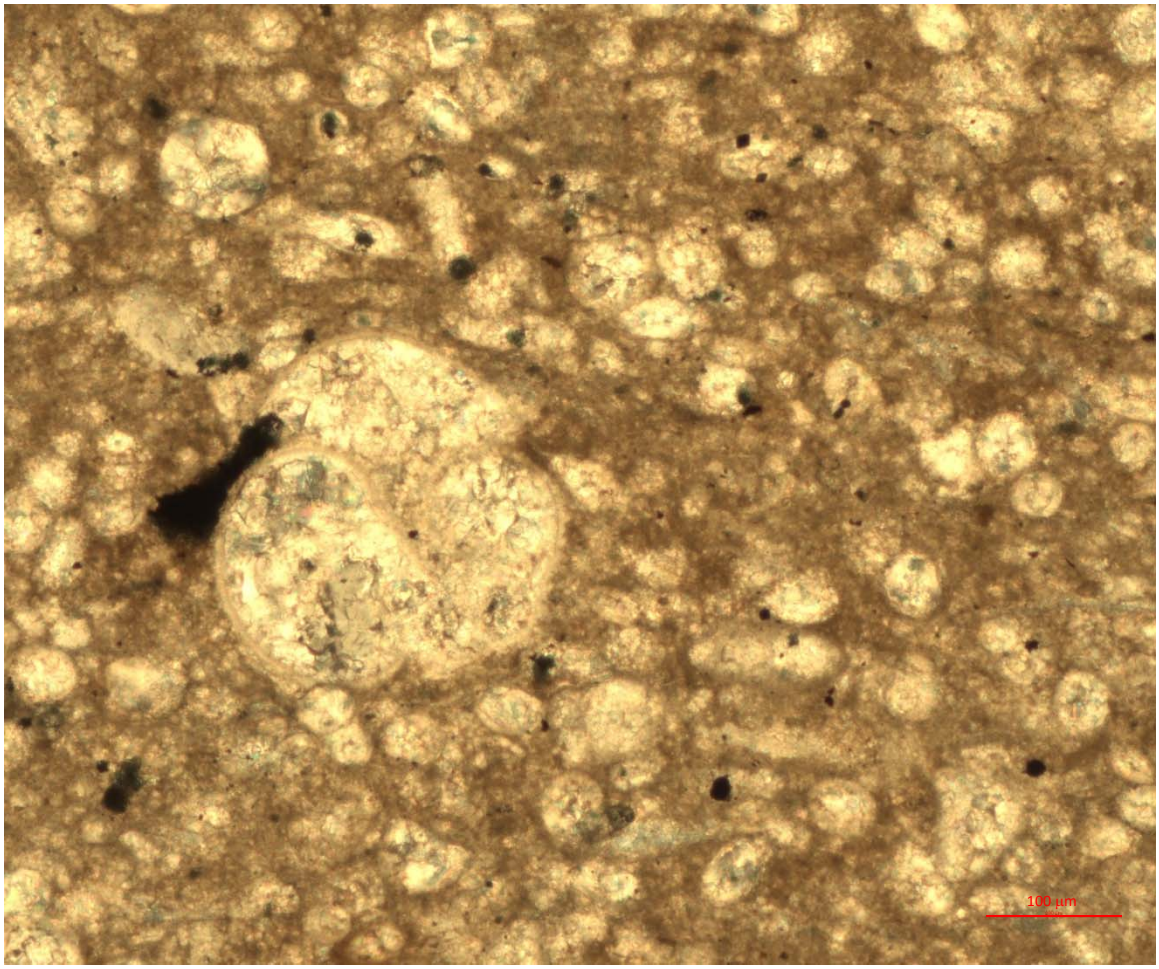

11072’11” - calcisphere packstone, with abundant calcispheres, and planktonic foraminifera; taken with cross-polarized light.

Sante North Unit A 1H

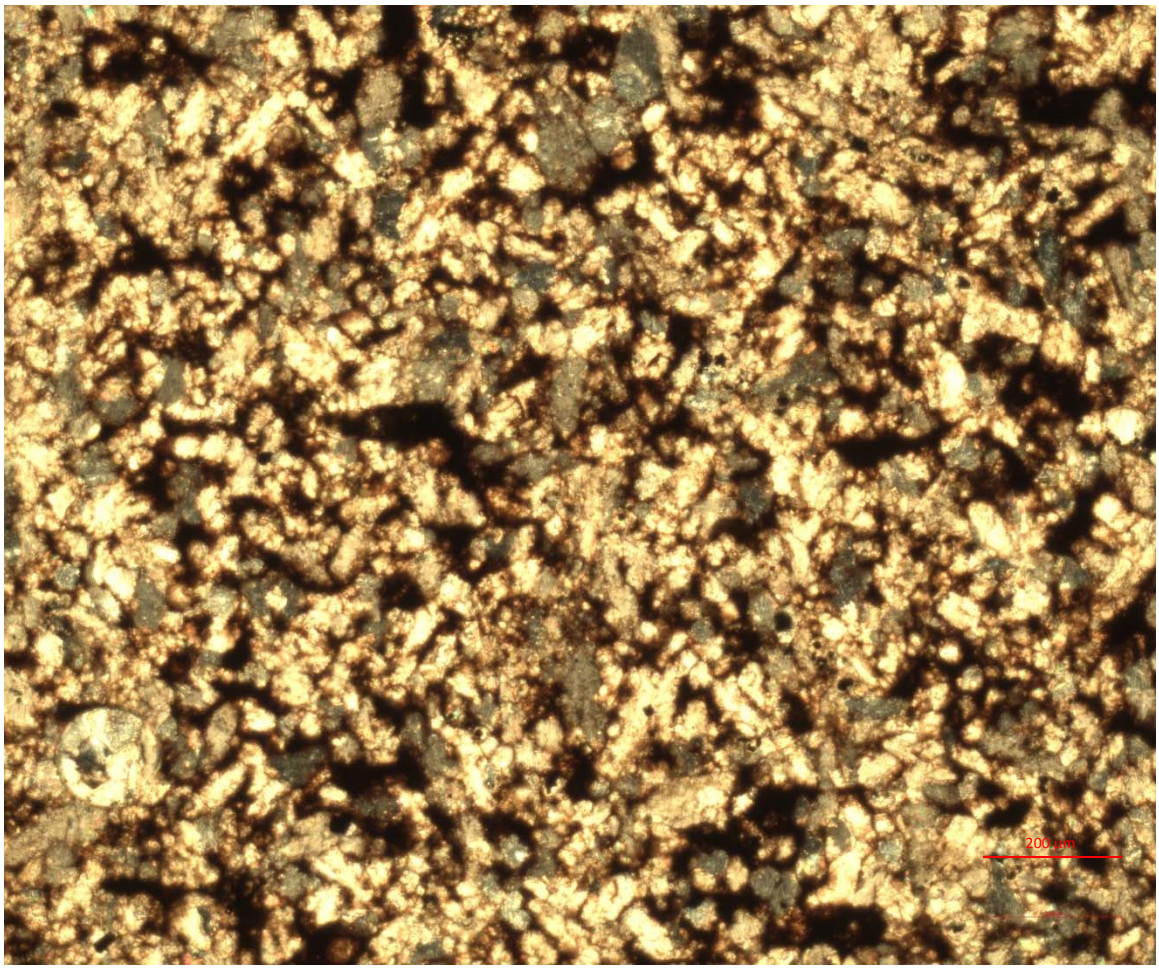

11301'5" - Recrystallized limestone with calcite filled foraminifera; taken with cross-polarized light.

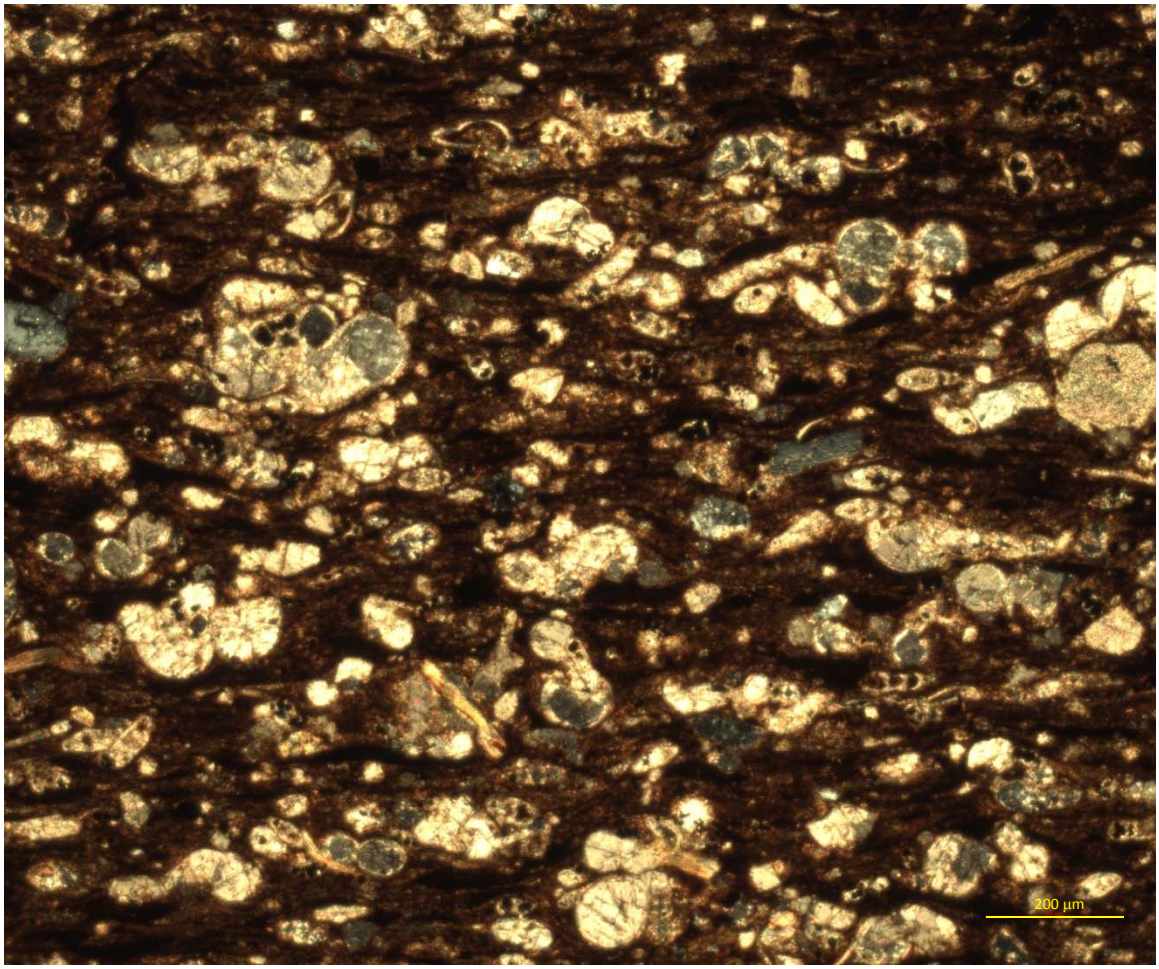

11301’5” - indistinctly laminated mudstone with calcite filled foraminifera; taken with cross-polarized light.

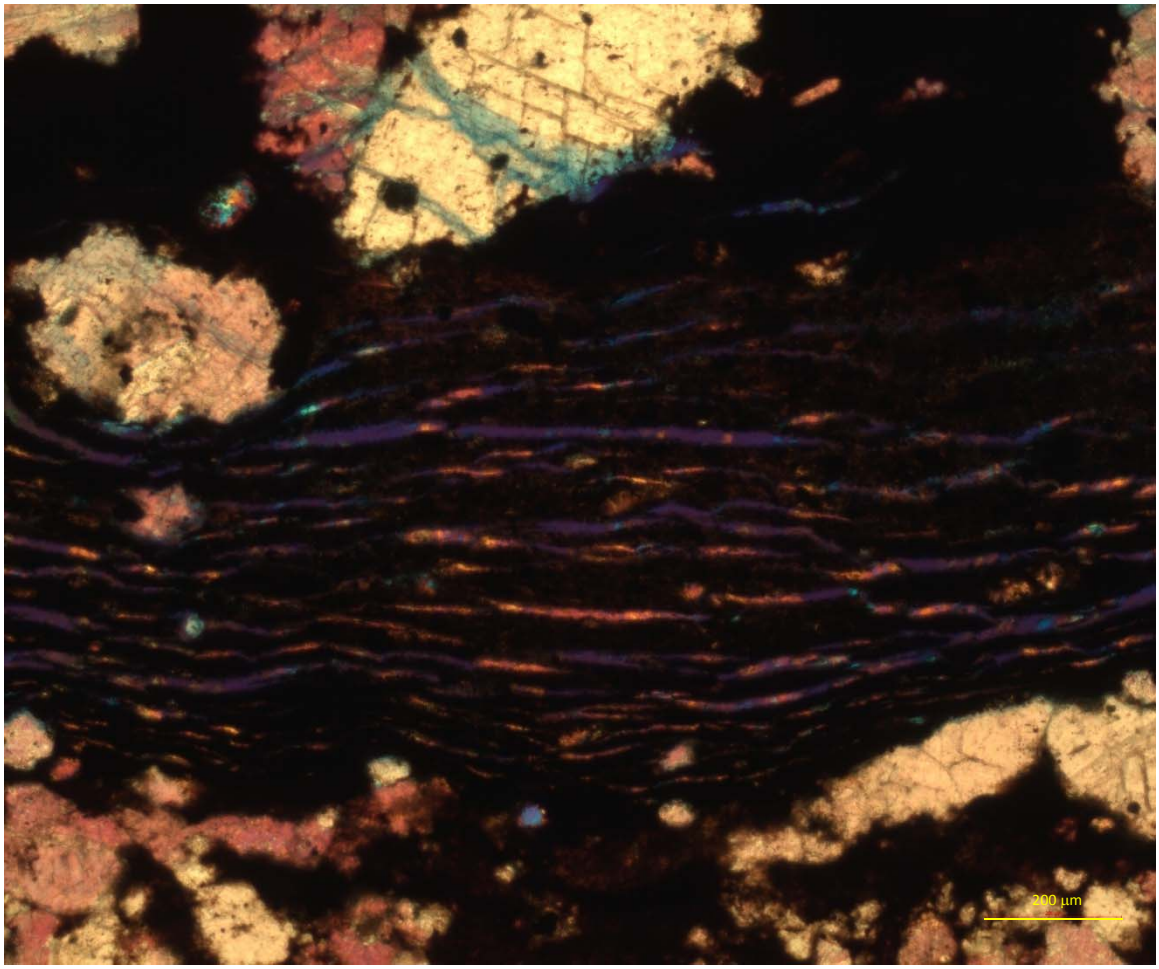

11305’9” - recrystallized limestone and ash bed; taken with quartz plate under cross-polarized light.

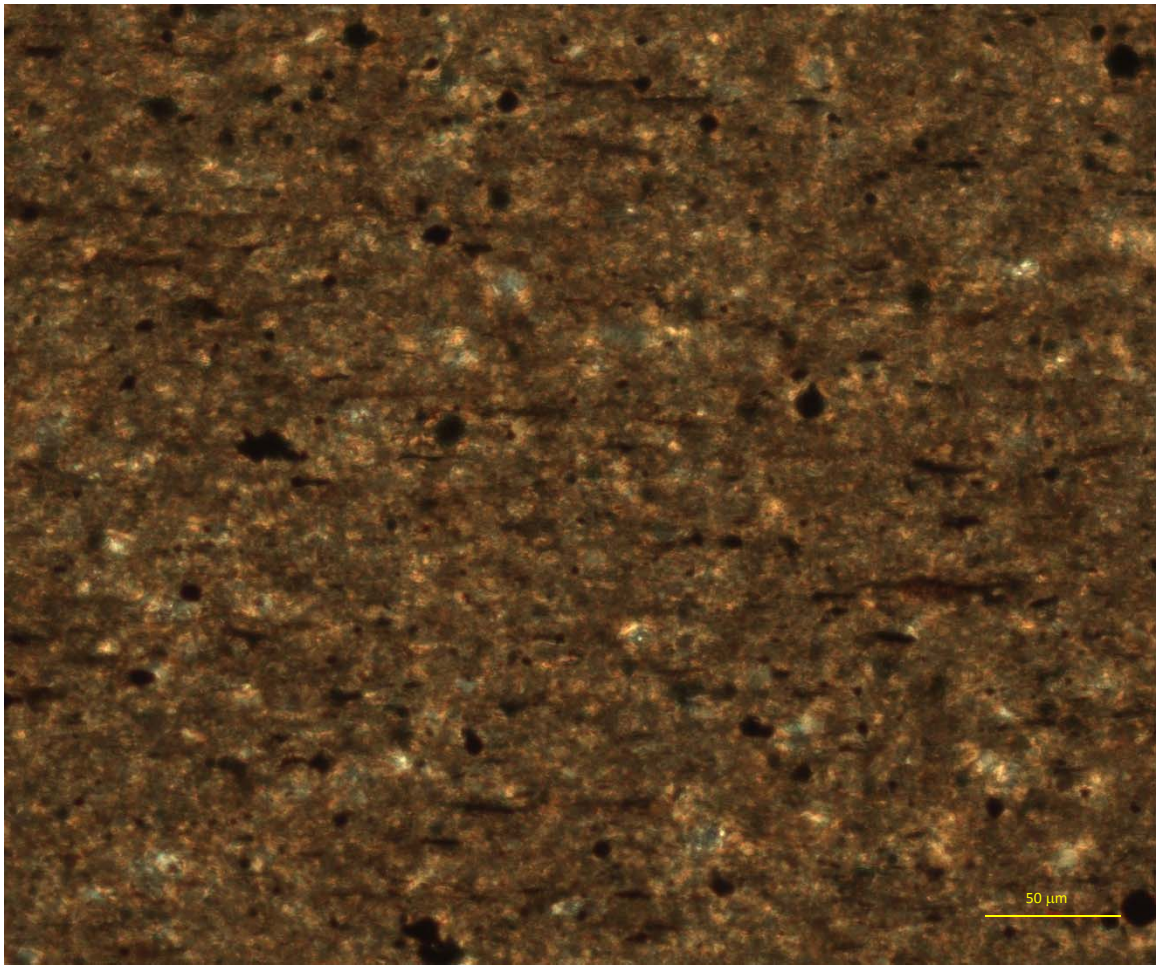

11308’5” - massive argillaceous mudstone; taken with cross-polarized light.

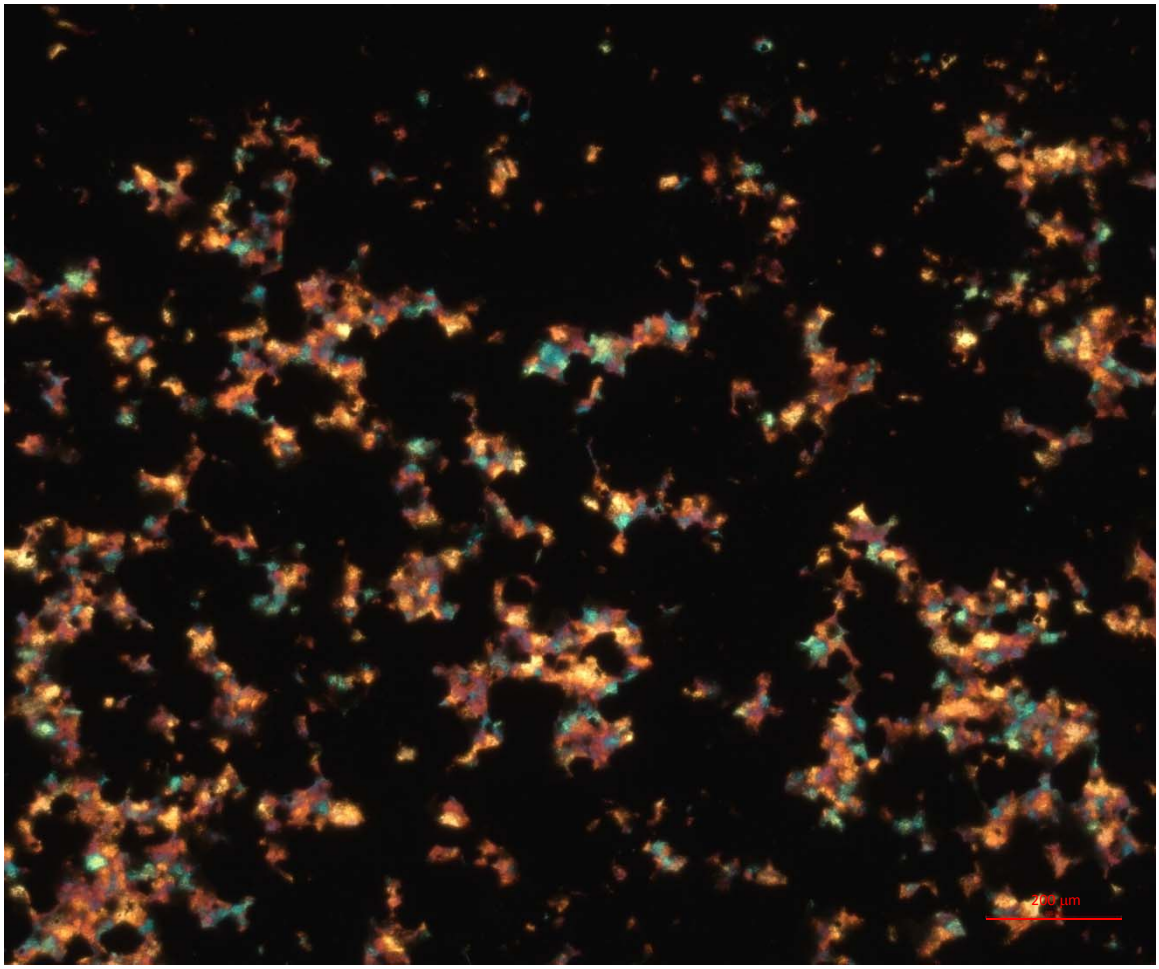

11313’3” – large (1.5 cm) pyrite nodule with calcite cement; taken with quartz plate under cross-polarized light.

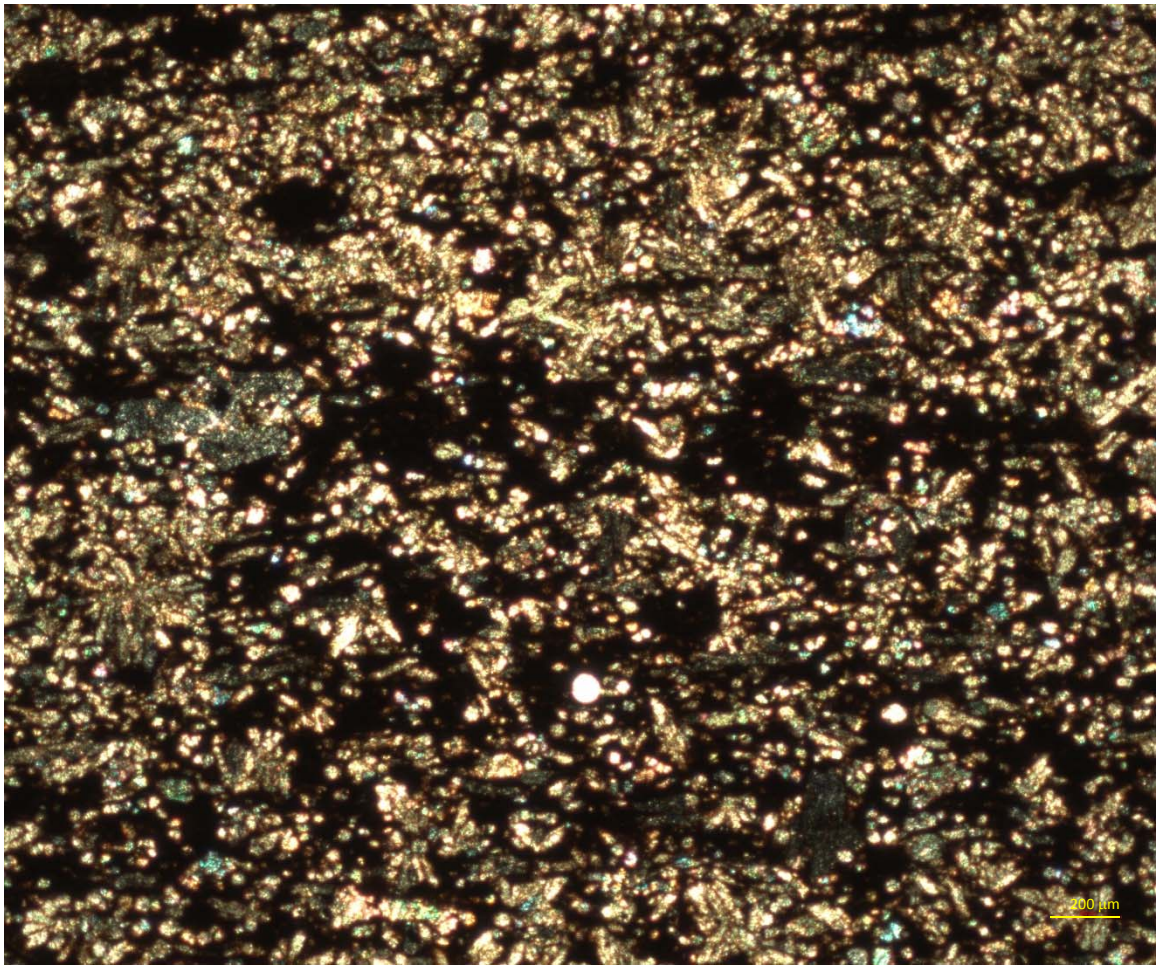

11322’0” - recrystallized laminated limestone; taken with cross-polarized light.

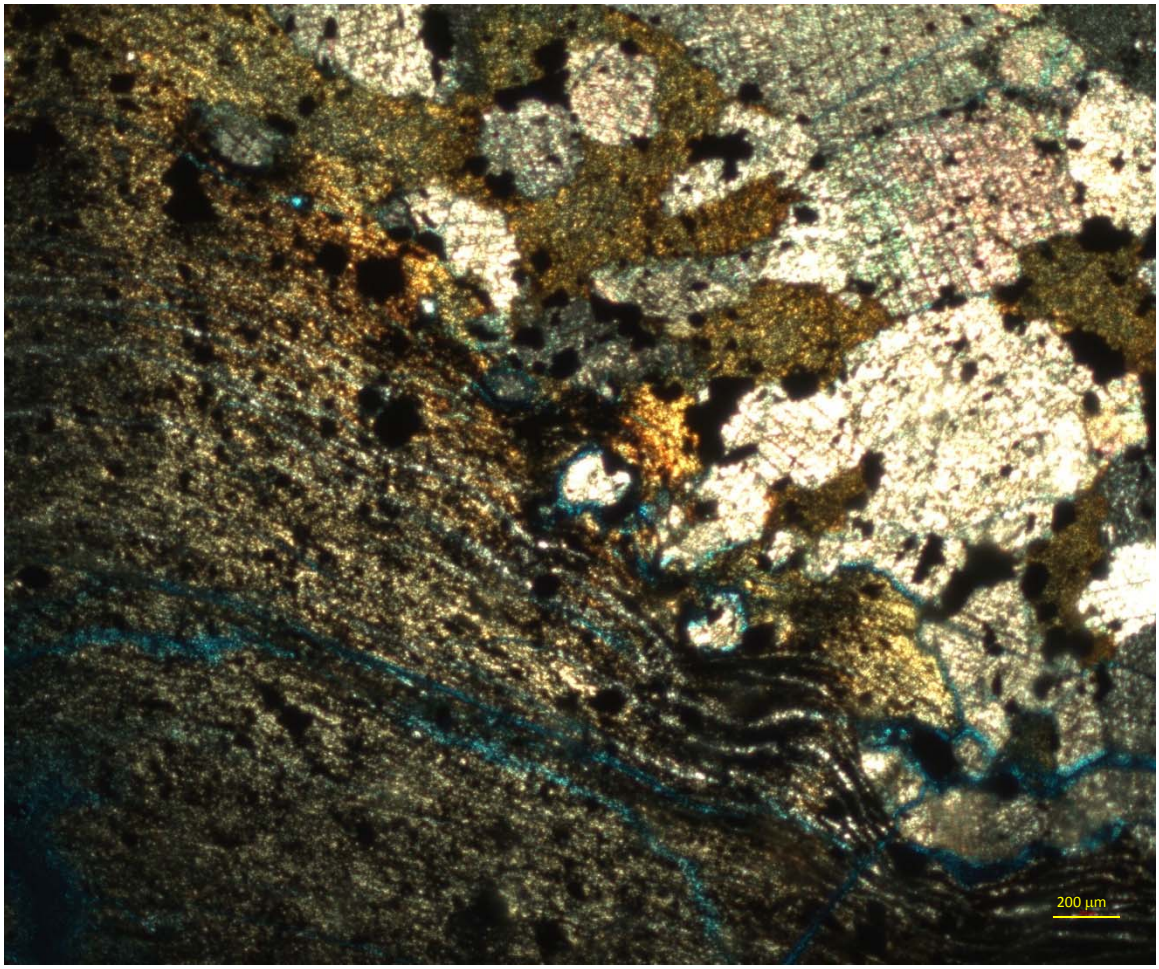

11327’6” - fibrous calcite; ash bed with pyrite; taken under cross-polarized light

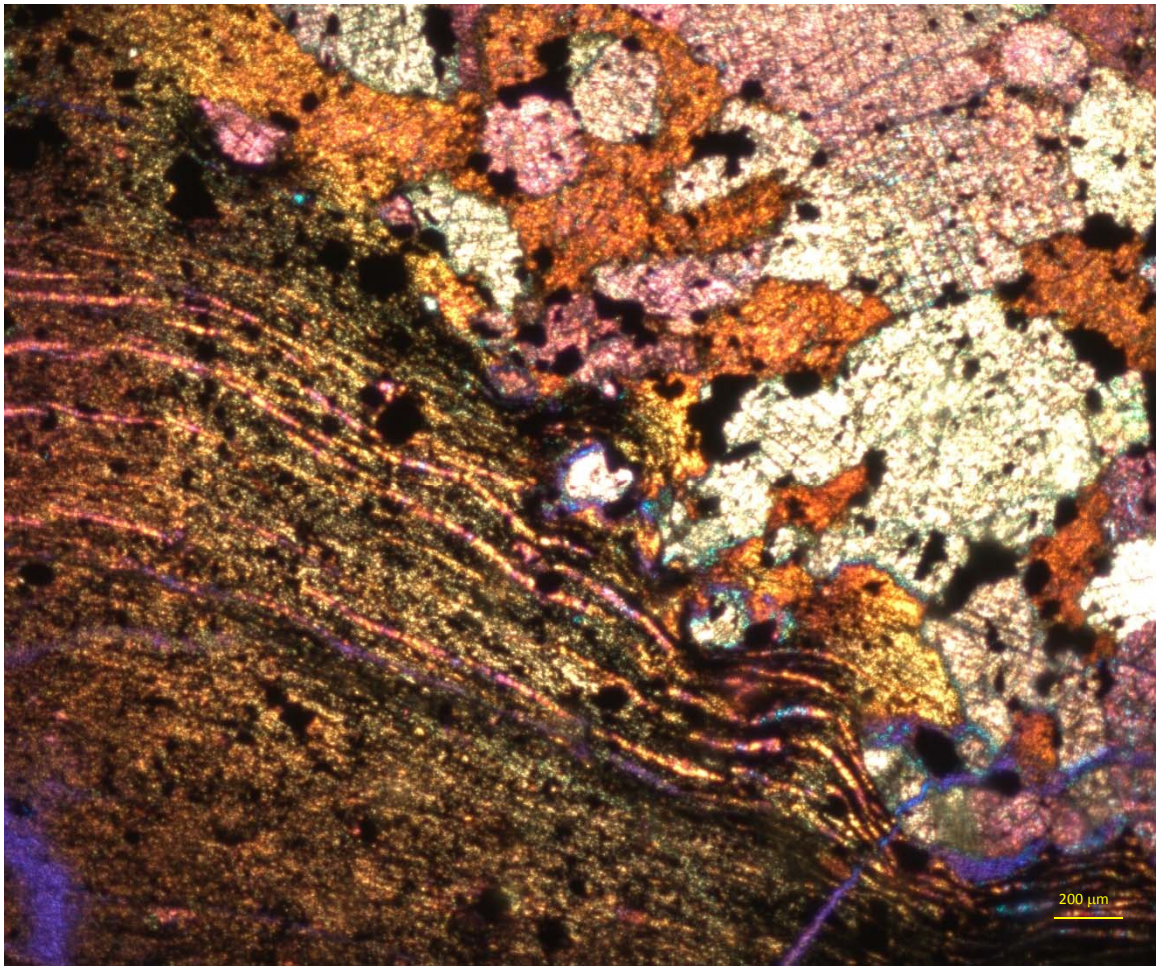

11327'6" - fibrous calcite; ash bed with pyrite; taken with quartz plate under cross-polarized light.

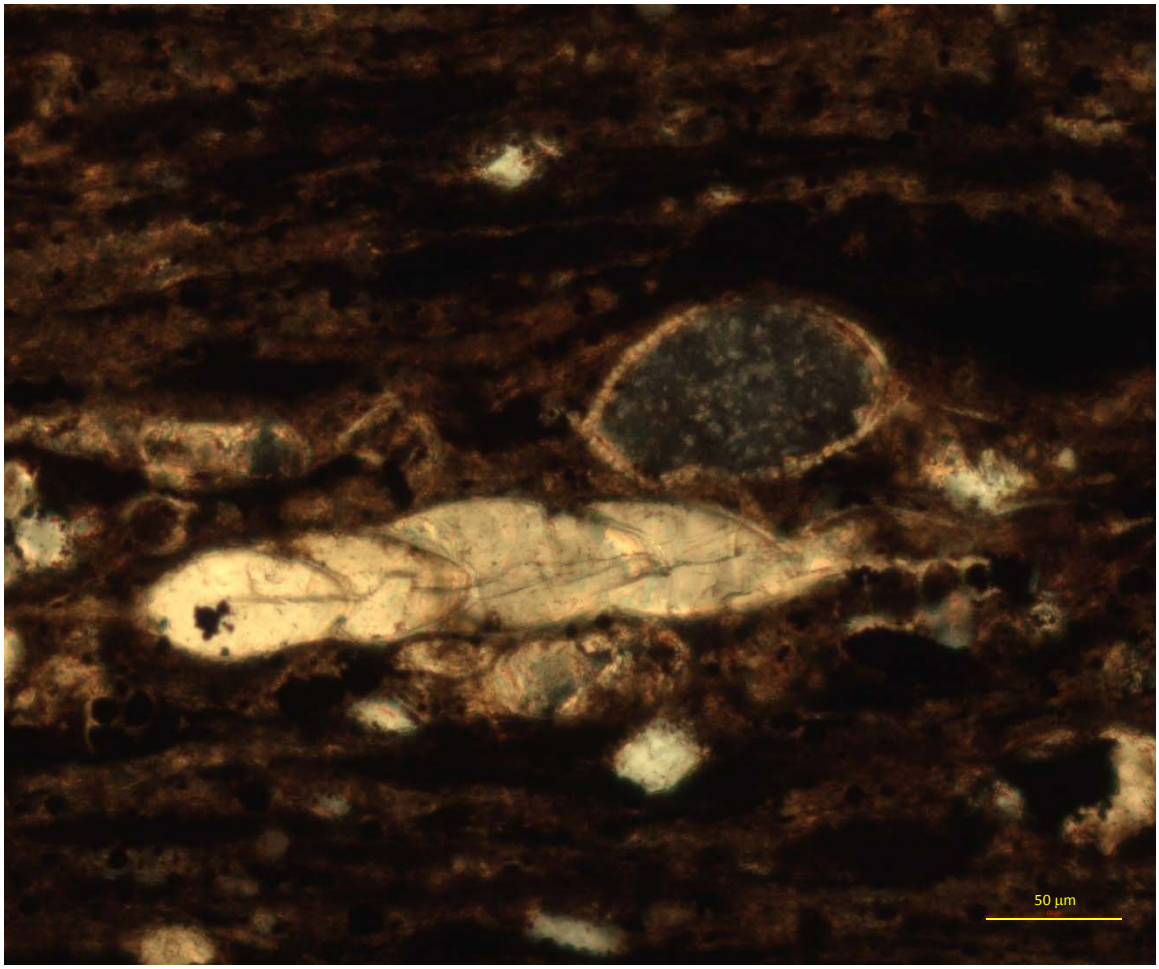

11334’9” - calcite-filled benthic foraminifera within a massive argillaceous mudstone; taken with cross-polarized light.

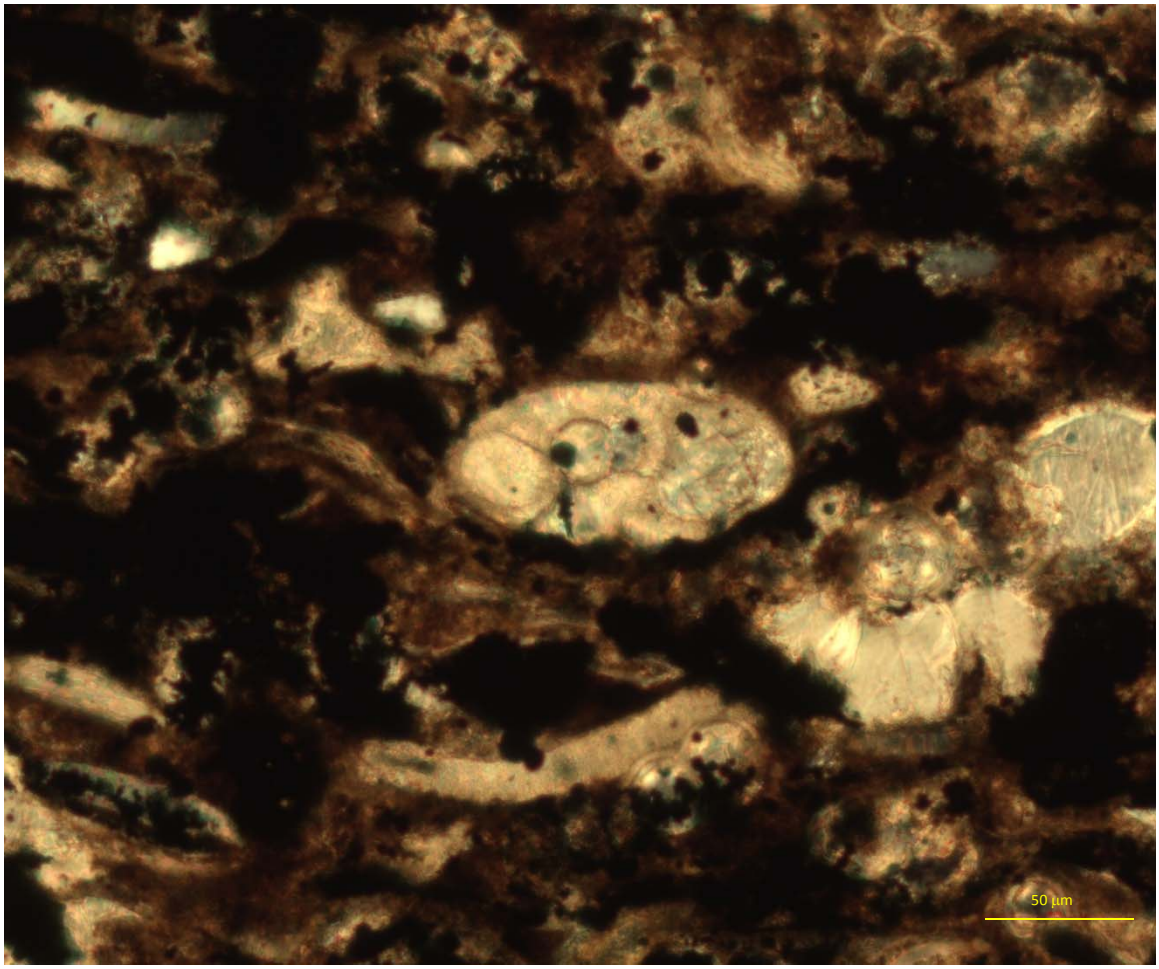

11334’9” - calcite-filled benthic foraminifera within a massive argillaceous mudstone; taken with cross-polarized light.

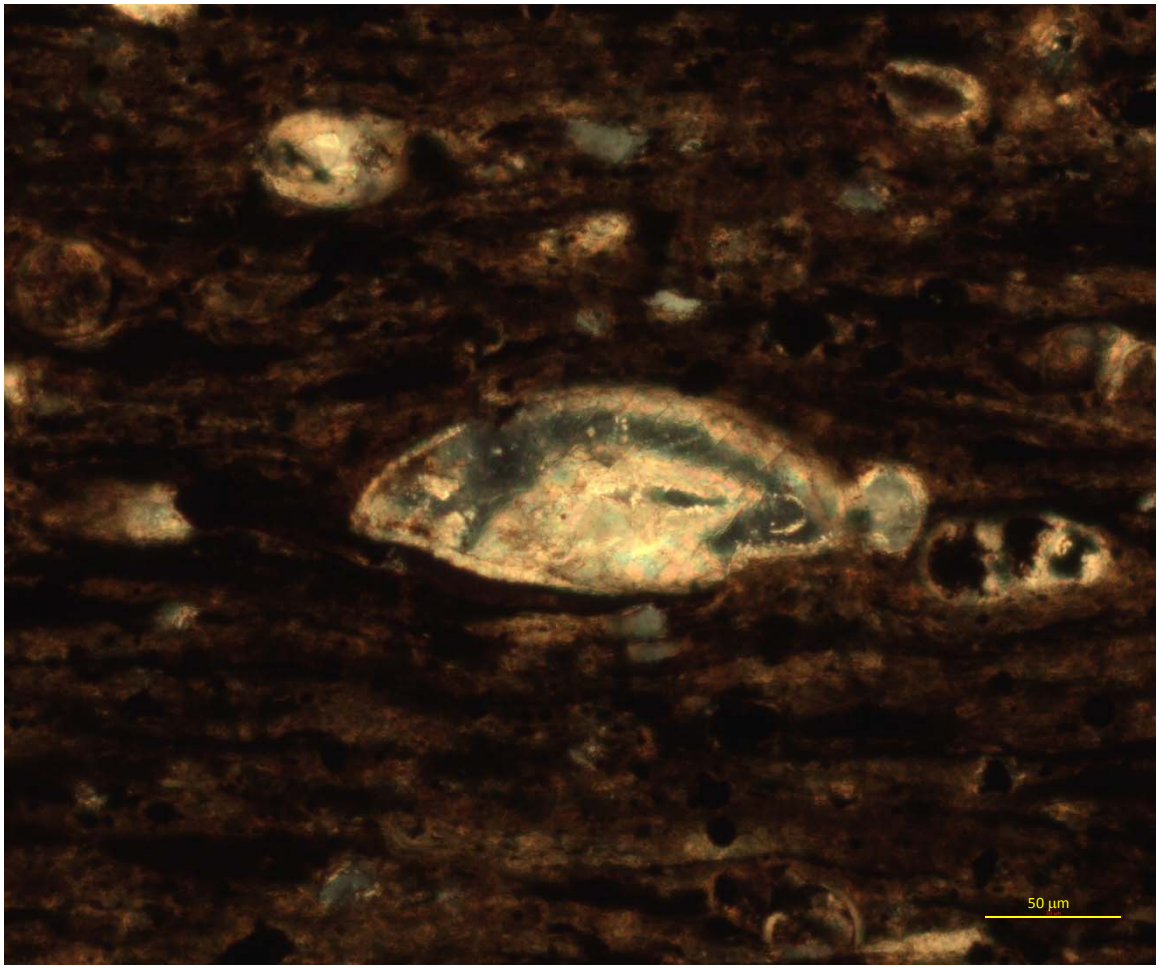

11334’9” - ostracod within a massive argillaceous mudstone; taken with cross-polarized light.

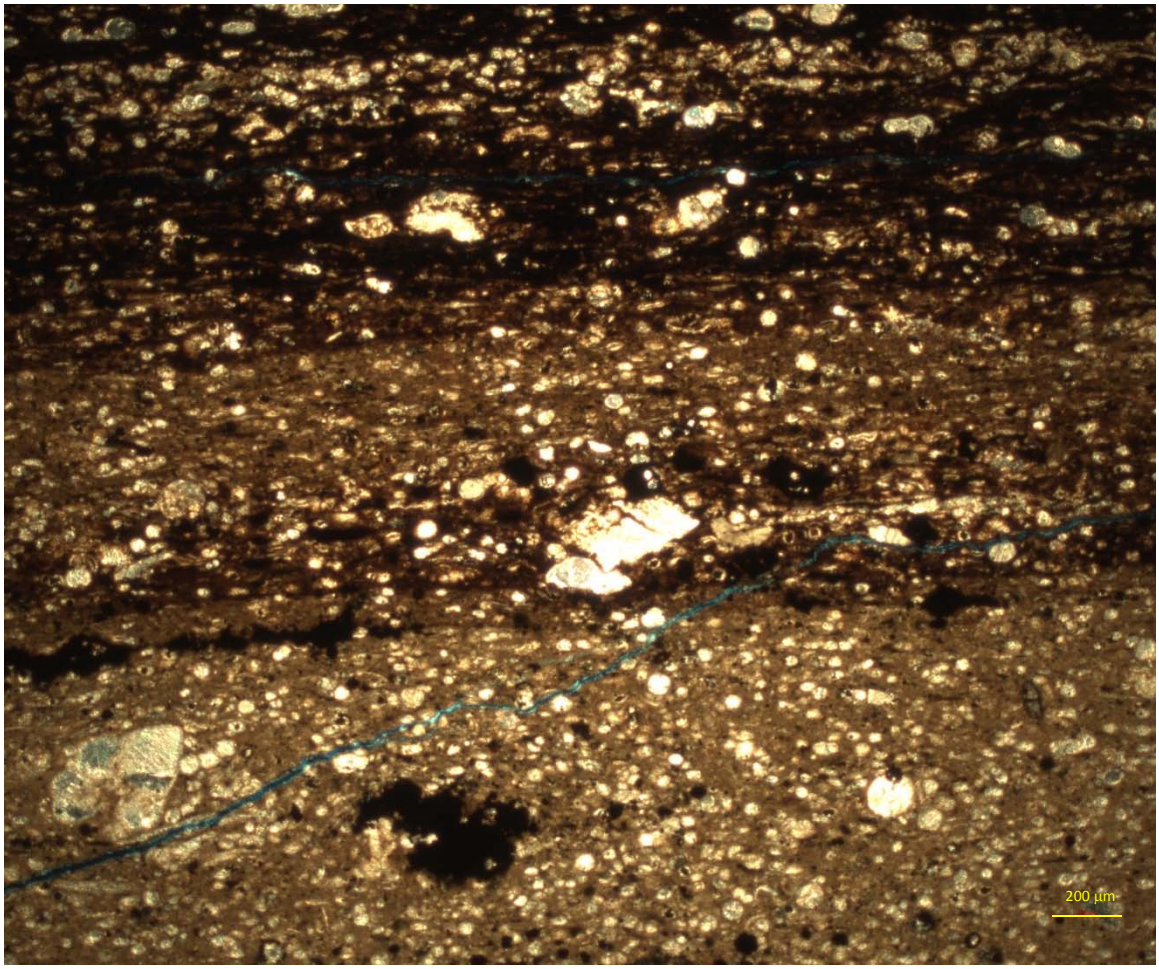

11335'1" - Maness/Buda contact with alternating calcisphere packstone and foraminifera-rich indistinctly laminated mudstone; taken with cross-polarized light.

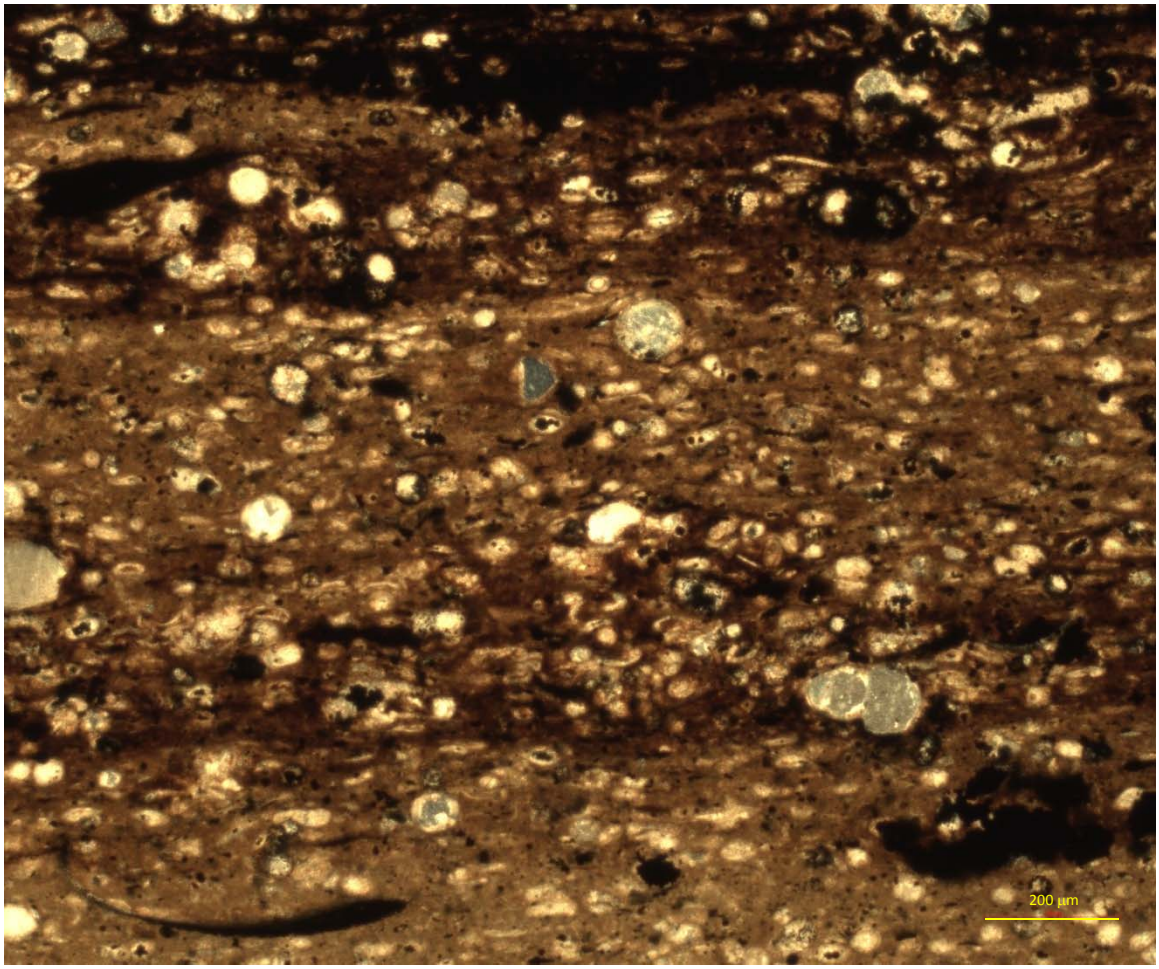

11335'1" - Maness/Buda contact with alternating calcisphere packstone and indistinctly laminated mudstone; taken with cross-polarized light.

PROST G 5H

Phase	Type	10988' 4"		11024' 7"		11042' 10"		11044' 9"		11046' 0"		11047' 11"		11060' 1"	
		LEF		*LEF*		*phos*		*phos*		*MAN*		*MAN*		*MAN*	
		Wt%	±	Wt%	±	Wt%	±	Wt%	±	Wt%	±	Wt%	±	Wt%	±
Quartz	*Silica*	13.2	0.8	11.5	0.8	12	0.7	9.2	0.6	5.2	0.3	24	1.4	21	1.2
Pyrite	*Sulfide*	2.8	0.2	3.7	0.3	6.1	0.4	4	0.3	4.6	0.3	3.5	0.2	4	0.3
Albite	*Feldspar*	3.2	0.4												
Microcline	*Feldspar*	1.9	0.3	4.3	0.5			3.2	0.3	7.5	0.5	10.2	0.7	8.4	0.6
Anorthite	*Feldspar*	17.2	1.6												
Calcite	*Carbonate*	24.2	1.4	56.8	3.6	45.8	2.7	45.3	2.8	49.6	2.9	10.9	0.7	14.4	0.9
Fluorapatite	*Phosphate*					9.3	0.6								
Illite-1M	*Clay - Mica Group*	11.7	1.1	6.2	1.1	10.1	0.9	8.5	0.9	12.1	1.2	10.3	1.2	12	1.2
Illite-2M2	*Clay - Mica Group*	24.1	1.8	13.2	1.5	12.8	1.2	25.2	2.2	6.9	1	33.5	2.5	30.7	2.2
Montmorillonite	*Clay - Smectite Group*	0.4	0.1	0.4	0.1	0.5	0.1	1.4	0.2	0.3	0.1	0.8	0.2	1.1	0.2
Kaolinite-1A	*Clay - Kaolinite Group*			0.9	0.2	3.5	0.3	3.3	0.2	9.2	0.6	6.8	0.5	8.5	0.6
Halloysite-7A	*Clay - Kaolinite Group*			2.8	0.3					4.6	0.4				
Clinochlore-1MIIb	*Clay - Chlorite Group*	1.4	0.2	0.2	0.1										

Clay Group Abundances													
	Smectite	0.4		0.4		0.5		1.4		0.3		0.8		1.1	
	Chlorite	1.4		0.2		0		0		0		0		0	
	Illite+Mica	35.8		19.4		22.9		33.7		19		43.8		42.7	
	Kaolinite	0		3.7		3.5		3.3		13.8		6.8		8.5	
	Total Clays	**37.6**		**23.7**		**26.9**		**38.4**		**33.1**		**51.4**		**52.3**	

Relative Clay Proportions													
	Smectite	1.1%		1.7%		1.9%		3.6%		0.9%		1.6%		2.1%	
	Chlorite	3.7%		0.8%		0.0%		0.0%		0.0%		0.0%		0.0%	
	Illite+Mica	95.2%		81.9%		85.1%		87.8%		57.4%		85.2%		81.6%	
	Kaolinite	0.0%		15.6%		13.0%		8.6%		41.7%		13.2%		16.3%	

PROST G 5H

Phase	Type	11063' 8"		11065' 5"		11066' 10"		11068' 7"		11071' 8"		11072' 1"		11072' 9"	
		MAN		*MAN*		*MAN*		*MAN*		*MAN*		*Buda*		*Buda*	
		Wt%	**±**	**Wt%**	**±**	**Wt%**	**±**	**Wt%**	**±**	**Wt%**	**±**	**Wt%**	**±**	**Wt%**	**±**
Quartz	*Silica*	22.4	1.3	23.8	1.4	13.8	0.8	0.8	0.1	19.9	1.2	1.7	0.1	1.3	0.1
Pyrite	*Sulfide*	4.2	0.3	4.5	0.3	2.5	0.2	2.8	0.2	5.7	0.4	0.6	0.1	0.3	0.1
Albite	*Feldspar*					3.2	0.4								
Microcline	*Feldspar*	4.4	0.3	7	0.5					6.1	0.4				
Anorthite	*Feldspar*														
Calcite	*Carbonate*	23.6	1.4	18.1	1.1	40.7	2.5	94	7	30.8	1.8	97.7	6.9	98.4	6.9
Fluorapatite	*Phosphate*					0.7	0.1								
Illite-1M	*Clay - Mica Group*	15.8	1.3	13.7	1.3	8.2	0.9			10.1	1				
Illite-2M2	*Clay - Mica Group*	22.2	1.7	25.1	1.6	25.6	2.1	0.1	0	21	1.7				
Montmorillonite	*Clay - Smectite Group*	1	0.2	1.7	0.2	0.6	0.1			0.7	0.2				
Kaolinite-1A	*Clay - Kaolinite Group*	6.3	0.4	6.2	0.4	3.7	0.3	1.7	0.2	5.8	0.4				
Halloysite-7A	*Clay - Kaolinite Group*					1	0.1	0.7	0.2						
Clinochlore-1MIIb	*Clay - Chlorite Group*														

Clay Group Abundances						
	Smectite	1	1.7	0.6	0	0.7
	Chlorite	0	0	0	0	0
	Illite+Mica	38	38.8	33.8	0.1	31.1
	Kaolinite	6.3	6.2	4.7	2.4	5.8
	Total Clays	**45.3**	**46.7**	**39.1**	**2.5**	**37.6**

Relative Clay Proportions						
	Smectite	2.2%	3.6%	1.5%	0.0%	1.9%
	Chlorite	0.0%	0.0%	0.0%	0.0%	0.0%
	Illite+Mica	83.9%	83.1%	86.4%	4.0%	82.7%
	Kaolinite	13.9%	13.3%	12.0%	96.0%	15.4%

Continued...

SANTE NORTH UNIT A 1H

Phase	Type	11257' 0"		11289' 6"		11300' 9"		11301' 5"		11305' 9"		11308' 8"		11313' 3"	
		LEF		*LEF*		*LEF*		*LEF*		*phos*		*MAN*		*MAN*	
		Wt%	**±**	**Wt%**	**±**	**Wt%**	**±**	**Wt%**	**±**	**Wt%**	**±**	**Wt%**	**±**	**Wt%**	**±**
Quartz	*Silica*	17.3	1	27.1	1.6	5.5	0.4	6	0.4	14.6	0.9	22.6	1.3	20.8	1.3
Pyrite	*Sulfide*	2.2	0.2	2.6	0.2	2.7	0.3	2.8	0.2	3.8	0.3	2.7	0.2	3.3	0.2
Albite	*Feldspar*			0.8	0.2			0.2	0.1						
Microcline	*Feldspar*	5.5	0.4	5.8	0.5			2.8	0.3			9.1	0.7	2.6	0.5
Anorthite	*Feldspar*													10.6	1.7
Calcite	*Carbonate*	21.2	1.2	14.9	0.9	31.6	2.1	33.3	1.9	55.2	3.3	8.2	0.6	4.6	0.5
Ankerite	*Carbonate*	3.4	0.4			3.2	2.3	7.9	1						
Kutnohorite, Magnesian	*Carbonate*					41.2	3.1	29.3	1.9						
Fluorapatite	*Phosphate*					3.6	0.3								
Illite-1M	*Clay - Mica Group*	17.4	1.4	13.6	1.3	1.9	0.8	10.4	0.9	10.4	0.9	13.8	1.4	11.8	1.3
Illite-2M2	*Clay - Mica Group*	25	1.9	29.6	2.2	6.6	1.3	3.1	0.6	10.9	1.1	33	2.5	36.6	2.2
Montmorillonite	*Clay - Smectite Group*	0.8	0.2	1.1	0.2	2.4	0.5	0.4	0.1	0.4	0.1	1.2	0.2	0.6	0.1
Kaolinite-1A	*Clay - Kaolinite Group*	7.3	0.5	4.4	0.3	1.3	0.2	3.8	0.3	4.7	0.4	9.5	0.6	9	0.6

Clay Group Abundances							
Smectite	0.8	1.1	2.4	0.4	0.4	1.2	0.6
Chlorite	0	0	0	0	0	0	0
Illite+Mica	42.4	43.2	8.5	13.5	21.3	46.8	48.4
Kaolinite	7.3	4.4	1.3	3.8	4.7	9.5	9
Total Clays	**50.5**	**48.7**	**12.2**	**17.7**	**26.4**	**57.5**	**58**

Relative Clay Proportions							
Smectite	1.6%	2.3%	19.7%	2.3%	1.5%	2.1%	1.0%
Chlorite	0.0%	0.0%	0.0%	0.0%	0.0%	0.0%	0.0%
Illite+Mica	84.0%	88.7%	69.7%	76.3%	80.7%	81.4%	83.4%
Kaolinite	14.5%	9.0%	10.7%	21.5%	17.8%	16.5%	15.5%

SANTE NORTH UNIT A 1H

Phase	Type	11322' 0"		11327' 6"		11329' 0"		11329' 6"		11334' 9"		11335' 1"	
		MAN		*MAN*		*MAN*		*MAN*		*MAN*		*MAN/BUDA*	
		Wt%	**±**	**Wt%**	**±**	**Wt%**	**±**	**Wt%**	**±**	**Wt%**	**±**	**Wt%**	**±**
Quartz	*Silica*	11.9	0.7	10.6	0.6	20.6	1.2	20.9	1.2	12.4	0.8	9.5	0.6
Pyrite	*Sulfide*	7.5	0.5	5.3	0.3	3.7	0.2	3.8	0.3	2.7	0.2	2.1	0.2
Albite	*Feldspar*												
Microcline	*Feldspar*	4.8	0.4	6.2	0.5	8.9	0.6	9.5	0.7	1.8	0.2		
Anorthite	*Feldspar*												
Calcite	*Carbonate*	16	1	32.6	1.9	9	0.6	10.2	0.7	33	2.1	73.1	4.6
Ankerite	*Carbonate*	7.7	0.6	1.9	0.2								
Kutnohorite, Magnesian	*Carbonate*												
Fluorapatite	*Phosphate*												
Illite-1M	*Clay - Mica Group*	22.3	1.8	8.9	1	8.1	1	12.2	1.3	10.6	1.1	5.5	0.6
Illite-2M2	*Clay - Mica Group*	10.4	1.4	17.6	1.5	37.3	2.8	31.9	2.4	34.1	2.8	5.7	0.7
Montmorillonite	*Clay - Smectite Group*	2.1	0.3	0.1	0.1	0.8	0.2	0.5	0.2	1.5	0.2	0.5	0.1
Kaolinite-1A	*Clay - Kaolinite Group*	17.2	1	16.8	1	11.6	0.7	10.9	0.7	3.9	0.3	3.5	0.3

Clay Group Abundances						
Smectite	2.1	0.1	0.8	0.5	1.5	0.5
Chlorite	0	0	0	0	0	0
Illite+Mica	32.7	26.5	45.4	44.1	44.7	11.2
Kaolinite	17.2	16.8	11.6	10.9	3.9	3.5
Total Clays	**52**	**43.4**	**57.8**	**55.5**	**50.1**	**15.2**

Relative Clay Proportions						
Smectite	4.0%	0.2%	1.4%	0.9%	3.0%	3.3%
Chlorite	0.0%	0.0%	0.0%	0.0%	0.0%	0.0%
Illite+Mica	62.9%	61.1%	78.5%	79.5%	89.2%	73.7%
Kaolinite	33.1%	38.7%	20.1%	19.6%	7.8%	23.0%

Continued...

APPENDIX E – Geomechanical Data

Prost G 5H

Sample Number	FM	Depth (Ft, in)	Dimpler Diameter (Tick Marks)	Average Dimple (Divisions)	Average Dimple (in)	DIMPLE UCS (psi)	Bambino Average L' (5 Samples)	UCS - Enderlin (psi)	UCS - Aoki and Matsukura 2008 (psi)	UCS - Zahm et al 2014 - (psi)	Length of Core Piece (in)
1	AUSTIN CHALK	10946'	5,5,5	5.0	0.025000	8,985	665	16,041	13,232	15,208	2 12/16 in
2		10946'9"	7,7,7	7.0	0.035000	4,121	584	11,474	9,563	10,435	5 in
3		10947'	8,7,10	8.3	0.041667	2,978	401	3,776	3,736	3,508	5 3/16 in
4		10947'4"	5,5,5	5.0	0.025000	8,985	662	15,863	13,083	15,010	5 3/16 in
5		10948'	5,5,5	5.0	0.025000	8,985	663	15,922	13,133	15,076	2 15/16 in
6		10948'2"	5,4,4	4.3	0.021667	15,416	656	15,508	12,789	14,619	2 15/16 in
7		10949'	5,5,5	5.0	0.025000	8,985	661	15,804	13,034	14,945	5 in
8		10949'9"	5,5,5	5.0	0.025000	8,985	611	12,935	10,707	11,897	3 14/16 in
9		10950'	,,								11/16 in
10		10950'8"	7,6,8	7.0	0.035000	4,121	461	5,827	5,294	5,256	1 4/16 in
11		10951'	5,5,5	5.0	0.025000	8,985	649	15,098	12,450	14,171	1 13/16 in
12		10951'1"	6,4,5	5.0	0.025000	8,985	659	15,685	12,936	14,814	5 4/16 in
13		10951'4"	5,5,4	4.7	0.023333	11,725	656	15,508	12,789	14,619	5 4/16 in
14		10951'10"	4,4,4	4.0	0.020000	20,091	636	14,345	11,836	13,364	3 in
15		10953'	5,5,5	5.0	0.025000	8,985	647	14,981	12,355	14,045	3 11/16 in
16		10954'	5,5,4	4.7	0.023333	11,725	667	16,160	13,332	15,341	3 2/16 in
17		10954'1"	6,4,6	5.3	0.026667	7,125	480	6,578	5,857	5,909	1 4/16 in
18		10955'	5,4,5	4.7	0.023333	11,725	647	14,981	12,355	14,045	4 14/16 in
19		10955'6"	5,5,5	5.0	0.025000	8,985	639	14,518	11,976	13,547	3 10/16 in
20		10956'	4,4,4	4.0	0.020000	20,091	625	13,718	11,331	12,704	5 8/16 in
21		10957'	4,5,4	4.3	0.021667	15,416	640	14,575	12,023	13,609	1 11/16 in
22		10957'1"	4,4,4	4.0	0.020000	20,091	643	14,749	12,165	13,795	4 8/16 in
23		10957'6"	5,5,5	5.0	0.025000	8,985	642	14,691	12,117	13,733	5 6/16 in
24		10958'	4,5,5	4.7	0.023333	11,725	584	11,474	9,563	10,435	5 9/16 in
25		10958'6"	5,6,6	5.7	0.028333	6,111	582	11,368	9,482	10,332	3 13/16 in
26		10959'	5,5,5	5.0	0.025000	8,985	649	15,098	12,450	14,171	5 8/16 in
27		10960'	6,6,5	5.7	0.028333	6,111	591	11,846	9,852	10,802	5 6/16 in
28		10961'	5,5,6	5.3	0.026667	7,125	618	13,324	11,016	12,296	3 13/16 in
29		10962'	6,5,5	5.3	0.026667	7,125	589	11,739	9,769	10,696	2 8/16 in
30		10962'3"	5,5,5	5.0	0.025000	8,985	575	11,002	9,199	9,976	4 10/16 in
31		10963'	4,5,6	5.0	0.025000	8,985	665	16,041	13,232	15,208	4 3/16 in
32		10963'1"	5,5,5	5.0	0.025000	8,985	666	16,101	13,282	15,275	5 in
33		10963'4"	6,7,6	6.3	0.031667	4,966	527	8,634	7,398	7,747	5 in
34		10964'	4,5,4	4.3	0.021667	15,416	662	15,863	13,083	15,010	3 7/16 in
35		10964'6"	4,5,5	4.7	0.023333	11,725	637	14,402	11,883	13,425	5 12/16 in
36		10965'	5,4,5	4.7	0.023333	11,725	656	15,508	12,789	14,619	2 4/16 in
37		10966'	5,5,5	5.0	0.025000	8,985	664	15,982	13,182	15,142	3 1/16 in
38		10966'1"	5,4,5	4.7	0.023333	11,725	680	16,940	13,991	16,225	4 4/16 in
39		10966'6"	4,3,4	3.7	0.018333	25,748	679	16,880	13,939	16,156	2 10/16 in
40		10967'	6,6,5	5.7	0.028333	6,111	540	9,250	7,862	8,315	6 in
41		10967'6"	4,5,5	4.7	0.023333	11,725	615	13,157	10,883	12,124	2 9/16 in
42		10968'	4,4,4	4.0	0.020000	20,091	674	16,579	13,684	15,813	2 3/16 in
43	EAGLE FORD	10969'	5,5,5	5.0	0.025000	8,985	527	8,634	7,398	7,747	3 7/16 in
44		10969'1"	9,8,9	8.7	0.043333	2,768	365	2,783	2,953	2,670	4 4/16 in
45		10970'	9,8,9	8.7	0.043333	2,768	406	3,928	3,854	3,636	3 7/16 in
46		10971'	10,8,8	8.7	0.043333	2,768	445	5,232	4,847	4,744	1 4/16 in
47		10971'2"	5,5,5	5.0	0.025000	8,985	693	17,730	14,669	17,141	2 7/16 in
48		10972'	8,9,7	8.0	0.040000	3,213	386	3,340	3,397	3,141	1 in
49		10972'1"	8,8,8	8.0	0.040000	3,213	388	3,397	3,441	3,188	1 in
50		10973'	8,9,9	8.7	0.043333	2,768	430	4,706	4,449	4,295	3 13/16 in

Continued…

Prost G 5H												
Sample Number	FM	Depth (Ft, in)	Dimpler Diameter (Tick Marks)	Average Dimple (Divisions)	Average Dimple (in)	DIMPLE UCS (psi)		Bambino Average L' (5 Samples)	UCS - Enderlin (psi)	UCS - Aoki and Matsukura 2008 (psi)	UCS - Zahm et al 2014 - (psi)	Length of Core Piece (in)
51	EAGLE FORD	10973'7"	5,4,5	4.7	0.023333	11,725		687	17,365	14,354	16,714	5 1/16 in
52		10974'	7,8,8	7.7	0.038333	3,478		352	2,468	2,697	2,404	1 2/16 in
53		10975'	7,7,7	7.0	0.035000	4,121		452	5,488	5,040	4,964	2 12/16 in
54		10975'1"	6,6,7	6.3	0.031667	4,966		427	4,604	4,372	4,209	2 14/16 in
55		10976'	7,7,8	7.3	0.036667	3,779		395	3,598	3,598	3,358	4 8/16 in
56		10977'	8,7,7	7.3	0.036667	3,779		433	4,809	4,527	4,382	2 7/16 in
57		10977'8"	7,7,7	7.0	0.035000	4,121		406	3,928	3,854	3,636	2 13/16 in
58		10978'	7,7,8	7.3	0.036667	3,779		401	3,776	3,736	3,508	12/16 in
59		10978'7"	7,7,8	7.3	0.036667	3,779		398	3,686	3,667	3,432	4 13/16 in
60		10979'	7,7,8	7.3	0.036667	3,779		436	4,913	4,606	4,471	3 10/16 in
61		10979'6"	8,7,7	7.3	0.036667	3,779		425	4,537	4,321	4,152	4 8/16 in
62		10980'	6,7,7	6.7	0.033333	4,514		408	3,990	3,901	3,688	3 11/16 in
63		10981'	7,7,7	7.0	0.035000	4,121		407	3,959	3,878	3,662	2 15/16 in
64		10981'1"	7,7,8	7.3	0.036667	3,779		438	4,983	4,659	4,531	4 8/16 in
65		10982'	5,6,6	5.7	0.028333	6,111		519	8,265	7,120	7,411	6 8/16 in
66		10983'	7,6,8	7.0	0.035000	4,121		377	3,094	3,202	2,933	5 11/16 in
67		10985'	7,8,7	7.3	0.036667	3,779		372	2,962	3,097	2,821	4 11/16 in
68		10986'	7,7,7	7.0	0.035000	4,121		393	3,540	3,553	3,309	5 2/16 in
69		10987'	7,8,8	7.7	0.038333	3,478		381	3,202	3,288	3,024	2 12/16 in
70		10987'1"	8,8,8	8.0	0.040000	3,213		360	2,659	2,853	2,566	4 15/16 in
71		10988'	8,7,7	7.3	0.036667	3,779		365	2,783	2,953	2,670	3 4/16 in
72		10989'	8,7,7	7.3	0.036667	3,779		331	2,008	2,313	2,011	2 12/16 in
73		10990'	7,7,7	7.0	0.035000	4,121		372	2,962	3,097	2,821	3 14/16 in
74		10990'2"	8,7,7	7.3	0.036667	3,779		389	3,425	3,463	3,212	3 14/16 in
75		10990'8"	5,5,5	5.0	0.025000	8,985		616	13,213	10,928	12,181	3 2/16 in
76		10991'	7,7,7	7.0	0.035000	4,121		389	3,425	3,463	3,212	3 in
77		10991'6"	7,7,6	6.7	0.033333	4,514		377	3,094	3,202	2,933	4 10/16 in
78		10992'	7,8,8	7.7	0.038333	3,478		362	2,708	2,893	2,607	1 9/16 in
79		10993'	7,7,8	7.3	0.036667	3,779		386	3,340	3,397	3,141	3 1/16 in
80		10993'3"	7,8,8	7.7	0.038333	3,478		349	2,399	2,640	2,345	3 3/16 in
81		10993'9"	5,6,5	5.3	0.026667	7,125		582	11,368	9,482	10,332	3 12/16 in
82		10994'	6,7,6	6.3	0.031667	4,966		398	3,686	3,667	3,432	4 14/16 in
83		10994'6"	6,6,5	5.7	0.028333	6,111		455	5,600	5,124	5,060	2 10/16 in
84		10995'	7,7,7	7.0	0.035000	4,121		426	4,571	4,346	4,180	5 13/16 in
85		10996'	7,7,7	7.0	0.035000	4,121		409	4,021	3,925	3,714	2 in
86		10996'1"	7,7,8	7.3	0.036667	3,779		440	5,053	4,712	4,591	3 10/16 in
87		10996'6"	7,7,6	6.7	0.033333	4,514		455	5,600	5,124	5,060	2 2/16 in
88		10997'	7,7,6	6.7	0.033333	4,514		412	4,115	3,998	3,794	3 in
89		10998'	7,7,7	7.0	0.035000	4,121		435	4,878	4,579	4,441	2 15/16 in
90		10998'5"	5,5,5	5.0	0.025000	8,985		651	15,215	12,547	14,298	4 2/16 in
91		10999'	6,6,5	5.7	0.028333	6,111		424	4,504	4,295	4,123	5 5/16 in
92		10999'1"	8,7,8	7.7	0.038333	3,478		382	3,230	3,309	3,047	2 12/16 in
93		10999'5"	7,7,7	7.0	0.035000	4,121		383	3,257	3,331	3,070	4 7/16 in
94		11000'	8,7,7	7.3	0.036667	3,779		372	2,962	3,097	2,821	2 1/16 in
95		11001'	7,7,7	7.0	0.035000	4,121		403	3,836	3,783	3,559	4 5/16 in
96		11001'5"	4,5,4	4.3	0.021667	15,416		591	11,846	9,852	10,802	5 11/16 in
97		11002'	7,7,7	7.0	0.035000	4,121		430	4,706	4,449	4,295	3 10/16 in
98		11002'5"	7,6,8	7.0	0.035000	4,121		425	4,537	4,321	4,152	3 in
99		11003'	7,8,8	7.7	0.038333	3,478		441	5,089	4,739	4,621	5 10/16 in
100		11003'6"	6,7,7	6.7	0.033333	4,514		361	2,684	2,873	2,586	5 8/16 in

Continued…

Prost G 5H												
Sample Number	FM	Depth (Ft, in)	Dimpler Diameter (Tick Marks)	Average Dimple (Divisions)	Average Dimple (in)	DIMPLE UCS (psi)		Bambino Average L' (5 Samples)	UCS - Enderlin (psi)	UCS - Aoki and Matsukura 2008 (psi)	UCS - Zahm et al 2014 - (psi)	Length of Core Piece (in)
101	EAGLE FORD	11004'	6,6,7	6.3	0.031667	4,966		406	3,928	3,854	3,636	4 4/16 in
102		11005'	7,6,7	6.7	0.033333	4,514		432	4,774	4,501	4,353	1 10/16 in
103		11005'1"	7,9,8	8.0	0.040000	3,213		383	3,257	3,331	3,070	5 in
104		11006'	9,10,9	9.3	0.046667	2,411		368	2,859	3,014	2,734	2 4/16 in
105		11006'3"	8,8,9	8.3	0.041667	2,978		397	3,657	3,644	3,407	2 12/16 in
106		11007'	7,7,7	7.0	0.035000	4,121		458	5,713	5,209	5,157	4 12/16 in
107		11007'7"	6,5,6	5.7	0.028333	6,111		587	11,633	9,686	10,591	5 13/16 in
108		11008'	8,8,8	8.0	0.040000	3,213		459	5,751	5,237	5,190	2 3/16 in
109		11008'9"	7,7,7	7.0	0.035000	4,121		421	4,405	4,220	4,039	3 13/16 in
110		11010'	9,7,8	8.0	0.040000	3,213		463	5,904	5,352	5,322	5 9/16 in
111		11011'	6,6,7	6.3	0.031667	4,966		501	7,463	6,519	6,690	2 7/16 in
112		11011'1"	6,6,6	6.0	0.030000	5,493		508	7,770	6,749	6,965	3 12/16 in
113		11011'8"	6,7,6	6.3	0.031667	4,966		534	8,963	7,646	8,050	4 11/16 in
114		11012'	7,9,8	8.0	0.040000	3,213		477	6,456	5,766	5,802	6 6/16 in
115		11012'9"	7,8,8	7.7	0.038333	3,478		443	5,160	4,793	4,682	5 8/16 in
116		11013'	7,7,9	7.7	0.038333	3,478		474	6,336	5,676	5,697	5 4/16 in
117		11013'9"	6,8,7	7.0	0.035000	4,121		466	6,020	5,439	5,423	4 5/16 in
118		11014'4"	7,8,8	7.7	0.038333	3,478		384	3,285	3,353	3,094	3 4/16 in
119		11015'	8,9,8	8.3	0.041667	2,978		394	3,569	3,575	3,333	3 10/16 in
120		11015'5"	7,7,8	7.3	0.036667	3,779		423	4,471	4,270	4,095	5 12/16 in
121		11016'3"	8,8,8	8.0	0.040000	3,213		454	5,563	5,096	5,028	2 4/16 in
122		11017'	7,7,7	7.0	0.035000	4,121		480	6,578	5,857	5,909	2 15/16 in
123		11017'3"		7.3	0.036667	3,779		484	6,742	5,980	6,053	4 7/16 in
124		11017'8"	7,8,7	7.3	0.036667	3,779		490	6,992	6,167	6,273	6 in
125		11018'	7,7,7	7.0	0.035000	4,121		490	6,992	6,167	6,273	3 13/16 in
126		11019'	8,8,9	8.3	0.041667	2,978		425	4,537	4,321	4,152	3 10/16 in
127		11020'	6,6,5	5.7	0.028333	6,111		522	8,402	7,223	7,536	2 in
128		11020'2"	5,5,5	5.0	0.025000	8,985		582	11,368	9,482	10,332	4 4/16 in
129		11021'	5,5,6	5.3	0.026667	7,125		599	12,277	10,189	11,232	5 in
130		11021'5"	5,5,5	5.0	0.025000	8,985		612	12,990	10,751	11,953	3 15/16 in
131		11022'	7,7,7	7.0	0.035000	4,121		476	6,416	5,736	5,767	4 7/16 in
132		11022'8"	7,7,7	7.0	0.035000	4,121		474	6,336	5,676	5,697	5 4/16 in
133		11023'3"	8,7,7	7.3	0.036667	3,779		482	6,660	5,918	5,981	4 3/16 in
134		11023'9"	7,7,7	7.0	0.035000	4,121		492	7,077	6,230	6,347	4 2/16 in
135		11024'	7,7,7	7.0	0.035000	4,121		457	5,675	5,180	5,125	2 7/16 in
136		11025'	7,6,5	6.0	0.030000	5,493		536	9,058	7,718	8,137	7 4/16 in
137		11025'6"	7,7,6	6.7	0.033333	4,514		491	7,034	6,198	6,310	7 4/16 in
138		11026'	7,6,7	6.7	0.033333	4,514		463	5,904	5,352	5,322	3 in
139		11026'2"	7,7,7	7.0	0.035000	4,121		429	4,672	4,423	4,266	5 2/16 in
140		11027'	7,8,7	7.3	0.036667	3,779		454	5,563	5,096	5,028	3 7/16 in
141		11027'4"	7,7,7	7.0	0.035000	4,121		493	7,119	6,262	6,385	4 12/16 in
142		11028'	7,7,7	7.0	0.035000	4,121		424	4,504	4,295	4,123	5 in
143		11029'	8,8,7	7.7	0.038333	3,478		430	4,706	4,449	4,295	5 2/16 in
144		11029'1"	7,8,7	7.3	0.036667	3,779		446	5,268	4,874	4,775	1 14/16 in
145		11030'	6,6,8	6.7	0.033333	4,514		578	11,159	9,319	10,127	6 8/16 in
146		11030'7"	6,7,7	6.7	0.033333	4,514		491	7,034	6,198	6,310	3 8/16 in
147		11031'	7,7,8	7.3	0.036667	3,779		462	5,865	5,323	5,289	3 11/16 in
148		11031'6"	7,7,7	7.0	0.035000	4,121		474	6,336	5,676	5,697	6 8/16 in
149		11032'	7,7,7	7.0	0.035000	4,121		460	5,789	5,266	5,223	4 8/16 in
150		11033'	7,7,6	6.7	0.033333	4,514		483	6,701	5,949	6,017	3 1/16 in

Continued…

Prost G 5H											
Sample Number	FM	Depth (Ft, in)	Dimpler Diameter (Tick Marks)	Average Dimple (Divisions)	Average Dimple (in)	DIMPLE UCS (psi)		Bambino Average L' (5 Samples)	UCS - Enderlin (psi)	UCS - Aoki and Matsukura 2008 (psi)	UCS - Zahm et al 2014 - (psi)	Length of Core Piece (in)
151	EAGLE FORD	11033'8"	7,7,8	7.3	0.036667	3,779		435	4,878	4,579	4,441	4 6/16 in
152		11034'3"	7,8,7	7.3	0.036667	3,779		444	5,196	4,820	4,713	2 4/16 in
153		11035'	8,8,7	7.7	0.038333	3,478		435	4,878	4,579	4,441	4 4/16 in
154		11035'1"	6,5,5	5.3	0.026667	7,125		549	9,688	8,194	8,723	3 7/16 in
155		11035'5"	5,5,5	5.0	0.025000	8,985		651	15,215	12,547	14,298	3 1/16 in
156		11035'10"	7,7,7	7.0	0.035000	4,121		462	5,865	5,323	5,289	6 3/16 in
157		11036'4"	8,8,7	7.7	0.038333	3,478		439	5,018	4,685	4,561	3 14/16 in
158		11036'9"	7,6,8	7.0	0.035000	4,121		498	7,333	6,422	6,575	3 11/16 in
159		11037'	6,7,6	6.3	0.031667	4,966		483	6,701	5,949	6,017	5 2/16 in
160		11037'6"	5,5,5	5.0	0.025000	8,985		573	10,899	9,119	9,875	5 1/16 in
161		11038'	7,7,7	7.0	0.035000	4,121		499	7,376	6,454	6,613	1 6/16 in
162		11038'9"	7,7,7	7.0	0.035000	4,121		450	5,414	4,984	4,900	2 7/16 in
163		11039'4"	6,6,5	5.7	0.028333	6,111		603	12,495	10,360	11,450	2 3/16 in
164		11040'6"	8,7,7	7.3	0.036667	3,779		464	5,943	5,381	5,356	4 2/16 in
165		11041'	6,7,7	6.7	0.033333	4,514		518	8,219	7,086	7,370	1 4/16 in
166		11041'1"	"									13/16 in
167		11041'8"	6,6,5	5.7	0.028333	6,111		552	9,836	8,307	8,862	2 4/16 in
168	PHOSPHATE	11042'	6,6,7	6.3	0.031667	4,966		459	5,751	5,237	5,190	2 10/16 in
169		11042'6"	7,7,7	7.0	0.035000	4,121		458	5,713	5,209	5,157	6 4/16 in
170		11043'	8,8,7	7.7	0.038333	3,478		430	4,706	4,449	4,295	4 5/16 in
171		11044'	8,7,8	7.7	0.038333	3,478		401	3,776	3,736	3,508	3 12/16 in
172		11044'1"	8,7,8	7.7	0.038333	3,478		353	2,492	2,716	2,424	13/16 in
173		11044'4"	7,7,7	7.0	0.035000	4,121		351	2,445	2,678	2,384	3 4/16 in
174		11044'7"	8,7,8	7.7	0.038333	3,478		471	6,216	5,586	5,593	4 3/16 in
175		11045'	7,7,7	7.0	0.035000	4,121		605	12,604	10,446	11,561	6 12/16 in
176		11045'7"	7,6,6	6.3	0.031667	4,966		573	10,899	9,119	9,875	3 in
177	MANESS	11046'7"	8,8,8	8.0	0.040000	3,213		334	2,070	2,366	2,064	2 11/16 in
178		11047'	8,8,9	8.3	0.041667	2,978		366	2,808	2,974	2,692	1 1/16 in
179		11047'1"	8,9,9	8.7	0.043333	2,768		385	3,313	3,375	3,117	1 3/16 in
180		11047'7"	6,7,7	6.7	0.033333	4,514		599	12,277	10,189	11,232	4 14/16 in
181		11048'	9,8,9	8.7	0.043333	2,768		350	2,422	2,659	2,364	4 9/16 in
182		11048'2"	10,8,10	9.3	0.046667	2,411		297	1,384	1,764	1,469	4 9/16 in
183		11048'6"	9,10,11	10.0	0.050000	2,120		292	1,305	1,691	1,398	2 6/16 in
184		11048'8"	10,8,9	9.0	0.045000	2,580		364	2,758	2,933	2,649	1 13/16 in
185		11049'	9,10,10	9.7	0.048333	2,258		320	1,790	2,125	1,823	1 2/16 in
186		11049'6"	10,10,10	10.0	0.050000	2,120		339	2,176	2,455	2,155	4 4/16 in
187		11050'	9,8,8	8.3	0.041667	2,978		347	2,353	2,603	2,306	1 4/16 in
188		11050'2"	8,7,8	7.7	0.038333	3,478		548	9,639	8,157	8,677	3 in
189		11050'4"	7,8,6	7.0	0.035000	4,121		567	10,590	8,882	9,578	4 2/16 in
190		11050'5"	8,9,8	8.3	0.041667	2,978		395	3,598	3,598	3,358	4 2/16 in
191		11050'10"	9,9,9	9.0	0.045000	2,580		334	2,070	2,366	2,064	3 in
192		11052'	9,8,10	9.0	0.045000	2,580		310	1,605	1,963	1,663	1 14/16 in
193		11052'6"	10,10,10	10.0	0.050000	2,120		226	520	891	665	12/16 in
194		11052'10"	9,9,9	9.0	0.045000	2,580		356	2,563	2,775	2,484	3 5/16 in
195		11053'	9,10,9	9.3	0.046667	2,411		357	2,587	2,794	2,504	1 7/16 in
196		11053'6"	9,9,10	9.3	0.046667	2,411		281	1,140	1,536	1,251	1 8/16 in
197		11054'	9,9,9	9.0	0.045000	2,580		312	1,641	1,995	1,694	3 12/16 in
198		11054'6"	10,10,10	10.0	0.050000	2,120		293	1,320	1,705	1,412	4 10/16 in
199		11055'	8,9,8	8.3	0.041667	2,978		300	1,433	1,809	1,512	1 14/16 in
200		11055'6"	9,10,9	9.3	0.046667	2,411		366	2,808	2,974	2,692	1 9/16 in

Continued...

Prost G 5H												
Sample Number	FM	Depth (Ft, in)	Dimpler Diameter (Tick Marks)	Average Dimple (Divisions)	Average Dimple (in)	DIMPLE UCS (psi)		Bambino Average L' (5 Samples)	UCS - Enderlin (psi)	UCS - Aoki and Matsukura 2008 (psi)	UCS - Zahm et al 2014 - (psi)	Length of Core Piece (in)
201		11056'	9,10,9	9.3	0.046667	2,411		361	2,684	2,873	2,586	9 8/16 in
202		11056'2"	8,9,9	8.7	0.043333	2,768		357	2,587	2,794	2,504	2 4/16 in
203		11056'6"	10,10,10	10.0	0.050000	2,120		304	1,501	1,870	1,571	2 8/16 in
204		11057'	10,12,12	11.3	0.056667	1,679		309	1,587	1,947	1,647	1 6/16 in
205		11057'6"	9,9,10	9.3	0.046667	2,411		316	1,714	2,060	1,758	2 7/16 in
206		11058'3"	10,10,10	10.0	0.050000	2,120		330	1,987	2,295	1,993	1 5/16 in
207		11058'9"	8,9,9	8.7	0.043333	2,768		333	2,049	2,348	2,046	3 1/16 in
208		11059'10"	7,7,6	6.7	0.033333	4,514		575	11,002	9,199	9,976	4 8/16 in
209		11060'4"	10,10,9	9.7	0.048333	2,258		297	1,384	1,764	1,469	4 1/16 in
210		11060'8"	9,10,10	9.7	0.048333	2,258		335	2,091	2,383	2,082	4 1/16 in
211		11061'	6,6,5	5.7	0.028333	6,111		599	12,277	10,189	11,232	2 9/16 in
212		11061'6"	10,10,10	10.0	0.050000	2,120		272	1,016	1,416	1,138	1 4/16 in
213		11061'9"	9,9,9	9.0	0.045000	2,580		369	2,885	3,035	2,756	3 5/16 in
214		11062'	9,10,8	9.0	0.045000	2,580		353	2,492	2,716	2,424	3 2/16 in
215		11062'6"	10,8,8	8.7	0.043333	2,768		297	1,384	1,764	1,469	3 4/16 in
216		11063'	9,9,9	9.0	0.045000	2,580		360	2,659	2,853	2,566	4 8/16 in
217	MANESS	11063'6"	9,8,8	8.3	0.041667	2,978		361	2,684	2,873	2,586	3 8/16 in
218		11063'9"	9,9,8	8.7	0.043333	2,768		393	3,540	3,553	3,309	4 15/16 in
219		11064'	10,9,10	9.7	0.048333	2,258		317	1,733	2,076	1,774	5 in
220		11064'3"	6,7,7	6.7	0.033333	4,514		622	13,549	11,196	12,528	5 in
221		11064'6"	10,8,10	9.3	0.046667	2,411		347	2,353	2,603	2,306	15/16 in
222		11065'	9,9,10	9.3	0.046667	2,411		388	3,397	3,441	3,188	1 10/16 in
223		11065'1"	9,8,9	8.7	0.043333	2,768		343	2,264	2,528	2,230	2 2/16 in
224		11065'6"	8,9,8	8.3	0.041667	2,978		349	2,399	2,640	2,345	3 10/16 in
225		11066'	8,9,9	8.7	0.043333	2,768		341	2,220	2,491	2,192	2 in
226		11066'5"	9,8,9	8.7	0.043333	2,768		352	2,468	2,697	2,404	14/16 in
227		11066'10"	6,5,7	6.0	0.030000	5,493		580	11,263	9,400	10,229	3 8/16 in
228		11068'	9,10,9	9.3	0.046667	2,411		302	1,467	1,839	1,541	1 2/16 in
229		11058'6"	7,9,7	7.7	0.038333	3,478		427	4,604	4,372	4,209	1 4/16 in
230		11068'7"		6.7	0.033333	4,514		587	11,633	9,686	10,591	5 1/16 in
231		11069'	9,10,10	9.7	0.048333	2,258		336	2,112	2,401	2,100	5 1/16 in
232		11069'6"	8,7,9	8.0	0.040000	3,213		359	2,635	2,833	2,545	3 2/16 in
233		11070'	8,9,10	9.0	0.045000	2,580		308	1,570	1,932	1,632	2 in
234		11070'4"	8,9,9	8.7	0.043333	2,768		403	3,836	3,783	3,559	1 12/16 in
235		11071'	8,9,9	8.7	0.043333	2,768		383	3,257	3,331	3,070	2 1/16 in
236		11071'1"	8,10,10	9.3	0.046667	2,411		366	2808	2974	2692	1 in
237		11071'6"	8,9,8	8.3	0.041667	2,978		427	4604	4372	4209	2 9/16 in
238		11072'	4,4,3	3.7	0.018333	25,748		627	13831	11422	12823	2 4/16 in
239	BUDA	11072'6"	4,5,4	4.3	0.021667	15,416		708	18653	15476	18239	5 12/16 in
240		11073'	3,5,5	4.3	0.021667	15,416		706	18529	15367	18090	3 2/16 in
241		11073'6"	6,5,6	5.7	0.028333	6,111		608	12769	10576	11728	2 5/16 in
242		11074'	6,6,5	5.7	0.028333	6,111		594	12007	9978	10962	2 12/16 in

Sante North Unit A 1H												
Sample Number	FM	Depth (Ft, in)	Dimpler Diameter (Tick Marks)	Average Dimple (Divisions)	Average Dimple (in)	DIMPLE UCS (psi)		Bambino Average L' (5 Samples)	UCS - Enderlin (psi)	UCS - Aoki and Matsukura 2008 (psi)	UCS - Zahm et al 2014 - (psi)	Length of Core Piece (in)
1	AUSTIN CHALK	11223'6"	4,5,3	4.0	0.020000	20,091		640	14,575	12,023	13,609	7 6/16 in
2		11224'5"	5,4,5	4.7	0.023333	11,725		651	15,215	12,547	14,298	2 in
3		11225'4"	4,4,4	4.0	0.020000	20,091		670	16,339	13,482	15,542	3 5/16 in
4		11226'6'	5,5,5	5.0	0.025000	8,985		641	14,633	12,070	13,671	5 8/16 in
5		11227'	4,4,4	4.0	0.020000	20,091		682	17,061	14,094	16,364	3 5/16 in
6		11227'10"	5,5,5	5.0	0.025000	8,985		673	16,519	13,634	15,745	5 7/16 in
7		11229'5"	5,5,5	5.0	0.025000	8,985		626	13,775	11,376	12,763	3 11/16 in
8		11230'	5,5,4	4.7	0.023333	11,725		626	13,775	11,376	12,763	4 4/16 in
9		11230'	,,									
10		11230'11"	4,4,4	4.0	0.020000	20,091		661	15,804	13,034	14,945	10 13/16 in
11		11231'10"	4,5,5	4.7	0.023333	11,725		666	16,101	13,282	15,275	6 8/16 in
12		11232'2"	4,4,4	4.0	0.020000	20,091		662	15,863	13,083	15,010	6 13/16 in
13		11233'	5,5,5	5.0	0.025000	8,985		669	16,279	13,432	15,475	6 1/16 in
14		11233'5"	5,5,4	4.7	0.023333	11,725		544	9,444	8,009	8,495	4 2/16 in
15		11234'	5,4,4	4.3	0.021667	15,416		653	15,332	12,643	14,426	6 8/16 in
16		11234'10"	4,4,4	4.0	0.020000	20,091		616	13,213	10,928	12,181	6 4/16 in
17		11235'3"	5,4,5	4.7	0.023333	11,725		503	7,550	6,584	6,768	3 13/16 in
18		11236'	5,5,4	4.7	0.023333	11,725		646	14,923	12,307	13,982	10 9/16 in
19		11236'6"	4,5,4	4.3	0.021667	15,416		630	14,002	11,559	13,001	4 10/16 in
20		11237'	5,5,5	5.0	0.025000	8,985		608	12,769	10,576	11,728	11 1/16 in
21		11237'9"	5,4,5	4.7	0.023333	11,725		604	12,550	10,403	11,506	11 1/16 in
22		11238'9"	5,5,4	4.7	0.023333	11,725		652	15,273	12,595	14,362	3 7/16 in
23	EAGLE FORD	11239'	5,5,5	5.0	0.025000	8,985		609	12,824	10,620	11,784	5 11/16 in
24		11239'7"	4,5,4	4.3	0.021667	15,416		688	17,425	14,406	16,784	4 3/16 in
25		11240'	5,5,5	5.0	0.025000	8,985		624	13,662	11,286	12,646	4 12/16 in
26		11240'8"	4,4,4	4.0	0.020000	20,091		669	16,279	13,432	15,475	9 14/16 in
27		11241'	5,5,5	5.0	0.025000	8,985		578	11,159	9,319	10,127	3 11/16 in
28		11241'7"	5,6,5	5.3	0.026667	7,125		619	13,380	11,061	12,354	7 12/16 in
29		11242'	5,5,5	5.0	0.025000	8,985		632	14,116	11,651	13,121	7 12/16 in
30		11243'	4,4,4	4.0	0.020000	20,091		622	13,549	11,196	12,528	8 2/16 in
31		11243'11"	5,4,4	4.3	0.021667	15,416		661	15,804	13,034	14,945	4 5/16 in
32		11243'3"	4,5,5	4.7	0.023333	11,725		621	13,493	11,151	12,470	8 2/16 in
33		11244'2"	5,5,5	5.0	0.025000	8,985		646	14,923	12,307	13,982	3 8/16 in
34		11245'1"	7,7,7	7.0	0.035000	4,121		284	1,184	1,577	1,290	4 5/16 in
35		11246'	7,7,7	7.0	0.035000	4,121		434	4,843	4,553	4,412	0 15/16 in
36		11246'11"	7,8,7	7.3	0.036667	3,779		431	4,740	4,475	4,324	3 10/16 in
37		11247'1"	7,6,7	6.7	0.033333	4,514		373	2,988	3,118	2,844	6 11/16 in
38		11248'	7,6,6	6.3	0.031667	4,966		431	4,740	4,475	4,324	4 9/16 in
39		11248'2"	7,8,7	7.3	0.036667	3,779		455	5,600	5,124	5,060	7 9/16 in
40		11249'	7,7,7	7.0	0.035000	4,121		407	3,959	3,878	3,662	7 7/16 in
41		11249'8"	7,6,7	6.7	0.033333	4,514		486	6,825	6,042	6,126	3 2/16 in
42		11250'1"	7,7,7	7.0	0.035000	4,121		422	4,438	4,245	4,067	2 13/16 in
43		11251'	6,7,8	7.0	0.035000	4,121		310	1,605	1,963	1,663	1 7/16 in
44		11251'6"	7,6,7	6.7	0.033333	4,514		422	4,438	4,245	4,067	2 9/16 in
45		11252'	7,7,7	7.0	0.035000	4,121		425	4,537	4,321	4,152	0 15/16 in
46		11252'10"	6,7,7	6.7	0.033333	4,514		419	4,339	4,170	3,984	3 6/16 in
47		11253'2"	7,8,8	7.7	0.038333	3,478		363	2,733	2,913	2,628	5 1/16 in
48		11254'	7,7,7	7.0	0.035000	4,121		450	5,414	4,984	4,900	3 14/16 in
49		11254'9"	7,6,7	6.7	0.033333	4,514		453	5,525	5,068	4,996	2 14/16 in
50		11255'	7,8,7	7.3	0.036667	3,779		368	2,859	3,014	2,734	3 14/16 in

Continued…

Sante North Unit A 1H											
Sample Number	FM	Depth (Ft, in)	Dimpler Diameter (Tick Marks)	Average Dimple (Divisions)	Average Dimple (in)	DIMPLE UCS (psi)		Bambino Average L' (5 Samples)	UCS - Enderlin (psi)	UCS - Aoki and Matsukura 2008 (psi)	UCS - Zahm et al 2014 - (psi)	Length of Core Piece (in)
51	EAGLE FORD	11255'10"	7,7,7	7.0	0.035000	4,121		427	4,604	4,372	4,209	2 6/16 in
52		11256'1"	6,7,7	6.7	0.033333	4,514		447	5,305	4,902	4,806	1 14/16 in
53		11257'	7,7,7	7.0	0.035000	4,121		427	4,604	4,372	4,209	1 7/16 in
54		11257'7"	7,7,7	7.0	0.035000	4,121		432	4,774	4,501	4,353	4 12/16 in
55		11258'	7,7,7	7.0	0.035000	4,121		351	2,445	2,678	2,384	2 8/16 in
56		11258'10"	7,7,7	7.0	0.035000	4,121		475	6,376	5,706	5,732	2 2/16 in
57		11259'1"	7,6,7	6.7	0.033333	4,514		320	1,790	2,125	1,823	4 5/16 in
58		11260'	7,8,7	7.3	0.036667	3,779		370	2,910	3,055	2,778	3 13/16 in
59		11260'4"	8,8,9	8.3	0.041667	2,978		365	2,783	2,953	2,670	8 8/16 in
60		11261'	8,7,7	7.3	0.036667	3,779		316	1,714	2,060	1,758	0 14/16 in
61		11261'9"	8,9,8	8.3	0.041667	2,978		385	3,313	3,375	3,117	1 15/16 in
62		11262'9"	8,8,8	8.0	0.040000	3,213		391	3,482	3,508	3,260	4 15/16 in
63		11263'	7,8,7	7.3	0.036667	3,779		371	2,936	3,076	2,800	4 15/16 in
64		11263'7"	8,8,7	7.7	0.038333	3,478		390	3,454	3,485	3,236	2 4/16 in
65		11264'	7,8,7	7.3	0.036667	3,779		334	2,070	2,366	2,064	4 6/16 in
66		11264'10"	7,8,8	7.7	0.038333	3,478		409	4,021	3,925	3,714	1 8/16 in
67		11265'1"	8,8,8	8.0	0.040000	3,213		368	2,859	3,014	2,734	6 6/16 in
68		11266'	7,8,7	7.3	0.036667	3,779		415	4,210	4,071	3,875	7 13/16 in
69		11266'4"	7,8,7	7.3	0.036667	3,779		371	2,936	3,076	2,800	3 13/16 in
70		11267'	6,6,7	6.3	0.031667	4,966		347	2,353	2,603	2,306	2 10/16 in
71		11267'10"	7,7,7	7.0	0.035000	4,121		422	4,438	4,245	4,067	2 4/16 in
72		11268'1"	7,8,7	7.3	0.036667	3,779		353	2,492	2,716	2,424	2 14/16 in
73		11269'	7,6,7	6.7	0.033333	4,514		468	6,098	5,498	5,491	4 1/16 in
74		11269'3"	8,7,7	7.3	0.036667	3,779		433	4,809	4,527	4,382	2 8/16 in
75		11270'	7,8,7	7.3	0.036667	3,779		421	4,405	4,220	4,039	1 9/16 in
76		11271'2"	7,6,9	7.3	0.036667	3,779		368	2,859	3,014	2,734	2 10/16 in
77		11272'	7,7,6	6.7	0.033333	4,514		354	2,515	2,736	2,443	1 6/16 in
78		11272'9"	10,8,9	9.0	0.045000	2,580		312	1,641	1,995	1,694	2 5/16 in
79		11273'	8,7,7	7.3	0.036667	3,779		289	1,258	1,647	1,357	2 9/16 in
80		11273'6"	7,7,7	7.0	0.035000	4,121		387	3,369	3,419	3,164	1 10/16 in
81		11274'2"	7,7,8	7.3	0.036667	3,779		407	3,959	3,878	3,662	3 7/16 in
82		11275'	7,7,8	7.3	0.036667	3,779		370	2,910	3,055	2,778	4 6/16 in
83		11275'8"	6,8,8	7.3	0.036667	3,779		375	3,041	3,160	2,888	3 in
84		11276'	7,7,9	7.7	0.038333	3,478		376	3,068	3,181	2,910	1 12/16 in
85		11276'11"	7,8,9	8.0	0.040000	3,213		378	3,121	3,223	2,955	1 8/16 in
86		11277'2"	7,8,8	7.7	0.038333	3,478		372	2,962	3,097	2,821	2 14/16 in
87		11278'	7,7,7	7.0	0.035000	4,121		334	2,070	2,366	2,064	2 14/16 in
88		11278'10"	8,8,8	8.0	0.040000	3,213		367	2,834	2,994	2,713	4 in
89		11279'	7,7,7	7.0	0.035000	4,121		401	3,776	3,736	3,508	4 in
90		11279'10"	8,8,8	8.0	0.040000	3,213		376	3,068	3,181	2,910	2 12/16 in
91		11280'2"	9,9,9	9.0	0.045000	2,580		384	3,285	3,353	3,094	3 2/16 in
92		11281'	8,8,8	8.0	0.040000	3,213		341	2,220	2,491	2,192	3 in
93		11281'7"	8,8,10	8.7	0.043333	2,768		352	2,468	2,697	2,404	2 6/16 in
94		11282'	7,7,8	7.3	0.036667	3,779		383	3,257	3,331	3,070	5 8/16 in
95		11282'11"	8,10,10	9.3	0.046667	2,411		354	2,515	2,736	2,443	7 10/16 in
96		11283'1"	7,8,7	7.3	0.036667	3,779		350	2,422	2,659	2,364	4 1/16 in
97		11284'	9,7,7	7.7	0.038333	3,478		338	2,155	2,437	2,137	3 14/16 in
98		11284'3"	10,9,7	8.7	0.043333	2,768		363	2,733	2,913	2,628	4 in
99		11285'	9,9,8	8.7	0.043333	2,768		359	2,635	2,833	2,545	1 9/16 in
100		11285'1"	7,6,7	6.7	0.033333	4,514		323	1,848	2,176	1,873	1 4/16 in

Continued…

Sante North Unit A 1H											
Sample Number	FM	Depth (Ft, in)	Dimpler Diameter (Tick Marks)	Average Dimple (Divisions)	Average Dimple (in)	DIMPLE UCS (psi)		Bambino Average L' (5 Samples)	UCS - Enderlin (psi)	UCS - Aoki and Matsukura 2008 (psi)	UCS - Zahm et al 2014 - (psi)	Length of Core Piece (in)
101	EAGLE FORD	11286'9"	7,7,7	7.0	0.035000	4,121		380	3,175	3,266	3,001	3 9/16 in
102		11287'	7,8,8	7.7	0.038333	3,478		419	4,339	4,170	3,984	3 11/16 in
103		11287'11"	8,8,8	8.0	0.040000	3,213		355	2,539	2,755	2,464	4 12/16 in
104		11287'3"	7,7,8	7.3	0.036667	3,779		399	3,716	3,690	3,457	3 11/16 in
105		11288'	8,8,8	8.0	0.040000	3,213		342	2,242	2,510	2,211	4 12/16 in
106		11288'9"	8,8,7	7.7	0.038333	3,478		350	2,422	2,659	2,364	4 in
107		11289'	7,7,8	7.3	0.036667	3,779		377	3,094	3,202	2,933	4 in
108		11289'1"	7,8,8	7.7	0.038333	3,478		393	3,540	3,553	3,309	3 15/16 in
109		11289'8"	7,7,7	7.0	0.035000	4,121		356	2,563	2,775	2,484	3 11/16 in
110		11290'	7,8,7	7.3	0.036667	3,779		400	3,746	3,713	3,482	0 15/16 in
111		11290'10"	7,7,7	7.0	0.035000	4,121		375	3,041	3,160	2,888	4 8/16 in
112		11290'3"	6,7,7	6.7	0.033333	4,514		409	4,021	3,925	3,714	3 11/16 in
113		11291'	8,9,8	8.3	0.041667	2,978		353	2,492	2,716	2,424	4 8/16 in
114		11291'10"	7,7,8	7.3	0.036667	3,779		407	3,959	3,878	3,662	3 4/16 in
115		11292'2"	7,7,8	7.3	0.036667	3,779		384	3,285	3,353	3,094	4 2/16 in
116		11292'8"	7,7,7	7.0	0.035000	4,121		341	2,220	2,491	2,192	2 8/16 in
117		11293'	6,7,7	6.7	0.033333	4,514		359	2,635	2,833	2,545	3 5/16 in
118		11293'10"	7,8,8	7.7	0.038333	3,478		413	4,147	4,022	3,821	0 13/16 in
119		11293'3"	7,7,8	7.3	0.036667	3,779		431	4,740	4,475	4,324	5 8/16 in
120		11294'	8,8,7	7.7	0.038333	3,478		403	3,836	3,783	3,559	8 in
121		11294'10"	8,8,7	7.7	0.038333	3,478		396	3,627	3,621	3,382	3 in
122		11295'	7,8,8	7.7	0.038333	3,478		396	3,627	3,621	3,382	1 7/16 in
123		11295'5"										
124		11295'9"	8,7,7	7.3	0.036667	3,779		345	2,308	2,565	2,268	4 9/16 in
125		11296'	8,7,8	7.7	0.038333	3,478		381	3,202	3,288	3,024	4 9/16 in
126		11296'3"	7,7,7	7.0	0.035000	4,121		437	4,948	4,632	4,501	5 in
127		11296'9"	7,6,7	6.7	0.033333	4,514		466	6,020	5,439	5,423	4 14/16 in
128		11297'	7,8,7	7.3	0.036667	3,779		459	5,751	5,237	5,190	4 6/16 in
129		11297'10"	6,7,6	6.3	0.031667	4,966		428	4,638	4,397	4,237	3 3/16 in
130		11297'5"	6,6,6	6.0	0.030000	5,493		465	5,981	5,410	5,389	3 6/16 in
131		11298'1"	7,7,7	7.0	0.035000	4,121		363	2,733	2,913	2,628	4 11/16 in
132		11298'8"	7,6,6	6.3	0.031667	4,966		412	4,115	3,998	3,794	5 14/16 in
133		11299'1"	7,7,7	7.0	0.035000	4,121		408	3,990	3,901	3,688	4 5/16 in
134		11299'11"	7,7,6	6.7	0.033333	4,514		422	4,438	4,245	4,067	4 9/16 in
135		11299'7"	6,7,6	6.3	0.031667	4,966		412	4,115	3,998	3,794	1 12/16 in
136		11300'4"	5,5,5	5.0	0.025000	8,985		576	11,054	9,239	10,026	6 5/16 in
137		11300'9"	5,5,5	5.0	0.025000	8,985		499	7,376	6,454	6,613	4 8/16 in
138		11301'1"	6,6,6	6.0	0.030000	5,493		560	10,235	8,611	9,239	3 6/16 in
139		11301'6"	5,5,5	5.0	0.025000	8,985		593	11,953	9,936	10,908	6 14/16 in
140	PHOPSHATE	11302'	6,7,8	7.0	0.035000	4,121		330	1,987	2,295	1,993	1 10/16 in
141		11302'10"	7,6,8	7.0	0.035000	4,121		393	3,540	3,553	3,309	3 7/16 in
142		11303'3"	6,6,7	6.3	0.031667	4,966		389	3,425	3,463	3,212	5 3/16 in
143		11303'9"	6,7,7	6.7	0.033333	4,514		386	3,340	3,397	3,141	3 in
144		11304'10"	7,6,7	6.7	0.033333	4,514		338	2,155	2,437	2,137	3 2/16 in
145		11304'4"	5,5,6	5.3	0.026667	7,125		420	4,372	4,195	4,012	5 12/16 in
146		11304'8"	5,5,5	5.0	0.025000	8,985		603	12,495	10,360	11,450	3 10/16 in
147		11305'10"	6,6,5	5.7	0.028333	6,111		452	5,488	5,040	4,964	5 in
148		11305'2"	5,5,5	5.0	0.025000	8,985		537	9,106	7,754	8,181	2 9/16 in
149	MANI	11306'9"	7,7,8	7.3	0.036667	3,779		368	2,859	3,014	2,734	0 15/16 in
150		11307'	7,6,6	6.3	0.031667	4,966		490	6,992	6,167	6,273	2 6/16 in

Continued…

Sante North Unit A 1H												
Sample Number	FM	Depth (Ft, in)	Dimpler Diameter (Tick Marks)	Average Dimple (Divisions)	Average Dimple (in)	DIMPLE UCS (psi)		Bambino Average L' (5 Samples)	UCS - Enderlin (psi)	UCS - Aoki and Matsukura 2008 (psi)	UCS - Zahm et al 2014 - (psi)	Length of Core Piece (in)
151	MANESS	11307'1"	9,8,8	8.3	0.041667	2,978		348	2,376	2,621	2,325	2 in
152		11307'6"	9,9,8	8.7	0.043333	2,768		283	1,169	1,563	1,277	3 12/16 in
153		11307'8"	8,8,9	8.3	0.041667	2,978		327	1,927	2,244	1,941	2 3/16 in
154		11308'	8,8,8	8.0	0.040000	3,213		375	3,041	3,160	2,888	3 14/16 in
155		11308'1"	6,5,5	5.3	0.026667	7,125		563	10,387	8,727	9,384	3 14/16 in
156		11308'6"	9,9,9	9.0	0.045000	2,580		308	1,570	1,932	1,632	5 in
157		11308'7"	8,8,8	8.0	0.040000	3,213		296	1,368	1,749	1,454	5 in
158		11309'	7,8,8	7.7	0.038333	3,478		354	2,515	2,736	2,443	4 2/16 in
159		11309'1"	8,9,8	8.3	0.041667	2,978		361	2,684	2,873	2,586	4 2/16 in
160		11309'6"	7,7,8	7.3	0.036667	3,779		336	2,112	2,401	2,100	4 4/16 in
161		11309'9"	9,10,11	10.0	0.050000	2,120		295	1,352	1,734	1,440	4 9/16 in
162		11310'9"	5,5,5	5.0	0.025000	8,985		585	11,527	9,604	10,487	6 12/16 in
163		11311'11"	8,7,8	7.7	0.038333	3,478		288	1,243	1,633	1,343	5 4/16 in
164		11311'5"	7,8,7	7.3	0.036667	3,779		380	3,175	3,266	3,001	5 2/16 in
165		11311'6"	7,7,8	7.3	0.036667	3,779		332	2,028	2,330	2,029	5 2/16 in
166		11312'	8,8,9	8.3	0.041667	2,978		333	2,049	2,348	2,046	1 10/16 in
167		11312'3"	9,9,8	8.7	0.043333	2,768		322	1,828	2,159	1,856	2 6/16 in
168		11312'7"	8,7,9	8.0	0.040000	3,213		261	877	1,277	1,010	1 14/16 in
169		11313'	7,8,9	8.0	0.040000	3,213		328	1,947	2,261	1,959	1 1/16 in
170		11313'1"	8,8,8	8.0	0.040000	3,213		281	1,140	1,536	1,251	2 in
171		11313'8"	9,9,10	9.3	0.046667	2,411		308	1,570	1,932	1,632	2 6/16 in
172		11314'	9,10,10	9.7	0.048333	2,258		304	1,501	1,870	1,571	1 7/16 in
173		11314'1"	9,8,8	8.3	0.041667	2,978		318	1,752	2,092	1,790	1 10/16 in
174		11314'4"	8,9,8	8.3	0.041667	2,978		314	1,678	2,027	1,726	1 6/16 in
175		11315'0"	7,8,8	7.7	0.038333	3,478		331	2,008	2,313	2,011	4 7/16 in
176		11315'10"	6,6,6	6.0	0.030000	5,493		613	13,046	10,795	12,010	3 12/16 in
177		11315'6"	9,9,9	9.0	0.045000	2,580		282	1,154	1,550	1,264	3 14/16 in
178		11316'1"	8,9,10	9.0	0.045000	2,580		370	2,910	3,055	2,778	4 in
179		11316'6"	10,8,8	8.7	0.043333	2,768		320	1,790	2,125	1,823	4 14/16 in
180		11316'9"	9,9,9	9.0	0.045000	2,580		270	990	1,390	1,114	3 4/16 in
181		11317'6"	8,8,8	8.0	0.040000	3,213		348	2,376	2,621	2,325	3 9/16 in
182		11318'10"	8,8,8	8.0	0.040000	3,213		373	2,988	3,118	2,844	3 in
183		11319'	8,8,10	8.7	0.043333	2,768		380	3,175	3,266	3,001	1 1/16 in
184		11319'1"	9,8,8	8.3	0.041667	2,978		363	2,733	2,913	2,628	1 2/16 in
185		11319'5"	8,10,8	8.7	0.043333	2,768		284	1,184	1,577	1,290	1 9/16 in
186		11320'	8,9,10	9.0	0.045000	2,580		349	2,399	2,640	2,345	5 10/16 in
187		11320'1"	6,7,6	6.3	0.031667	4,966		539	9,202	7,826	8,270	5 10/16 in
188		11320'6"	5,6,6	5.7	0.028333	6,111		640	14,575	12,023	13,609	2 15/16 in
189		11321'1"	9,8,9	8.7	0.043333	2,768		358	2,611	2,814	2,524	3 10/16 in
190		11321'7"	9,9,9	9.0	0.045000	2,580		346	2,331	2,584	2,287	4 6/16 in
191		11322'	8,9,9	8.7	0.043333	2,768		369	2,885	3,035	2,756	5 4/16 in
192		11322'11"	5,5,5	5.0	0.025000	8,985		603	12,495	10,360	11,450	4 1/16 in
193		11322'3"	6,5,5	5.3	0.026667	7,125		622	13,549	11,196	12,528	5 4/16 in
194		11322'6"	9,8,9	8.7	0.043333	2,768		323	1,848	2,176	1,873	3 12/16 in
195		11323'8"	8,8,8	8.0	0.040000	3,213		359	2,635	2,833	2,545	2 10/16 in
196		11324'	8,8,9	8.3	0.041667	2,978		367	2,834	2,994	2,713	3 2/16 in
197		11324'4"	9,9,9	9.0	0.045000	2,580		320	1,790	2,125	1,823	3 in
198		11325'0"	10,8,10	9.3	0.046667	2,411		276	1,070	1,468	1,187	1 12/16 in
199		11325'1"	8,8,8	8.0	0.040000	3,213		307	1,552	1,916	1,617	2 12/16 in
200		11325'6"	9,9,9	9.0	0.045000	2,580		362	2,708	2,893	2,607	4 1/16 in

Continued...

Sante North Unit A 1H												
Sample Number	FM	Depth (Ft, in)	Dimpler Diameter (Tick Marks)	Average Dimple (Divisions)	Average Dimple (in)	DIMPLE UCS (psi)		Bambino Average L' (5 Samples)	UCS - Enderlin (psi)	UCS - Aoki and Matsukura 2008 (psi)	UCS - Zahm et al 2014 - (psi)	Length of Core Piece (in)
201		11325'8"	8,8,8	8.0	0.040000	3,213		371	2,936	3,076	2,800	3 4/16 in
202		11326'8"	9,9,9	9.0	0.045000	2,580		318	1,752	2,092	1,790	1 1/16 in
203		11327'	8,9,8	8.3	0.041667	2,978		204	356	690	494	1 9/16 in
204		11327'2"	8,8,8	8.0	0.040000	3,213		351	2,445	2,678	2,384	1 9/16 in
205		11327'6"	6,5,6	5.7	0.028333	6,111		604	12,550	10,403	11,506	2 6/16 in
206		11328'11"	7,7,7	7.0	0.035000	4,121		362	2,708	2,893	2,607	3 11/16 in
207		11328'7"	8,9,9	8.7	0.043333	2,768		364	2,758	2,933	2,649	4 4/16 in
208		11329'1"	8,9,8	8.3	0.041667	2,978		348	2,376	2,621	2,325	4 9/16 in
209		11329'7"	7,8,8	7.7	0.038333	3,478		317	1,733	2,076	1,774	5 in
210	MANESS	11330'0"	8,8,10	8.7	0.043333	2,768		403	3,836	3,783	3,559	4 7/16 in
211		11330'10"	7,7,7	7.0	0.035000	4,121		427	4,604	4,372	4,209	4 14/16 in
212		11330'5"	8,8,8	8.0	0.040000	3,213		392	3,511	3,530	3,284	3 6/16 in
213		11331'1"	7,8,7	7.3	0.036667	3,779		389	3,425	3,463	3,212	2 7/16 in
214		11331'4"	7,8,7	7.3	0.036667	3,779		398	3,686	3,667	3,432	5 6/16 in
215		11332'	10,8,10	9.3	0.046667	2,411		244	688	1,079	830	5 11/16 in
216		11332'2"	8,7,8	7.7	0.038333	3,478		377	3,094	3,202	2,933	5 11/16 in
217		11332'6"	9,8,8	8.3	0.041667	2,978		386	3,340	3,397	3,141	4 13/16 in
218		11333'0"	7,6,7	6.7	0.033333	4,514		558	10,135	8,534	9,144	3 12/16 in
219		11333'6"	9,9,9	9.0	0.045000	2,580		373	2,988	3,118	2,844	2 in
220		11334'0"	8,8,9	8.3	0.041667	2,978		373	2,988	3,118	2,844	4 1/16 in
221		11334'11"	7,8,7	7.3	0.036667	3,779		379	3,148	3,245	2,978	4 in
222		11335'11"	5,4,5	4.7	0.023333	11,725		679	16,880	13,939	16,156	5 10/16 in
223		11336'	6,6,6	6.0	0.030000	5,493		617	13,269	10,972	12,239	5 10/16 in
224		11336'11"	5,5,6	5.3	0.026667	7,125		639	14,518	11,976	13,547	2 12/16 in
225		11336'7"	5,5,5	5.0	0.025000	8,985		679	16,880	13,939	16,156	3 3/16 in
226		11337'	6,6,6	6.0	0.030000	5,493		597	12,169	10,104	11,123	1 1/16 in
227		11338'	5,6,5	5.3	0.026667	7,125		679	16,880	13,939	16,156	3 8/16 in
228		11338'5"	6,6,5	5.7	0.028333	6,111		544	9,444	8,009	8,495	1 8/16 in
229	BUDA	11339'	6,5,5	5.3	0.026667	7,125		684	17,182	14,197	16,503	6 12/16 in
230		11339'0"										
231		11339'11"	4,4,4	4.0	0.020000	20,091		669	16,279	13,432	15,475	3 3/16 in
232		11340'10"	4,5,5	4.7	0.023333	11,725		637	14,402	11,883	13,425	6 6/16 in
233		11340"1"	4,5,5	4.7	0.023333	11,725		707	18,591	15,421	18,164	3 in
234		11341'3"	5,5,6	5.3	0.026667	7,125		584	11,474	9,563	10,435	4 7/16 in
235		11341"9"	5,5,5	5.0	0.025000	8,985		667	16,160	13,332	15,341	4 8/16 in
236												

Vita

Samantha Patterson was born in Springfield, Missouri on June 6, 1991. She then moved to Syracuse, New York before beginning grade school in Colleyville, Texas where she graduated from Grapevine High School in 2009. She earned her Bachelors of Science in Environmental Earth Resources (now known as Applied Geoscience) from Texas Christian University in 2013, where she participated in the Alpha Chi Omega sorority and rode for the NCAA TCU equestrian team.

After completing her undergraduate career, Samantha began her career as an associate geologist and later as a geologist for Lonestar Resources in Fort Worth, Texas. While continuing to work, Samantha returned to graduate school at Texas Christian University to further her education in the technical aspect of geology. She is a member of the American Association of Petroleum Geologist and the Fort Worth Geological Society.

Samantha currently resides in Fort Worth, Texas with her dog, River, and her horse, Deacon. Following graduation, she will continue to work as a geologist for Lonestar Resources.

ABSTRACT

THE MANESS SHALE: A COMPARISON OF THE GEOMECHANICAL AND MINERALOGICAL PROPERTIES WITHIN THE LOWER EAGLE FORD FORMATION, SOUTH TEXAS

By Samantha Patterson, M.S., 2018

Department of Geology

Texas Christian University

Thesis Advisor: Richard Denne, Hunter Enis Chair in Petroleum Geology

The Maness Shale is a clay-rich mudrock that has been correlated to the basal Lower Eagle Ford in South Texas. Where present, the Maness may prove beneficial, acting as a fracture barrier between hydraulically fractured Eagle Ford wellbores and underlying aquifers. Geomechanical studies demonstrate that the Maness is 34% weaker than the Eagle Ford and 76% weaker than the Buda. XRD analyses found that the samples from the Maness contain an average of 10% more clay than the Eagle Ford.

A regression analysis established a 91.7% correlation between Maness thickness and oil/water ratios, which are based on cumulative first year oil and water production, indicating that the Maness may be acting as a fracture barrier in the region. This analysis also found a 50% decrease in oil/water ratios between Maness thicknesses of 5 to 10 ft (1.5 to 3.1 m), suggesting that a minimum of 10 ft is needed for the Maness to effectively act as a fracture barrier.